

AD-A145 990

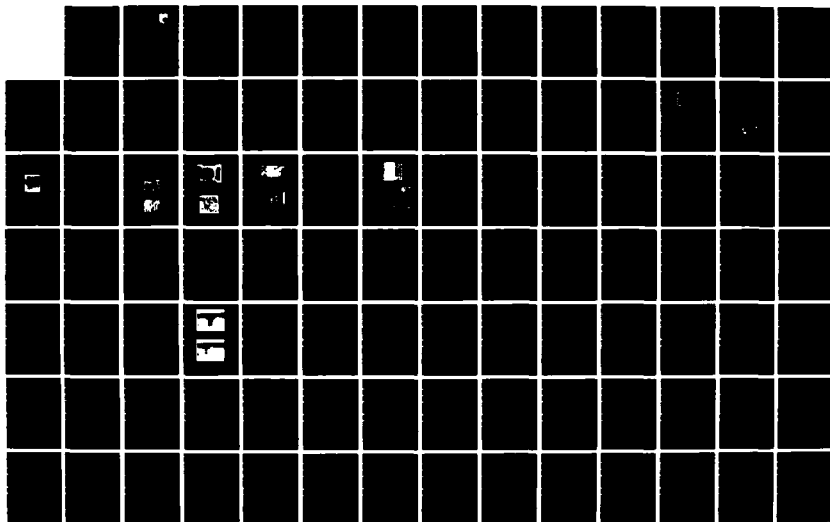
RESEARCH IN QUANTITATIVE NDE TECHNIQUES(U) SYSTEMS
RESEARCH LABS INC DAYTON OH RESEARCH APPLICATIONS DIV
D A STUBBS ET AL MAR 84 SRL-6575 AFWAL-TR-84-4026
F33615-80-C-5015

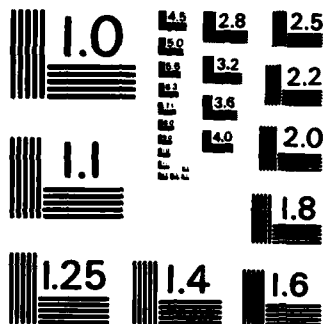
1/3

UNCLASSIFIED

F/G 13/8

NL





MICROCOPY RESOLUTION TEST CHART
NATIONAL BUREAU OF STANDARDS-1963-A

AD-A145 990

DTIC FILE COPY

AFWAL-TR-84-4026

RESEARCH IN QUANTITATIVE NDE TECHNIQUES



D. Stubbs
W. Hoppe

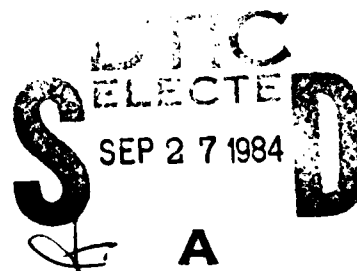
Research Applications Division
Systems Research Laboratories, Inc.
2800 Indian Ripple Road
Dayton, OH 45440-3696

March 1984

Final Report for Period 30 April 1980 - 31 August 1983

Approved for public release; distribution unlimited.

MATERIALS LABORATORY
AIR FORCE WRIGHT AERONAUTICAL LABORATORIES
AIR FORCE SYSTEMS COMMAND
WRIGHT-PATTERSON AIR FORCE BASE, OH 45433



84 09 24 012

NOTICE

When Government drawings, specifications, or other data are used for any purpose other than in connection with a definitely related Government procurement operation, the United States Government thereby incurs no responsibility nor any obligation whatsoever; and the fact that the government may have formulated, furnished, or in any way supplied the said drawings, specifications, or other data, is not to be regarded by implication or otherwise as in any manner licensing the holder or any other person or corporation, or conveying any rights or permission to manufacture use, or sell any patented invention that may in any way be related thereto.

This report has been reviewed by the Office of Public Affairs (ASD/PA) and is releasable to the National Technical Information Service (NTIS). At NTIS, it will be available to the general public, including foreign nations.

This technical report has been reviewed and is approved for publication.

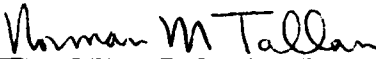


ROBERT L. CRANE
Nondestructive Evaluation Branch
Metals and Ceramics Division



DONALD M. FORNEY, JR., Chief
Nondestructive Evaluation Branch
Metals and Ceramics Division

FOR THE COMMANDER



NORMAN M. TALLAN
Chief, Metals and Ceramics Division

"If your address has changed, if you wish to be removed from our mailing list, or if the addressee is no longer employed by your organization please notify AFWAL/MLLT, W-PAFB, OH 45433 to help us maintain a current mailing list".

Copies of this report should not be returned unless return is required by security considerations, contractual obligations, or notice on a specific document.

UNCLASSIFIED

SECURITY CLASSIFICATION OF THIS PAGE

REPORT DOCUMENTATION PAGE

1a. REPORT SECURITY CLASSIFICATION Unclassified			1b. RESTRICTIVE MARKINGS		
2a. SECURITY CLASSIFICATION AUTHORITY			3. DISTRIBUTION/AVAILABILITY OF REPORT Approved for public release; distribution unlimited.		
2b. DECLASSIFICATION/DOWNGRADING SCHEDULE					
4. PERFORMING ORGANIZATION REPORT NUMBER(S) 6575 Final			5. MONITORING ORGANIZATION REPORT NUMBER(S) AFWAL-TR-84-4026		
6a. NAME OF PERFORMING ORGANIZATION Systems Research Laboratories, Inc.		6b. OFFICE SYMBOL (If applicable)		7a. NAME OF MONITORING ORGANIZATION Materials Laboratory (AFWAL/MLLP) Air Force Wright Aeronautical Laboratories (AFSC)	
6c. ADDRESS (City, State and ZIP Code) 2800 Indian Ripple Road Dayton, OH 45440-3696				7b. ADDRESS (City, State and ZIP Code) Wright-Patterson Air Force Base Ohio 45433	
8a. NAME OF FUNDING/SPONSORING ORGANIZATION		8b. OFFICE SYMBOL (If applicable)		9. PROCUREMENT INSTRUMENT IDENTIFICATION NUMBER F33615-80-C-5015	
8c. ADDRESS (City, State and ZIP Code)		10. SOURCE OF FUNDING NOS.			
		PROGRAM ELEMENT NO.		PROJECT NO.	TASK NO.
		62102F		2306	P5
11. TITLE (Include Security Classification) Research in Quantitative NDE Techniques		WORK UNIT NO. 06			
12. PERSONAL AUTHOR(S) Stubbs, David A. and Hoppe, Wally C.					
13a. TYPE OF REPORT Final Report		13b. TIME COVERED FROM 80-4-30 TO 83-8-31		14. DATE OF REPORT (Yr., Mo., Day) March 1984	
				15. PAGE COUNT 210	
16. SUPPLEMENTARY NOTATION					
17. COSATI CODES			18. SUBJECT TERMS (Continue on reverse if necessary and identify by block number)		
FIELD	GROUP	SUB. GR.	NDE, Ultrasound, Composites, Leaky Rayleigh Waves, Rayleigh Surface Waves, Layered Interface, Reflection of Finite Acoustic Beams, Cylindrical Rayleigh Waves, Plate Waves,		
20	01				
11	04				
19. ABSTRACT (Continue on reverse if necessary and identify by block number)					
<p>Analyses of nonspecular reflection of acoustic waves from an interface between a fluid and both a planar, layered halfspace and a corrugated halfspace were conducted. Dispersion of the velocity, the Schoch displacement parameter of leaky Rayleigh waves, and the amplitude distribution of the reflected field were studied. For the planar halfspace one exact and two approximate models are presented. In a study of reflection of Rayleigh surface waves from surface cracks, it was found theoretically and confirmed experimentally that transverse in-plane stresses in the surface wave cause reflections from cracks oriented normal to wavefronts.</p> <p>Several studies were conducted on the interaction of ultrasound and fibrous composites. A model developed and experimentally confirmed describes the interaction of plane waves normally incident on a unidirectional composite with fibers oriented normal to the surface. An acoustic backscattering technique was developed, empirically tested for use on mapping</p>					
20. DISTRIBUTION/AVAILABILITY OF ABSTRACT UNCLASSIFIED/UNLIMITED <input checked="" type="checkbox"/> SAME AS RPT. <input type="checkbox"/> DTIC USERS <input type="checkbox"/>			21. ABSTRACT SECURITY CLASSIFICATION Unclassified		
22a. NAME OF RESPONSIBLE INDIVIDUAL Robert L. Crane, Ph.D.			22b. TELEPHONE NUMBER (Include Area Code) (513) 255-5561		22c. OFFICE SYMBOL AFWAL/MLLP

UNCLASSIFIED

SECURITY CLASSIFICATION OF THIS PAGE

Block 18 continued.

Lamb Waves, C-Scan, Acoustic Backscattering, Graphite/Epoxy, Glass/Epoxy, Boron/Epoxy, Silicon Carbide/Titanium, Corrosion Detection, Pulsed Schlieren System, Inspection of Complex Shapes, Periodic Rough Surfaces, High-Impedance Transducer Backings.

Block 19 continued.

transverse cracks in multilayered composites, and used to detect corrosion in multilayered, metallic samples.

Two systems--C-scan and pulsed Schlieren--were designed as aids in studying NDE techniques. The former has state-of-the-art computer control and data-processing capabilities, and the latter can operate at repetition rates up to 250 pulses per second.

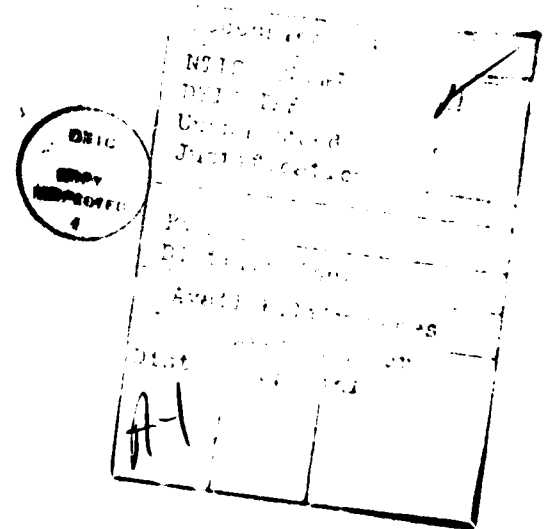
Ultrasonic NDE areas also investigated include using mating parts to improve coupling of acoustic energy into complex-shaped structures and manufacturing a matched-impedance backing to produce a broad-band transducer.

UNCLASSIFIED

PREFACE

This report was prepared by D. Stubbs and W. Hoppe with the assistance of Dr. Y. Bar-Cohen, D. Grosjean, and P. A. Benadum and covers work performed during the period 30 April 1980 through 31 August 1983 under Contract F33615-80-C-5015 (Project 2306, Task P5) by the Research Applications Division of Systems Research Laboratories, Inc., 2800 Indian Ripple Road, Dayton, OH, 45440-3696. Portions of the work discussed herein were accomplished by Drs. Y. Bar-Cohen, A. Nayfeh, and N. K. Batra and Messrs. P. A. Benadum and S. A. Pitman. The contract was administered under the direction of the Air Force Wright Aeronautical Laboratories, Materials Laboratory (AFWAL/MLLP), Wright-Patterson Air Force Base, OH, with Dr. R. L. Crane acting as the Government Project Monitor.

The authors would like to acknowledge for editorial assistance Mrs. Marian Whitaker and Mrs. Helena L. Henrich for preparation of this report.



LIST OF ILLUSTRATIONS

<u>Figure</u>		<u>Page</u>
1	Detection of Corrosion in Multilayered Structure Using Acoustic Backscattering.	14
2	Reflection and Transmission Energy-Flux Coefficients Versus Incident Angle for Water/Al Interface. Note peak in transmitted shear-wave at 16 deg.	15
3	a) Backscatter C-Scan of Corroded Al Plate at Incident Angle of 16 deg. b) C-Scan of Same Sample at Incident Angle of 20 deg.	16
4	Backscatter C-Scan of Porosity in Epoxy Adhesive. Note similarity to results from corrosion as seen in Fig. 3.	17
5	Backscatter C-Scan of 150- μ m-diam. W Particles Imbedded in Al Plate. Individual particles can be detected, thus giving indication of resolution of backscattering technique.	17
6	Backscatter C-Scan of Al Plate with Series of Scratches. Scratches run perpendicular to scanning direction. 50- μ m and 30- μ m scratches are detected even under thick layer of paint.	19
7	Backscatter C-Scan of Three Al plates with Corrosion on Bottom Side. Each plate was exposed to a salt-fog environment for (a) 170 hr, (b) 498 hr., and (c) 998 hr. to produce varying degrees of corrosion.	21
8	Through-Transmission of Al/Epoxy/Al Sandwich. Heavily corroded inner surface is not detected. Varying degrees of lightness are due to varying thickness of epoxy layer. Supports holding sandwich are seen on left and right sides.	22
9	Backscatter C-Scan of Same Sample as in Fig. 8. Incident angle is 16 deg. Corrosion is easily detected.	22
10	Through-Transmission C-Scan of Al/Sealant/Graphite-Epoxy Sample. Irregularities in Sealant are detected.	23
11	Backscatter C-Scan of Same Sample as in Fig. 10. Dark areas could be an indication of corrosion; however, visual inspection showed sealant to be very porous in these areas. Four dark circular areas are reflections from rivets holding layers together.	23

LIST OF ILLUSTRATIONS (Continued)

<u>Figure</u>		<u>Page</u>
12	Backscatter C-Scan of a) Periodic Rough Front Surface of Al Plate, b) Corroded Back Surface Insonified from Front Side, and c) Corroded Back Surface Insonified from Back Side.	25
13	Components of C-Scan System.	27
14	Diagram Showing Components of Pulsed Schlieren System. Rays showing light path are drawn.	30
15	Schematic Diagram of Power Supply Employed to Produce High-Voltage Pulse.	31
16	Schematic Diagram of Pulse Electronics.	32
17	Angles at Which Anomalies Occur in Reflection Coefficient for Various Orders, n, Versus Frequency of Exciting Ultrasonic Wave for Al Sample with Periodic Rough Surface with Period 0.74 mm.	37
18	Test Setup Used to Search for Anomalies in Reflection Coefficient. "T" is transmitter and "R" is receiver (wide angle of reception).	39
19	Test Setup Used To Search for Anomalies in Reflection Coefficient Suggested by Rollings (Ref. 7). Transmitter is also receiver. Smooth surface is reference reflector.	39
20	Test Setup Used to Search for Anomalies in Reflection Coefficient. Transmitter is also receiver. Cylindrical object is reference reflector.	40
21	Sample Scan of Rough-Surface Sample at 3 MHz While Angle is Varied. Reflectance was measured by method described using cylindrical reflector.	42
22	Measured Reflection Coefficient of Acoustic Beam Normally Incident upon 0.74-mm-Period Al Sample. Insonifying beam is toneburst.	43
23	Measured Reflection Coefficient of Acoustic Beam Normally Incident upon 0.14-mm-Period Brass Sample. Insonifying beam is toneburst.	43
24	Block Diagram of Pulse-Echo Technique Used to Search for Anomalies in Reflection Coefficient of Acoustic Beam Normally Incident upon Periodic Rough Surface.	45

LIST OF ILLUSTRATIONS (Concluded)

<u>Figure</u>		<u>Page</u>
25	Results of Pulse-Echo Technique Used to Search for Anomalies in Reflection Coefficient of Acoustic Wave Normally Incident upon 0.74-mm Corrugated Al Sample. a) Reference Pulse from Flat Al Sample, b) Received Pulse from Corrugated Al Sample, c) Reflection Coefficient of Corrugated Al Sample Calculated by Deconvolution of Signal in a) from signal in b). Frequency domain.	46
26	Results of Pulse-Echo Technique Used to Search for Anomalies in Reflection Coefficient of Acoustic Beam Normally Incident upon 0.14-mm-Period Corrugated Brass Sample. a) Reference Pulse from Flat Brass Sample, b) Pulse from Corrugated Brass Sample, and c) Deconvolved Reflection Coefficient in Frequency Domain.	47
27	a) Result of Time Gate Applied to Pulse in Fig. 25(a), Gating on "Ringing Tail." Represents Surface Wave Mode, b) Frequency Domain of Gated Pulse in (a).	48
28	Schlieren Photograph of Reflected Beam from 0.74-mm Corrugated Al Sample Showing No Beam Displacement.	50
29	Schlieren Photograph of Reflected Beam from 0.74-mm Corrugated Al Sample Showing Beam Displacement. Angle of incidence is same as in Fig. 28.	50
30	Sample Field Distributions of Reflected Beam from 0.74-mm Al Sample at 12-deg. Angle of Incidence. a) Reference Distribution from Flat Surface, b) - d) Distributions Obtained from Corrugated Surface at Three Different Frequencies.	52
31	Experimentally Determined Values for Mean Position of Energy in Reflected Field from 0.74-mm Corrugated Al Sample and from Reference Flat Al Sample. Angles of incidence are (top to bottom) 12, 18, 25, and 31 deg.	53
32	Experimentally Determined Values for Variance of Energy in Reflected Field from 0.74-mm Corrugated Al Sample and from Reference Flat Al Sample. Angles of incidence are (top to bottom) 12, 18, 25, and 31 deg.	54
33	Data from Experiment to Measure Imaginary Part of Wavenumber of Surface Acoustic Wave on 0.74-mm Corrugated Al Sample. Log of amplitude of received signal is plotted versus lateral position of receiving transducer.	56

Section 1

INTRODUCTION

The purpose of the research described herein was to develop NDE techniques for quantitative characterization of flaws found in multilayered structures and coated aerospace components. The main thrust of the effort was on utilization of the interactive characteristics of ultrasound with the various materials of interest, including primarily the study and use of surface-wave and backscattering phenomena for the detection and characterization of flaws.

Engine components used in high-temperature, corrosive environments generally have protective coatings. A number of other aerospace structures are plated or coated to protect against corrosion. A frequent problem with such structures is the development of surface fatigue cracks. Due to the proximity of the cracks to the surface, detection by bulk-wave ultrasonic techniques is difficult. In addition, protective coatings perturb the ultrasonic surface waves, making data interpretation unwieldy. This effort involved analyses of the interaction of Rayleigh surface waves with coated substrates, the coating being described as either a loading layer or a stiffening layer. Experimental data have confirmed the accuracy of the theoretical models. The development of these models is described briefly in Section 2. Appendix A contains publications describing the models in detail and the results of these efforts.

The study of surface waves prompted interest in a specific case--that of ultrasonic wave interaction with a crack oriented parallel to the wave-propagation direction. In this case, one would ordinarily expect difficulties in detection of the crack. However, surface-wave reflections were observed. Section 3 contains a brief description, with the details being contained in the publication in Appendix B.

An interesting class of multilayer structures--composites--is becoming increasingly important in aerospace systems. Such structures consist of multiple layers of varying orientation, each layer containing many rows of parallel fibers bound together with a matrix. In one study leaky, plate-wave modes in fiber-reinforced plastic composites were observed. The amplitude

distribution of the reflected field was recorded as a function of position. Also, the frequency dependence of the plate-mode phase velocities was studied. Both unidirectional and cross-ply composites were investigated.

An analytical model describing the reflection of ultrasonic waves incident parallel to the fiber direction of a unidirectional composite was also developed. Experimental data were collected, showing the model to provide a good fit to the data in certain frequency ranges. This model is discussed in Section 4 along with the leaky-plate-wave observations. Appendix C contains publications giving more detailed accounts.

Studies conducted on commonly used graphite/epoxy composites showed that fiber-matrix interface and interlaminar interface damage generally precedes either fiber breakage or complete failure. An additional form of failure is transverse cracking due to in-plane tensile stress normal to the fiber direction. Conventional ultrasonic detection of these types of flaws is difficult due to the inhomogeneous, anisotropic, layered nature of composites. The backscattering technique described in Section 5 and in the publications of Appendix D, utilizes the complex nature of composites to an advantage. In this work, which is empirical in nature, success has been achieved in the detection and mapping of transverse cracks, porosity, and fiber orientation.

A backscattering technique was also found to be useful in detecting corrosion in multilayered material. The advantages and limitations of this technique are discussed in Section 6.

To aid in the research effort, two NDE systems were designed and constructed. A high precision, C-scan system was developed for use in testing the various ultrasonic techniques as well as in providing quantitative inspection of test samples. This system is described in Section 7, and Appendix E contains details of the unique electronic interfaces. Additionally, as an aid in visualizing the complex interaction of ultrasonic waves with the surfaces of test samples, a pulsed-Schlieren system was developed; details are contained in Section 8.

Several other areas of NDE were also studied during this research effort. Currently, many complex engine components are manufactured by powder-metallurgy techniques to produce a near-net-shape product. Frequently, non-destructive techniques employing ultrasonics cannot be utilized successfully for inspecting these complex-shaped parts because of the difficulty involved in coupling the acoustical energy to all regions of interest. In an effort to solve this problem, a study was conducted using mating parts--parts that have a surface which is a complement of the test part--to allow complete insonification of all areas of the component being inspected. This work demonstrates that the mating part effected a large transmission of ultrasound into the test piece for incident angles up to 80°. Section 9 contains a description of this work; the resulting publication can be found in Appendix F.

Another area of research was the study of the interaction of ultrasound with corrugated surfaces. The main emphasis was placed on observing the amplitude and displacement of reflected energy at the various angles where surface waves are predicted to be excited. The study showed that for some samples, the surface wave velocity appeared to be unperturbed by the corrugated surface. A description of this work and the results are found in Section 10 and Appendix G.

A third area of additional research was the development of a high-impedance, broadband, ultrasonic, transducer backing. Efforts were made to find materials which would be superior to the tungsten and epoxy combination currently in widespread use for backings. The research showed that a different matrix was needed; a low melting point alloy was selected to be used in place of epoxy. A combination of tungsten, copper, and an indium-lead alloy was used to produce a backing which met the required specifications. When this backing was adhered to a piezoelectric blank, the ultrasonic output from the blank was very broadband, exceeding the bandwidth of available commercial transducers having similar center frequency. Section 11 and Appendix H contain descriptions of this effort and the resulting publication, respectively.

Section 2

SURFACE WAVE INTERACTIONS WITH LAYERED HALF-SPACES

The necessity for detecting surface or near-surface cracks or defects in aerospace structures has provided the impetus for the development of viable surface-acoustic-wave NDE techniques. Many of these structures have platings or coatings applied to protect against corrosion. Inspection of such structures with surface acoustic waves requires an understanding of the phenomenon of leaky Rayleigh waves on layered substrates. Appendix A contains four papers which describe studies conducted under this contract on this subject. In addition to dispersion of the surface wave velocity and the displacement parameter Δ_s , the amplitude distribution of the leaking wave is modeled in these publications.

Three approaches to the study of the reflection of finite beams from layered halfspaces in fluids are presented. The first model is approximate and assumes that the layer is thin compared to the wavelength in the fluid, implying that the particle displacement across the layer is constant. From this assumption and an averaging procedure, the effect of the layer is found to be contained in a modification of the stress boundary conditions for an unlayered halfspace in the form of a nonzero homogeneous term. These modified boundary-value conditions then produce the reflection coefficient from which a characteristic equation is extracted. The complex roots of the characteristic equation correspond to poles in the reflection coefficient in the complex wave-number space. From these roots, the wave velocity and the displacement parameter Δ_s , also known as the Schoch displacement, can be calculated. Difficulties in solving for the roots of the characteristic equation are overcome by assuming that the wave velocity is unperturbed by the presence of the fluid. This simplified equation yields the velocity. A separate analysis is performed to solve for Δ_s which involves the assumption that the magnitude of the reflection coefficient is approximately one. Finally, through the use of the formalism derived by Bertoni and Tamir,¹ an analytical expression for the amplitude distribution is derived. In this formalism, the reflection coefficient is approximated by a Laurent expansion about the surface wave pole. Reasonably good agreement exists between

experiment and theory for ratios of layer thickness to incident wavelength of less than 0.3.² For higher ratios, the agreement deteriorates.

The second model, the extended approximate model, does not make the preliminary assumption that the layer is thin but uses exact expressions for the wave potential in each of the three media. The exact reflection coefficient is then derived. This coefficient is expected to be accurate for all layer thicknesses, provided acoustic attenuation can be neglected. Again, the velocity and Δ_s can be calculated from the location of the poles in the complex wave-number space. In this model the poles are located by numerical methods. Again, the wave velocity and the Δ_s are applied to the analysis given by Bertoni and Tamir, where the reflection coefficient is approximated by a Laurent expansion about the pole. From this formalism an analytical expression is derived to approximate the amplitude distribution of the reflected field.

As shown in Refs. 3 and 4, the behavior of Δ_s predicted by the extended approximate model is unexpected according to the first model. Also, shown is a comparison of experimental data and theoretical calculations of the surface wave velocity and the amplitude distribution for the case of a loading layer. Limited data are also presented on the stiffening layer case. Very good agreement is shown in most aspects considered.

The third model⁸ is essentially the same as the second, with the exception that the analysis of Bertoni and Tamir is carried out numerically, i.e., the reflection coefficient is not approximated by a Laurent expansion. It is, therefore, termed an exact treatment. Consequently, this model gives results for the wave velocity and Δ_s which are identical to the extended approximate model.

In the loading-layer case, good agreement is found between the amplitude distributions calculated from these models. However, for the stiffening case, such agreement is not always observed. As explained,⁵ for the stiffening-layer case when the surface wave speed is nearly equal to the transverse velocity in the substrate, the wave can no longer be generated (wave cutoff).

In this paper it is demonstrated that near this cutoff, because of a rapid change in the reflection coefficient which is unaccounted for in a Laurent expansion, the extended approximate model differs significantly from the exact treatment. The exact treatment is also shown to agree quite well with an experimentally determined amplitude distribution.

As a result of the study of leaky Rayleigh waves on layered halfspaces, it is clear that the phenomenon can be accurately modeled. Various aspects of this phenomenon can be exploited to enhance NDE techniques using surface acoustic waves as applied to coated structures. Again, the details of this study are found in Appendix A.

Section 3

TRANSVERSE STRESS IN RAYLEIGH SURFACE WAVES

Surface-connected cracks frequently encountered in inspected parts can be detected, in many instances, using ultrasonic surface waves. In general, it has been thought that reflections from these cracks can be observed only if the plane of the crack is perpendicular to the direction of propagation of the surface wave. In this research it was shown, both theoretically and experimentally, that surface-connected cracks parallel to the propagation direction of the interrogating surface wave can also be detected.

It can be shown theoretically that Rayleigh surface waves contain non-zero tractions on the free surface perpendicular to the direction of propagation. (See Appendix B). Any disturbance of these stresses causes scattering of the surface wave. A crack normal to the surface and parallel to the interrogating surface wave disturbs these stresses sufficiently to cause scattering; it was anticipated that this backscattering would be sufficiently strong to be detected. These theoretical results also hold for surface-connected cracks in bolt holes being interrogated by cylindrical Rayleigh waves.

To confirm the theoretical predictions, a surface-connected crack was produced in several glass plates with the crack plane being perpendicular to the surface and extending straight into the glass from one edge. A surface-wave transducer was placed on the glass and oriented in such a way that the surface wave would propagate parallel to the crack. In practice, the crack had closed so tightly that no reflection could be detected. However, once the crack was slightly opened (with a knife blade), a reflection from it occurring at the expected time delay (see Fig. 2 in Appendix B), could be easily detected.

An additional test was performed to eliminate the possibility of reflection from the high stress fields around the tip of the crack. The tip was covered with a small piece of electrical tape to dampen the surface waves. The crack was opened and, with the use of polarized light, the stress field could be easily seen to extend at least 1 cm beyond the tape. However, under these

conditions no reflection of the surface waves was observed. Upon the removal of the tape, the signal from the crack could again be detected. Appendix B contains the publication resulting from this effort. Both theoretical and experimental details are given.

Section 4

ACOUSTIC REFLECTION FROM COMPOSITE MATERIAL

An empirical study of the leaky phenomenon of plate waves in composite plates was conducted. It was found that for a composite plate immersed in a fluid, plate modes can be excited which then leak back into the fluid. When the reflected field is plotted as a function of position, a minimum and a long decaying tail are observed, similar to the characteristics of leaky Rayleigh waves from isotropic materials. In addition, the phase velocities of the plate modes were found to be dependent upon the ultrasonic frequency and plate thickness. Appendix C contains information on the reflected field profiles for unidirectional and cross-ply composites. A dispersion curve for the cross-ply plate is also given.

Theoretical studies of acoustic reflection from composites were also conducted. Due to the inhomogeneous, anisotropic layered nature of composites, analytical models describing ultrasonic wave propagation in and reflection from these materials are very complicated. In an effort to gradually approach the complicated analysis involved in this problem, work was begun on a building-block approach to model development, with each analytical block increasing in complexity.

In the first analysis, completed in this contract period, a unidirectional composite was treated as a homogeneous, anisotropic dispersive medium by averaging the properties of the fiber and matrix. The material was assumed to be oriented such that its principle direction was parallel to the wave propagation. Details are contained in Appendix C. This analysis provided the reflection coefficient for the composite when insonified in a direction along the fibers. Experiments were performed to verify this model by measuring the longitudinal velocity in graphite/epoxy and boron/epoxy composites. The experimental reflection coefficient was calculated from the velocities and densities of the water and composite. As seen in Appendix C, in the frequency range where the wavelength in water was greater than approximately twice the diameter of the fibers (the range over which model assumptions were valid), the agreement between the model and experiment was quite satisfactory.

Section 5

ULTRASONIC BACKSCATTERING FOR NDE OF COMPOSITES

In recent years new materials such as composites have found increasing use in primary aerospace structures. In general these materials are anisotropic, inhomogeneous, and layered in nature. An obstacle to the widespread acceptance of these materials has been the inability to test them adequately and nondestructively. The use of ultrasonics on composites such as graphite/epoxy has met with little success due to the profuse scattering and reflection from the different layers and bundles of fibers which obscure scattering from the flaws.

When an ultrasonic beam is incident on a composite material, a large portion of its energy is specularly reflected. If a flaw is present, a small amount of the beam will be scattered in all directions and a detection transducer will intercept only a small solid angle of this scattered signal. To a large extent, this low-level signal is masked by the specular reflections from the various interfaces of the material. However, the specular signal is at a minimum--and flaw signal-to-noise at a maximum--if the detector is positioned coincident with the transmitter (backscattering mode). In this work the viability of utilizing backscattering as an NDE method for composites was examined.

Several different types of flaws and failure mechanisms are found in composites. Generally, fiber-matrix and interlaminar interface damage precede either fiber breakage or total failure. Transverse cracking in the matrix often originates from small stress sites such as inclusions or porosity. It was expected that the backscattering technique could be used successfully to detect all of these types of flaws. In this research, the detection of transverse cracks, porosity, and fiber misalignment was emphasized. For this study several different types of composites were examined, including graphite/epoxy, glass/epoxy, boron/epoxy, and silicon carbide/titanium.

Initial results showed a substantial increase in the amplitude of the back-scattered signal when the composites were insonified perpendicular to a fiber

axis, which suggested that the orientation of the plies could also be observed. Tests using a commercial C-scan system confirmed this fact, providing a map of the various plies and their orientations. Further tests were conducted to determine whether flaws, such as transverse cracks, within a single layer were observable. The results showed that for a single particular ply small transverse cracks could be detected and mapped. Further work also indicated that fiber misalignment and porosity were observable in a backscattering configuration. The details of the technique are contained in the publications in Appendix D. Experimental results are discussed along with some advantages and limitations.

Section 6

ACOUSTIC BACKSCATTERING AS A NONDESTRUCTIVE EVALUATION METHOD FOR CORROSION DAMAGE

Corrosion is a deterioration of metallic structures which may severely shorten the lifetime of the structure. In most cases it occurs due to a failure in an inhibition mechanism, e.g., chipping of paint or anodization from a portion of the surface. Corrosion can appear in many forms, depending upon the alloy on which it is generated and the environment to which the material is exposed. Common types of corrosion include 1) uniform surface corrosion--an even decrease in metal thickness over an entire surface, 2) pitting corrosion--localized corrosion to which metals with thin coatings are particularly susceptible, 3) galvanic corrosion--generated at the interface of two dissimilar metals which are in contact, 4) crevice corrosion--trapped moisture in crevices, 5) intergranular corrosion--selective attack along grain boundaries, and 6) stress corrosion--an accelerated corrosion under stress conditions.

Corrosion degrades the performance of structures through generation of stress-concentration sites. When directly accessible, corrosion can be visually detected due to the change in color and the generation of surface damage. Visual aides such as lenses and boroscopic devices are commonly used for periodic quality-assurance inspection of metallic structures. In some cases, radiographic inspection--primarily x-ray and gamma radiography--is used. Eddy-current techniques are also sensitive to corrosion, but their applicability is limited primarily by the need for direct access to the damaged surface. Presently, attempts are made to test inaccessible areas, such as the interface of multilayered structures, using conventional ultrasonic methods. These methods consist of pulse-echo or through-transmission modes and involve measuring the relative increase in attenuation caused by the presence of corrosion which serves as a scattering source. These methods are unreliable due to their vulnerability to artifacts such as the presence of sealant at the back plate of the test structure.

Since corrosion has a random-roughness topography, resulting ultrasonic scattering is not unidirectional. As described in the previous section, the nature of the backscattering techniques eliminates the interference of specular reflections from various interfaces which might mask the corrosion signal. The backscattering technique, therefore, has a detection capability higher than the other commonly used ultrasonic NDE techniques.

Many theoretical analyses of surface roughness are dedicated primarily to periodic roughness. In the present form of these models, the results cannot be inverted to determine the corrosion structure which is random in nature. Due to this limitation of the currently available analytical tools, the investigation described herein dealt with the NDE of corrosion from an empirical point of view, in an attempt to determine the feasibility of using acoustic backscattering as a means of detection and evaluation of corrosion damage. The experimental setup consisted of a commercial pulser/receiver (Automation Industries) and a C-scan system using commercial transducers. Figure 1 is a schematic diagram of a multilayered structure with corrosion damage.

In an attempt to determine an optimal incident angle for the backscattering test, reflection and transmission coefficients were calculated theoretically as a function of incident angle for a longitudinal wave incident on an aluminum/water interface. The results are shown in Fig. 2, where it can be seen that at 16 deg., a maximum transmission coefficient of the shear wave is obtained. This angle was verified experimentally using a corroded sample and C-scanning at two angles, 16 and 20 deg., for purposes of comparison. The sample was exposed to a salt-fog environment for 720 hr. The test results are shown in Fig. 3.

In order to evaluate the effect of the presence of porosity in the adhesive layer of a tested structure, a sample was prepared from 1-mm-thick glass plates, glued together using Devcon 2-ton epoxy adhesive. The sample was prepared in such a way as to insure porosity in the epoxy. The air bubbles were ~ 0.5 mm in diam. and were spread randomly throughout the adhesive layer. The C-scan of this sample is shown in Fig. 4. The test results were verified by comparing them to the porosity content of the adhesive observed

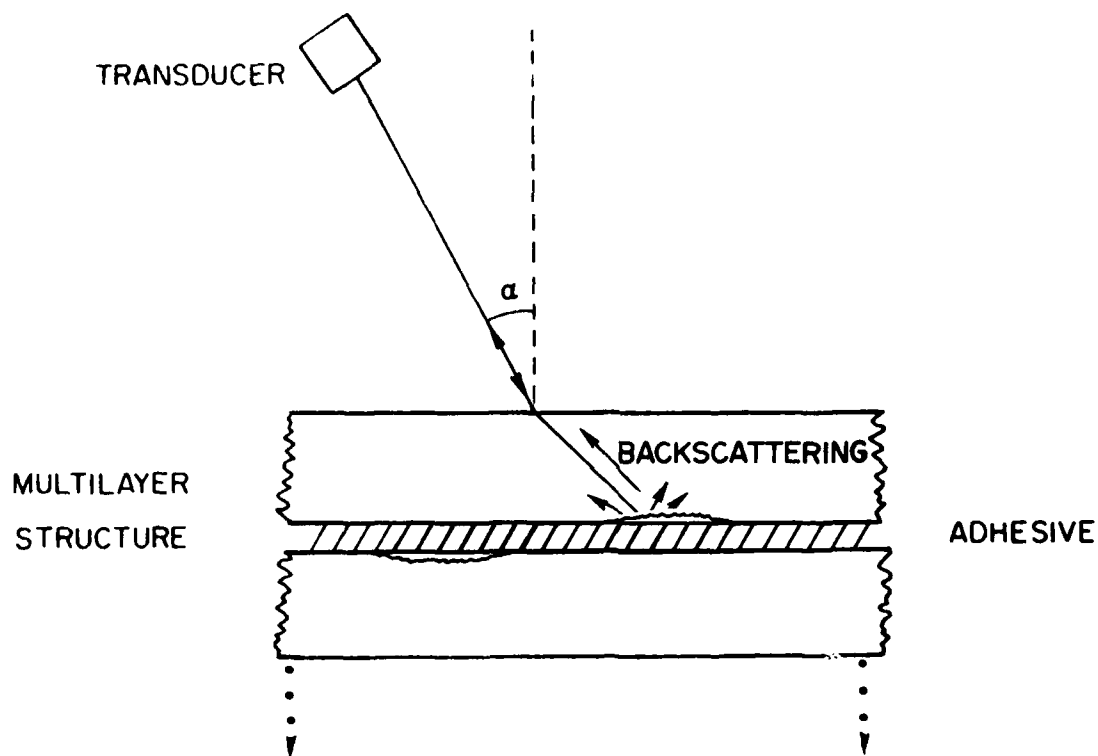


Figure 1. Detection of Corrosion in Multilayered Structure Using Acoustic Backscattering.

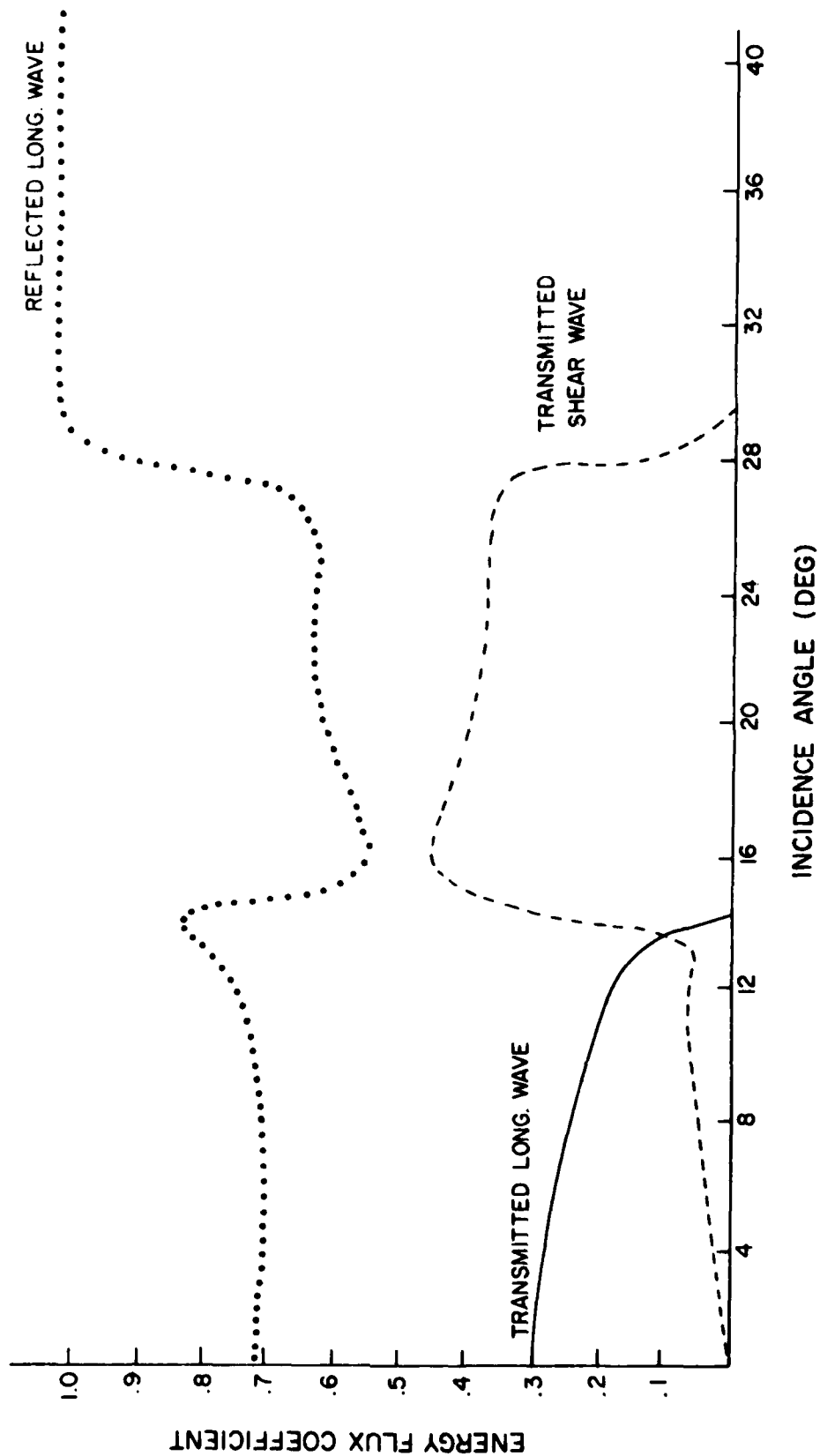


Figure 2. Reflection and Transmission Energy-Flux Coefficients Versus Incident Angle for Water/A1 Interface. Note peak in transmitted shear-wave at 16 deg.



(a)



(b)

Figure 3. a) Backscatter C-Scan of Corroded Al Plate at Incident Angle of 16 deg. b) C-Scan of Same Sample at Incident Angle of 20 deg.

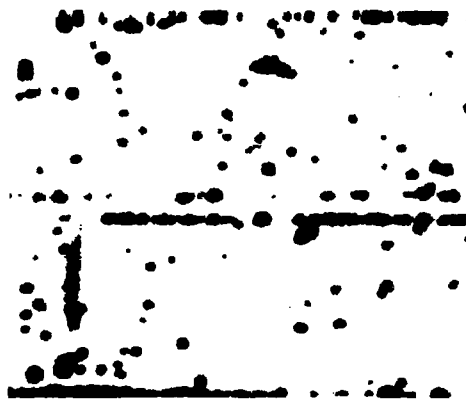


Figure 4. Backscatter C-Scan of Porosity in Epoxy Adhesive. Note similarity to results from corrosion as seen in Fig. 3.



Figure 5. Backscatter C-Scan of 150- μ m-diam. W Particles Imbedded in Al Plate. Individual particles can be detected, thus giving indication of resolution of backscattering technique.

through the glass. As can be seen, porosity in the adhesive layer caused significant backscattering. When comparing this C-scan to those of corroded samples shown later, it is clear that backscattering from porosity is similar to that from corrosion. This ambiguity can cause difficulties in evaluating the source of the indication on the C-scan.

In order to determine the sensitivity and resolution of the technique empirically, a sample was made of 7075T6 aluminum plate, 3 mm in thickness with 150- μ m-diam. tungsten particles imbedded on one side. The particles were pressed into the plate in clusters as well as individually. This sample was C-scanned in a backscatter mode; the results are shown in Fig. 5. The individual particles can be detected easily; however, their apparent size is larger than their actual size due to the directivity of the transducer. The resolution of this C-scan can be improved using a new system now available in the Materials Laboratory which employs improved measurement and signal-processing techniques (described in Section 7).

Several other experiments were performed to test the sensitivity and resolution of the backscattering technique. An aluminum plate was prepared with a series of small scratches. For an additional test, a portion of the scratched area of the sample was coated with a thick layer of paint. A photograph of the C-scan of this test specimen is shown in Fig. 6. The scanning direction was normal to the length of the scratches; the incident angle of the 25-MHz (nominal) ultrasonic beam was optimum at 16 deg. The horizontal bands of shading represent regions where the scratches were of the same size. The scratch widths were, from top to bottom, 15, 25, 30, and 50 μ m. The vertical band near the left of the photograph represents the unpainted region. The results revealed that the regions of 50- and 30- μ m scratches can be detected easily in both painted and unpainted areas.

Further tests of resolution and sensitivity were conducted using sandwich structures made up of layers of epoxy between aluminum plates. In these experiments spherical and diamond-shaped (Knoop) indentations were made on an inside surface and on the bottom surface of the samples. These samples were scanned at 5 MHz; angles of incidence of the ultrasonic wave were 16 and 20 deg. It was found in studying these C-scans that the resolution of the

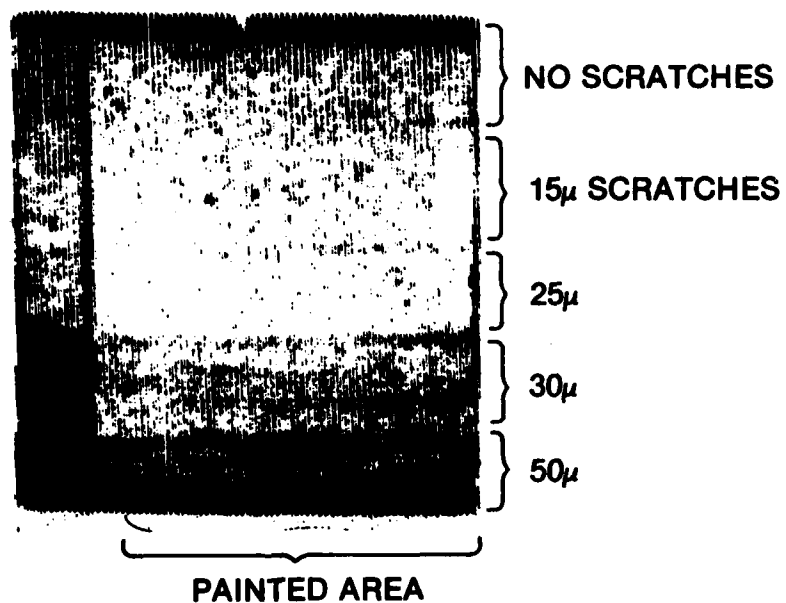


Figure 6. Backscatter C-Scan of Al Plate with Series of Scratches. Scratches run perpendicular to scanning direction. 50- μ m and 30- μ m scratches are detected even under thick layer of paint.

C-scan printer was the major limitation to overall system resolution. It was also found, on an inner surface, that even the smallest spherical indents, 0.3 mm in diam., could be detected. Spherical indents 1.0 mm in diam. could be detected on the bottom surface. The Knoop indents (major axis 0.38 mm, minor-axis 0.06 mm) could not be detected unless located in concentrated groups of 15 to 20. In addition, the results were slightly better for 2.3-mm-thick aluminum samples as compared to 1.6-mm-thick samples, presumably because of the increased time resolution between interfaces in the plates.

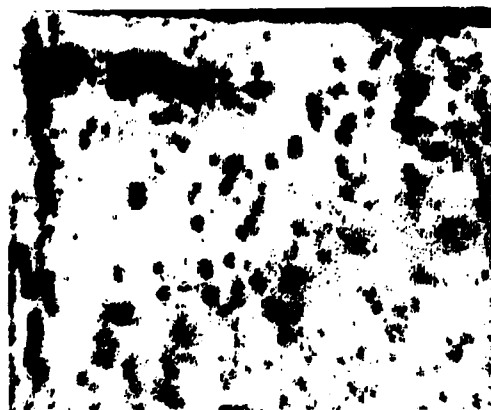
Following the study of sensitivity and resolution using imbedded particles, scratches, and indentations, several single-plate corroded aluminum samples were inspected in the backscatter C-scan mode. The rear surface of these samples was corroded. The C-scans of three of these samples are shown in Fig. 7. These results and those from visual inspection showed very good agreement. It is interesting to note that the preferred direction of the intergranular corrosion with the grains of the rolled plates can be seen clearly in Fig. 7.

Sandwiches of aluminum/epoxy/aluminum samples were also inspected. The aluminum was 1.5 mm thick and the epoxy layer $\sim 50 \mu\text{m}$ thick. Through-transmission scans were made using a 22-MHz (nominal) transducer, and these were compared with backscattering scans using a 5-MHz transducer. Figure 8 is the through-transmission C-scan of the sandwich in which an inner surface was heavily corroded. Figure 9 is the backscatter C-scan of the same sample. Comparison of these two photographs will show that while the through-transmission C-scan revealed no sign of corrosion, the backscatter technique easily detected it. A similar result was obtained in the case of a sandwich having the corrosion on the backside. In each case a direct correlation was found between the C-scans and the visually observed corrosion damage.

An additional experiment was conducted on samples of an aluminum plate riveted to a graphite-epoxy composite, with a sealant being used at the aluminum/composite interface. Sample scans of the aluminum/sealant/graphite-epoxy sandwich are shown in Figs. 10 and 11. Figure 10 is a through-transmission scan and shows irregularities in the sealant in certain areas. The backscatter scans in Fig. 11 also detected these areas of irregularity;



(a)



(b)



(c)

Figure 7. Backscatter C-Scan of Three Al Plates with Corrosion on Bottom Side. Each plate was exposed to salt-fog environment for (a) 170 hr., (b) 498 hr., and (c) 998 hr. to produce varying degrees of corrosion.



Figure 8. Through-Transmission of Al/Epoxy/Al Sandwich. Heavily corroded inner surface is not detected. Varying degrees of lightness are due to varying thickness of epoxy layer. Supports holding sandwich are seen on left and right sides.

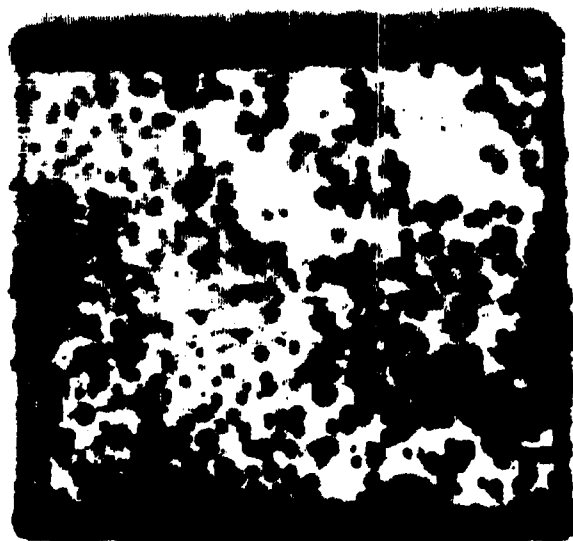


Figure 9. Backscatter C-Scan of Same Sample as in Fig. 8. Incident angle is 16 deg. Corrosion is easily detected.



Figure 10. Through-Transmission C-Scan of Al/Sealant/Graphite-Epoxy Sample. Irregularities in Sealant are detected.

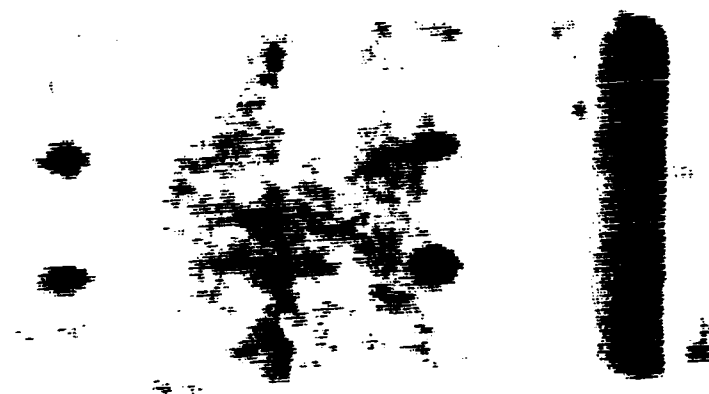


Figure 11. Backscatter C-Scan of Same Sample as in Fig. 10. Dark areas could be an indication of corrosion; however, visual inspection showed sealant to be very porous in these areas. Four dark circular areas are reflections from rivets holding layers together.

other areas were free of indications. When the samples were taken apart and examined visually, the sealant was found to be somewhat porous in the areas of irregularity observed in the scans; however, no corrosion was present. These same results were found in other aluminum/composite samples tested. Thus, for these samples the results from the backscattering method was determined to be inconclusive, and it was also shown that backscattering alone may produce results which cannot be easily attributed to porosity or actual corrosion.

A final investigation was conducted in an attempt to understand the effect of front-surface periodic roughness on the resolution of the backscattering technique when used to image corrosion on the back surface. C-scans of such a sample are given in Fig. 12 where the front- and back-surface signals were separated to produce scans of both surfaces. Also shown for comparison is a scan of the sample insonified from the corroded side. Recognizing that Fig. 12(b) and Fig. 12(c) are mirror images of each other, the details of the damage are clear despite some loss of resolution.

In conclusion, backscattering has been found to be a successful method of detecting corrosion--corrosion that was undetectable using through-transmission--even through bonded layers. With this method, small areas of corrosion in its initial stages can also be detected. Furthermore, when this technique is combined with through-transmission measurements, it is possible to distinguish between porosity and corrosion. Finally, although resolution is degraded, it is possible to detect corrosion through periodic rough surfaces.



(a)



(b)

(c)

Figure 12. Backscatter C-Scan of a) Periodic Rough Front Surface of Al Plate, b) Corroded Back Surface Insonified from Front Side, and c) Corroded Back Surface Insonified from Back Side.

Section 7

C-SCAN SYSTEM

The ultrasonic C-scan system developed during the course of this contract was designed to maintain previous data-acquisition capabilities while enhancing the data-processing aspects. A- and B-type scans can also be performed with this system.

Mechanically, the basic system consists of a two-axis horizontal carriage assembly mounted above a specially designed water tank. The base of the tank is a ground-granite slab, isolated from the floor-supports by air pads. Motion of the two independent axes is accomplished by screw-rods turned by stepper motors. Position information is generated by linear optical encoders. A three-axes--one vertical, two angular--manipulator, for transducer mounting, is also included. This vertical axis is computer-controllable via a stepper motor. Over the entire X-Y range of the carriage assembly, parallelism with the tank base is maintained within $\pm 40 \mu\text{m}$.

A Digital Equipment Corp. LSI-11 minicomputer is the central element of the control system. Referring to Fig. 13, the LSI-11 is used to communicate with all of the test instruments on the IEEE-488 interface bus. A video monitor displays the image as it is formed, and an ink-jet printer is utilized for generating a hardcopy. A dual 8-in. floppy disk drive holds the programs used by the computer plus the data representing an image.

Control of the transducer X-Y position (horizontal carriage assembly) is maintained by a Superior Electric Co. Modulynx motion control unit. The Modulynx system allows the computer to control the movement of the transducers with stepper motors. A microstep translator is used to divide each normal step into 10 discrete steps, thus minimizing low-speed resonances and smoothing out the movement. The maximum rate of translation is $\sim 1 \text{ in./sec}$. Speed is limited by the maximum rate of programable steps/sec. and the gear ratio of the mechanical system. The capability to program the number of steps and the rate allows the motion-control system to operate in an open-loop fashion, i.e., positional feedback is not required.

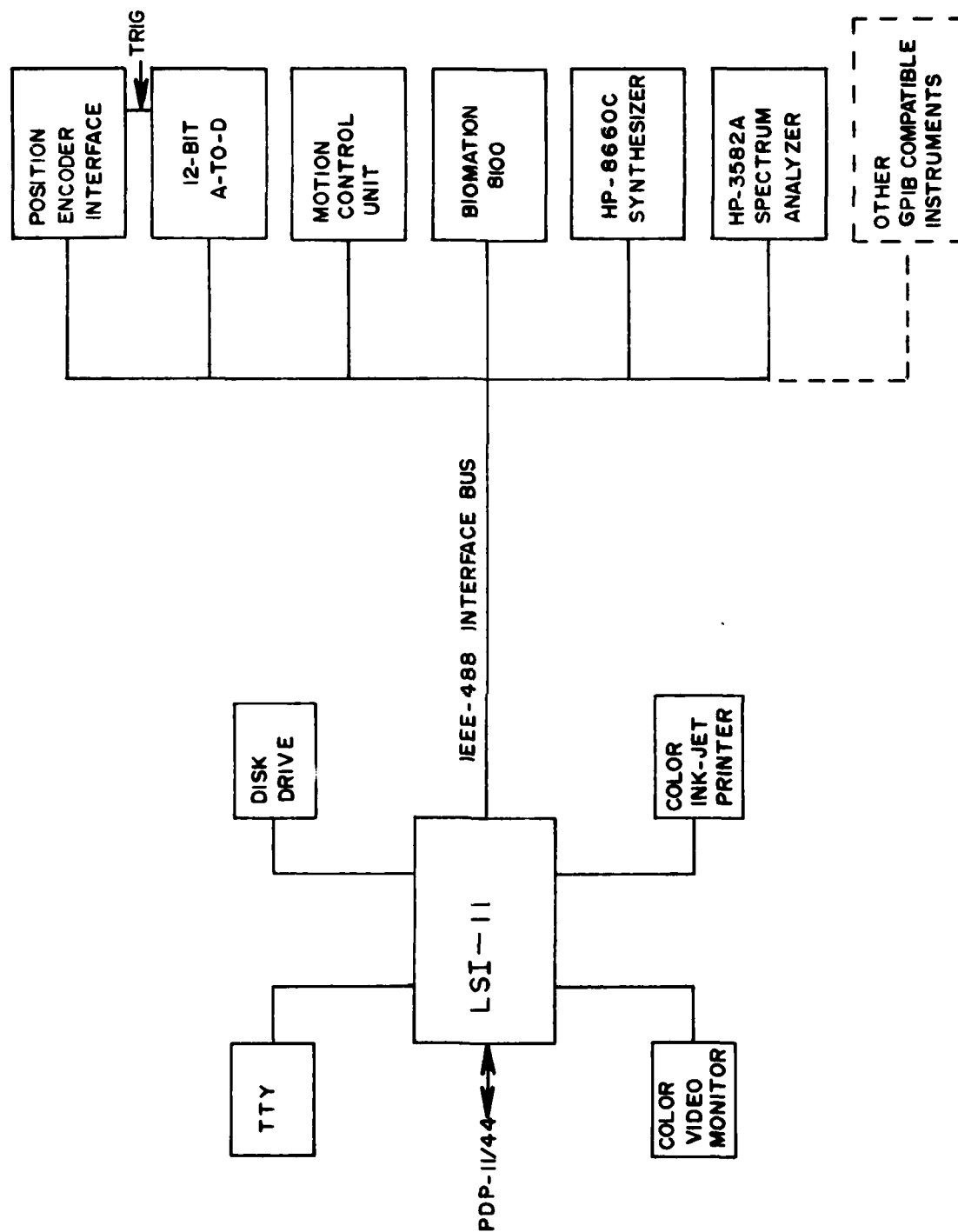


Figure 13. Components of C-Scan System.

Positional information on the horizontal carriage is generated by optical scale spars mounted on the mechanical system. As stated previously this information is not used in controlling the motion of the transducer but to provide data to a position encoder--an interface which couples a Mitutoyo display unit to the LSI-11 (via the IEEE-488 bus). The primary purpose of the interface is to provide trigger pulses to an analog-to-digital (A/D) converter. The total number of pulses to be generated and the distance between them (in terms of physical movement of the mechanics) are programmable.

A 12-bit A/D module with an interface to the IEEE-488 bus has been constructed. Included with the interface is a memory buffer which is used to temporarily store acquired data during a single line-scan of the mechanics. After a line-scan has been completed, the data can be transferred to the LSI-11 for processing.

After processing of the raw data, the information from each line scan is transferred to a video-imaging board contained in the LSI-11 mainframe. The imaging board can store (and display) an image composed of 512×512 data points (X-Y) by 4 bits of amplitude information. The 4 bits of amplitude represents 16 levels of grey or 16-colors, depending upon the type of monitor used. If a permanent record is desired, an ink-jet printer can be used or the data can be stored on floppy disk for later processing or archival storage.

The position-encoder interface and the 12-bit A/D converter were custom designed and constructed by SRL. A more detailed explanation of their operation can be found in Appendix E. The remaining units shown in Fig. 13 were purchased "off-the-shelf;" detailed descriptions and operating instructions can be found in the appropriate manufacturer-supplied manuals.

Section 8

PULSED SCHLIEREN SYSTEM

The interaction of sound waves with a test sample is, in general, a fairly complicated process. Various propagation modes may be excited; rough surfaces may cause diffraction; and non-specular reflections may occur. To further complicate the matter, commercial transducers used in transmitting sound waves do not always emit energy perpendicular to their face and often have sidelobes. In view of the need to visualize ultrasonic waves, a Schlieren system was designed and built.

A schematic of the optics is shown in Fig. 14. Light from a source is passed through a slit and lens to form a parallel beam. This beam then passes through the windows of a water tank and is focused onto a knife edge which prevents the light from reaching the detector camera. If the beam is perturbed in its path, the beam position at the knife-edge will vary; an upward deflection in Fig. 14 will result in light striking the camera. This perturbation can result from the interaction of the light with high- or low-pressure areas in the water. The light is refracted by the change in the refractive index of the water due to the change in pressure caused by ultrasonic waves. In effect, the ultrasonic waves can be detected visually.

If a continuous (cw) light source is used, a cw sound beam appears as an illuminated area on the TV monitor. Reflection and diffraction of the sound beam from the sample are readily visible and, in general, all areas of insonification are illuminated. This has proved to be a very useful aid for studying the interaction of ultrasound with test samples.

The Schlieren system developed in this research effort originally utilized a cw light source, which was later replaced with a pulsed source that could be synchronized with an ultrasonic generator. Ultrasonic tonebursts or pulses could then be observed as well as the phase of the acoustic waves.

Schematic diagrams of the light-pulse electronics are shown in Figs. 15 and 16. The electronics produced a high-voltage pulse across an air gap between

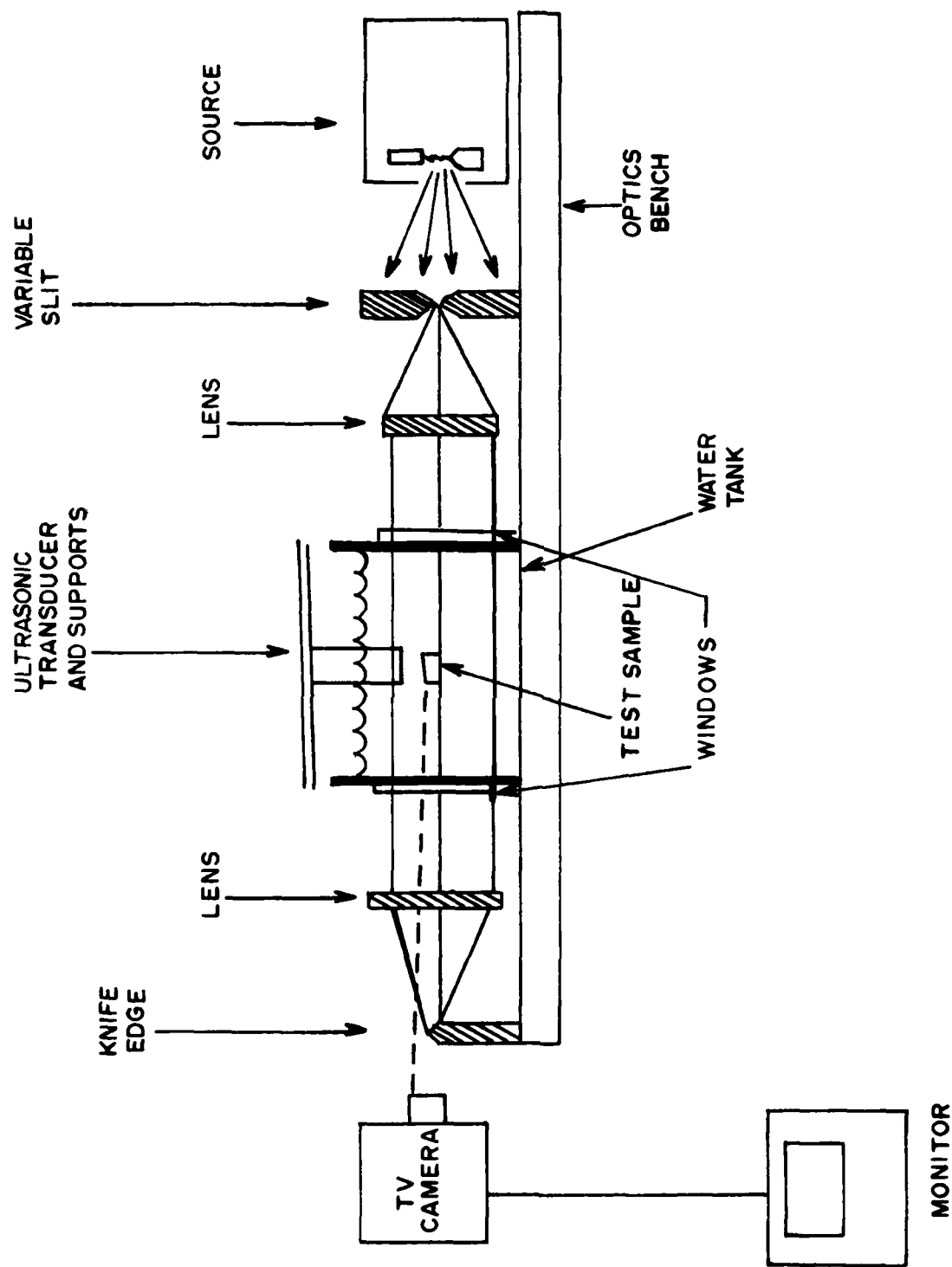


Figure 14. Diagram Showing Components of Pulsed Schlieren System. Rays showing light path are drawn.

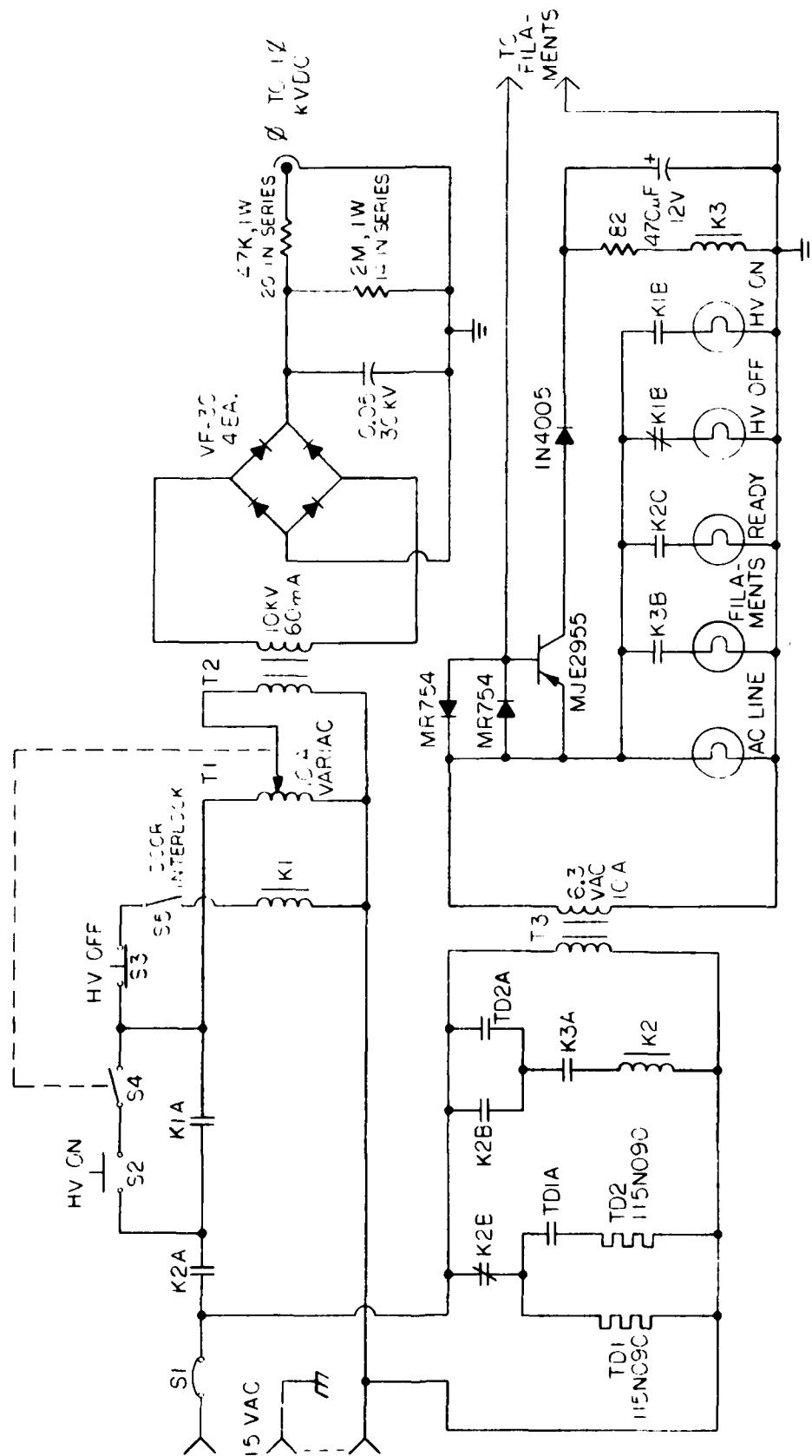


Figure 15. Schematic Diagram of Power Supply Employed to Produce High-Voltage Pulse.

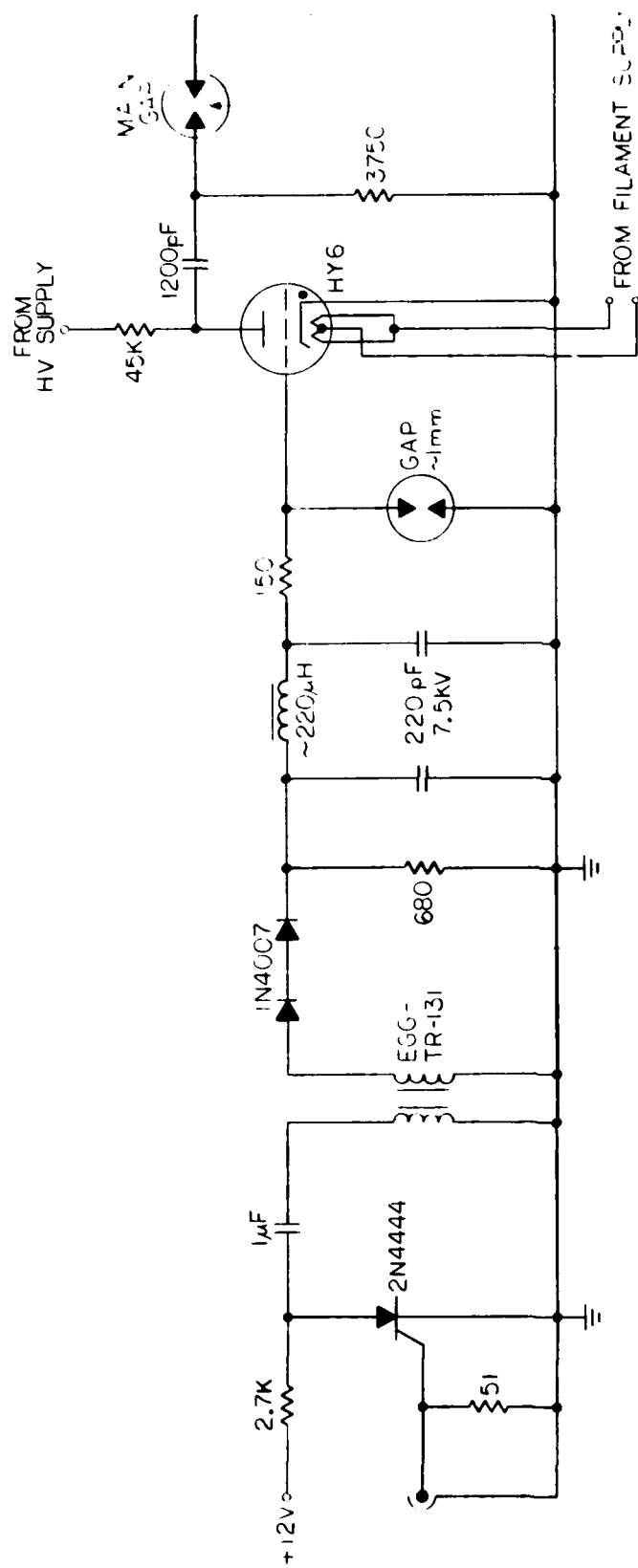


Figure 16. Schematic Diagram of Pulse Electronics.

two tungsten electrodes, resulting in a short-duration, white-light spark. Briefly, the design was adapted from Wyatt.⁶ The instrument consists of two units: a power-supply (Fig. 15) and a flash unit (Fig. 16). The power-supply provides all electrical power required by the flash unit. The flash unit contains a trigger circuit, a high-voltage switch, and the spark gap. A silicon-controlled rectifier (SCR) and a trigger transformer are used to fire the thyatron which provides a low-impedance path to ground to discharge the energy-storage capacitor through the spark gap. An auxiliary electrode near the main electrode of the spark gap facilitates breakdown of the gap at a consistent voltage, thereby reducing jitter.

The pulsed Schlieren system proved to be a useful tool for ultrasonic NDE. In many experiments the system provided the visualization needed for understanding the complicated interactions between the acoustic waves and the test sample.

Section 9

DETECTION OF DEFECTS IN COMPLEX SHAPES

The application of ultrasonics to the inspection of complex-shaped components such as turbine discs is limited by the difficulty of coupling ultrasound to the point of interest within, or on the surface of the component. Flaws near the surface or a corner are especially difficult to detect due to the masking effect produced by the large specular reflections from the surface or corner. One method of overcoming these problems is the use of a mating part, i.e., a part whose surface is a complement of the component surface.

In this research effort both the theoretical and experimental aspects of the problem were studied. Experimentally, a half cylinder and its mating part were machined from aluminum, and the surfaces were carefully machined to provide a close match; water was used as a coupling medium between the surfaces. Experiments were initiated to measure the reflection and transmission coefficients as a function of incidence angle. Also experiments were performed in which backscattering was observed from small holes drilled into the half cylinder.

Transmission and reflection coefficients for a solid/fluid/solid medium as a function of the angle were derived theoretically. The problem was treated as a simple boundary-value problem under the assumptions that the fluid layer was thin and that plane waves were incident upon the sample. The model predicted that through the half cylinder alone, 10-MHz longitudinal waves could be transmitted for incident angles of ≤ 13 deg. With the use of the mating part, however, the limiting angle increased to ~ 80 deg. Experimental data confirmed this angle and agreed very well with predictions of backscattered signals from near-surface and bulk drilled holes for incident angles of ≤ 50 deg.

As a final means of demonstrating the practicality of the method, a through-transmission test was made on a 1-in.-diam. nut-and-bolt assembly. The transmitted signal was clearly observed as were backscattered signals from the interfacing surfaces of the nut and bolt.

In conclusion, the use of mating parts effectively alleviates certain problems encountered in the inspection of complex shapes. It is anticipated that the use of a coupling medium having higher impedance than water would further enhance the results. The publication containing detailed discussion of the procedure and results is included in Appendix F.

Section 10

ACOUSTIC DIFFRACTION FROM A CORRUGATED SURFACE

The effect of periodic rough surfaces on the propagation of ultrasonic waves has been studied. The goal was to understand the phenomena of surface-wave generation and propagation at a corrugated interface between a liquid and a solid. The initial experimental arrangement consisted of an incident ultrasonic wave in water impinging upon a solid having a one-dimensional periodic rough surface. For a given angle of incidence in the plane defined by the surface-normal and the direction of the one-dimensional surface roughness, the grating formula predicts diffraction angles of various orders for any frequency by

$$\sin\theta_d = \sin\theta_i + \frac{nC_f}{\Lambda f} \quad 1(a)$$

where θ_d is the angle of the diffraction order, θ_i the angle of incidence, C_f is fluid velocity, n is the diffraction order, ($= 1, 2, 3, \dots$), Λ is surface-roughness period, and f is frequency. Once the grating formula is modified to a form involving phase velocities along the interface and specialized to surface wave generation, it takes the form

$$\frac{C_f}{C_s} = \sin\theta_i + \frac{nC_f}{\Lambda f} \quad 1(b)$$

where C_s is the surface wave velocity. By time-reversal symmetry, the grating formula also predicts the angles into which the surface wave will diffract. In Fig. 17, the angle of anomalies versus the frequency for the various diffraction orders is plotted for a 0.74-mm, 60-deg. sawtooth-cut aluminum sample. When a surface wave is generated (a Scholty, Rayleigh-type, or compressional surface wave), it will produce a displacement of energy from the region of insonification. Therefore, methods of detecting surface waves which are sensitive to the shift of energy were chosen as candidates for studies of the anomalies. As will be shown, the energy shift in some cases was not sufficiently large to be detected.

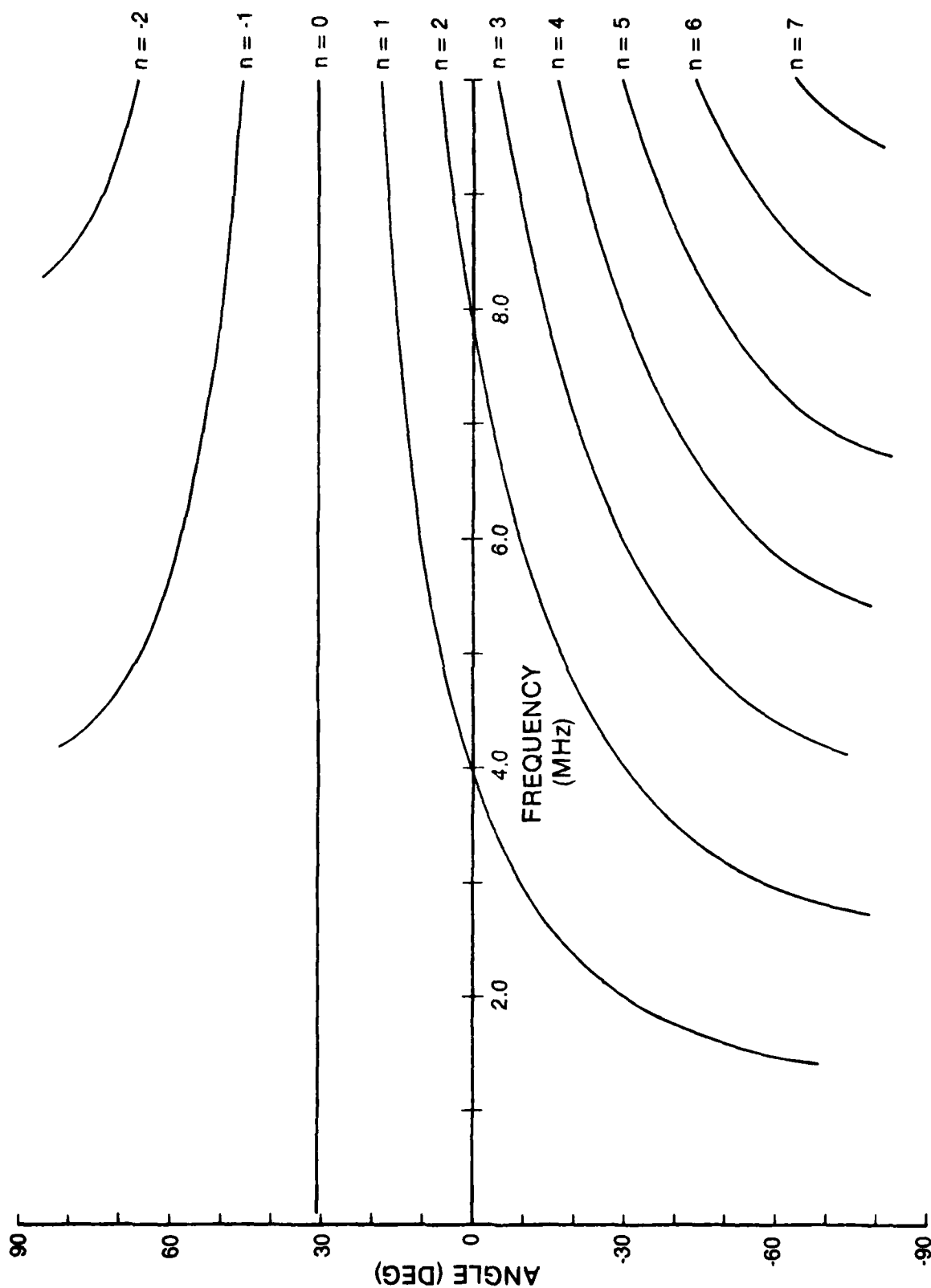


Figure 17. Angles at Which Anomalies Occur in Reflection Coefficient for Various Orders, n , Versus Frequency of Exciting Ultrasonic Wave for Al Sample with Periodic Rough Surface with Period 0.74 mm.

The first attempt to locate the surface anomalies consisted of the use of two transducers and a rough-surface sample which was positioned on a turntable immersed in a water tank. Figure 18 illustrates the test setup. Since the receiver had a wide angle of reception, its alignment was not critical. The sample was positioned in such a way that its surface was normal to the segment connecting the receiver and the turntable axis and was located half way between these two points. The incident beam was specularly reflected to the receiver at all angles of rotation of the turntable up to the geometrical limits of the set up. Any displacement of the energy was expected to result in a decrease in the receiver signal.

Evaluation of this test procedure as a candidate for studies of reflection from surface roughness indicated that the physical and geometrical limitations of this setup hampered its applicability for such studies. Apparently transmitter sidelobes incident on the rough surface complicated the received signal. The receiver directivity, convolved with the data, produced an additional complication.

Another experimental arrangement, based on a method suggested by Rollings⁷ is shown in Fig. 19. In this method the sample was centered on the turntable, with an aluminum flat-surface reference block being centered on the turntable normal to the sample. A single transducer in a back-reflection mode, employing tonebursts, was used to insonify the center of the turntable. Again, any displacement of the energy was expected to cause a decrease in the received signal. This method has proved to be effective for flat surfaces, but was found inapplicable for rough-surface studies due to the large number of diffraction orders involved. These orders, reflected from the normal plate, generated additional anomalies which were difficult to analyze. Moreover, sidelobes produced diffraction orders which further complicated the interpretation procedure.

The test setup of a third method consisted of a sample centered on the turntable, with a cylindrical reflector positioned in such a way that its center of curvature coincided with the turntable axis (see Fig. 20). A single transducer in a back-reflection mode, employing tonebursts, was again used to insonify the axis of the turntable where the sample surface was

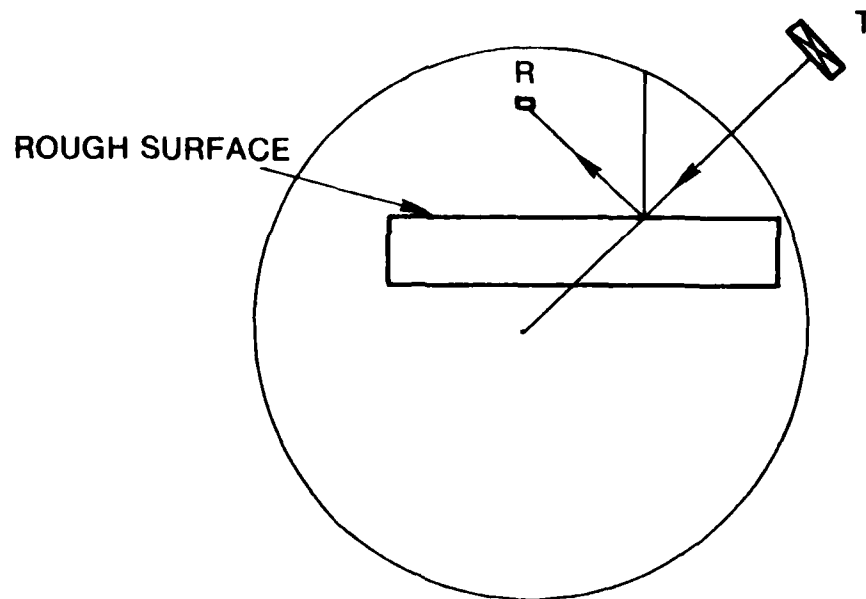


Figure 18. Test Setup Used to Search for Anomalies in Reflection Coefficient. "T" is transmitter and "R" is receiver (wide angle of reception).

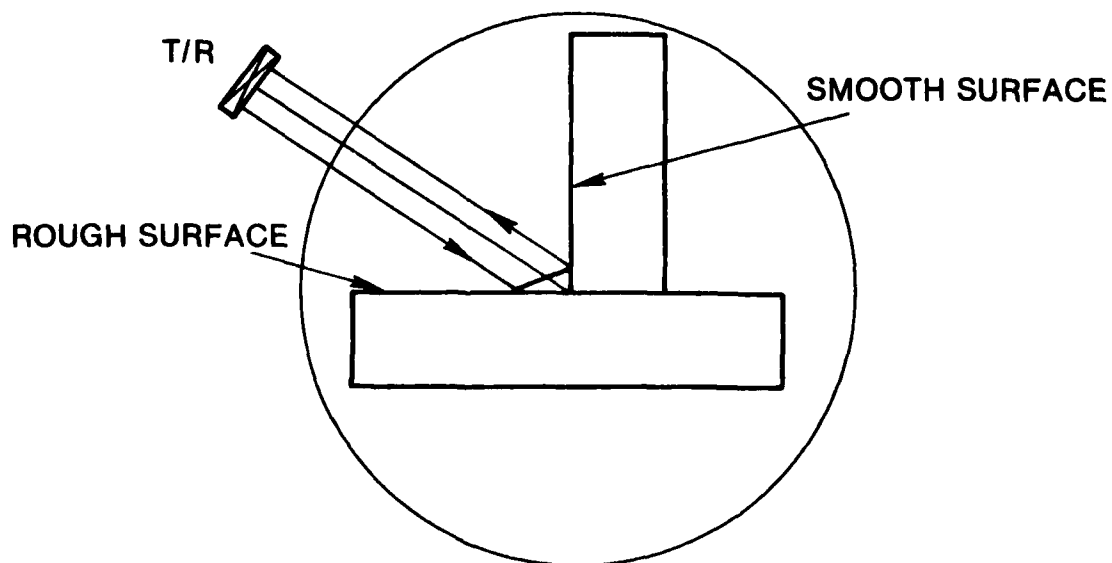


Figure 19. Test Setup Used To Search for Anomalies in Reflection Coefficient Suggested by Rollings (Ref. 7). Transmitter is also receiver. Smooth surface is reference reflector.

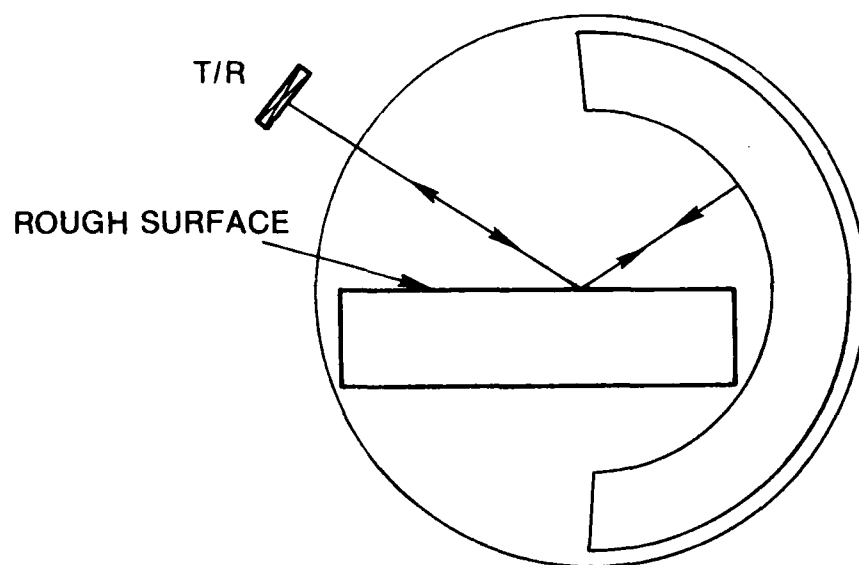


Figure 20. Test Setup Used to Search for Anomalies in Reflection Coefficient. Transmitter is also receiver. Cylindrical object is reference reflector.

centered. Displacement in the energy along the surface was expected to result in a minimum in the signal (as a function of angle) corresponding to angles at which the grating formula predicted anomalies. Data produced by sweeping through the various angles of incidence indicated variations in the reflection coefficient which were not necessarily related to the anomalies. The variations were possibly a result of the measured signal being an integration of all the scattered waves, including sidelobes and diffraction orders, which interfere on the receiver. As a result, the signal from the rough surface was too complicated to be interpreted. A typical scan using this technique is shown in Fig. 21.

In each of the above methods, the frequency was held constant as the angle was varied. In the following experiment, the angle was held constant while the frequency was swept. The simplest experimental setup using this approach consisted of a back reflection with the incident wave normal to the surface of the sample. It was expected that energy would be displaced out of the reflected beam when a surface wave was generated, which would cause a minimum to occur in the received field. Figures 22 and 23 show two minima in the data (received amplitude versus frequency) from an aluminum sample and a single minimum from a brass sample, respectively. The frequency at which these minima occur is not well defined because of the broad distribution in the data which is unsatisfactory. The large widths of the minima may have been caused by beam spreading. In other words, since the beam is composed of diverging rays, the incident wave may not have been defined to within a sufficiently small range of angles. In addition, the frequencies at which these minima were expected to occur are 3.9 (Al sample) and 13.6 MHz (brass sample). The result expected for a brass sample is consistent with the experimental data. Comparison of theory and experiment in the case of the aluminum sample presents a problem since a minimum exists on either side of the expected frequency of the surface-wave anomaly. This phenomenon will be discussed again later, along with possible explanations.

In another set of experiments, the angle of incidence was held constant (normal incidence), and the rough surface was insonified with a pulse. The received signal was then processed using a time gate, Wiener filter, and Fast Fourier Transform. It is important to note that the time-domain signal was

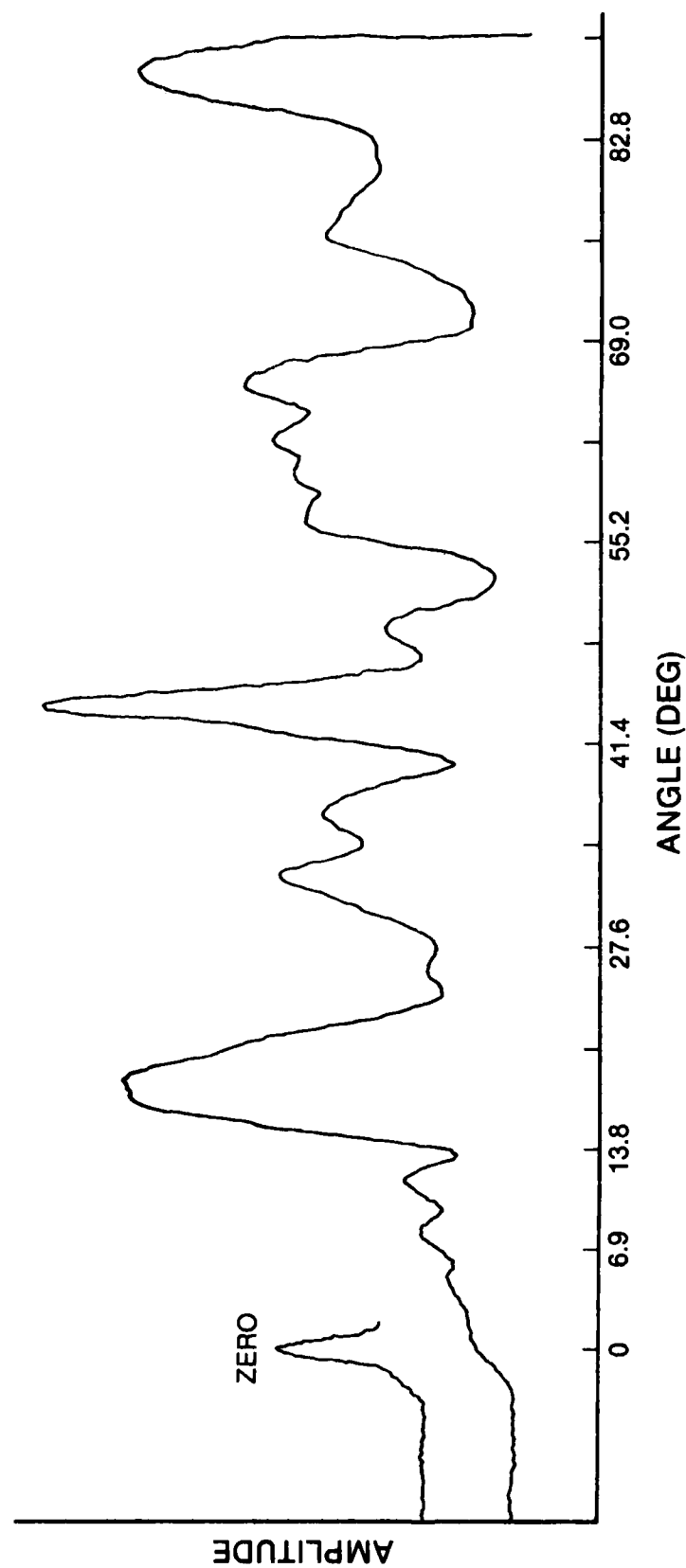


Figure 21. Sample Scan of Rough-Surface Sample at 3 MHz While Angle is Varied. Reflectance was measured by method described using cylindrical reflector.

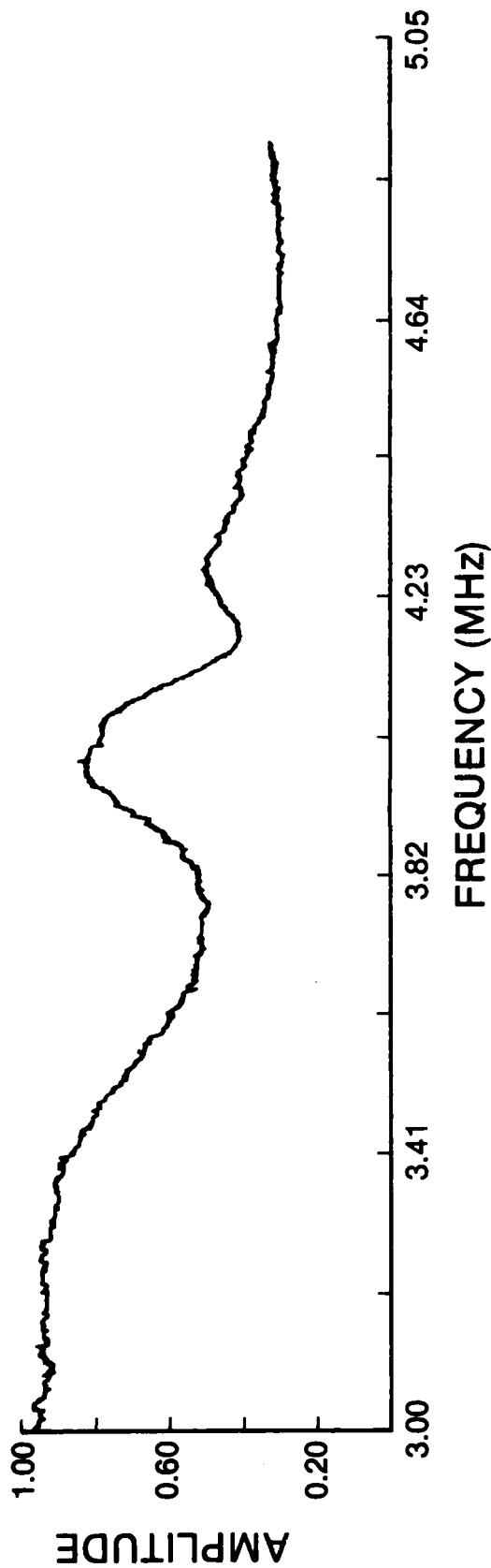


Figure 22. Measured Reflection Coefficient of Acoustic Beam Normally Incident upon 0.74-mm-Period Al Sample. Insonifying beam is toneburst.

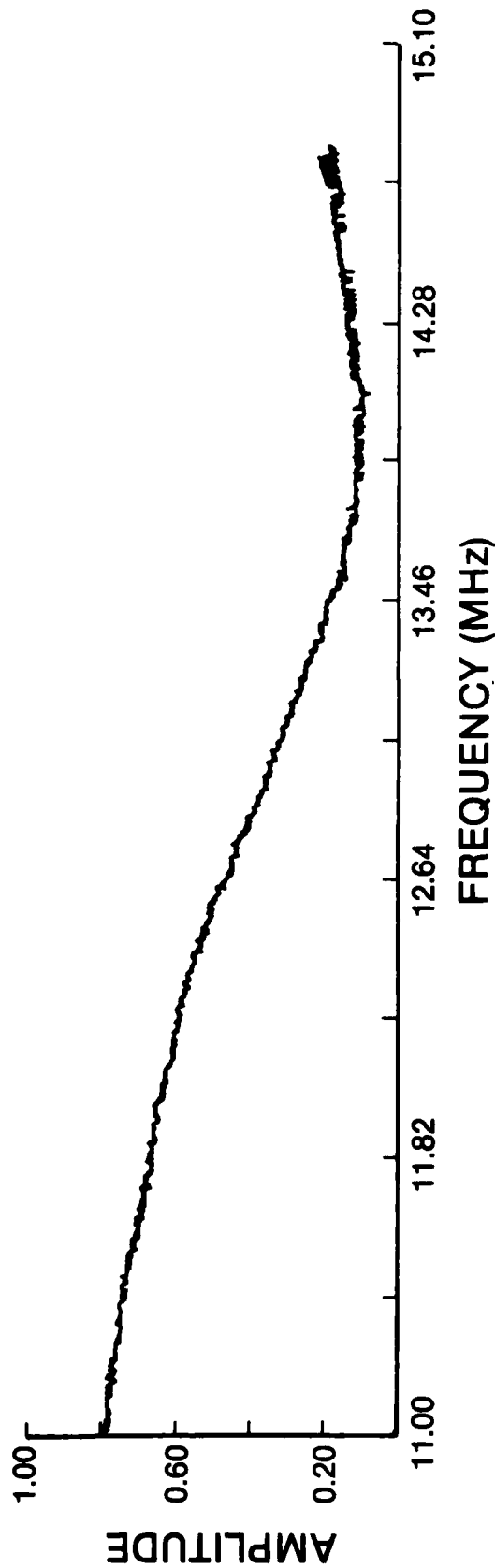


Figure 23. Measured Reflection Coefficient of Acoustic Beam Normally Incident upon 0.14-mm-Period Brass Sample. Insonifying beam is toneburst.

recorded using a sampling scope and a sweep-sampler plug-in module, as shown in Fig. 24 of the electrical setup. The computer was then able to read these data via the vertical output of the sweep sampler.

This method has several advantages over the previous methods. Since a pulse was used in this case, the "specular-reflection" portion of the signal arrived before the "leaky-wave" portion. Further, since the surface-wave mode occurs only at certain frequencies and since it is a type of resonant excitation of the surface, a ringing in the received signal resulted. By proper time-gating of the received pulse, it was possible to enhance the interference of the specular portion with the leaky-wave portion in the frequency domain. Both Figs. 25 and 26 show the response from a flat surface and the corrugated surface in the time domain and the response from the corrugated surface in the frequency domain of the received pulses from an aluminum and a brass sample, each with a time gate applied, followed by an appropriate Wiener filter. Again the expected frequencies of the minima are 3.9 and 13.6 MHz, respectively.

From a comparison of Figs. 22 and 25 for the aluminum sample and Figs. 23 and 26 for the brass sample, it is clear that there is no significant difference in the results from the two methods used. The broad minimum in the data from the brass sample in Fig. 26 again is consistent with theory. Similarly, there is a minimum on either side of the expected frequency of the anomaly in the aluminum data presented in Fig. 25, just as in Fig. 22.

A possible explanation for the inconsistency in theory and experiment for the aluminum sample is that the surface wave velocity may have been perturbed. If this were the case, then according to the above experimental results, the perturbation must have resulted in two surface wave modes--one with a slightly higher velocity and one with a slightly lower velocity, corresponding to the minima in Figs. 22 and 25 at 3.7 and 4.1 MHz, respectively. To test this hypothesis, an experiment was conducted in which the specular portion of the signal from the rough surface was gated out by positioning the time gate about the ringing tail. This resulted in a peak in the frequency domain corresponding to the frequency at which a surface wave was generated. Figure 27 shows the result of this experiment for the aluminum sample and proves

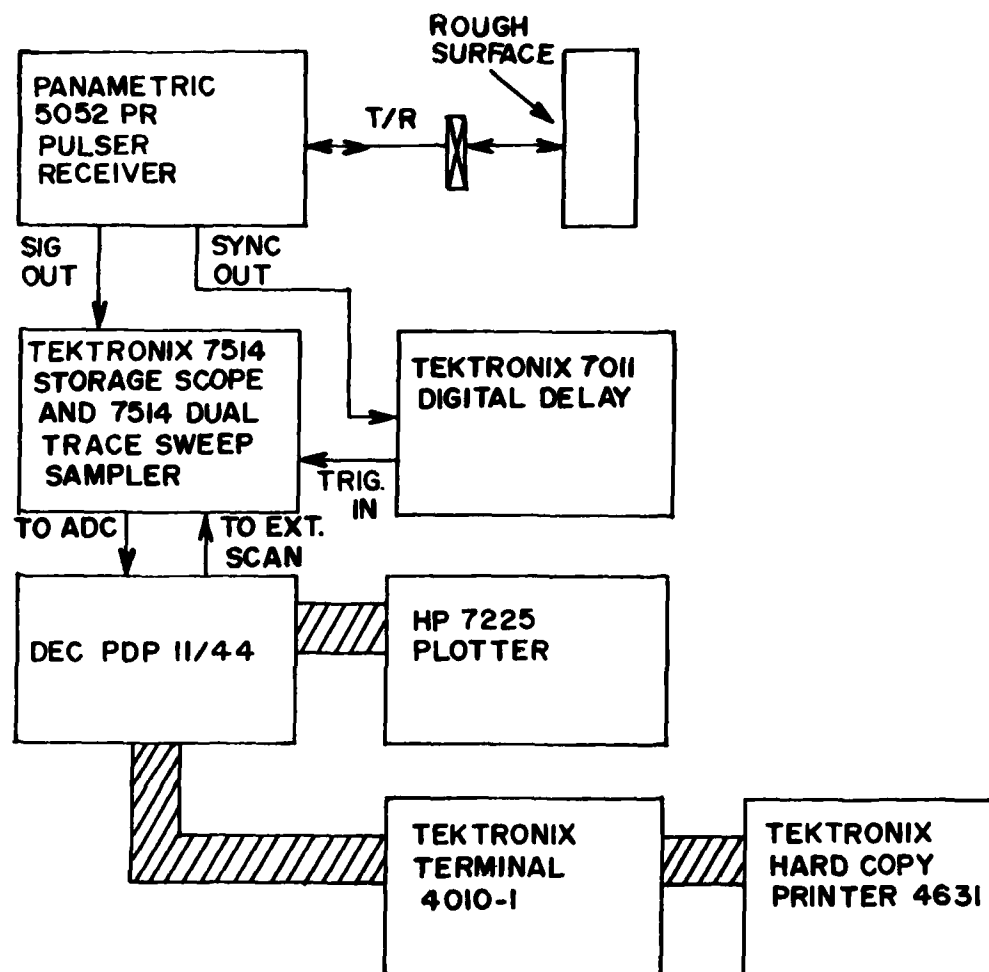


Figure 24. Block Diagram of Pulse-Echo Technique Used to Search for Anomalies in Reflection Coefficient of Acoustic Beam Normally Incident upon Periodic Rough Surface.

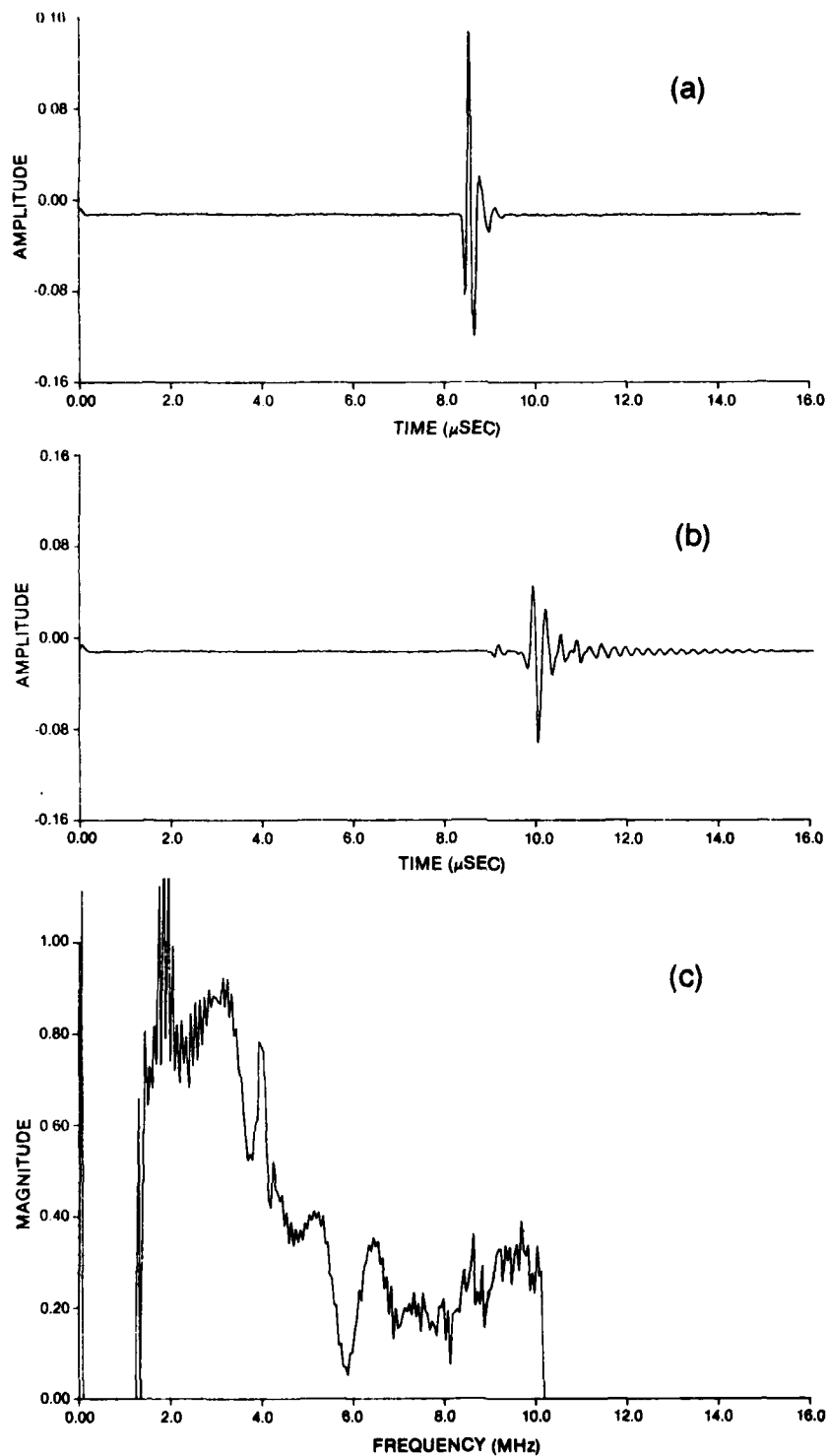


Figure 25. Results of Pulse-Echo Technique Used to Search for Anomalies in Reflection Coefficient of Acoustic Wave Normally Incident upon 0.74-mm Corrugated Al Sample. a) Reference Pulse from Flat Al Sample, b) Received Pulse from Corrugated Al Sample, c) Reflection Coefficient of Corrugated Al Sample Calculated by Deconvolution of Signal in a) from signal in b). Frequency domain.

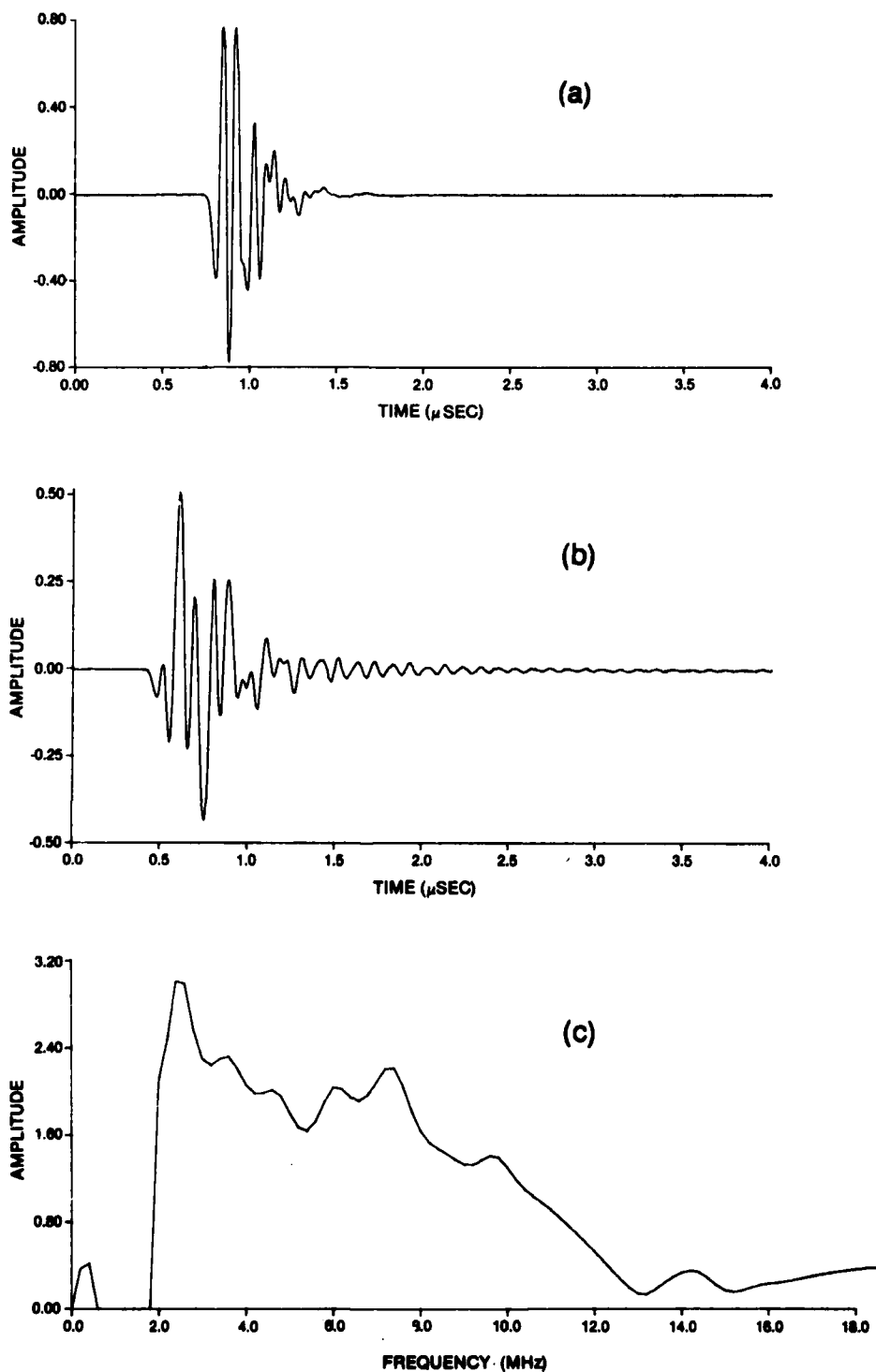


Figure 26. Results of Pulse-Echo Technique Used to Search for Anomalies in Reflection Coefficient of Acoustic Beam Normally Incident upon 0.14-mm-Period Corrugated Brass Sample. a) Reference Pulse from Flat Brass Sample, b) Pulse from Corrugated Brass Sample, and c) Deconvolved Reflection Coefficient in Frequency Domain.

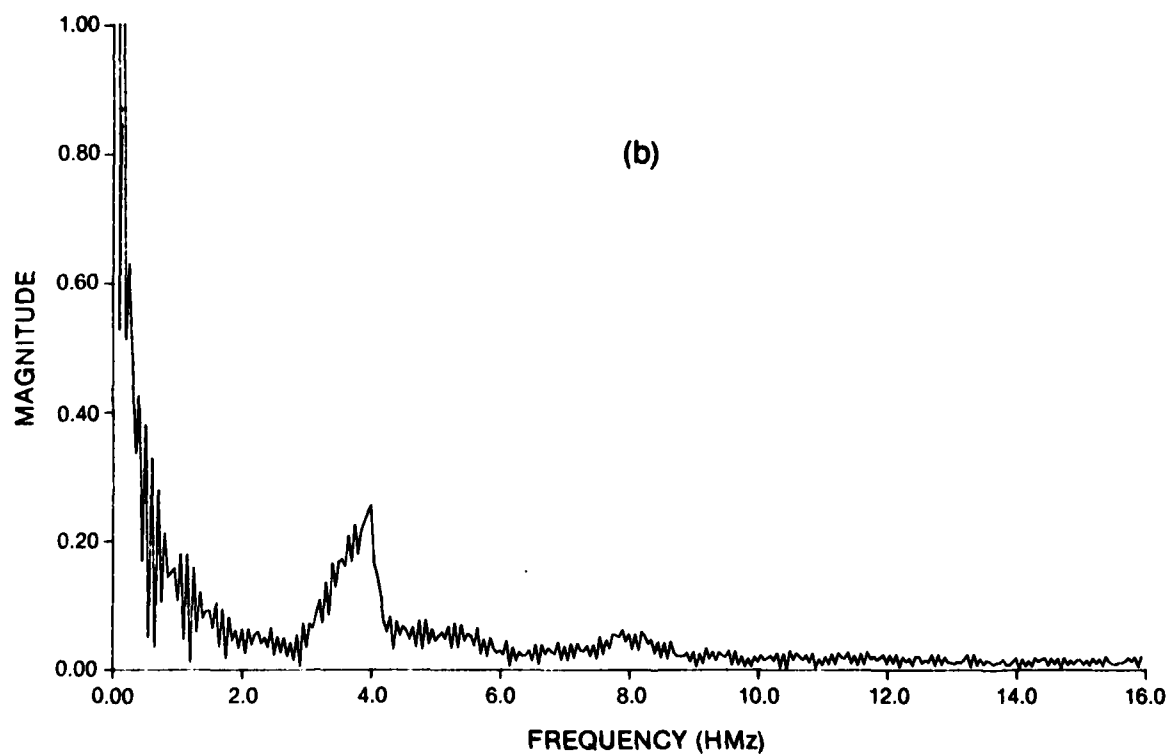
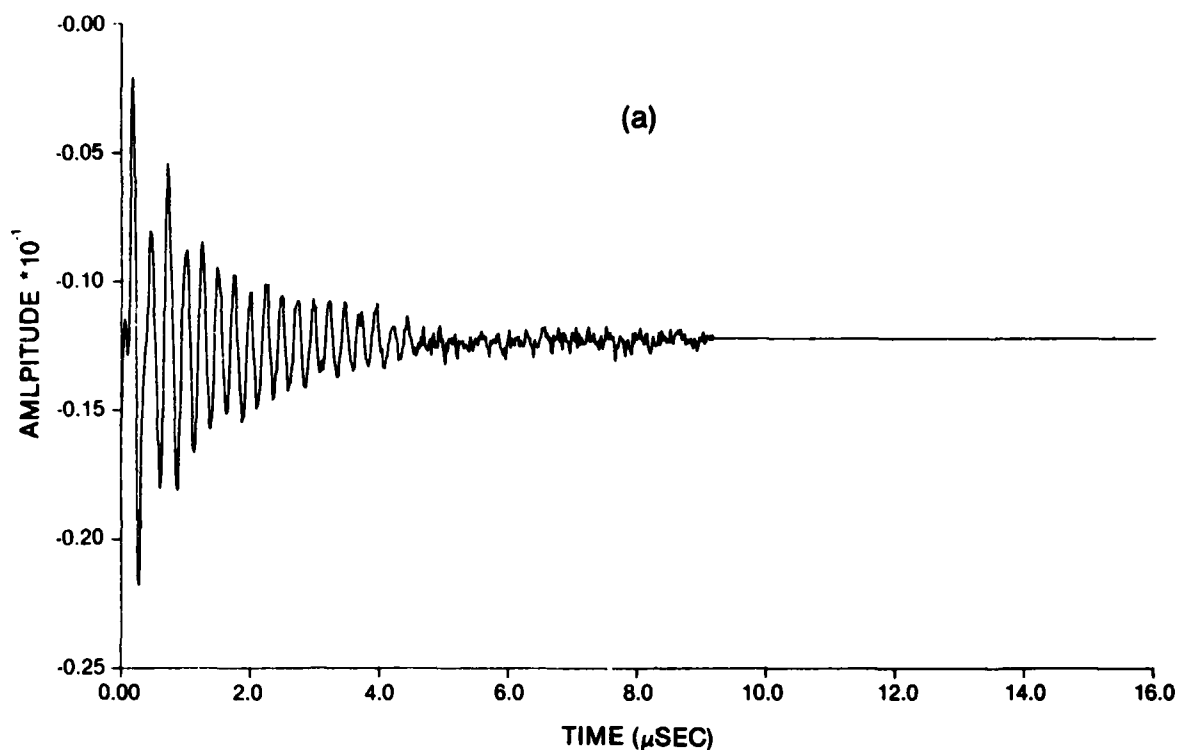


Figure 27. a) Result of Time Gate Applied to Pulse in Fig. 25(a), Gating on "Ringing Tail." Represents Surface Wave Mode, b) Frequency Domain of Gated Pulse in (a).

that only one surface mode exists and that this mode corresponds to the frequency expected for the surface-wave anomaly.

Another possible explanation is as follows. Define the frequency, f_0 , to be the frequency at which the incident beam is strongly coupled to the surface wave. Assume that at f_0 , the displacement of energy by the surface wave is insufficient to cause a significant change in the energy received by the transducer. The only evidence of the surface wave would then be a phase change relative to the specularly reflected signal. At other frequencies near f_0 , the energy in the incident beam would be less strongly coupled to the surface wave, causing a redistribution of energy between the specular and leaky wave portions of the received signal. At two frequencies, one greater and one less than f_0 , the specular and leaky-wave portions would produce maximum interference. This would result in two minima in the frequency response--one on either side of f_0 . It is suggested that those two minima correspond to those seen in Figs. 22 and 25. This hypothesis has not yet been tested.

An aid in the study of reflections is the Schlieren Visualization System (see Section 8). Using this experimental tool, a beam displacement was observed at frequencies and angles roughly corresponding to those given by the grating formula for surface-wave generation. This tool aided in the search for anomalies in the methods to follow. Figures 28 and 29 contain two schlieren photographs. In Fig. 28 the frequency was chosen such that the beam was not displaced; in Fig. 29 the frequency was changed to produce a displaced beam. It should be mentioned that there is both a forward and backward displacement of the beam in Fig. 29. Unfortunately, the schlieren system is not capable of providing accurate angle information.

Recently the single-axis scanning system and the corresponding software to control it were completed; it is now possible to perform experiments which involve scanning the receiving transducer parallel to the surface of the sample while holding the transmitter motionless and stepping through any given frequency range. Large amounts of data can now be accumulated in a systematic search for anomalies through location of the frequency of a given angle which produces the largest shift in the mean position of energy.



Figure 28. Schlieren Photograph of Reflected Beam from 0.74-mm Corrugated Al Sample Showing No Beam Displacement.

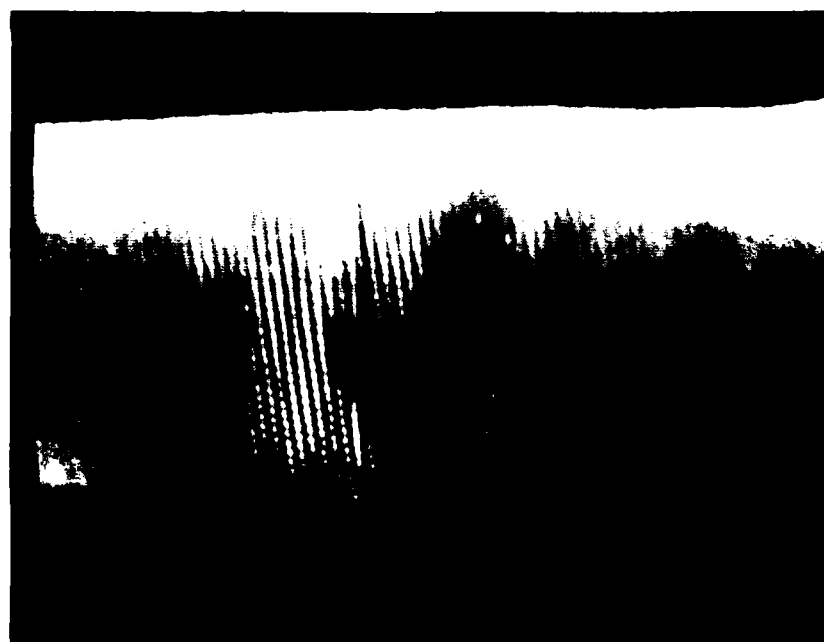


Figure 29. Schlieren Photograph of Reflected Beam from 0.74-mm Corrugated Al Sample Showing Beam Displacement. Angle of incidence is same as in Fig. 28.

This same search algorithm produces an amplitude distribution of the reflected signal from a rough surface (as a function of receiver position) which can be compared to a flat-surface distribution. From these distributions, it is possible to calculate such parameters as the mean location of energy, the width of the distribution as defined by the second moment of the energy distribution, and the total energy.

In this series of experiments, four different angles were examined. The angles of incidence and reception were held equal. At each of these angles, the frequency was stepped through a range centered on the expected location of the anomaly as given in the grating formula. This experiment was conducted on a 0.737-mm, 60-deg. sawtooth-cut aluminum sample. With this method the greatest degree of success was achieved, but this success depended upon the capability to control equipment and to collect and process large volumes of information by means of the computer. The mean position of the energy, $\langle X \rangle$, and the width of the reflected beam as defined by the second moment of the energy distribution, $\text{VAR}(X)$ were calculated. Sample field distributions are shown in Fig. 30. Plots of $\langle X \rangle$, and $\text{VAR}(X)$ for each angle examined are shown in Figs. 31 and 32, respectively. Also shown in these figures are the corresponding reference curves for a reflection from a flat surface. Note that since 31 deg. is the Rayleigh angle for aluminum, the flat-surface reflections for this angle show the expected displacements.

Several observations can be made regarding the amplitude-distribution measurements. As evident in the data collected, a bimodal distribution is not always associated with nonspecular reflections from a rough interface. Furthermore, a displacement of the mean position of energy does not always occur on the rough surface--even when predicted by the grating formula. This does not indicate that the formula is invalid but rather that little energy is coupled to the surface wave or that the coupling causes a redistribution of energy without a shift in the mean position. Neither of these possibilities is taken into account in the grating formula. Finally, it should be noted that a backward displacement of the reflected beam was observed in certain circumstances, for example, in the schlieren photos in Figs. 28 and 29 as well as the plots of $\langle X \rangle$ versus frequency in Figs. 31 and 32.

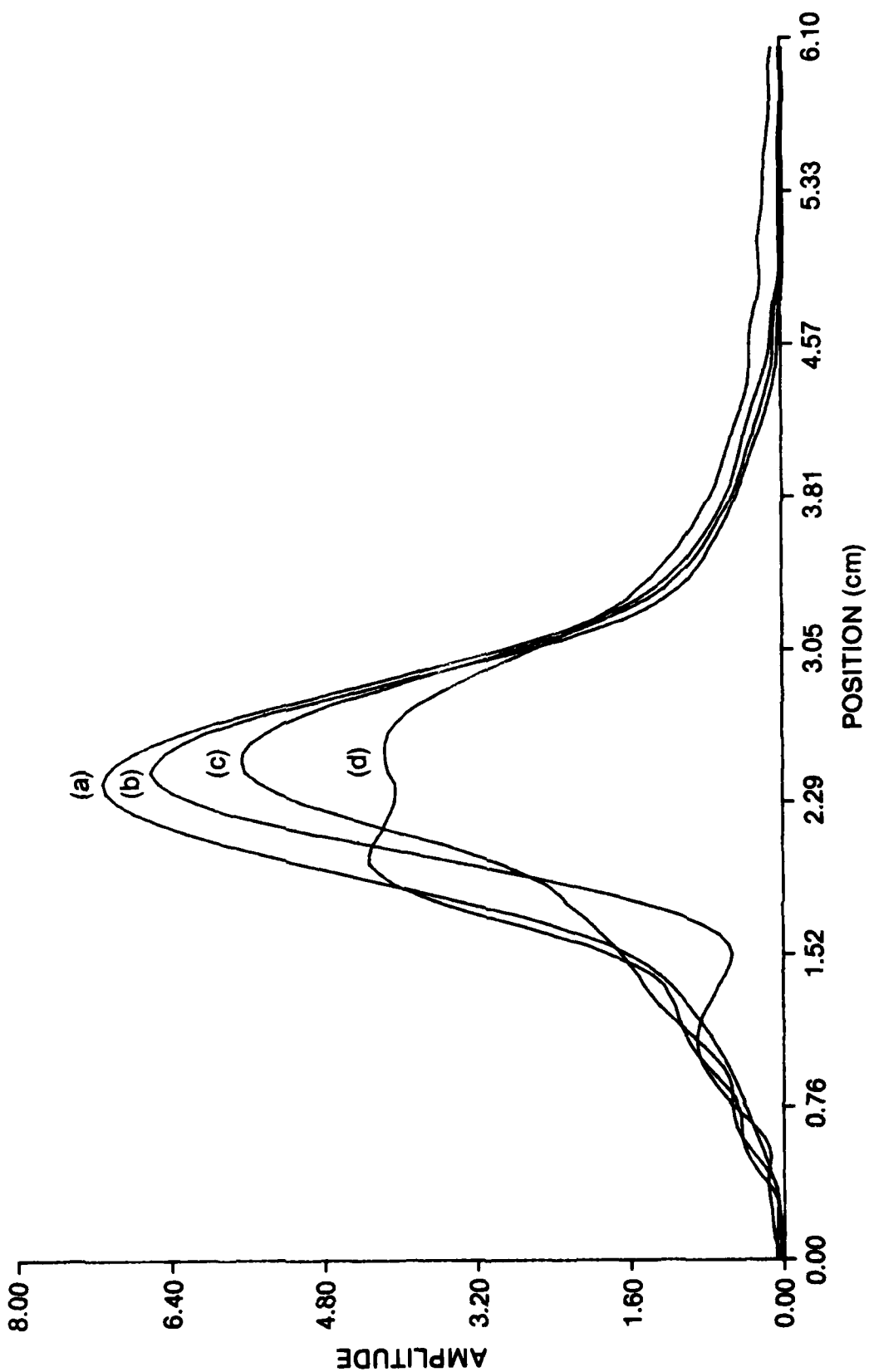


Figure 30. Sample Field Distributions of Reflected Beam from 0.74-mm Al Sample at 12-deg. Angle of Incidence. a) Reference Distribution from Flat Surface, b) - d) Distributions Obtained from Corrugated Surface at Three Different Frequencies.

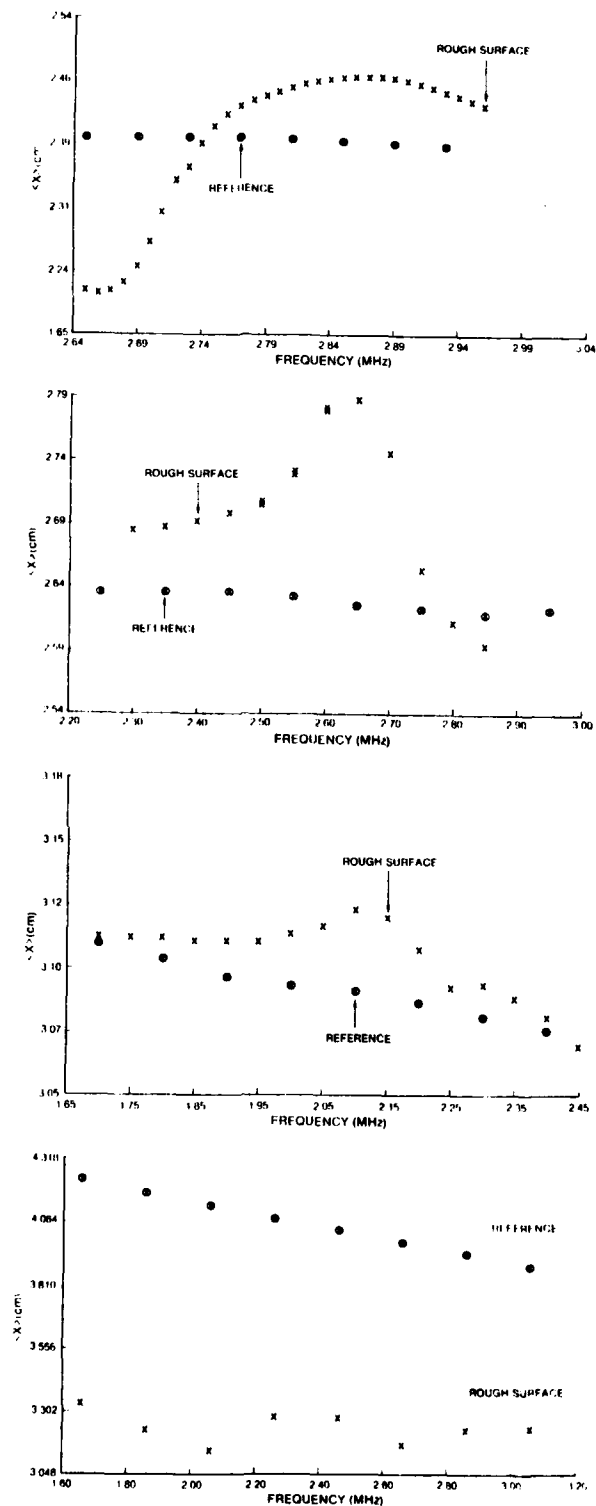


Figure 31. Experimentally Determined Values for Mean Position of Energy in Reflected Field from 0.74-mm Corrugated Al Sample and from Reference Flat Al Sample. Angles of incidence are (top to bottom) 12, 18, 25, and 31 deg.

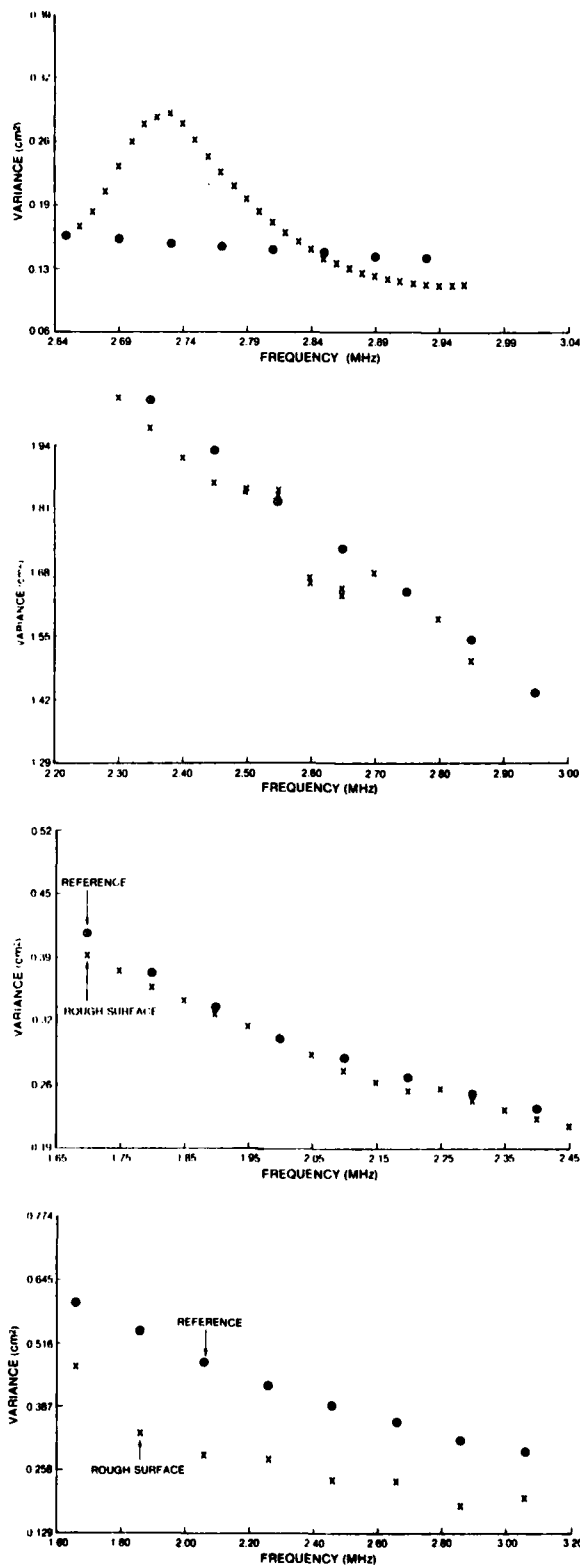


Figure 32. Experimentally Determined Values for Variance of Energy in Reflected Field from 0.74-mm Corrugated Al Sample and from Reference Flat Al Sample. Angles of incidence are (top to bottom) 12, 18, 25, and 31 deg.

Finally, measurements of the real and imaginary parts of the velocity (or wave number) of the surface wave were carried out using two transducers in a pitch-catch, normal incidence, toneburst mode. In order to prevent the bulk waves from interfering with the received leaky wave, a rubber pad extending to the surface of the sample was positioned between the transducers. This pad also eliminated the possibility of Scholty waves affecting the results. The receiving transducer was scanned laterally and the time-of-arrival of the leading edge of the received and rf-detected signal was plotted versus receiver position. From these data, the slope was calculated, which yielded the real part of the surface-wave velocity. The imaginary part of the wave number was calculated from the signal-amplitude-verses-receiver-position data given in Fig. 33. These measurements were taken at only one frequency.

The experimental value of the real part of the velocity was calculated to be 2.87 ± 0.03 mm/ μ sec. This value is to be compared with 2.906 mm/ μ sec. given in Ref. 8. The uncertainty was established by the resolution of the recording apparatus. Since, at present, no complete theoretical models exist with which to compare the experimental measurements, the following constitute model-independent conclusions and observations. First, from the data collected, it appears that the real part of the velocity of the surface wave which propagated along the rough surface of the tested sample was unperturbed by the roughness. Further tests would be required in order to determine whether a generalization is possible and to define its limits. One interpretation is that the effective path of the surface wave is not along the minute details of the surface but along the effective flat surface as if the roughness were nonexistent. It may be that the wave skims along beneath the roughness. Again, more study is required to answer questions posed by the possible interpretations of the results of this experiment.

The experimental value of the imaginary part of the wave number, α , was calculated to be 0.059 ± 0.002 mm⁻¹. The corresponding value for a flat aluminum surface at the same frequency is 0.75 mm⁻¹.¹ The measured value of α for the rough surface is much less than the value for a flat surface aluminum halfspace. Apparently, the rough surface allows the surface wave to propagate farther than a smooth surface. As a result, the coupling of the incident beam to the surface wave was less for the rough surface tested than

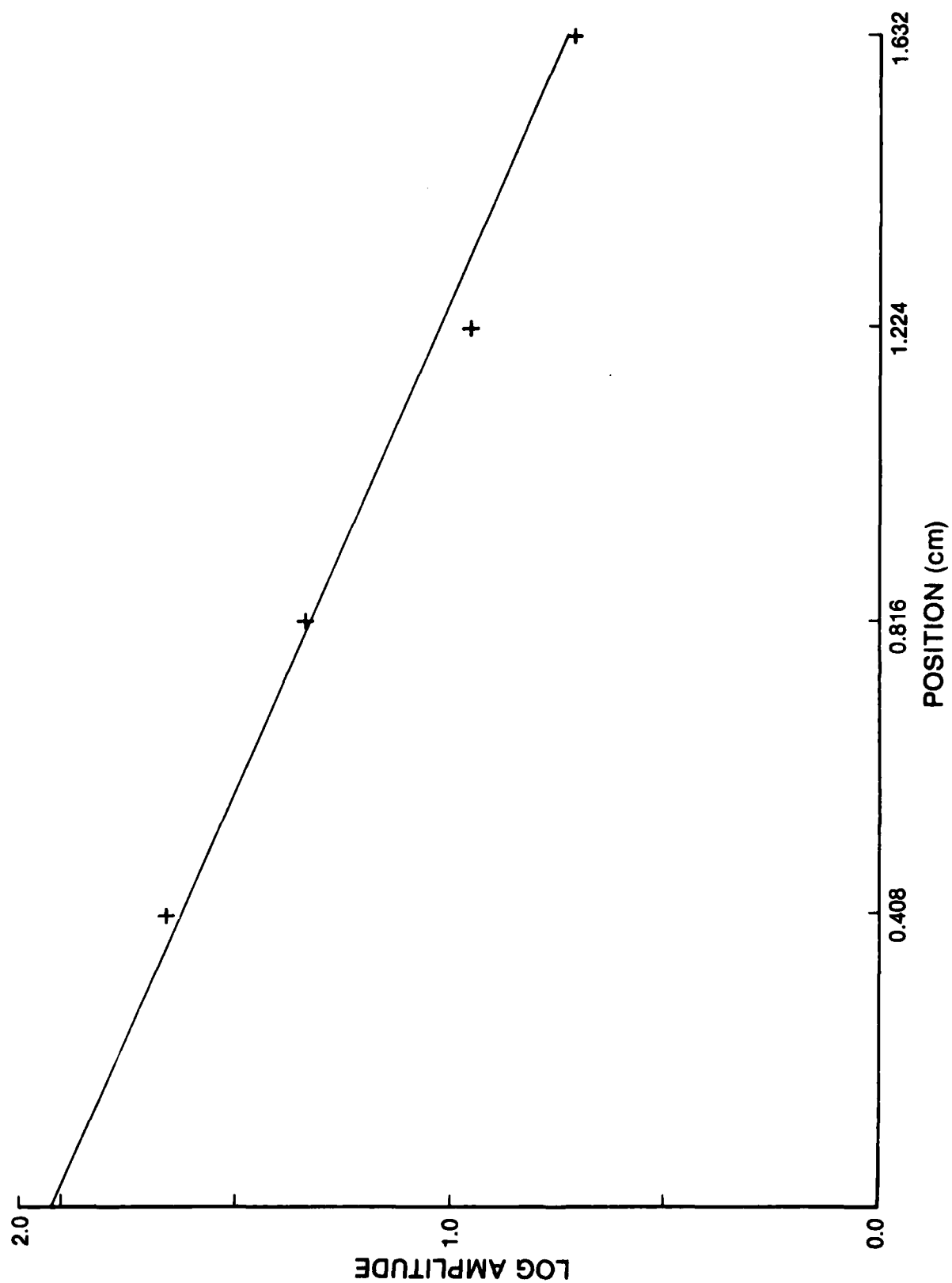


Figure 33. Data from Experiment to Measure Imaginary Part of Wavenumber of Surface Acoustic Wave on 0.74-mm Corrugated Al Sample. Log of amplitude of received signal is plotted versus lateral position of receiving transducer.

for a flat, (otherwise-equal) surface. It is important to note that this result is for the special case of normal incidence on the specific rough-surface sample which was tested. At a different angle or frequency or for a different sample, the coupling to the surface wave may be increased or decreased, implying a larger or smaller value for α . The fact that α is small for normal incidence on the 0.74 Al sample--with the corresponding conclusion that the coupling of energy to the surface wave from the incident wave is small--is consistent with the results of the experiment using both toneburst and pulsed back-reflection methods to excite the frequencies of anomalies. In the two methods, the results indicated shallow minima in the frequency domains verses amplitudes. This implies a small coupling of energy into the surface mode.

Appendix G presents the results of a theoretical study conducted on the interaction of elastic waves with a periodic rough interface layer between solids. This publication presents the initial stages in the modeling of this phenomenon. In the paper approximate boundary conditions were derived in three steps for a periodic rough interface layer between solids. The first step involved development of modified boundary conditions for a smooth thin layer (similar to work discussed in the papers of Appendix A described in Section 2). The second step was the development of modified conditions for a rough interface without a layer. Finally, the results of the first two steps were combined. In these steps, the amplitude of the surface roughness was assumed to be small, as was the layer thickness. Information is extracted from these boundary conditions concerning mode conversion, including surface-wave generation. This information is consistent with the grating formula given in Eqs. 1(a) and 1(b). Again, this publication presents only details of the initial stage of the study and is incomplete in that most of the experimental aspects discussed in this section cannot be understood in terms of that model in its present form.

In conclusion, several techniques were utilized in studying the phenomenon of surface-wave generation, propagation, and reradiation on periodic rough surfaces. The techniques that proved to be the most helpful in understanding the phenomenon were the pulsed Schlieren visualization technique, the pulsed time-gated FFT technique, the thorough-position and frequency-scan technique,

and the simple technique described for measuring the surface-wave velocity. Further theoretical and experimental studies are necessary to provide a more complete understanding of ultrasonic interactions with periodic rough surfaces.

Section 11

HIGH-IMPEDANCE BACKINGS FOR BROADBAND ULTRASONIC TRANSDUCERS

When ultrasonics are employed for NDE, it is frequently desirable to use short-duration acoustic pulses. These very short, or broadband, pulses provide much higher depth resolution than toneburst radiation. One of the simplest ways of producing broadband pulses is to back the piezoelectric blanks used for the generation of the ultrasound with a material having an acoustical impedance which matches that of the blank. This material must also be capable of sufficiently attenuating the sound waves entering it such that no energy is reflected back into the blank. Traditionally, backings have been produced using a mixture of tungsten and epoxy, the former producing the required high impedance and the latter serving as the matrix. A major problem with the use of tungsten/epoxy backings is that the desired impedance range of $30 - 35 \times 10^5 \text{ g/cm}^2\text{-sec.}$ requires a high volume fraction of tungsten, typically in the range 0.70 - 0.90. Methods of producing a cohesive backing which contains such high volume fractions of tungsten include centrifuging and hot pressing. These techniques generally produce backings with an impedance of $\leq 25 \times 10^5 \text{ g/cm}^2\text{-sec.}$ Accurate reproduction of the backing is difficult due to the steep slope of the impedance-versus-volume-fraction curve in this range. These limitations prompted the search for a more effective transducer backing.

Prerequisite to this search was a model for predicting the effective impedance of a mixture of two or more materials--a model describing the combined elastic stiffness moduli of the constituents. It was found that the lowest bound on the effective moduli produced acceptable fits to measured impedance data.

In order to reduce the volume fraction of tungsten, a binder having an impedance greater than that of the epoxy was required. Many other polymers which could serve as a matrix were examined, but all had an impedance less than $4 \times 10^5 \text{ g/cm}^2\text{-sec.}$ Other researchers⁹ who had made attempts with plastic metals such as tin as the matrix were forced to use very high compacting loads and even then, had not achieved complete success. The use

of molten metal was rejected since the high melting points involved were above the Curie temperature of some of the piezoelectric blanks. Finally, the use of low-melting-point alloys as a matrix was considered. Requirements for the selected alloy were as follows: the alloy must 1) effectively bond the various fillers employed, 2) have a melting point below 180°C, 3) be available in powder form with particle size less than 50 μ , and 4) adhere well to the gold electrodes on the piezoelectric blanks. A low-melting-point solder, In-Pb 50:50, was found to satisfy all of the above requirements.

The model was used to examine the impedance curves for mixtures of In-Pb 50:50, tungsten, and copper. The copper was added to aid in attaining a high attenuation and also to provide better fine tuning of the impedance without lowering the overall impedance. The results showed that the desired impedance range could be obtained using less than 60% tungsten. These three powders were mixed in a V-shaped mixer and hot pressed at 2000 psi at a temperature of 150°C. The impedance of the sample, calculated from the measurement of the longitudinal velocity and mass density, was as predicted by the model within experimental accuracy limits. In addition the backing was cohesive and had an attenuation of 15 dB/cm. Further tests showed that this mixture could also be hot pressed directly onto the piezoelectric blanks and would adhere very well to the gold electrode.

The ultrasonic output from a piezoelectric blank having a tungsten/In-Pb 50:50/copper backing was examined in a pulse-echo mode. The received pulse was very short and very broadband, surpassing the bandwidth of similar commercial transducers which have comparable center frequencies. Details of this study can be found in Appendix H.

Section 12

CONCLUSION

Work was accomplished in two major areas--ultrasonic leaky surface-wave phenomena on layered halfspaces and NDE of composites using ultrasonic backscattering. Several related projects were also carried out during the course of this contract. The study of surface waves led to an understanding of the interaction of transverse stresses with halfplane cracks normal to wavefronts. Reflection from composite interfaces and composite layers also fits naturally into the context of reflection from layered halfspaces. Additionally, the work on backscattering in composites precipitated the development of a corrosion-detection technique. Other areas of research included the coupling of energy into complex shapes, the reflection of finite acoustic beams from a periodic fluid-solid interface, and the production of impedance-matched backing materials to allow the manufacture of broadband transducers.

The leaky surface-wave phenomenon on a layered halfspace immersed in a fluid is now understood through models which have been developed, both analytical and numerical in nature. The observed behavior concerning the velocity dispersion and the amplitude distribution of the reflected field agrees very well with theoretical calculations. Experiments conducted by other researchers,¹⁰ confirm the theoretical trends found in the Shoch displacement parameter.

Existing theoretical models of wave propagation were exploited to predict and quantify the presence of a reflected surface wave from halfplane cracks oriented normal to the wavefronts. The expected reflection was observed in the laboratory on a glass sample having a corresponding surface crack. Efforts were made to assure that the reflection was from the crack tip and not from the fringe stress field about the tip.

A model of reflection of an acoustic wave incident on a fluid fibrous-composite interface was developed wherein the composite was unidirectional, with its principle direction being normal to the interface.

The model averaged the properties of the fibers and matrix to produce an effective, homogeneous dispersive medium. Experimental measurements verified the theoretical calculations.

The non-specular reflection of finite acoustic beams from a unidirectional, fibrous composite plate in a fluid at acute angles has been observed and measured. The fibers were oriented parallel to the plane of incidence and reflection, and parallel to the interface. An attempt was made to correlate these measurements with theoretical models involving Lamb waves. Preliminary study and experimental observation indicated that any model used to describe this behavior must take into account the dispersive anisotropic nature of the composite.

An acoustic backscattering technique has been shown to be extremely effective in NDE tests of composites, allowing mapping of subcritical flaws on a ply-by-ply basis. Fiber direction, fiber alignment, and porosity can be observed using this scanning procedure.

The applicability of the acoustic backscattering technique has been extended to the detection of corrosion. The resolution and sensitivity of detection of various types of surface flaws including corrosion have been measured. The effect of surface roughness, paint, epoxy, and porosity on the resolution and sensitivity has been examined. The feasibility of this technique has been demonstrated. As was shown, care must be taken to differentiate between porosity and corrosion due to the similar backscattering characteristics.

Two research systems were designed and built to aid in future NDE work within the AFWAL Material Laboratory. These are; 1) a precision, state-of-the-art, computerized C-scan system, and 2) a high repetition-rate pulsed schlieren system.

The problem of coupling acoustic energy into complex-shaped structures was analyzed. One possible solution, that of utilizing a mating (or complement) part was examined theoretically and experimentally to determine its efficiency at various angles. The efficiency of coupling energy into a part at

high angles of incidence in both through-transmission and backscattering modes was found to be significantly increased through the use of a mating part.

The effect of periodic rough surfaces on the reflection of finite acoustic beams from fluid/solid interfaces was investigated. Existing physical arguments concerning phase and a new theoretical development have predicted the generation of surface waves at angles other than the Rayleigh angle. This was confirmed experimentally. The nature of these non-specular reflections was observed experimentally, answering some questions and posing others. The surface-wave velocity of one rough-surface sample was shown to be unperturbed. Further work is required from a theoretical perspective in order to fully appreciate and understand the observed behavior of this phenomenon.

Finally, a high-impedance, broadband, ultrasonic, attenuative transducer backing was developed. This was accomplished by use of a low-melting-point alloy as a matrix, In-Pb, and a combination of tungsten and copper powders. This combination met the specific requirements for the backing when used in the proportions specified by a model extracted from existing theory which gives lower bounds to the effective properties of the particulate mixtures in a matrix. The backing was adhered to a piezoelectric blank to produce a broadband transducer.

REFERENCES

1. H. L. Bertoni and T. Tamir, "Unified Theory of Rayleigh-Angle Phenomena for Acoustic Beams at Liquid-Solid Interfaces," *Appl. Phys.* 21, 172 (1973).
2. A. H. Nayfeh, D. E. Chimenti, L. Adler, and R. L. Crane, "Ultrasonic Leaky Waves in the Presence of a Thin Layer," *J. Appl. Phys.* 52(8) (August 1981).
3. D. E. Chimenti and A. H. Nayfeh, "Leaky Rayleigh Waves at a Layered Halfspace-Fluid Interface," *Ultrasonics Symposium* (IEEE, NY, 1981), p. 291.
4. D. E. Chimenti, A. H. Nayfeh, and D. L. Butler, "Leaky Rayleigh Waves on a Layered Halfspace," *J. Appl. Phys.* 53(1), 170 (January 1982).
5. A. H. Nayfeh and D. E. Chimenti, "Reflection of Finite Acoustic Beams from Loaded and Stiffened Halfspaces," *J. Acoust. Soc. Amer.* 75, 1360 (1984).
6. R. C. Wyatt, "A Compact Stroboscopic Spark Light Source with Short Flash Duration and With Low Time Jitter," *J. Phys. E: Sci. Instrum.* 7, 437 (1974).
7. F. R. Rollings, "Ultrasonic Examination of Liquid-Solid Boundaries Using a Right-Angle Reflector Technique," *J. Acoust. Soc. Amer.* 44(2), 431 (1968).
8. D. E. Chimenti and R. L. Crane, "Elastic Wave Propagation Through Multilayered Media," Technical Report AFML-TR-79-4214 (Air Force Materials Laboratory, Wright-Patterson Air Force Base, OH, 1979).
9. S. Rokhlin, S. Golan, and Y. Gefin, "Acoustic Properties of Tungsten-Tin Composites," *J. Acoust. Soc. Amer.* 69(5), 1505 (1981).
10. D. E. Chimenti, "Energy Leakage from Rayleigh Waves on a Fluid-Loaded Layered Halfspace," *Appl. Phys. Lett.* 43(1), 46 (1 July 1983).

APPENDIX A

PUBLICATIONS ON SURFACE-WAVE INTERACTIONS WITH LAYERED HALF-SPACES

Ultrasonic leaky waves in the presence of a thin layer

A. H. Nayfeh^{a)}

Systems Research Laboratories, Dayton, Ohio 45440

D. E. Chimenti, Laszlo Adler,^{b)} and R. L. Crane

AFWAL Materials Laboratory, Wright-Patterson AFB, Ohio 45433

(Received 5 January 1981; accepted for publication 23 February 1981)

This paper presents theoretical and experimental results on the problem of bounded acoustic beam reflection at the Rayleigh angle from a fluid-solid interface which is loaded by a thin solid layer. The theoretical development exploits the framework of existing theory to yield a simple, analytic model which is reasonably accurate for thin layers. It is shown that the influence of the layer is contained entirely in the dispersive Rayleigh wavespeed and the thickness-dependent displacement parameter Δ . Measurements of the reflected acoustic field amplitude have been performed on several samples of stainless steel loaded with a copper layer. We have found reasonably good agreement between the theoretical model calculations and experimental measurements for ratios of the layer thickness to the Rayleigh wavelength as large as 0.3. Beyond this value, some disparity is observed, particularly in the calculation of the thickness-dependent Rayleigh wavespeed.

PACS numbers: 43.20.Fn, 43.30.Dr, 43.30.Ft

I. INTRODUCTION

The energy redistribution that occurs when a bounded acoustic beam is reflected from a fluid-solid interface has been the subject of many analytical and experimental investigations. Following the discovery of analogous effects in optics by Goos and Hänchen,¹ Schoch predicted,² and later experimentally verified,³ the beam-displacement effect for an acoustic beam incident on a liquid-solid interface. According to Schoch's predictions, the beam is nonspecularly reflected in that it is laterally displaced while retaining, more or less, its original profile. In contrast to these predictions, many experiments⁴⁻⁷ have revealed that the reflected beam may also suffer severe distortion if it is incident at, or near, the Rayleigh angle. Physically, resonant transfer of acoustic energy from a longitudinal wave in the liquid to a pseudo-Rayleigh wave propagating along the liquid-solid interface occurs. As it propagates, the Rayleigh wave reradiates into the liquid at the Rayleigh angle because of the resonant coupling. The result is a redistribution of the reflected field intensity such that a sizable fraction of the acoustic energy seems linearly displaced along the interface. This energy redistribution includes, in addition to the lateral displacement, a null region and a trailing field which becomes weaker as it extends along the interface away from the incident beam.

Bertoni and Tamir⁸ have examined the reflection coefficient for angles close to the Rayleigh angle and constructed a model which explains these distortion phenomena. Specifically, they pointed out that the suitably simplified reflection coefficient has a singularity which leads to solutions corresponding to radiating (leaky) Rayleigh waves. According to their analysis the distortion is the result of interference between the geometrically reflected field and the field of a

leaky Rayleigh wave created by the incident beam at the Rayleigh angle. Braezeale, Adler, and Scott⁹ experimentally verified the Bertoni and Tamir model, while Pitts, Plona, and Mayer¹⁰ have recently presented theoretical results for the case of a finite beam incident on a solid plate in a liquid. Their results show that distortion of the reflected beam at the Lamb angle can also occur.

This paper investigates theoretically and experimentally, the influence of a thin layer bonded to a solid upon the shift and distortion of the reflected beam. This problem differs from the no-layer case in that the reflection coefficient is not readily available in closed form, and therefore must be derived. The results of this analysis reveal new phenomena that occur in the presence of the layer. Both the Rayleigh wavespeed and the parameter associated with the energy redistribution are frequency dependent in the layer case. These two new effects, in turn, influence the lateral displacement and distortion of the reflected beam.

A solution to the equations that result from an analysis of the above model could be obtained formally by solving the field equations in the fluid, layer, and solid halfspace with the appropriate boundary conditions. However, the results would be quite complicated algebraically. Furthermore, such detailed analysis of the wave motion in the layer would greatly complicate the problem. An attempt to obtain the exact solution of this problem could, therefore, obscure important features of the solution for a thin layer. However, since we are mainly interested in the thin-layer case (thickness small compared to the incident wavelength), we can proceed in a much less cumbersome way by including the effect of the layer as a nonzero homogeneous term in the boundary conditions. To this end, we shall develop modified boundary conditions, referring to the reformulated problem as the "reduced model."

In Sec. II the complete theoretical treatment for leaky Rayleigh waves in the presence of a thin layer is developed. Section III outlines experimental considerations, and we

^{a)}Consultant. Permanent address: Department of Aerospace Engineering and Applied Mechanics, University of Cincinnati, Ohio 45221.

^{b)}Visiting Scientist. Permanent address: Department of Welding Engineering, Ohio State University, Columbus, Ohio 43211.

present our measurements together with results from the theoretical model in Sec. IV.

II. THEORY

A. Formulation of the problem

Consider a thin elastic layer of thickness $2h$ tightly bonded to a solid elastic halfspace of different material. Overlying this structure is a fluid (water) halfspace as shown in Fig. 1. A system is chosen with the origin located at the center of the layer, the positive z axis pointing downward into the semi-infinite solid. The layer extends from $-h \leq z \leq h$, with the solid halfspace extending from $z = -h$ to ∞ and the fluid extending from $z = -h$ to $-\infty$. In our subsequent analysis we shall identify the field variables and properties of the layer, fluid, and solid substrate with the subscripts 0, f , and s , respectively. The fluid medium is subjected to a time-harmonic, bounded acoustic beam incident onto the fluid-solid interface at an angle θ , with respect to the surface normal. To reduce the analysis to two dimensions, we assume that no acoustic wave, incident or reflected, has a y dependence. Alternatively, all particle motion is confined to the x - z plane.

In order to study the behavior of the reflected beam, one must solve the appropriate field equations in each of the three media (liquid, layer, and substrate), incorporating the appropriate continuity conditions. Formal solutions are obtained by introducing the potential functions ϕ and ψ for each of the media. These functions are related to the particle displacements and stresses by

$$u = \frac{\partial \phi}{\partial x} - \frac{\partial \psi}{\partial z}, \quad (1)$$

$$w = \frac{\partial \phi}{\partial z} + \frac{\partial \psi}{\partial x}, \quad (2)$$

$$\sigma_x = (\lambda + 2\mu) \frac{\partial^2 \phi}{\partial z^2} + \lambda \frac{\partial^2 \phi}{\partial x^2} + 2\mu \frac{\partial^2 \psi}{\partial x \partial z}, \quad (3)$$

$$\sigma_{xz} = \mu \left(2 \frac{\partial^2 \phi}{\partial x \partial z} + \frac{\partial^2 \psi}{\partial x^2} - \frac{\partial^2 \psi}{\partial z^2} \right). \quad (4)$$

Since the fluid cannot support a shear wave, the shear potential ψ is identically zero in this medium. In the two solid media ψ has only a single nonvanishing component because particle motion is restricted to the plane of incidence.

The wave potentials ϕ and ψ satisfy separate wave equations for linear, isotropic media, namely,

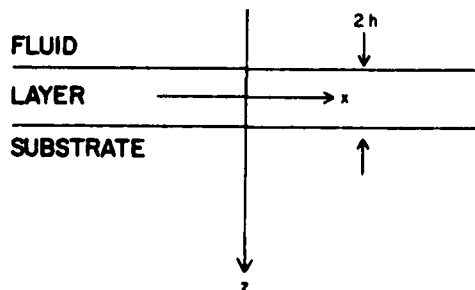


FIG. 1. Coordinate geometry.

$$\frac{\partial^2 \phi}{\partial x^2} + \frac{\partial^2 \phi}{\partial z^2} = \frac{1}{c_1^2} \frac{\partial^2 \phi}{\partial t^2}, \quad (5a)$$

$$\frac{\partial^2 \psi}{\partial x^2} + \frac{\partial^2 \psi}{\partial z^2} = \frac{1}{c_2^2} \frac{\partial^2 \psi}{\partial t^2}. \quad (5b)$$

The longitudinal and shear wavespeeds for each medium are given respectively by

$$c_1 = [(\lambda + 2\mu)/\rho]^{1/2}, \quad c_2 = (\mu/\rho)^{1/2}. \quad (6)$$

Solutions of Eqs. (1)–(6) must also satisfy the continuity conditions at the interfaces; in our notation these are

$$u_s = u_0, \quad w_s = w_0, \quad \sigma_{zs} = \sigma_{z0}, \quad \sigma_{xzs} = \sigma_{xz0}, \quad \text{at } z = h, \quad (7)$$

$$w_0 = w_f, \quad \sigma_{x0} = \sigma_{xf}, \quad \sigma_{xz0} = 0, \quad \text{at } z = -h. \quad (8)$$

B. Reduced model

In principle solutions to Eqs. (1)–(5) subject to the continuity conditions of Eqs. (7) and (8) could be formally obtained, but the results would be quite complicated algebraically. An attempt to obtain an exact solution could obscure important features of the problem. Moreover, since our principal interest in this problem centers on the case of a thin layer, we include the effect of the layer as a nonzero, homogeneous term in the boundary conditions. To this end we rewrite Eqs. (1)–(5) for the layer in terms of displacements and stresses. These relations include the two-dimensional momentum and constitutive equations

$$\frac{\partial \sigma_{x0}}{\partial x} + \frac{\partial \sigma_{xz0}}{\partial z} = \rho_0 \ddot{u}_0, \quad (9)$$

$$\frac{\partial \sigma_{x0}}{\partial z} + \frac{\partial \sigma_{xz0}}{\partial x} = \rho_0 \ddot{w}_0, \quad (10)$$

$$\sigma_{x0} = (\lambda_0 + 2\mu_0) \frac{\partial u_0}{\partial x} + \lambda_0 \frac{\partial w_0}{\partial z}, \quad (11)$$

$$\sigma_{x0} = (\lambda_0 + 2\mu_0) \frac{\partial w_0}{\partial z} + \lambda_0 \frac{\partial u_0}{\partial x}, \quad (12)$$

$$\sigma_{xz0} = \mu_0 \left(\frac{\partial u_0}{\partial z} + \frac{\partial w_0}{\partial x} \right). \quad (13)$$

Since we assume that $2h$ is finite but small, variations in the displacements u_0 and w_0 across the thickness of the layer can be neglected. Equations (9)–(13) may be integrated across the thickness of the layer using the following definition of average value:

$$\langle \bar{\cdot} \rangle = \frac{1}{2h} \int_{-h}^h (\cdot) dz. \quad (14)$$

With this procedure, we obtain the following:

$$2h \left(\frac{\partial \bar{\sigma}_{x0}}{\partial x} - \rho_0 \ddot{u}_0 \right) = \sigma_{xz0}(-h) - \sigma_{xz0}(h), \quad (15)$$

$$2h \left(\frac{\partial \bar{\sigma}_{0xz}}{\partial x} - \rho_0 \ddot{w}_0 \right) = \sigma_{x0}(-h) - \sigma_{x0}(h). \quad (16)$$

$$\bar{\sigma}_{x0} = (\lambda_0 + 2\mu_0) \frac{\partial u_0}{\partial x}, \quad (17)$$

$$\bar{\sigma}_{x0} = \lambda_0 \frac{\partial u_0}{\partial x}, \quad (18)$$

$$\bar{\sigma}_{xz0} = \mu_0 \frac{\partial w_0}{\partial x} \quad (19)$$

If Eqs. (17)–(19) are substituted in Eqs. (15) and (16), they lead to

$$2h \left((\lambda_0 + 2\mu_0) \frac{\partial^2 u_0}{\partial x^2} - \rho_0 \ddot{u}_0 \right) = \sigma_{xz0}(-h) - \sigma_{xz0}(h), \quad (20)$$

$$2h \left(\mu_0 \frac{\partial^2 w_0}{\partial x^2} - \rho_0 \ddot{w}_0 \right) = \sigma_{xz0}(-h) - \sigma_{xz0}(h). \quad (21)$$

Using the continuity relations Eqs. (7) and (8), Eqs. (20) and (21) may be recast into the following forms:

$$2h \left((\lambda_0 + 2\mu_0) \frac{\partial^2 u_0}{\partial x^2} - \rho_0 \ddot{u}_0 \right) = -\sigma_{xz0}(h), \quad (22)$$

$$2h \left(\mu_0 \frac{\partial^2 w_0}{\partial x^2} - \rho_0 \ddot{w}_0 \right) = \sigma_{xz0}(-h) - \sigma_{xz0}(h). \quad (23)$$

Equations (22) and (23) are significant since they are the only relations that reflect the effect of the layer via the modified longitudinal and shear stress boundary conditions. In the absence of the layer ($h = 0$) they reduce to $\sigma_{xz}(0) = \sigma_{xz}(0)$, $\sigma_{xz}(0) = 0$, which are the classical liquid-solid stress continuity relations. With these approximations the displacement continuity conditions, Eqs. (7) and (8), reduce to

$$u_0 = u_s = u_f, \quad w_0 = w_s = w_f, \quad \text{at } z = 0. \quad (24)$$

To first-order approximation in h , Eqs. (22) and (23) can be recast into the approximate forms

$$2h \left((\lambda_0 + 2\mu_0) \frac{\partial^2 u_0}{\partial x^2} - \rho_0 \ddot{u}_0 \right) = -\sigma_{xz0}(0), \quad (25)$$

$$2h \left(\mu_0 \frac{\partial^2 w_0}{\partial x^2} - \rho_0 \ddot{w}_0 \right) = \sigma_{xz0}(0) - \sigma_{xz0}(0). \quad (26)$$

C. Reflection coefficient and leaky wave dispersion

To determine the reflection coefficient for plane harmonic waves incident from a fluid onto a solid surface, we begin by writing the Fourier transforms of the wave potentials with respect to the x coordinate and assume exponential solutions in the z coordinate. These steps lead to formal solutions given by

$$\hat{\phi}(\xi) = \Phi \exp(i\xi z), \quad \hat{\psi}(\xi) = \Psi \exp(i\xi z) \quad (27a, b)$$

and

$$\hat{\phi}_r(\xi) = \Phi_r \exp(i\xi z) + \Phi'_r \exp(-i\xi z), \quad (27c)$$

where the caret indicates a transform and the prime designates a reflected field. The circular frequency is ω and the complex amplitudes Φ , Ψ , Φ_r , and Φ'_r are constants to be determined from the boundary conditions. The wave-vector components are given by

$$\xi_{1,2} = (k_{1,2}^2 - \xi^2)^{1/2}, \quad \xi_f = (k_f^2 - \xi^2)^{1/2}, \quad (28)$$

where $\xi \equiv k_f \sin \theta$ with the angle θ measured from the surface normal. The longitudinal and shear wave numbers are $k_{1,2} = \omega/c_{1,2}$. In the fluid we shorten this notation to $k_f = \omega/c_f$, since there can be no ambiguity. From Eq. (27c) the reflection coefficient R is given by

$$R = \Phi'_r / \Phi_r. \quad (29)$$

Inserting the Fourier transformed stresses and displacements into the continuity conditions Eqs. (7) and (8) yields a

system of linear equations that relate the wave potential amplitudes. Using these relations the value of R becomes

$$R = \frac{\xi_f(a_1 b_2 + a_2 b_1) + \rho_f \omega^2 (\xi a_2 - \xi_1 b_2)}{\xi_f(a_1 b_2 + a_2 b_1) - \rho_f \omega^2 (\xi a_2 - \xi_1 b_2)}, \quad (30)$$

where

$$a_1 = \mu_1 (2\xi^2 - k_{1,2}^2) - 2ih\mu_1 \xi_1 \xi_{20}^2, \quad (31a)$$

$$b_1 = 2i\xi (\mu_1 \xi_{20} - h\mu_1 \xi_{20}^2), \quad (31b)$$

$$a_2 = 2i\xi [\mu_1 \xi_{10} - h(\lambda_0 + 2\mu_0) \xi_{10}^2], \quad (31c)$$

$$b_2 = \mu_1 (2\xi^2 - k_{1,2}^2) - 2ih\xi_{20} (\lambda_0 + 2\mu_0) \xi_{10}^2. \quad (31d)$$

In the absence of the layer ($h = 0$) Eq. (30) correctly predicts the reflection coefficient of a liquid-solid interface (see Ref. 13 for example). Now we consider the dispersion of the propagating surface waves at the liquid-solid interface. This dispersion is produced by a layer and, therefore, vanishes in its absence.

The expression Eq. (30) for the reflection coefficient contains, as a by-product, the characteristic equation for the propagation of a modified (leaky) Rayleigh surface wave which propagates along the interface between the fluid and a thin layer bonded to the solid. The vanishing of the denominator in Eq. (30),

$$\xi_f(a_1 b_2 + a_2 b_1) - \rho_f \omega^2 (\xi a_2 - \xi_1 b_2) = 0 \quad (32)$$

is the characteristic equation for such waves. If Eq. (31) is substituted into Eq. (32), then for a real frequency ω , Eq. (32) will admit complex solutions of the form

$$\xi = k_r + i\alpha. \quad (33)$$

From Eq. (33) the phase velocity of the Rayleigh wave is given as $c_r = \omega/k_r$, and α is the attenuation coefficient. Note that α vanishes in the absence of the fluid, and hence no attenuation (leaking of energy in the fluid) occurs. In the presence of a fluid these surface waves are called leaky waves. It will later be shown (Viktorov¹¹ also notes this) that c_r is hardly affected by the presence of the fluid, and therefore, α is very small. However, as shown by Bertoni and Tamir,⁸ α is important because it is related to the lateral displacement of the reflected beam. Examination of Eq. (32) indicates that in the layer case, the medium is dispersive, and c_r and α depend on the frequency in a rather complicated fashion. Notice also that Eq. (32) contains the classical characteristic equation for a surface wave, which is obtained by setting $h = 0$ and $\rho_f = 0$. Graphical results of c_r as a function of frequency are presented and compared to measurements in Sec. IV.

D. Field of the incident beam

In this section we discuss the propagation in the liquid of a finite-width beam having a Gaussian profile in the plane of incidence. This choice simplifies considerably the analytic evaluation of the integrals in this and the next subsection. To this end, consider a two-dimensional, finite-width Gaussian beam generated in a liquid at an arbitrary location $z = -L$, and propagating toward the interface at an angle θ , with the normal to the surface. The profile of the beam is characterized by an effective width $2a$ that is large compared to the wavelength λ in the liquid. Therefore, the acoustic field has significant amplitude only for a distance a on either side of the beam axis. We further assume that the beam consists of

rays that are parallel to the axis of the beam. If the incident-beam field is known at some position, e.g., $z = 0$, then the beam field can be determined at any location by solving the wave equation subject to the initial conditions. From Eq. (27c), we have

$$\phi_f(x, z) = \frac{1}{2\pi} \int_{-\infty}^{\infty} \Phi_f(\xi) \exp(i\xi x + i\xi_f z) d\xi, \quad (34)$$

where

$$\Phi_f(\xi) = \int_{-\infty}^{\infty} \phi_f(x, 0) e^{-i\xi x} dx. \quad (35)$$

Since it is assumed that $\phi_f(x, 0)$ is Gaussian, the

$$\phi_f(x, 0) = \frac{\Gamma_0 \exp[-(x/a_0)^2 + ik_f x]}{\sqrt{\pi a \cos\theta_i}}, \quad (36)$$

where Γ_0 represents the amplitude of the potential in appropriate units. Here $k_i = k_f \sin\theta_i$, and $a_0 = a \sec\theta_i$ is the half-width acoustic beam along the x axis. Substitution from Eq. (36) into Eq. (35) yields

$$\Phi_f = \Gamma_0 \frac{\exp[-(\xi - k_i)^2 (a_0/2)^2]}{\cos\theta_i}, \quad (37)$$

$$\phi_f(x, z) = \frac{\Gamma_0}{2\pi} \int_{-\infty}^{\infty} \exp\left\{-(\xi - k_i)^2 \left[\left(\frac{a_0}{2}\right)^2 + \frac{iz}{2k_f \cos^3\theta_i}\right]\right\} \exp[i\xi(x - z \tan\theta_i)] \exp\left(\frac{izk_f}{\cos\theta_i}\right) \frac{d\xi}{\cos\theta_i}. \quad (41)$$

Comparing the integrals of Eqs. (41) and (38), it is evident that Eq. (41) can be inverted directly to give

$$\phi_f(x, z) = \Gamma_0 \frac{\exp[ik_f(x \sin\theta_i + z \cos\theta_i)]}{\sqrt{\pi a_r \cos^2\theta_i}} \exp\left(-\left(\frac{x_r}{a_r}\right)^2\right), \quad (42)$$

where

$$x_r = x - z \tan\theta_i, \quad (43a)$$

$$a_r^2 = a_0^2 + 2iz/k_f \cos^3\theta_i. \quad (43b)$$

The beam in Eq. (42) is also Gaussian and propagates in the direction $x \sin\theta_i + z \cos\theta_i$, with an effective complex width of $2a_r$, as given by Eq. (43b). If the plane at which the beam field is known is located at $z = -L$, rather than at $z = 0$, the relations Eqs. (43a), and (43b) have to be modified by substituting $z + L$ for z . Note that if two, rather than three, terms are retained in the expansion of Eq. (40), the width of the beam a_r would reduce to a_0 ; hence, the beam in Eq. (42) would only be shifted without a change in shape (spreading and reduction in amplitude). It is the inclusion of the third term in the expansion which is responsible for the analytical spreading of the Gaussian beam.

E. Field of the reflected beam

Upon reflection of the incident beam into the fluid the beam profile of Eq. (34) is modulated by the reflection coefficient $R(\xi)$. This reflected beam is described by

$$\phi'_f = \frac{1}{2\pi} \int_{-\infty}^{\infty} \Phi_f(\xi) R(\xi) \exp(i\xi x - i\xi_f z) d\xi, \quad (44)$$

where z has been replaced by $-z$ to indicate reflection. The evaluation of the integral in Eq. (44) is more complicated than the corresponding integral of Eq. (34). This complica-

tion, if used with Eq. (34) yields

$$\phi_f(x, z) = \frac{\Gamma_0}{2\pi} \int_{-\infty}^{\infty} \exp\left[-(\xi - k_i)^2 \left(\frac{a_0}{2}\right)^2\right] \times \exp(i\xi x + i\xi_f z) \frac{d\xi}{\cos\theta_i}. \quad (38)$$

Examination of Eq. (38) reveals that it cannot be inverted to give exact analytic results. However, the principal contribution to the integral comes from values of ξ lying in the vicinity of the incident wave number k_i . Accordingly, approximate values of $\phi_f(x, z)$ can be obtained by expanding ξ in a Taylor series about k_i . Using terms up to the third order, we obtain

$$\xi_f = \frac{k_f^2}{(k_f^2 - k_i^2)^{1/2}} - \frac{k_i \xi}{(k_f^2 - k_i^2)^{1/2}} - \frac{k_f^2 (\xi - k_i)^2}{2(k_f^2 - k_i^2)^{3/2}} \quad (39)$$

Since $k_i = k_f \sin\theta_i$, ξ_f becomes

$$\xi_f = k_f / \cos\theta_i - \xi \tan\theta_i - (\xi - k_i)^2 / 2k_f \cos^3\theta_i. \quad (40)$$

Substituting from Eq. (40) into Eq. (38) and collecting terms yields

tion is due to the additional dependence of $R(\xi)$ on ξ . Therefore, in order to develop a tractable model describing the reflection phenomena, it is also necessary to approximate $R(\xi)$ for values of ξ close to k_i . In adopting any form of approximation, care must be used. The straightforward approximation, such as the Taylor-series expansion, is adequate in ranges where $R(\xi)$ is well-behaved, specifically away from the surface-wave pole at $k_r + i\alpha$ (see above discussion of the dispersion effects). If this fact is not taken into consideration, the results of this simple expansion for incident waves near or at the Rayleigh angle are inadequate to explain the distortion of the reflected beam. By including the influence of the Rayleigh wave pole, Bertoni and Tamir⁸ were able to explain these phenomena. In Ref. 8 it was also shown that Schoch's results are correct only for very wide beams. Before considering the influence of the Rayleigh wave pole on the reflected beam, we shall apply Schoch's approach to the present problem to obtain an expression for the beam displacement parameter Δ_r . By considering the case of total internal reflection ($\theta_i > \theta_c$), we may write the reflection coefficient in the following form:

$$R(\xi) = |R(\xi)| e^{iS(\xi)}, \quad (45)$$

where the amplitude $|R(\xi)|$ is very close to unity, and $S(\xi)$ is the phase of $R(\xi)$. Consistent with our previous approximation, the Taylor-series expansion about k_i is used for $S(\xi)$; this result is equivalent to the Fresnel expansion.⁸ Then retaining the first two terms we obtain

$$R(\xi) \approx R(k_i) \times \exp\{i[(\xi - k_i)S'(k_i) + \frac{1}{2}(\xi - k_i)^2 S''(k_i)]\} \quad (46)$$

where $S'(k_i) = \partial S(\xi) / \partial \xi$ evaluated at $\xi = k_i$; the same holds

for $S''(k_r)$. The inclusion of the second term in the expansion was also retained by Brekhovskikh¹²; it is of the same order of magnitude as the term in the exponent of Φ_r as shown in Eq. (37). Substituting from Eq. (46) into Eq. (44) and comparing with Eq. (38), we deduce that, apart from a constant multiplier, the influence of $R(\xi)$ is twofold; first, it accounts for the lateral displacement of the reflected beam along the x axis through the following relation:

$$\Delta_s = -S'(k_r) \quad (47)$$

and, second, the beam width is modified to a new complex width,

$$a_r = [a_r^2 - 2iS''(k_r)]^{1/2}. \quad (48)$$

Both effects indicated in Eqs. (47) and (48) exist regardless of the value of z . The subscript on the displacement parameter Δ_s refers to the developer of this formalism^{2,3}; we retain this terminology because of its widespread use in the literature. It follows then that the reflected beam profile at any location (x, z) of a Gaussian beam at angles different from the Rayleigh angle has the approximate form of Eq. (42), if z is replaced by $-z$ to indicate reflection and the parameters x_r and a_r are redefined as follows:

$$x_r = x + z \tan \theta_i - S'(k_r), \quad (49)$$

$$a_r^2 = a_0^2 - 2iz/k_f \cos^2 \theta_i - 2iS''(k_r). \quad (50)$$

It now remains to derive specific expressions for $S'(k_r)$ and $S''(k_r)$. This can be done easily by differentiating Eq. (45) with respect to ξ . Noting that since $|R(\xi)|$ is approximately unity, we have

$$S'(k_r) = R'(k_r)/iR(k_r). \quad (51)$$

Now, by rewriting $R(\xi)$ as

$$R = 1 - 2F/(G + F), \quad (52)$$

where

$$F = -(\rho_f \omega^2 / \xi_f)(\xi_1 b_2 + \xi a_2),$$

$$G = a_1 b_2 + a_2 b_1,$$

we obtain

$$\Delta_s = -S'(k_r) = 2 \left(\frac{F'G - G'F}{i(G+F)(G-F)} \right)_{\xi=k_r} \quad (53)$$

and

$$S''(k_r) = -2 \left(\frac{F'G - G'F}{i(G+F)(G-F)} \right)'_{\xi=k_r}. \quad (54)$$

Substituting for F and G into Eq. (53), we obtain the lateral displacement of the reflected beam at or near the Rayleigh angle. Since F and G are functions of the frequency ω , Δ_s will also depend on ω in a manner that may be seen from Eq. (53). In the absence of the layer ($h = 0$), Eq. (53) yields the results that are reported by Schoch.²

For the special case when the beam is incident at the Rayleigh angle, $\xi = k_r + i\alpha$, one finds that $G(k_r) \sim 0$ and Eq. (53) reduces to the form

$$\Delta_s = -S'(k_r) = -2iG'(k_r)/F(k_r). \quad (55)$$

Employing the expressions for F and G in the above equation, we obtain, after some algebraic manipulations and reductions,

$$\Delta_s = -(\lambda \rho_s / \rho_f)(rs)^{1/2}(T_f D_1 / T_1 D_2), \quad (56)$$

where

$$s = (c_{2s}/c_r)^2, \quad r = (c_{2s}/c_f)^2, \quad q = (c_{2s}/c_{1s})^2,$$

$$s_{10} = [\rho_0/(\lambda_0 + 2\mu_0)]^{1/2} = 1/c_{10},$$

$$s_{20} = (\rho_0/\mu_0)^{1/2} = 1/c_{20},$$

$$\bar{\mu}_0 = \mu_0/\mu_s, \quad \bar{E}_0 = (\lambda_0 + 2\mu_0)/\mu_s,$$

$$P_{10} = s^2 - s_{10}^2, \quad P_{20} = s^2 - s_{20}^2,$$

$$T = (s-1)^{1/2}, \quad T_1 = (s-q)^{1/2}, \quad T_f = (r-s)^{1/2},$$

$$D_1 = 16s - 4s(T/T_1 + T_1/T) - 8TT_1 - 8$$

$$- Q[(2T^2 + P_{10})\bar{E}_0/T + (2T_1^2 + P_{20})\mu_0/T_1],$$

$$D_2 = 1 - Q\bar{E}_0 P_{10}(T - s/T_1),$$

and

$$Q = 2hk_{2s} = 2h\omega/c_{2s}. \quad (57)$$

In the absence of the layer Eq. (56) reduces to

$$\Delta_s = \frac{2\lambda \rho_s}{\pi \rho_f} \left(\frac{r(r-s)}{s(s-1)} \right)^{1/2} \left(\frac{1 + 6s^2(1-q) - 2s(3-2q)}{s-q} \right), \quad (58)$$

which is identical with the results obtained by Schoch (see also Ref. 12).

The dependence of Δ_s/λ on the dimensionless frequency Q for a specific set of elastic constants discussed later is shown in Fig. 2. In addition to the explicit appearance of Q in Eq. (56), c_r contains an implicit dependence on frequency and layer thickness, which also modifies the behavior of Δ_s/λ . The correct value of c_r as a function of Q is obtained from Eq. (32). At $Q = 0$, corresponding to long wavelength or small layer thickness, the value of Δ_s/λ from Fig. 2 is that appropriate for the substrate material above, as verified in Eq. (58). As the layer thickness or the frequency increases, Δ_s/λ decreases towards the value predicted by Eq. (58) for the material properties of the layer. In fact, one wouldn't expect the model to retain validity much beyond $Q = 1$, considering the approximation implicit in Eqs. (17)–(19). How-

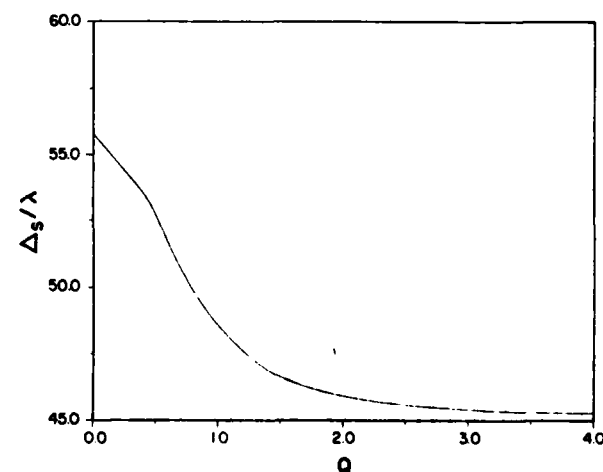


FIG. 2. Displacement parameter over wavelength plotted as a function of the dimensionless frequency-thickness product. Elastic constants are appropriate for a copper layer on stainless steel.

ever, the results seem fairly insensitive to the assumption of constant displacement across the layer, although we have determined that the sensitivity can be strongly dependent on the specific combination of properties of the layer and substrate. In any case good agreement with experimental measurements is observed up to $Q \approx 1.5$ ($2h/\lambda \approx 0.25$), as we show in Sec. IV.

With the above results the integral of Eq. (44) may now be evaluated. Following the procedure outlined in earlier work,^{8,13} the reflection coefficient in Eq. (30) is approximated by a truncated Laurent expansion about $\xi = k_r + i\alpha$, keeping only the first term. In this way we consider the influence of only the Rayleigh wave pole on the reflected field, and, correspondingly, the final result will be valid only when θ_r is at or near the Rayleigh angle. Since k_r is constant, the ξ dependence of ζ_r can be explicitly developed by a suitable expansion of terms in Eq. (28). After a change of variable, an application of the convolution theorem, and a contour integration around the upper half-plane, we obtain the final result for the wave potential of the reflected field at the Rayleigh angle

$$\phi_r' = \phi_{sp} + \phi_{lw},$$

where the subscripts sp and lw stand for specular and leaky wave, respectively. These two wave potential components of the reflected field are given explicitly from the above analysis by

$$\phi_{sp}(x,z) = - \frac{\Gamma_0 \exp(-x^2/a_r^2)}{\sqrt{\pi} a_r \cos \theta_r} \times \exp[ik_r(x \sin \theta_r - z \cos \theta_r)] \quad (59)$$

and

$$\phi_{lw}(x,z) = -2\phi_{sp} \left[1 - \sqrt{\pi} a_r \exp(-\gamma^2) \operatorname{erfc}(\gamma)/\Delta_r \right], \quad (60)$$

where

$$\gamma \equiv a_r/\Delta_r - x/a_r, \quad (61)$$

$\operatorname{erfc}(\gamma)$ is the complementary error function, and a_r is given by Eq. (50) neglecting $S''(k_r)$. It should be noted that apart from a generalization which includes the z dependence, Eqs. (59) and (60) are identical to Bertoni and Tamir's⁸ result. This fact indicates that the modification of the reflected field due to the layer is contained entirely in the dispersive Rayleigh wavespeed c_r , the displacement parameter Δ_r , and the dimensionless frequency Q . The model presented here combines the new features that emerge in the layer case with previous results to yield an accurate, yet analytic, expression for the total reflected field.

III. EXPERIMENTAL PROCEDURE

Experiments in support of the theoretical development of the previous sections have been performed to test dependences on important parameters of the model. We have varied the layer thickness, ultrasonic frequency, incident angle, and transducer-interface separation distance in the course of many measurements on several samples. For rapid data acquisition and reduction an on-line computer is employed.

A. Sample preparation

The specimens used in these measurements are 302 stainless steel electroplated with high-purity copper. Both surfaces of the stainless steel plates ($50 \times 100 \times 10$ mm) are machine ground to assure parallelism, then abrasively polished to a mirror finish. The side to be electroplated is pickled and nickel-activated to achieve good adhesion of the copper layer. After electroplating, the plated surface is also mirror smooth, occasionally interrupted by small pits approximately $30 \mu\text{m}$ in diameter. Although the thickness of the deposited layer is carefully controlled in the deposition process, a separate measurement of thickness is made to confirm the estimate of the electroplating. We cut into the specimen at several places along its edges with a high-speed abrasive cutter to a depth of 2 or 3 mm. The exposed surface is chemically etched with a weak acid solution to remove any traces of copper smeared during the cutting operation. Then each etched surface is examined with a cathetometer, and the copper layer thickness is measured. Variations in the readings are less than 5%, indicating a uniform layer.

To permit as detailed a comparison with theory as possible, ultrasonic velocity measurements of a representative steel sample have been undertaken. We find for the longitudinal wavespeed a value of 5.69 ± 0.02 km/sec, while the transverse wavespeed is 3.13 ± 0.01 km/sec. These results are within 0.5% of the quoted values for 302 stainless steel.¹⁴ A possible source of uncertainty is the wavespeeds of the copper layers. Careless electroplating can lead to porous or spongy films. Microscopic examination of our samples has revealed no such problems. However, we have used literature values¹⁵ of 4.76 and 2.2 km/sec, where the transverse wavespeed represents a 5% degradation of the value for bulk copper at room temperature. The densities are 8.93 g/cm^3 for copper and 7.9 g/cm^3 for stainless steel.

B. Apparatus

Linear and angular transducer orientation is critical for accurate comparisons with the theoretical model. Precision linear positioning is accomplished through the use of translation slides mounted to the automated bridge of an ultrasonic inspection tank. Translational resolution of this system is 0.02 mm. Angular alignment is performed by attaching θ -

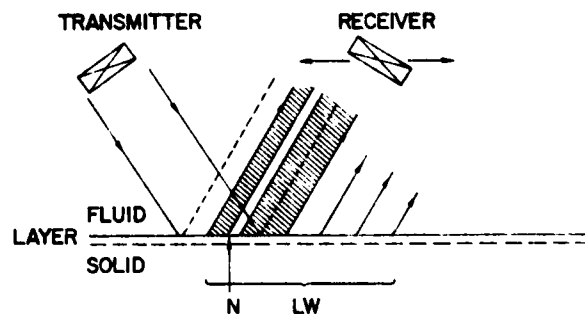


FIG. 3. Schematic of leaky-wave experiment. Transmitter is fixed, while receiver scans along x axis. Dashed lines in reflected field indicate specular reflection. Shaded regions contain most of the acoustic power. Null zone is denoted by N and leaky-wave reflected field by LW .

ϕ manipulators¹⁶ to the translation slides, and the transducers are connected to the manipulators through short (5-cm) search tubes. Approximately 0.10° is the limit of angular resolution. We measure the angles of incidence and reflection using a protractor with bubble level. The repeatability of the angular settings is very good, while the absolute angular accuracy is no better than $\pm 0.25^\circ$. Care has been taken to ensure that the transducer face is indeed perpendicular to the stainless steel search tube on which the protractor rests.

The transducers used in these experiments are either commercial wideband immersion-type transducers or specially designed Gaussian beam transducers. These latter are based on an earlier design¹⁷ and consist of circular quartz plate resonators 2.5 cm in diameter with the water-side electrode completely covering one face, while the other face has a strip electrode either 6.4 or 3.6 mm in width. This configuration produces a beam whose amplitude distribution in the transducer midplane, perpendicular to the strip electrode accurately describes a Gaussian profile, as we have verified in measurements at several frequencies. The Gaussian beam is essential since it corresponds to the incident beam profile assumed in the theoretical model of the previous section. For measurements to determine Rayleigh critical angles the wideband immersion transducers have proven more accurate.

Instrumentation for our measurements is fairly standard. All the data we present here have been collected by exciting the transducers with long (50–100- μ sec) tone bursts, which represent a quasi-cw excitation for which the theory is valid. The rf signal is obtained from a stable, spectrally pure source. It is gated with a diode switch to produce tone bursts that are amplified and applied to the transducer through an impedance matching network. The received signal is boosted by a wideband preamp, then further amplified by a tuned amp, and finally detected and filtered. The video signal is processed with a gated, integrating amplifier whose aperture may be set to a width somewhat exceeding that of the tone burst or much shorter than the tone burst. A consideration here is that the time delay between the transmitter and receiver signals is changing during the scan since the water path is a function of receiver position. The choice of aperture width depends on the type of transducer being employed. For all measurements an independent calibration of the entire receiver system is performed. This procedure corrects for any nonlinearities in the gain of the amplifiers or video detector. Data are acquired by fixing the position of the transmitting transducer with respect to the sample and scanning the receiving transducer across the reflected field, as indicated in Fig. 3. At each point in the discrete scan, the receiver comes to a complete halt, and the data point is read directly into the memory of an on-line computer. Then the receiver position is incremented automatically and the process repeated.

C. Data analysis

Comparing the measurements with the theoretical model of the previous section requires careful reduction of the data. First, we correct the measurements on the basis of the calibration mentioned earlier. Second, we need to determine the proper relationship between measured and calcu-

lated quantities. Since the transducer voltage is proportional to the particle displacement, let us express the rms acoustic power per unit area in terms of the displacement

$$P_a = \frac{1}{2} \rho_f c_f \omega^2 |d|^2,$$

where $|d|^2 = |u|^2 + |w|^2$. This relation demonstrates that the transducer signal is proportional to $P_a^{1/2}$. From Eqs. (1) and (2)

$$P_a = \frac{1}{2} \rho_f c_f (|\xi \phi_f'|^2 + |\zeta_f \phi_f'|^2 + |\zeta_f \phi_f''|^2) \\ = (\rho_f \omega^2 / 2 c_f) |\phi_f'|^2.$$

Therefore, $|\phi_f'| \sim P_a^{1/2}$, and we obtain the following proportionality between wave potentials in Eqs. (59) and (60) and the transducer signal

$$A_{tr}(x, z) \sim |\phi_{sp} + \phi_{1w}|. \quad (62)$$

No attempt is made to compare absolute amplitudes, so the data are simply normalized by matching the maximum amplitude of both curves. Third, uncertainty in the transducer-specimen separation makes absolute position determinations difficult, so we further operate on the data by shifting the entire curve by a constant so that, once again, the experimental and theoretical maxima have the same x coordinate. Since Δ_x is reflected in the detailed shape of the amplitude distribution curve, we lose no generality by this procedure.

IV. RESULTS AND DISCUSSION

Measurements of the Rayleigh wavespeed in three different samples as a function of $Q (= 2h\omega/c_{25})$ are shown along with the theoretical prediction in Fig. 4. The quantity c_r is inferred by determining the Rayleigh angle with the following procedure. We adjust transmitter and receiver in Fig. 3 to the same angle, then vary the receiver position and frequency until an absolute minimum in the null region is achieved. Changing angles, the procedure is repeated. From Eq. (56) the beam displacement parameter Δ_x decreases with increasing frequency until the null region becomes indistinct. Measurements at higher Q values may then be accomplished with a thicker layer. The three samples in Fig. 4 have

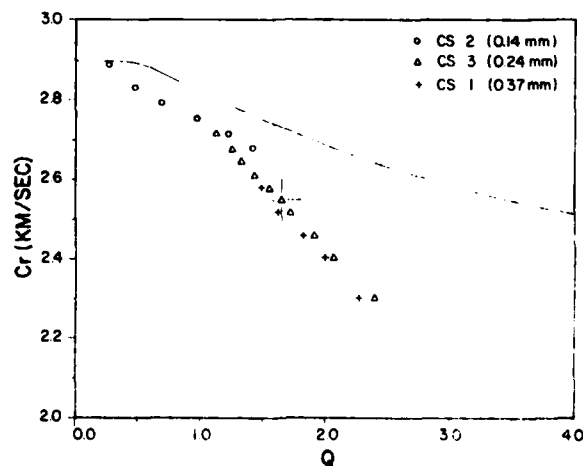


FIG. 4. Surface wave phase velocity plotted vs frequency-thickness product. Solid line is approximate theory, while experimental data points for three samples correspond to symbols indicated on graph. Typical error bars shown for a representative point.

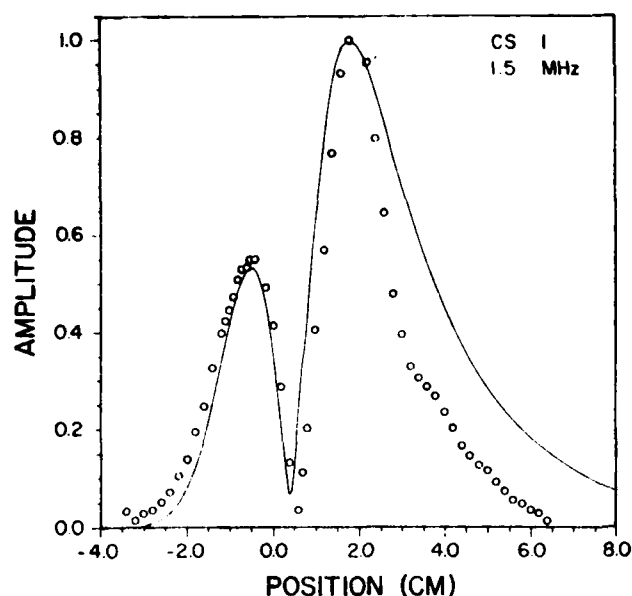


FIG. 5. Reflected acoustic field amplitude plotted vs receiver position for sample CS1 at 1.5 MHz. Points are experimental data and solid curve is theory from Eq. (62).

progressively increasing layer thicknesses, spanning the region from $Q = 0$ to 3. A representative error bar indicates the uncertainty in the data points. Good overlap between the data sets lends confidence to the measurements, but the theoretical curve begins to deviate seriously from the data at about $Q = 1.5$. By $Q = 3$ this disparity has grown to 45% of the range of $c_r(Q)$. The size of this deviation has led us to try to fit other theoretical results in the literature. From this attempt we find that agreement between the approximate model presented here and more complicated exact results is strongly dependent on the specific material parameters of the substrate and layer. In particular as the ratio of substrate-to-layer wavespeeds increases, so does the observed agreement. As mentioned earlier, however, the nature of the assumption suggests that some deviation beyond $Q = 1(2h/\lambda \approx 0.2)$ is not unexpected.

The amplitude distribution curve for sample CS1 at a frequency of 1.5 MHz is shown as a function of receiver position in Fig. 5. These data are recorded by incrementing the x coordinate of the receiver transducer with the transmitter in a fixed position as described earlier. The individual points are the experimental data, while the solid curve is the theoretical result from Eqs. (59)–(62). In view of the disagreement between the theoretical value of $c_r(Q)$ and that inferred from Rayleigh angle measurements, we have inserted the experimentally derived c_r into the expression for Δ_r from Eq. (56) used to derive the theory curve of Fig. 5. Because of

signal averaging and system calibration, experimental uncertainty in the signal level is no larger than the plotting symbols in this and subsequent curves.

The features of the reflected field indicated schematically in Fig. 3 are apparent in a quantitative sense in Fig. 5. First, near $x = -1.0$ cm, a precursor peak appears, due to the coherent sum of ϕ_{rp} and ϕ_{tw} from Eqs. (59) and (60). At higher values of receiver position near $x = 1.5$ cm, a larger displaced reflection is observed, which arises mostly from the leaky-wave term. Between the two peaks is the null region where phase cancellation reduces the signal amplitude to near zero. Similar observations have been made in previous work.^{8,9} From $x = -3.0$ to 3.0 cm agreement between the data of Fig. 5 and the theoretical prediction is relatively good. The precursor peak height and location of the null are fairly well predicted. Beyond $x = 3.5$ cm the experimental trailing field decreases more rapidly than predicted. This occurrence, noticed in several cases, is probably due to the finite y dimension of the Gaussian beam, which is only 20 mm long. When compared to an acoustic path length of 160 mm, the assumption of y -independent incident beam profile appears difficult to fulfill. We have determined the incident acoustic beam half-width from measurements at several frequencies with two transducers at varying separations. The wide transducer (6.4 mm) is used for generation, whereas the narrower one (3.6 mm) is the receiver. Inserting this estimate for $a/2$ into Eq. (50), we examine the theoretical fit, adjusting $a/2$ by no more than 10% to achieve the best effective width in light of the finite y extent of the transducer. Additional parameters used in the theory are summarized for this and subsequent curves in Table I.

Figure 6 displays the amplitude distribution for sample CS2 for $Q = 0.82$. Here the solid-theory curve fits the data points somewhat better than the previous example, although there is still a tendency for the measured field to decrease slightly more rapidly than the model calculation. In addition, we have plotted for comparison the reflected field of the same beam at the same angle of incidence and frequency for a stainless steel sample with no layer present. Although the layer is rather thin ($2h/\lambda \approx 0.15$), the effect on the reflected field is quite pronounced. The dashed curve, consisting of connected data points, indicates this field in Fig. 6. A small residual beam displacement remains since we are less than 2° from the appropriate Rayleigh angle for the stainless steel surface (30.8°). Far from all critical angles, the only contribution to the expression in Eq. (62) is ϕ_{rp} , and the undistorted beam would be centered on $x = 0$.

The reflected field of sample CS2 at $Q = 0.41$ is given in Fig. 7. This frequency is half of the previous value, and the amplitude distribution is only slightly perturbed from the

TABLE I. Experimental parameters.

Figure	Sample	$2h$ (mm)	Freq. (MHz)	Q	θ_r (deg)	z (mm)	$a/2$ (mm)
5	CS 1	0.37	1.5	1.1	33.6	94.0	10.0
6	CS 2	0.14	3.0	0.82	32.5	70.0	5.0
6	S 1	0.0	3.0	0.0	32.5	70.0	5.0
7	CS 2	0.14	1.5	0.41	31.5	70.0	8.0
8	CS 2	0.14	4.5	1.23	33.2	70.0	9.0

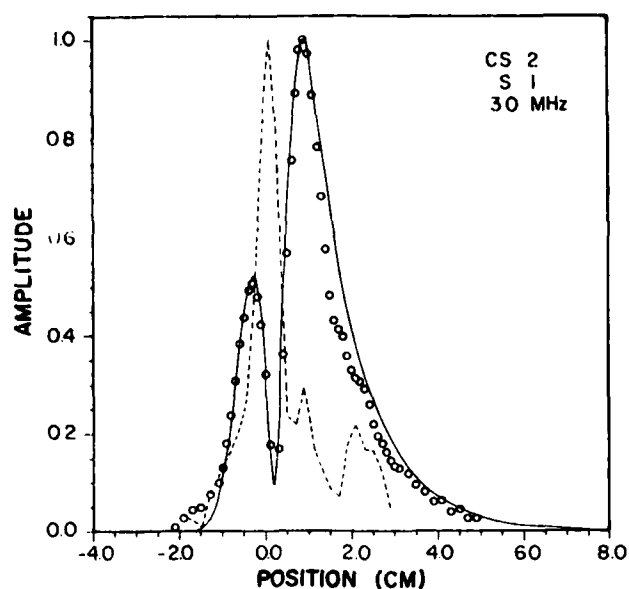


FIG. 6. Reflected acoustic field vs receiver position for sample CS2 at 3 MHz. Experimental data are plotted discretely, solid curve is theory, and broken curve is experimental data for no-layer case.

case for no layer where θ_i equals the Rayleigh angle of the steel substrate. Some disparity in both the precursor and trailing field beam widths are evident again here. While the null coordinate and precursor height are correctly predicted, the position of the precursor maximum is slightly displaced. Results at higher frequency with $Q = 1.23$ for the same sample are shown in Fig. 8. At an incident angle of 33.2° the precursor peak decreases significantly in amplitude. The maximum of the leaky-wave peak has moved nearer to the origin, and at very high frequency or when $a/\lambda \gg 1$, the phenomenon approaches a simple displacement of the nearly

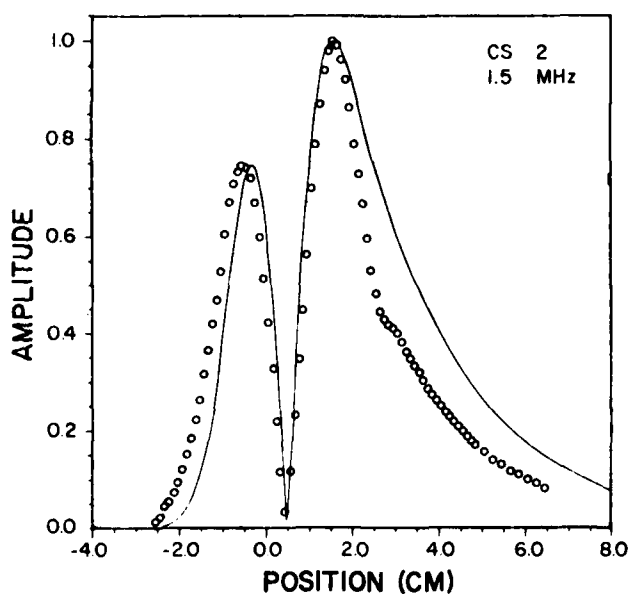


FIG. 7. Reflected field amplitude vs receiver position. Data are plotted discretely and solid curve is theory.

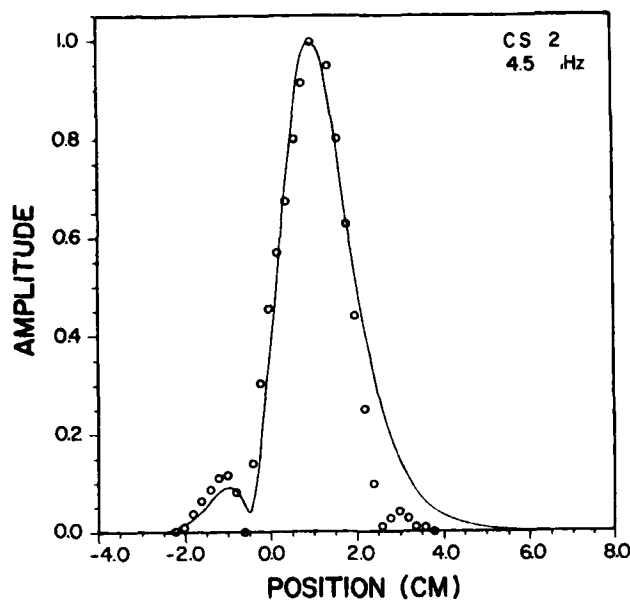


FIG. 8. Reflected field amplitude vs receiver position. Data are plotted discretely and solid curve is theory.

Gaussian reflected beam, as predicted by Schoch² and later theoretically confirmed⁸ for wide beams. Eventually, Δ_s goes to zero for very large a/λ , and specular reflection results.

Although the comparison between the experimental data and the theory developed in Sec. II of this paper is reasonably satisfactory, some discrepancies do exist. These have been cited in the presentation of the data as they have appeared. Reviewing Figs. 5–8, we see that the most common difficulty occurs in the width of the reflected beam, particularly the leaky-wave and trailing-field portions. Since the experimentally realizable transducer is not a very good approximation to the two-dimensional beam assumed in the theory, some disagreement may be expected. We have further determined in the course of these measurements that transducer alignment is critical. The maximum sensitivity direction of both transducers must lie accurately in a plane perpendicular to the fluid-solid interface. This procedure ensures that y -axis sidelobes do not interfere with the signal and that the receiver senses uniform, simultaneously arriving wavefronts.

As a first-order theory for acoustic reflection at fluid-solid interfaces loaded by a thin layer, the model we present here is quite adequate, particularly in the region $Q < 1$. However, several shortcomings should be pointed out. The calculation of c_s as a function of Q is prohibitively complicated. Expanding Eq. (32) and collecting coefficients of powers of the Rayleigh wavespeed reveals a characteristic equation which is 40th order in c_s . Instead of proceeding in this manner, we have solved Eq. (32) implicitly for c_s by noting that the equation is only second order in Q . The difficulty with this method is that we know an exact complex solution for Eq. (32) at only one value of Q , namely $Q = 0$. Developing a functional dependence of $Q(c_s)$ for $Q > 0$ requires assumptions concerning the behavior of c_s in the complex plane. Fortunately, we are aided at this point by the fact that

$\text{Im}(c_s)/\text{Re}(c_s) \ll 1$, implying that these assumptions do not seriously affect the results. A more general approach, however, would be needed to eliminate this problem and produce a result in better agreement with the data. Additional limitations are the assumption of the Gaussian beam profile and the intrinsic two-dimensionality of the analysis. The first of these could be circumvented by evaluating the reflected field numerically,¹⁰ but expanding the analysis to three dimensions would be a very significant complication.

In conclusion, we have developed an approximate model for acoustic reflection at the Rayleigh angle from a fluid-solid interface in the presence of a thin solid layer based, in part, on previous calculations.^{2,8,13} We have shown in detail how key parameters in the model are derived and how the presence of the layer modifies the calculation. At each stage, we examine the limiting behavior as the layer thickness vanishes, and we show the results for the no-layer case are recovered. In addition, we present experimental results on reflected field amplitudes of three samples of differing layer thicknesses and at values of the dimensionless frequency Q from 0.41 to 1.23. Comparison between the experimental data and our model indicates reasonably good agreement over this range of Q .

ACKNOWLEDGMENTS

The authors are pleased to acknowledge helpful discussions with Dr. T. J. Moran. Capable technical assistance was

given by D. L. Butler, R. D. Griswold, and K. D. Shimmin. The technical support of S. Pittman during sample preparation is also greatly appreciated.

¹F. Goos and H. Hänchen, *Ann. Phys.* **1**, 333 (1947).

²A. Schoch, *Acustica* **2**, 18 (1952).

³A. Schoch, *Ergeb. Exakten Naturwiss.* **23**, 127 (1953).

⁴W. G. Neubauer, *J. Appl. Phys.* **44**, 48 (1973).

⁵W. G. Neubauer and L. R. Dragonette, *J. Appl. Phys.* **45**, 618 (1974).

⁶O. I. Diachok and W. G. Mayer, *J. Acoust. Soc. Am.* **47**, 155 (1970).

⁷W. G. Neubauer, *Physical Acoustics*, edited by W. P. Mason and R. N. Thurston (Academic, New York, 1973), Vol. X, pp. 104-125.

⁸H. L. Bertoni and T. Tamir, *Appl. Phys.* **2**, 157 (1973).

⁹M. A. Breazeale, L. Adler, and G. W. Scott, *J. Appl. Phys.* **48**, 530 (1977).

¹⁰L. E. Pitts, T. J. Plona, and W. G. Mayer, *IEEE Trans. Sonics Ultrason.* **SU-24**, 101 (1977); T. D. K. Ngoc and W. G. Mayer, *IEEE Trans. Sonics Ultrason.* **SU-27**, 229 (1980).

¹¹I. A. Viktorov, *Rayleigh and Lamb Waves* (Plenum, New York, 1967).

¹²L. M. Brekhovskikh, *Waves in Layered Media* (Academic, New York, 1960), pp. 100-122.

¹³T. Tamir and H. L. Bertoni, *J. Opt. Soc. Am.* **61**, 1397 (1971).

¹⁴*Metals Handbook*, Vol. II, edited by H. E. Boyer (American Society for Metals, Metals Park, Ohio, 1976).

¹⁵G. W. C. Kaye and T. H. Laby, *Tables of Physical and Chemical Constants* (Longman, London, 1973).

¹⁶Mini-manipulator available from Automation Industries, Inc.

¹⁷F. D. Martin and M. A. Breazeale, *J. Am. Acoust. Soc.* **49**, 1668 (1971).

LEAKY RAYLEIGH WAVES AT A LAYERED HALFSPACE-FLUID INTERFACE

D. E. Chimenti

AFWAL Materials Laboratory
Wright-Patterson AFB, Ohio 45433

A. H. Nayfeh*

Systems Research Laboratories, Inc.
Dayton, Ohio 45440

ABSTRACT

Experimental and theoretical results on the nonspecular reflection of finite acoustic beams incident at and near the Rayleigh angle onto a fluid-solid interface in contact with an elastic layer are presented. Measurements with Gaussian-shaped acoustic beams have been performed on the reflected field amplitude distribution and surface wavespeed dispersion for loading and stiffening layers where the fluid medium is water. It is shown that existing theory can be utilized to explain the results by constructing and solving boundary condition equations for the Rayleigh wave pole appropriate for the lossless layered half-space with the fluid. Good agreement with the exact treatment is observed in most aspects of the measurements. In the model calculation the imaginary part of the Rayleigh wave pole is found to display an unexpected maximum at a value of layer thickness over wavelength where the real part corresponds nearly to the transverse wavespeed in the layer.

INTRODUCTION

Nonspecular reflection of finite-aperture acoustic beams at a liquid-solid interface occurs when incidence at or near the Rayleigh critical angle $\theta_r (= \sin^{-1} c_f/c_r)$ favors the generation of surface waves at the interface. Rapid reradiation of the surface-wave energy into the liquid results in a lateral shift of part of the reflected beam and leads to a redistribution of acoustic amplitude in the reflected field. The distortion of the reflected beam is generally manifested as a bimodal amplitude distribution consisting of a the superposition of the specular component and the leaky wave with its trailing field. If conditions permit, a zone near the center of the distribution develops where the amplitude is suddenly very small, due to phase cancellation of the component fields. The situation is illustrated in Fig. 1. The dashed lines indicate the

specular reflection, while the components of the leaky-wave field are represented as shaded regions. A weak trailing field caused by the decaying surface wave persists beyond the leaky-wave maximum for several attenuation lengths.

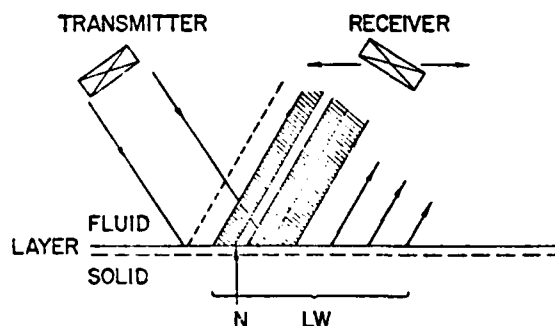


Figure 1 - Leaky-Wave Schematic. Shaded Regions Contain Most of the Power. The Null Zone is N, and LW is the Leaky Wave.

This problem has been investigated fairly extensively, both experimentally¹⁻⁷ and theoretically⁶⁻⁸, for reflection at the interface of a liquid and homogeneous solid. The additional complication we consider here consists of a solid, elastic layer of differing material in welded contact to the solid. It has been shown⁹ that in the presence of a layer the Rayleigh wave velocity is dispersive, varying as the ratio of acoustic wavelength to layer thickness. While the additional effect of the liquid only slightly perturbs the Rayleigh velocity on the composite solid, the damping portion of the wavevector is strongly dependent on the presence of the liquid and is also dispersive. We demonstrate that the approximate

analysis carried out previously⁸ for the homogeneous solid can be extended to include the case of the layered solid by solving the expanded characteristic equation for the kd -dependent Rayleigh wave pole. Experimental measurements are presented in conjunction with the calculations.

Theoretical Summary

The plan here is to express the acoustic waves in the three media, solid, layer and liquid, by their wave potentials combined with the appropriate phase factors. Requiring the wave potentials to satisfy plane-strain boundary conditions leads to a system of linear equations for the wave potentials in terms of the frequency, layer thickness, and material properties of the three media. The formal solutions are of the form:

$$\phi_s = \phi_{s1} \exp(i\zeta_{ls} z + i\eta) \quad (1a)$$

$$\psi_s = \psi_{s1} \exp(i\zeta_{ts} z + i\eta) \quad (1b),$$

where ϕ and ψ are amplitudes of the longitudinal and transverse waves, respectively. Subscripts 1 and 2 refer to incident and reflected waves.

The wavevector components are given by

$$\zeta_{\alpha\beta} = (k_{\alpha\beta}^2 - \xi^2)^{1/2} \quad (2a)$$

$$k_{\alpha\beta} = (\omega/c_{\alpha\beta}), \quad (2b)$$

where $\alpha = l, t$ for longitudinal and transverse components and $\beta = f, o, s$ for fluid, layer, and solid, respectively. The circular frequency is ω , $c_{\alpha\beta}$ is the appropriate acoustic bulk velocity, and $\eta = \xi x - \omega t$. The invariant x component of the wavevector is $\xi = k_f \sin \theta$, where θ is the incident angle. Combining (1) with the usual boundary conditions imposed on the displacements and stresses yields a seventh order system of equations. The characteristic equation is solved by a Newton-Raphson method. To insure that it iterates to the desired root, the routine is seeded with an approximate solution of a simpler case, the one for which the density of the liquid vanishes. Once the root is found, the Rayleigh wavespeed and the beam displacement

parameter defined by Schoch¹ are obtained immediately.

$$c_r = \omega/\text{Re}(\xi_p) \quad (3a)$$

$$\Delta_s = 2/\text{Im}(\xi_p), \quad (3b)$$

where ξ_p is the Rayleigh wave pole. With this information the theoretical model of Bertoni and Tamir⁸ can be extended to include the case of layered substrate. The variation of ξ_p as a function of $Q(=k_{ts}d)$ in the complex plane is shown in Fig. 2. At intervals of 0.5 a plotting symbol appears, indicating the relative rate of change of ξ_p with Q . The elastic constants employed here are appropriate for a copper layer on stainless steel. For the loading layer the Rayleigh wavespeed of the composite structure decreases monotonically from $Q=0$ to $Q>1$, where the plotting symbols cluster as minimal further change occurs. A maximum in the attenuation occurs near $Q=2.2$, at which point $\text{Im}(\xi_p)$ is significantly larger than the values at either of the limiting points of Q . This non-monotonic aspect of the leaky Rayleigh wave attenuation is absent from our earlier approximate model.⁶ An interesting

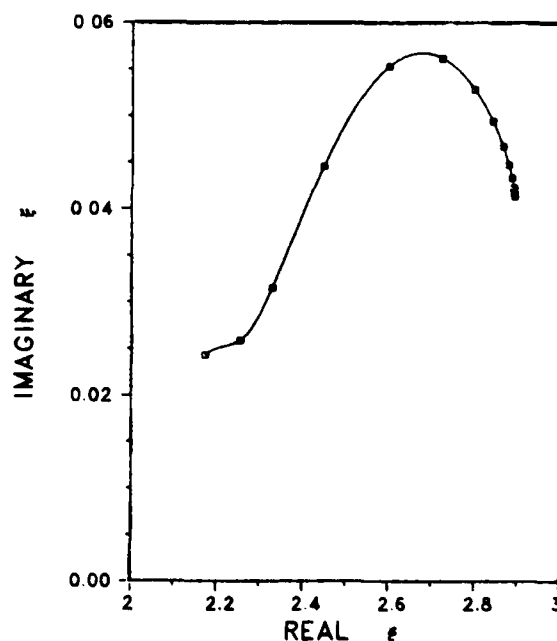


Figure 2 - Rayleigh Wave Pole Loci vs Q for Copper on Stainless Steel.

correlation exists between the occurrence of the maximum in $\text{Im}(\xi_p)$ and the transverse wavespeed of the substrate. At $\text{Im}(\xi_p)_{\text{max}}$ the real part of the wavevector assumes the value of $\text{Re}(\xi_p) = \omega/c_{ts}$. The limiting points of $\text{Im}(\xi_p)$ in both models, however, correspond to the values appropriate for the substrate and layer materials alone.

For a layer having stiffer elastic constants than the substrate, the situation changes. Only a single surface-wave mode is present, and its wavespeed is limited by the transverse wavespeed of the substrate, as described by others.^{9,10} Figure 3 gives the variation of ξ_p as Q changes from zero at the upper right to 1.8 at the lower left. The range of c_r is restricted to less than 10% of c_{ts} , while $\text{Im}(\xi_p)$ decreases toward zero as the cutoff value of Q is approached. The implication from Eq. (3b) is that the beam displacement parameter Δ_s increases rapidly near the cutoff, and this behavior strongly influences the reflected field amplitude.

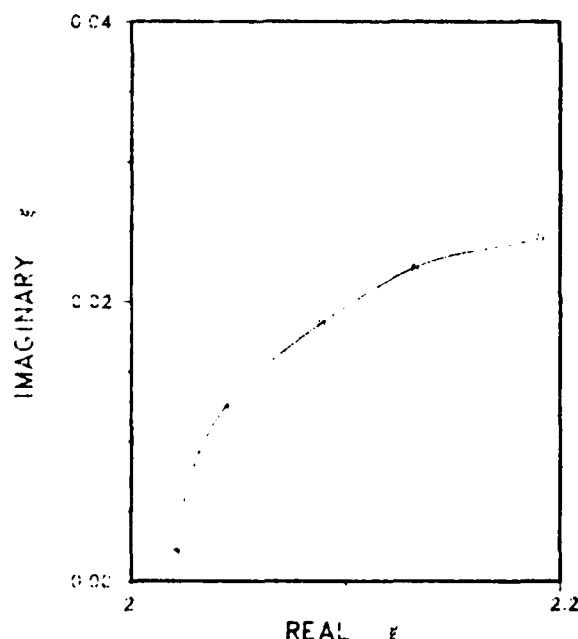


Figure 3 - Rayleigh Wave Pole Loci vs Q for Chromium on Stainless Steel.

Results and Discussion

Since the analytical model⁸ we have employed in part of our calculations assumes a Gaussian distribution for the incident beam profile, we use specially designed transducer elements which approximate the two dimensional profile of the calculation. Samples used in this study are stainless steel plated with either copper or chromium. The elastic constants used in this model are: $c_{ls} = 5.69 \text{ km/s}$, $c_{ts} = 3.1$, $\rho_s = 7.9$, $c_{lo} = 4.76$, $c_{to} = 2.3$, $\rho_o = 8.9$ (copper), $c_{lo} = 6.6$, $c_{to} = 4.0$, $\rho_o = 7.2$ (chromium). Further details concerning the experimental arrangement are given elsewhere.⁶

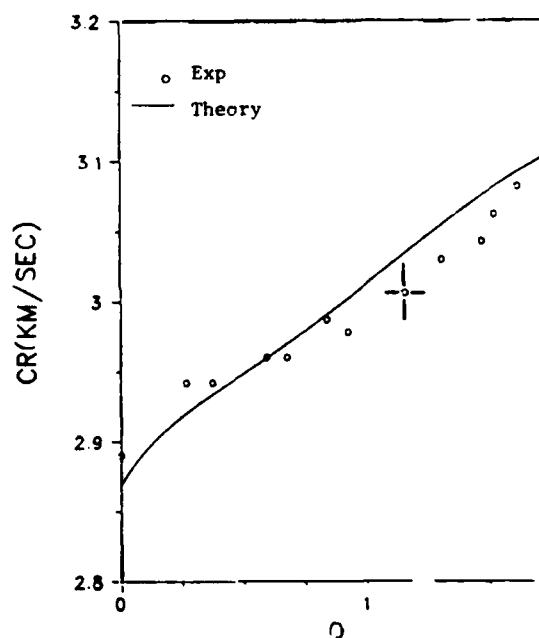


Figure 4 - Rayleigh Wavespeed vs Q for Chromium on Stainless Steel.

The dispersion of the phase velocity for a chromium layer on stainless steel is given in Fig. 4. Several samples of differing layer thickness allow the entire range of Q to be covered. The trend of the data is fairly well represented by the theoretical curve. At the predicted cutoff, however, the observed behavior deviates from the model. Instead of extinguishing sharply at the value of Q corresponding to $c_r = 2.1 \text{ km/s}$, a leaky wave persists up to about 130% of this cutoff Q , probably due to the finite angular spread of the measuring beam.

The theoretical curve of Fig. 4 is, of course, derived from the plane-wave reflection coefficient. Figure 5 gives an example of the reflected field amplitude distribution for a chromium layer on stainless steel. The frequency is 5.5 MHz and the angle of incidence is 29° . With a layer thickness of 0.135 mm, the corresponding value of Q is 1.51. For $x > 2$ cm, the predicted leaky wave appears much stronger than the measured amplitude. Closer to the cutoff angle, the beam displacement parameter increases quickly, as inferred from Fig. 3, and the leaky-wave peak stretches out and decreases in amplitude, eventually leaving all the power in the specular component.

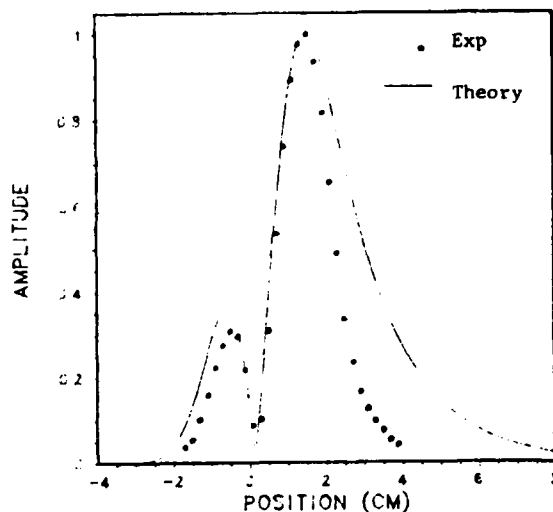


Figure 5 - Reflected Amplitude Distribution for Chromium Layer.

Better agreement between experimental results and the model is observed in the data of Fig. 6. These data correspond to a frequency of 3 MHz and an incident angle of 32.5° for a copper layer on stainless steel. Here, the tail of the predicted leaky wave follows the data quite well.

Acknowledgements

The authors wish to express their thanks to R. H. Latiff and K. D. Shimmin for assistance in these measurements.

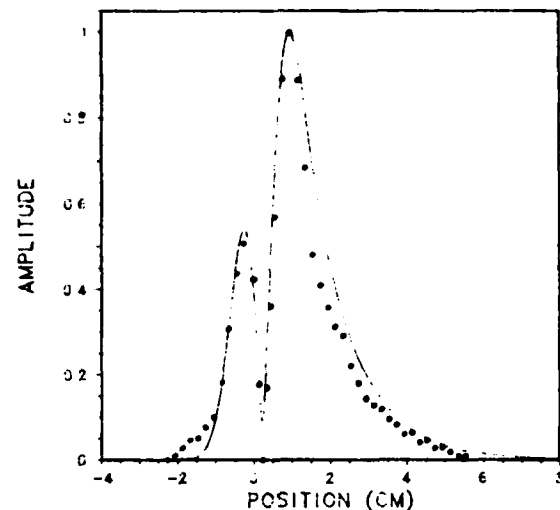


Figure 6 - Reflected Amplitude Distribution for Copper Layer.

References

1. A. Schoch, *Ergeb. Exakten Naturwiss.* **23**, 127(1953).
2. O. I. Diachock and W. G. Mayer, *J. Acoust. Soc. Am.* **47**, 155(1970).
3. M. A. Breazeale, L. Adler, and G. W. Scott, *J. Appl. Phys.* **48**, 530(1977).
4. T. D. K. Ngoc and W. G. Mayer, *J. Appl. Phys.* **50**, 7948(1979); *J. Acoust. Soc. Am.* **67**, 1149 (1980).
5. M. Luukkala and M. Hattunen, *Appl. Phys.* **2**, 257(1973).
6. A. H. Nayfeh, D. E. Chimenti, L. Adler, and R. L. Crane, *J. Appl. Phys.* **52**, 4985(1981).
7. D. E. Chimenti, A. H. Nayfeh, and D. L. Butler, *J. Appl. Phys.*, to be published.
8. H. L. Bertoni and T. Tamir, *Appl. Phys.* **2**, 157 (1973).
9. G. W. Farnell and E. L. Adler, in *Physical Acoustics IX*, ed. W. P. Mason and R. N. Thurston (Academic Press, New York, 1972) pp. 35-126.
10. B. A. Auld, *Acoustic Fields and Waves in Solids* (Wiley-Interscience, New York, 1973) Chap. 10.
11. F. D. Martin and M. A. Breazeale, *J. Am. Acoust. Soc.* **49**, 1668(1971).

*Consultant. Permanent address: Department of Aerospace Engineering and Applied Mechanics, University of Cincinnati, Ohio 45221.

Leaky Rayleigh waves on a layered halfspace

D. E. Chimenti

AFWAL Materials Laboratory, Wright-Patterson Air Force Base, Ohio 45433

A. H. Nayfeh^{a)}

Systems Research Laboratories, Dayton, Ohio 45440

D. L. Butler^{b)}

AFWAL Materials Laboratory, Wright-Patterson Air Force Base, Ohio 45433

(Received 15 June 1981; accepted for publication 19 August 1981)

Experimental and theoretical results on the nonspecular reflection of finite acoustic beams incident at and near the Rayleigh angle onto a fluid-solid interface loaded by an elastic layer are presented. Measurements with Gaussian-shaped acoustic beams have been performed on the reflected field amplitude distribution and surface wave speed dispersion in copper-loaded stainless-steel specimens where the fluid medium is water. It is shown that existing theory can be utilized to explain the results by constructing and solving boundary condition equations for the Rayleigh wave pole appropriate for the lossless layered halfspace with the fluid. Excellent agreement with the exact treatment is observed in most aspects of the measurements. In the model calculation the imaginary part of the Rayleigh wave pole is found to display an unexpected maximum at a value of layer thickness over wavelength where the real part corresponds nearly to the transverse wave speed in the layer.

PACS numbers: 43.20.Fn, 43.30.Dr, 62.30.+d

I. INTRODUCTION

Investigation of reflection phenomena of bounded acoustic beams incident upon a fluid-solid interface at or near the Rayleigh angle has received considerable attention.¹⁻¹⁵ Experimental demonstrations have indicated the possible utility of these Rayleigh-angle phenomena in the detection of surface¹⁶ or subsurface¹⁷ defects. Since practical inspection situations might also include the presence of an elastic layer of dissimilar material bonded to the solid, analysis of this problem is of some interest. The phenomenon consists of resonant energy transfer between the longitudinal wave in the liquid and a Rayleigh-type wave on the solid-liquid interface. At the Rayleigh angle θ_r , wave fronts of the incident longitudinal wave propagate along the interface at the surface wave speed strongly exciting a surface wave. This surface excitation differs from a classical Rayleigh wave in that it is effectively damped at about 0.5 dB/wavelength by the presence of the liquid through an inverse process to the one described above, the energy reappearing in the liquid. Since the energy "leaks" into the fluid, the excitation has been termed a "leaky" wave. The result, depending on the exact values of the beam diameter and wavelength, is an apparent shift and distortion of the reflected field of a finite-aperture acoustic beam. The addition of an elastic layer changes the propagation characteristics of the Rayleigh wave. We have recently undertaken a model calculation¹⁸ of the reflected field of a bounded beam for the special case of a thin layer. In that paper it is shown that for ratios of the layer thickness to the Rayleigh wavelength larger than 0.3, significant disparity between the approximate theory and experimental measurements is observed.

The current paper presents an exact model calculation, supported by experimental measurements, of bounded-beam reflection from a fluid-solid interface loaded by an elastic layer of any thickness. We combine elements of both an approximate model⁵ and an exact calculation to yield an accurate result for the reflected field of a finite-aperture beam. Our result is valid for any value of the layer-thickness-to-wavelength ratio, subject to the provision that the acoustic absorption in the elastic materials is small. The approach consists of setting up the usual simultaneous equations derived from the continuity conditions for the reflected field, then locating the leaky Rayleigh wave singularity in the plane of the complex wave vector by numerical methods. Once the pole coordinates are known to sufficient accuracy, the analysis proceeds along the lines of previous approximate calculations,⁵ yielding the amplitude distribution of the reflected acoustic field. We have verified the accuracy of these results by direct numerical evaluation⁸⁻¹⁰ of the Fourier integral corresponding to the reflected field. Since a finite-aperture beam can be represented by a superposition of plane waves, the spectral components of the reflected field are given by the product of the k -dependent reflection coefficient and the Fourier-transformed incident beam. The real-space reflected amplitude distribution is then the inverse transform of that product. This representation of the reflected acoustic field forms the basis of most of the calculations, exact or approximate, which have been performed on this problem and constitutes the Fourier integral mentioned above. Although numerical evaluation of this integral is attractive because it permits the consideration of a variety of beam profiles, we have not used it extensively. Its disadvantages are its numerical complication and the tendency of computer algorithms to conceal the role of the various parameters in determining the reflection properties.

In measurements of the Rayleigh wave speed we find

^{a)}Consultant. Permanent address: Dept. of Aerospace Engineering and Applied Mechanics, University of Cincinnati, Cincinnati, Ohio 45221.

^{b)}Present address: EDS Nuclear, Inc., Norcross, Georgia.

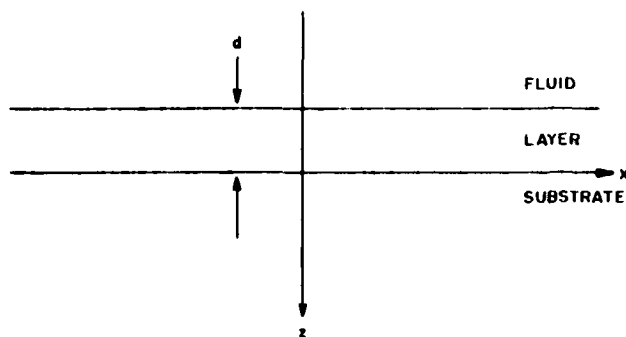


FIG. 1. Coordinate geometry.

excellent agreement, within experimental uncertainty, with theoretical results for this quantity deduced from the behavior of the reflection coefficient in the complex plane. Our measurements extend over a range of frequency from 1.5–6.0 MHz and layer thickness of 0.14–0.37 mm. Good agreement is also observed in comparisons of measured and calculated acoustic amplitude distributions in the reflected field, both near and at the Rayleigh angle. Section II covers the derivation of essential theoretical expressions, a summary of the experimental technique is given in Sec. III, and we present our results and analysis in Sec. IV.

II. THEORY

Let us postulate an elastic layer of thickness d overlaying and in welded contact with an elastic halfspace of differing material. Also in contact with the elastic layer is a semi-infinite fluid medium, as shown in Fig. 1. The coordinate system is chosen with the layer-substrate interface in the x - y plane. Therefore, the substrate extends from $0 < z < \infty$, the layer from $-d < z < 0$, and the fluid from $-\infty < z < -d$. We establish the convention that the field variables and properties of the fluid, layer, and substrate will be identified with the subscripts f , o , and s , respectively. The analysis is limited to two dimensions by assuming that all particle motion is confined to the x - z plane.

For each of the media, the potential functions Φ and Ψ are introduced, corresponding to longitudinal and transverse wave motion, respectively. Formal solutions of the field equations are combined with the proper interfacial continuity conditions to yield boundary condition equations which are solved for the amplitudes of the wave potentials. The potential functions Φ and Ψ are related to the particle displacements and stresses by

$$u = (\partial\Phi/\partial x) - (\partial\Psi/\partial z), \quad (1)$$

$$w = (\partial\Phi/\partial z) + (\partial\Psi/\partial x) \quad (2)$$

$$\sigma_{xx} = (\lambda + 2\mu) \frac{\partial^2\Phi}{\partial z^2} + \lambda \frac{\partial^2\Phi}{\partial x^2} + 2\mu \frac{\partial^2\Psi}{\partial x\partial z} \quad (3)$$

$$\sigma_{xz} = \mu \left(2 \frac{\partial^2\Phi}{\partial x\partial z} + \frac{\partial^2\Psi}{\partial x^2} - \frac{\partial^2\Psi}{\partial z^2} \right). \quad (4)$$

Here u and w are the x and z components of the particle displacement, and λ and μ are the Lamé constants which are related to the longitudinal and transverse wave speeds through

$$c_l^2 = (\lambda + 2\mu)/\rho, \quad c_t^2 = \mu/\rho, \quad (5)$$

where ρ is the mass density. Following our notation, solutions of the field equations must satisfy the interfacial continuity conditions

$$u_s = u_o, \quad w_s = w_o, \quad \sigma_{zxs} = \sigma_{zxo}, \quad \sigma_{xzs} = \sigma_{xzo}, \quad \text{at } z = 0, \quad (6)$$

$$w_o = w_f, \quad \sigma_{zso} = \sigma_{zsf}, \quad \sigma_{xso} = 0 \quad \text{at } z = -d. \quad (7)$$

The reflection coefficient for an acoustic wave incident from the fluid onto the layer is determined by solving the boundary condition equations which result from substitution of the formal wave-potential solutions into Eqs. (6) and (7). These formal solutions for the incident and reflected wave potentials in all three media are

$$\Phi_i = \phi_{i1} \exp(i\zeta_{i1}z + i\eta) \quad (8a)$$

$$\Psi_i = \psi_{i1} \exp(i\zeta_{i1}z + i\eta) \quad (8b)$$

$$\Phi_o = \phi_{o1} \exp(i\zeta_{o1}z + i\eta) + \phi_{o2} \exp(-i\zeta_{o1}z + i\eta), \quad (9a)$$

$$\Psi_o = \psi_{o1} \exp(i\zeta_{o1}z + i\eta) + \psi_{o2} \exp(-i\zeta_{o1}z + i\eta) \quad (9b)$$

$$\Phi_f = \phi_{f1} \exp[i\zeta_{f1}(z+d) + i\eta] + \phi_{f2} \exp[-i\zeta_{f1}(z+d) + i\eta], \quad (10)$$

where ϕ and ψ are unknown amplitudes, and the subscripts 1 and 2 refer to incident and reflected waves, respectively. The wave vector components are given by

$$\zeta_{\alpha\beta} = (k_{\alpha\beta}^2 - \xi^2)^{1/2}, \quad (11)$$

$$k_{\alpha\beta} = \omega/c_{\alpha\beta},$$

where $\alpha = l, t$ and $\beta = f, o, s$; ω is the circular frequency, and $\eta = \xi x - \omega t$. The invariant x component of the wavevector is just

$$\xi = k_f \sin \theta,$$

where θ is the angle of incidence. For the fluid there can be no ambiguity concerning mode, so the wave properties are denoted by a single subscript. Substituting from Eqs. (8)–(10) into Eqs. (1)–(4) and applying the interfacial continuity conditions [Eqs. (6) and (7)] we obtain, after some algebraic reductions, the following system of linear equations [see Eq. (13)] where

$$\bar{\zeta}_{\alpha\beta} = \zeta_{\alpha\beta}/\xi,$$

$$\bar{\omega} = \omega d/c_s = Q c_{s1}/c_s; \text{ i.e., } Q = \omega d/c_{s1}, \quad (12)$$

$$\bar{\mu}_o = \mu_o/\mu_s.$$

$$\begin{pmatrix}
 1 & 0 & -\bar{\xi}_{10} & 0 & -1 & \bar{\xi}_{1s} & 0 \\
 0 & \bar{\xi}_{10} & 0 & 1 & -\bar{\xi}_{1s} & -1 & 0 \\
 \bar{\mu}_o(\bar{\xi}_{10}^2 - 1) & 0 & 2\bar{\mu}_o\bar{\xi}_{10} & 0 & 1 - \bar{\xi}_{1s}^2 & -2\bar{\xi}_{1s} & 0 \\
 0 & -2\bar{\mu}_o\bar{\xi}_{10} & 0 & \bar{\mu}_o(\bar{\xi}_{10}^2 - 1) & 2\bar{\xi}_{1s} & 1 - \bar{\xi}_{1s}^2 & 0 \\
 \bar{\xi}_{10} \sin \bar{\omega}\bar{\xi}_{10} & -i\bar{\xi}_{10} \cos \bar{\omega}\bar{\xi}_{10} & (1 - \bar{\xi}_{10}^2)/2 & i(\bar{\xi}_{10}^2 - 1)/2 & 0 & 0 & 0 \\
 & & \times \sin \bar{\omega}\bar{\xi}_{10} & \times \cos \bar{\omega}\bar{\xi}_{10} & & & \\
 -i(\bar{\xi}_{10}^2 - 1) & (\bar{\xi}_{10}^2 - 1) & -2i\bar{\xi}_{10} \cos \bar{\omega}\bar{\xi}_{10} & 2\bar{\xi}_{10} \sin \bar{\omega}\bar{\xi}_{10} & 0 & 0 & \frac{i\rho_f c_f^2}{\rho_o c_{10}^2} \\
 \times \cos \bar{\omega}\bar{\xi}_{10} & \times \sin \bar{\omega}\bar{\xi}_{10} & & & & & \\
 -\bar{\xi}_{10} \sin \bar{\omega}\bar{\xi}_{10} & i\bar{\xi}_{10} \cos \bar{\omega}\bar{\xi}_{10} & -\sin \bar{\omega}\bar{\xi}_{10} & i \cos \bar{\omega}\bar{\xi}_{10} & 0 & 0 & i\bar{\xi}_f
 \end{pmatrix}$$

$$\times \begin{pmatrix} \phi_{o1} + \phi_{o2} \\ \phi_{o1} - \phi_{o2} \\ \psi_{o1} - \psi_{o2} \\ \psi_{o1} + \psi_{o2} \end{pmatrix} = \begin{pmatrix} 0 \\ 0 \\ 0 \\ 0 \end{pmatrix}$$

$$\begin{pmatrix} \phi_{s1} \\ \psi_{s1} \\ \phi_{f2} \end{pmatrix} = \begin{pmatrix} 0 \\ -i\rho_f c_f^2 / \rho_o c_{10}^2 \phi_{f1} \\ i\bar{\xi}_f \phi_{f1} \end{pmatrix} \quad (13)$$

Here, c_r is the dispersive Rayleigh wave speed, and μ_s is the shear modulus of the substrate. The reflection coefficient is defined as the ratio of the reflected wave amplitude in the fluid to the incident amplitude,

$$R = \phi_{f2} / \phi_{f1} \quad (14)$$

As an initial condition we set $\phi_{f1} = 1$ and solve for ϕ_{f2} in Eq. (13) by Cramer's Rule. If the layer thickness vanishes, we recover the reflection coefficient of a simple fluid-solid interface.¹⁹ Similar calculations of the dispersive Rayleigh wave speed in the absence of the fluid are given by Achenbach and Keshava²⁰ and Farnell and Adler.²¹ The case of a fluid-solid interface with no layer is treated in detail by Mott,²² and Auld²³ gives a perturbation solution for this case.

The Rayleigh wave speed c_r and the beam displacement parameter Δ_s can now be determined by examining the behavior of $R(\xi)$ in the complex plane. Expressing the determinants in the solution of Eq. (13) by their Laplace expansions on the seventh column, we obtain

$$R = \det \phi_{f2} / \det A \quad (15)$$

$$= \frac{\rho_o c_{10}^2 \bar{\xi}_f \det A_{6,7}^{7,7} + \rho_f c_f^2 \det A_{6,7}^{6,7}}{\rho_o c_{10}^2 \bar{\xi}_f \det A_{6,7}^{7,7} - \rho_f c_f^2 \det A_{6,7}^{6,7}} \quad (16)$$

where $\det A$ is the determinant of the coefficients in Eq. (13), and $\det \phi_{f2}$ is the Cramer's Rule substitution of the vector on the right-hand side of Eq. (13) into the column corresponding to ϕ_{f2} . The notation $\det A_n^{ij}$ indicates the minor of order n reduced from the (ij) element of A . A Rayleigh wave exists when the denominator in Eq. (15) vanishes.¹⁹ If there is no fluid present ($\rho_f = 0$), the condition $\det A = 0$ reduces to $\det A_{6,7}^{7,7} = 0$ by inspection of Eq. (13).

The latter condition yields a wave speed which differs very little ($\sim 0.1\%$) from the more general solution with the

fluid present. However, information on the beam displacement parameter Δ_s is contained in the imaginary part of the wave vector, and so long as $\rho_f = 0$, the solution of $\det A_{6,7}^{7,7} = 0$ for the lowest surface wave mode will be entirely real. The reflection coefficient exhibits a singularity in the complex plane corresponding to the generation of Rayleigh waves at the fluid-solid interface. Solving the general equa-

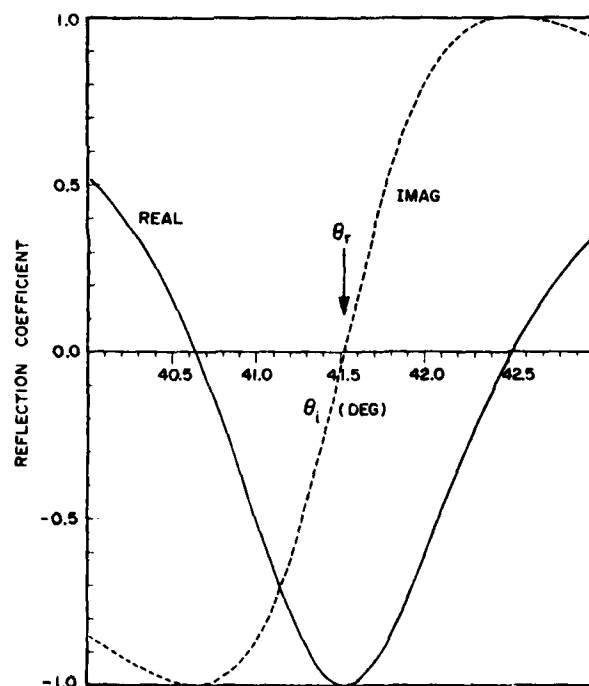


FIG. 2. Real and imaginary parts of the reflection coefficient as a function of incident angle for a layered substrate where $Q = 3$.

tion is equivalent to finding this Rayleigh-wave pole. In their analysis Bertoni and Tamir⁵ develop the reflection coefficient in a Laurent expansion, keeping only the most significant term. We have used the implied analyticity of R in the vicinity of the pole to employ a Newton-Raphson technique, generalized for functions of a complex variable, to locate numerically the appropriate zero of $\det A$ in the complex ξ plane. The Newton-Raphson routine is seeded with an approximate solution of $\det A^{(0)} = 0$, which insures rapid convergence to the desired root. Figure 2 demonstrates the rapid variation in the real and imaginary parts of $R(\xi)$ along the real ξ axis near the Rayleigh angle. Since $|R| = 1$, this variation implies a rapid change in the phase angle of the reflected wave, and this phase reversal manifests itself under suitable conditions as a null region observed in the reflected field-amplitude distribution.

The loci of ξ_p in the complex plane is shown in Fig. 3. To isolate the effect of the layer, the frequency is separately held constant. With this constraint the pole coordinates display a 50% variation in $\text{Re}(\xi_p)$ and a 200% excursion in $\text{Im}(\xi_p)$ as the dimensionless parameter Q progresses from $Q = 0$ to $Q = 6$. Re and Im refer to real and imaginary parts, respectively. Each interval of 0.6 in Q is denoted on the curve in Fig. 3 by a plotting symbol. From these, a qualitative estimate of the speed of variation of pole coordinates as a function of Q can be made. The most rapid change appears to occur between $Q = 1.2$ and $Q = 1.8$, and it would be in this regime where the reflected field is most sensitive to differences in film thickness. As Q increases beyond 3, the pole

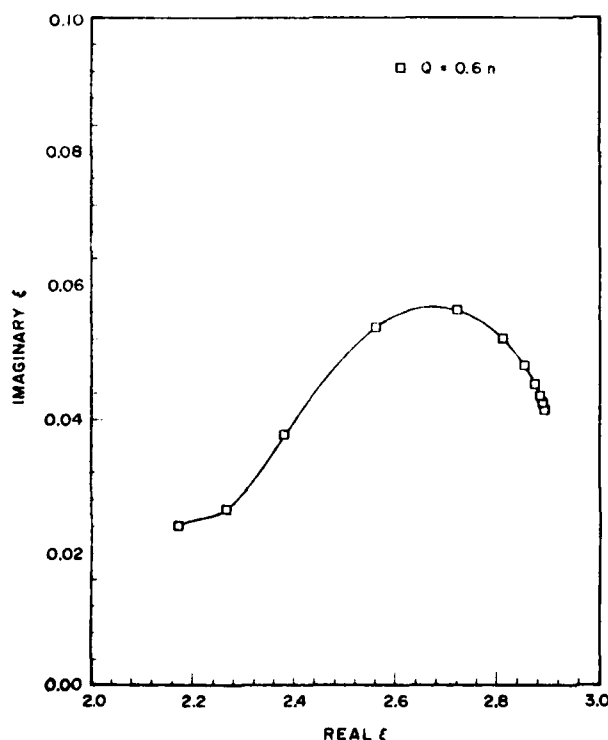


FIG. 3. Calculated Rayleigh wave pole trajectory in the complex ξ plane as a function of Q . Plotting symbols are placed at integral multiples of $Q = 0.6$ from $Q = 0$ to 6.0. Relative rate of change of ξ_p as a function of Q is indicated by the spacing between plotting symbols.

moves very little, indicating that the layer dominates the elastic behavior of the leaky Rayleigh wave past this point. Another interesting feature is that the attenuation reaches a maximum near $Q = 2.2$, which is significantly larger than the value at either of the limiting points of Q . Thereafter $\text{Im}(\xi_p)$ decreases to the value appropriate for the layer material alone. This nonmonotonic aspect of the reflection coefficient is absent from the approximate model¹⁸ and appears only in the exact treatment.

From the result of the numerical procedures to find the Rayleigh wave pole ξ_p , we obtain the Rayleigh wave speed c_r and the beam displacement parameter Δ_r ,

$$c_r = \omega / \text{Re}(\xi_p), \quad (17a)$$

$$\Delta_r = 2 / \text{Im}(\xi_p). \quad (17b)$$

The latter definition follows from Schoch's original analysis of the problem.^{1,2} These two quantities in Eq. (17) together with the beam width at the interface and the interface-to-receiver distance completely specify the solution, as given by Bertoni and Tamir.⁵ Although their analysis is approximate and rests on an assumption concerning the acoustic beam profile, it is rather accurate, as we have verified by direct numerical evaluation of the reflected-field integral. Moreover, it has the advantage of being a closed-form expression.

Figure 4 shows the displacement parameter Δ_r normalized by the acoustic wavelength in the fluid as a function of Q . The elastic constants are appropriate for copper on stainless steel.²⁴ The quantity Δ_r / λ is not explicitly frequency dependent and would be a constant at all frequency if the layer were absent. The strong dependence of Δ_r / λ on Q , particularly between $Q = 0$ and $Q = 2$, indicates the sub-

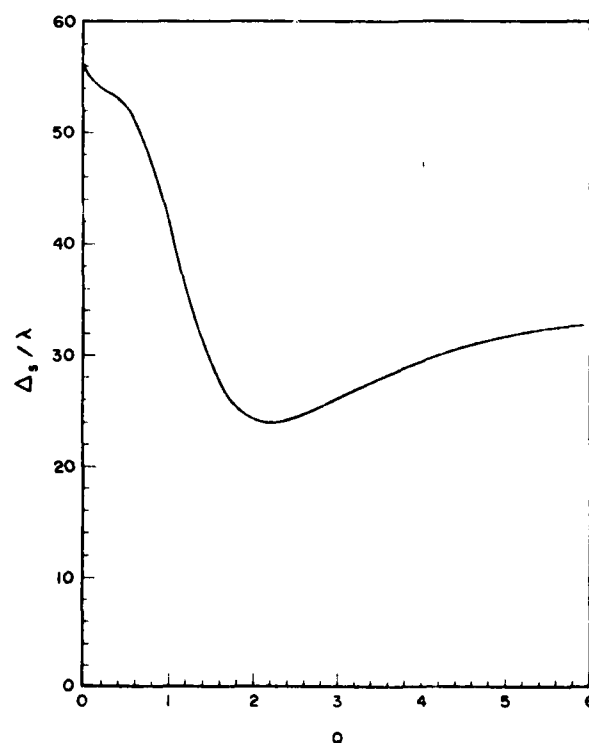


FIG. 4. Beam displacement parameter normalized by acoustic wavelength in the fluid as a function of Q , as calculated from Eq. (17b). Minimum approximately coincides in Q with $c_r(Q) = c_n$.

stantial effect of the layer on the leaky wave. Within this range the film thickness increases from $d = 0$ to $d \approx 0.3\lambda$. For $Q = 0$ or $Q \gg 1$, Δ_r assumes limiting values corresponding respectively to a halfspace of the substrate material alone or the layer material alone, as calculated from Schoch's expression.¹ The minimum in Δ_r/λ observed near $Q = 2.2$ mirrors the corresponding feature from Fig. 3. Some insight into the origin of the minimum may be achieved by considering the value of c_r at which it occurs. From Fig. 3 it is seen that the extremum in $\text{Im}(\xi_p)$ corresponds to a Rayleigh wave speed within 1% of the transverse wave speed of the layer. If c_{tr} is allowed to vary in the calculation, the value of c_r corresponding to the extremum in $\text{Im}(\xi_p)$ follows the layer transverse wave speed fairly accurately. Another way to state this is that the Rayleigh angle at the critical value of Q very nearly equals the critical angle for transverse wave propagation in the layer material. This transverse wave cannot have a net energy flux in the positive z direction since the transverse wave speed of the substrate is larger than c_r at $Q = 0$. While we can suggest no specific mechanism to explain the maximum of $\text{Im}(\xi_p)$, the correlation with c_{tr} is probably significant.

The real part of the Rayleigh wave pole contains the dispersive propagation constant, as indicated in Eq. (17a). The value of the calculated Rayleigh wave speed as a function of Q is shown in Fig. 5 together with the experimental results on three samples of copper-coated stainless steel. Different film thicknesses are denoted by different plotting symbols. Data are collected by searching for the characteristic minimum^{5,18} in the reflected field distribution which indi-

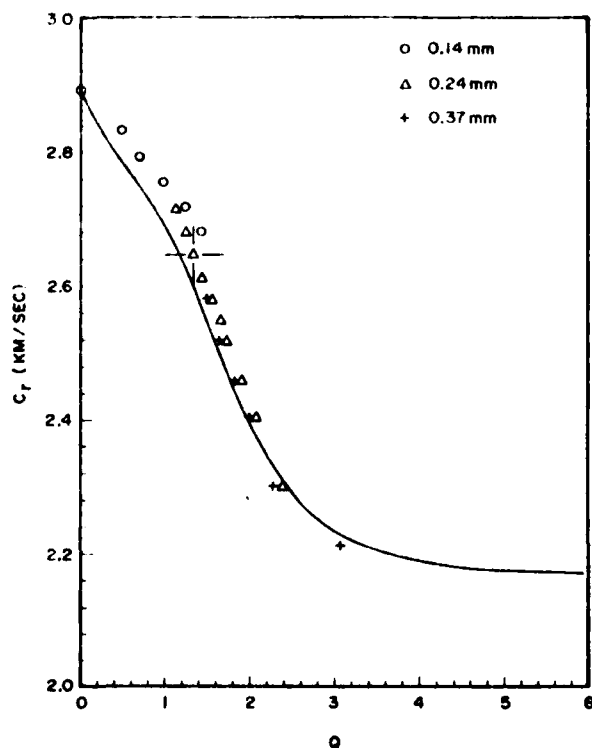


FIG. 5. Rayleigh wavespeed vs Q for different thicknesses of copper on stainless steel, indicated on figure. Experimental uncertainty is denoted by the sample error bars. Solid curve is model calculation from Eq. (17a).

cates the Rayleigh angle. Further experimental details are given in Sec. III. Within the error limits indicated in Fig. 5 agreement with the theoretical model is quite good from $Q = 0$ to $Q = 3$, where the Rayleigh wave speed has nearly reached the asymptotic value appropriate for the elastic properties of the layer. Similar results for samples of cadmium and zinc on iron have been observed by Luukala and Hattunen^{24,25} using a slightly different, but related, technique. Their analysis follows along the lines of other theoretical treatments,^{20,21} where the effect of the fluid has been neglected. In that case the lowest order Rayleigh wave singularity will fall on the real axis, as indicated earlier, and, therefore, the beam displacement parameter in the fluid cannot be found by this calculation.

III. EXPERIMENTAL DETAILS

Dependence of the important parameters in the theoretical model have been examined by performing a series of experiments on several samples of stainless steel loaded by a layer of copper. The copper is electrodeposited onto the polished stainless-steel substrate material to a controlled thickness, which is checked independently after deposition by use of an optical cathetometer. We have measured the ultrasonic velocities of the substrate material and found the values to be within 0.5% of the established results for 302 stainless steel.²⁶ The values of the remaining physical constants used in the calculations are recorded in Ref. 27.

The apparatus we employ in these measurements consists of an x - y bridge supported over an ultrasonic inspection tank. This system is capable of precision linear positioning and automated, computer-controlled stepping. The translational resolution of our bridge is 0.02 mm. Angular adjustment is achieved with two-angle manipulators attached to the translation frame. These permit a resolution of 0.1° , while the absolute accuracy is $\pm 0.25^\circ$.

Since the theoretical model⁵ we utilize to fit the amplitude distribution curves of the next section is based on the assumption that the incident acoustic beam has a Gaussian profile, we have employed specially configured transducers designed to fulfill this requirement. They are based on an earlier design²⁸ and consist of circular quartz plate resonators 25 mm in diameter with the fluid-side electrode completely covering one face, while the other face has a strip electrode 6.4 mm in width. This arrangement produces an acoustic beam whose amplitude distribution in the transducer midplane, perpendicular to the strip electrode accurately describes a Gaussian curve.

Data collection in these experiments has been accomplished by exciting the Gaussian-beam transducers with long (50–100 μsec) tone bursts which represent a good approximation to cw excitation. A continuous rf signal source is gated with a diode switch to produce tone bursts that are applied to a linear power amplifier, then sent through an impedance matching network to the transducer. A low-noise, wideband preamp on the detection side following a second matching network enables the signal to drive a long coax line to a tuned amplifier and video detector. The detector output is smoothed by centering the aperture (5 μsec in

duration) of a gated integrator on the received signal, using an integration time constant of about 0.5 sec. The sensitivity of this system is about 100 nV, although this level of sensitivity is seldom needed. An independent calibration of the system after each measurement insures that nonlinearities in the amplifiers or video detector can be compensated for in the data reduction.

The amplitude distribution curves are acquired by fixing the position of the transmitter with respect to the sample and scanning the receiver stepwise across the reflected field parallel to the sample surface. In comparisons between experimental and theoretical amplitude distributions the x coordinates of the curve maxima have been chosen to be equal. This procedure simplifies the measurements and does not seriously affect a critical comparison between experiment and theory, since the displacement parameter also influences the shape of the distribution. In addition, we perform relative measurements and therefore constrain the magnitude of the distributions to be equal at a single point, usually the absolute maximum corresponding to the leaky wave peak. A more complete description of the experimental technique can be found elsewhere.¹⁸

IV. RESULTS

The reflected acoustic field amplitude distribution for a 2.5-MHz bounded beam incident on a steel substrate loaded by a copper layer is shown in Fig. 6. Experimental points are indicated by the open circles, and the solid curve is the model calculation. Data are collected by fixing the position of the transmitting transducer and scanning the receiver in the x

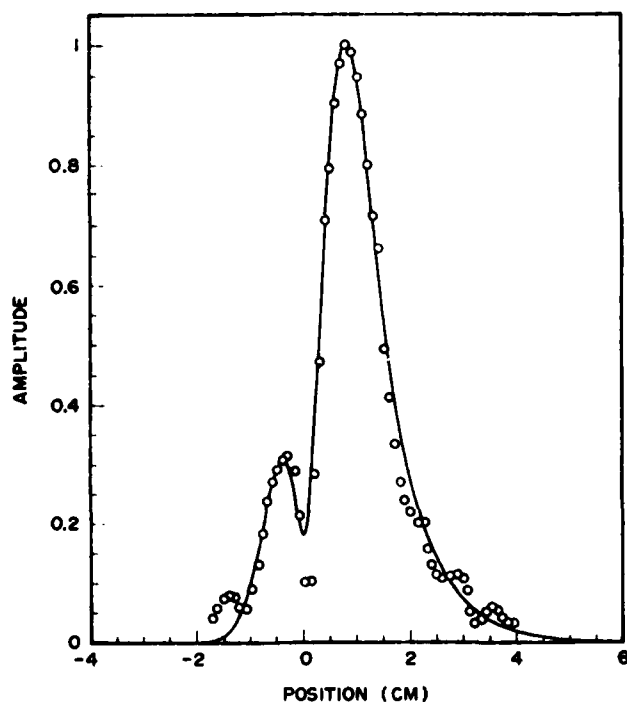


FIG. 6. Reflected field amplitude distribution as a function of receiver position at a frequency of 2.5 MHz and an incident angle of 37.5° . Layer thickness is 0.37 mm, and $Q = 1.86$. Solid curve is theoretical prediction, and open circles are data.

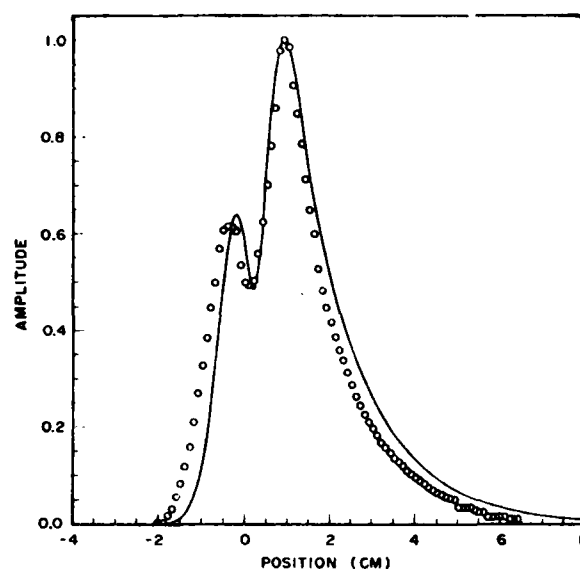


FIG. 7. Reflected field amplitude distribution as a function of receiver position at 2.5 MHz and 0.2° below θ_r . Layer thickness is 0.14 mm, and $Q = 0.68$. Solid curve is theory, and open circles are data.

direction across the reflected field. The receiver is halted at each point in the scan so that the response time of the gated integrator does not affect the amplitude. From Fig. 6 we see that agreement between the model calculation and the experiment is rather good. The shapes of the displaced leaky-wave beam and the remnant specular reflection to the left of $x = 0$ are both accurately reproduced by the theory. In addition, the model predicts the relative peak heights and separation to within experimental uncertainty, represented by the size of the plotting symbols. Some disparity, however, can be noted in the tails of the distribution, where diffraction effects, perhaps caused by the finite y extent of the transducer together with a small misalignment, appear in the data. Also, the degree of cancellation of the specular reflection and leaky wave in antiphase near $x = 0$ predicted by the model is less than that observed experimentally. For the data of Fig. 6, the dimensionless parameter Q is 1.86 ($\lambda/d = 2.6$), close to the point of maximum attenuation from Fig. 4. The fact that our model, augmented by the calculation along the lines of Bertoni and Tamir,⁵ accurately predicts most features of the data at a midrange value of Q tends to confirm the validity of this approach.

Figure 7 shows the results for a different sample of copper-loaded stainless steel, where the beam is not incident at the Rayleigh angle, and $Q = 0.68$. Away from the Rayleigh angle, coupling to the leaky wave weakens, and the two components of the reflected field are more nearly equal. Still farther from θ_r , the peaks would merge into one, which would then be Gaussian in shape and centered on $x = 0$. Reasonably good agreement is evidenced in the data of Fig. 7, particularly in the modeling of the relative peak amplitudes, their separation, and the depth of the null. Experimentally, the angle of incidence is $0.5^\circ \pm 0.15^\circ$ below the Rayleigh angle, whereas the best fit to the data occurs at a value of $\theta_r - \theta_i$ of approximately 0.2° . Either the measured angle is in error, or the theory overestimates the change in

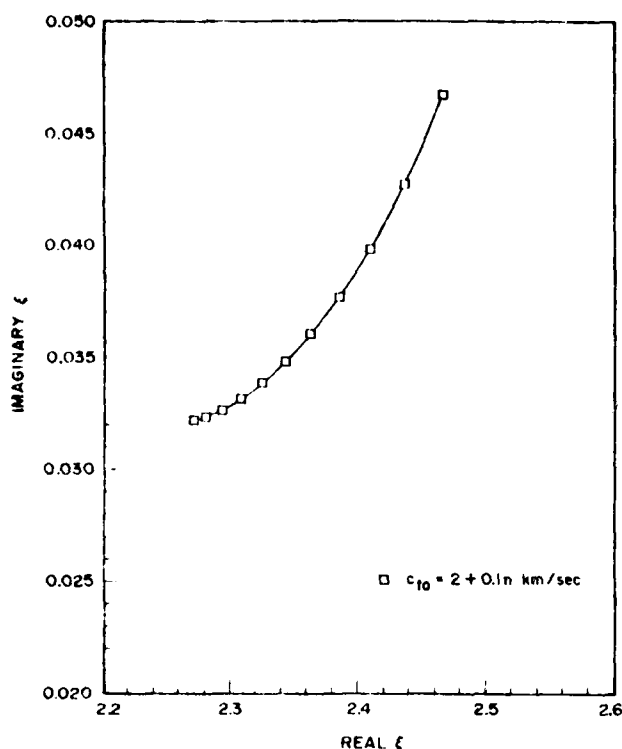


FIG. 8. Calculated Rayleigh wave pole trajectory for variation in layer transverse wavespeed. At upper right $c_{t0} = 2$ km/sec, and plotting symbols denote a change of 0.1 km/sec to $c_{t0} = 3$ km/sec at lower left.

amplitude distribution as the incident angle moves away from the Rayleigh angle. Considering the uncertainty in the angle determination, that source of error is most probably the cause of the apparent disagreement observed here. Regarding their general characteristics, the results presented in Figs. 6 and 7 are representative of data at lower and higher values of Q , where the model fits the data as well or better.

The sharpness of the extinction in the reflected field at the Rayleigh angle suggests a possible application of this phenomenon as a layer thickness gauge, as others noted.²⁵ Determination of the Rayleigh angle θ_r permits us to deduce the layer thickness from the functional relationship depicted graphically in Fig. 5. A related effect is the variation of the Rayleigh wave pole as a function of the layer transverse wave speed c_{t0} . An indication of this variation is given in Fig. 8, where the normalized real and imaginary parts of ξ_p are plotted as a function of c_{t0} . The curve begins at the upper right with $c_{t0} = 2$ km/sec, and Q is held constant at 1.2. Plotting symbols are spaced every 0.1 km/sec to a maximum value of $c_{t0} = 3$ km/sec. As c_{t0} approaches c_{ts} , the change in ξ_p becomes progressively smaller. A variation of about one part in 10^2 in c_{t0} at $Q = 1.2$ corresponds to a change in the Rayleigh angle of 0.1° , near the experimental limit of resolution. Because of the nonlinear relationship between θ_r and c_{t0} , which also depends on Q , the same fractional variation in c_{t0} will not be mirrored in θ_r . Generally, as Q increases, the layer transverse wave speed and the Rayleigh angle approach a linear dependence for small variations.

In conclusion, we have presented experimental measurements with finite Gaussian acoustic beams of the reflected field-amplitude distribution for water-steel interfaces loaded with a copper layer of various thicknesses. We have shown that it is possible to utilize an existing theoretical model¹ to explain our results by constructing and solving suitable boundary condition equations for the Rayleigh wave pole which is appropriate for the layered substrate with the fluid. Excellent agreement with our exact treatment is observed in most aspects of the measurements, at and near the Rayleigh angle, of the reflected acoustic field distribution and of the Rayleigh wave speed dispersion as a function of layer thickness over the acoustic wavelength. In the model calculation the imaginary part of the Rayleigh wave pole is found to display an unexpected maximum at a value of Q where the real part of ξ_p corresponds nearly to the transverse wave speed in the layer.

ACKNOWLEDGMENT

The authors wish to thank K. D. Shimmin for competent technical support throughout the course of this study.

- ¹A. Schoch, *Acustica* **2**, 18 (1952).
- ²A. Schoch, *Ergeb. Exakten Naturwiss.* **23**, 127 (1953).
- ³W. G. Neubauer and L. R. Dragonette, *J. Appl. Phys.* **45**, 618 (1974).
- ⁴O. I. Diachok and W. G. Mayer, *J. Acoust. Soc. Am.* **47**, 155 (1970).
- ⁵H. L. Bertoni and T. Tamir, *Appl. Phys.* **2**, 157 (1973).
- ⁶M. A. Breazeale, L. Adler, and G. W. Scott, *J. Appl. Phys.* **48**, 530 (1977).
- ⁷L. E. Pitts, T. J. Plona, and W. G. Mayer, *IEEE Trans. Sonics Ultrason.* **SU-24**, 101 (1977).
- ⁸T. D. K. Ngoc and W. G. Mayer, *IEEE Trans. Sonics Ultrason.* **SU-27**, 229 (1980).
- ⁹T. D. K. Ngoc and W. G. Mayer, *J. Appl. Phys.* **50**, 7948 (1979).
- ¹⁰T. D. K. Ngoc and W. G. Mayer, *J. Acoust. Soc. Am.* **67**, 1149 (1980).
- ¹¹A. Faure, G. Maze, and J. Ripoché, *J. Appl. Phys.* **48**, 869 (1977).
- ¹²D. A. Davids, *Rev. Sci. Instrum.* **51**, 1059 (1980).
- ¹³R. Fiorito, W. Madigosky, and H. Uberall, *J. Acoust. Soc. Am.* **66**, 1857 (1979).
- ¹⁴P. V. Burlin and I. Ya. Kucherov, *Pis'ma Zh. Eksp. Teor. Fiz.* **26**, 644 (1977) [*JETP Lett.* **26**, 490 (1977)].
- ¹⁵I. D. Ivanov, *Sov. Phys. -Acoust.* **21**, 259 (1975); *Sov. Phys. -Acoust.* **21**, 343 (1975).
- ¹⁶D. E. Chimenti and L. Adler, *Ultrasonics* **19**, 112 (1981).
- ¹⁷G. W. Scott and L. Adler, *Mater. Eval.* **33**, 54 (1977).
- ¹⁸A. H. Nayfeh, D. E. Chimenti, L. Adler, and R. L. Crane, *J. Appl. Phys.* **52**, 4985 (1981).
- ¹⁹L. M. Brekhovskikh, *Waves in Layered Media* (Academic, New York, 1960), pp. 30-45.
- ²⁰J. D. Achenbach and S. P. Keshava, *J. Appl. Mech.* **34**, 397 (1967).
- ²¹G. W. Farnell and E. L. Adler, in *Physical Acoustics IX*, edited by W. P. Mason and R. N. Thurston (Academic, New York, 1972), pp. 35-126.
- ²²G. Mott, *J. Acoust. Soc. Am.* **50**, 819 (1971).
- ²³B. A. Auld, *Acoustic Fields and Waves in Solids* (Wiley-Interscience, New York, 1973), Chap. 12.
- ²⁴M. Luukkala and M. Hattunen, *Appl. Phys. Lett.* **19**, 56 (1971).
- ²⁵M. Hattunen and M. Luukkala, *Appl. Phys.* **2**, 257 (1973).
- ²⁶*Metals Handbook*, Vol. 11, edited by H. E. Boyer (American Society for Metals, Metals Park, Ohio, 1976).
- ²⁷The elastic constants used in the calculations are: $c_f = 1.48$, $c_{t0} = 4.76$, $c_{t1} = 2.32$, $c_{t2} = 5.69$, $c_{t3} = 3.13$ km/sec; $\rho_f = 1$, $\rho_s = 8.93$, $\rho_l = 7.9$ g/cm³.
- ²⁸F. D. Martin and M. A. Breazeale, *J. Acoust. Soc. Am.* **49**, 1668 (1971).

Reflection of finite acoustic beams from loaded and stiffened half-spaces

A. H. Nayfeh

Department of Aerospace Engineering and Applied Mechanics, University of Cincinnati, Cincinnati, Ohio 45221

D. E. Chimenti

Materials Laboratory, Air Force Wright Aeronautical Laboratories, Wright Patterson AFB, Ohio 45433

(Received 4 February 1983; accepted for publication 6 February 1984)

Results of theoretical calculations and experimental measurements on the reflection of finite acoustic beams from a fluid-solid interface in the presence of a loading or stiffening layer on the solid are presented. Measurements with Gaussian-profile acoustic beams are reported on wave-speed dispersion and reflected-beam amplitude distribution for stiffening layers of chromium on either brass or stainless steel. Good agreement is generally observed. Detailed results of calculations of the reflection coefficient to delineate the behavior of cutoff modes for both stiffened and loaded half-spaces are given. A straightforward method for deducing the complex Rayleigh wavenumber directly from the reflection coefficient is discussed. Comparisons between direct numerical integration of the reflected beam distribution and results of an extended analytical model demonstrate decreasing accuracy of the latter as one nears a mode cutoff.

PACS numbers: 43.20.Fn, 68.25. + j, 43.20.Bi

INTRODUCTION

The lateral displacement and associated distortion of a finite-aperture acoustic wave incident from a fluid onto a fluid-solid interface at or near the Rayleigh critical angle is a phenomenon which has received considerable attention recently.¹⁻⁵ Physically, resonant generation of a Rayleigh-like wave and rapid reradiation of this surface-wave energy into the fluid are responsible for the characteristic displacement and distortion of the acoustic beam. These effects typically lead to a bimodal reflected acoustic field, composed of a remnant specular reflection summed coherently with the radiating surface wave. When conditions of beamwidth and wavelength are favorable, a portion of the field distribution shows a strong reduction in amplitude, due to the phase cancellation of component fields. The situation is illustrated schematically in Fig. 1. An acoustic beam incident at the Rayleigh angle suffers displacement and distortion with most of the

power contained in the shaded regions. The suppressed specular reflection is indicated by the dashed lines.

In two recent papers^{6,7} we analyzed, both analytically and experimentally, the reflected waves from liquid-solid interfaces separated by layers of different elastic materials in welded contact to the solid. In Ref. 6 we have derived the exact expression for the reflection coefficient from a layered half-space in a fluid. Using those results, we have further shown that an earlier approximate analysis⁸ may be extended to the case where a layer of differing density and elastic constants is in welded contact with the solid half-space. In the earlier paper,⁷ on the other hand, it was postulated that for cases in which the thickness of the layer is small compared with the incident wavelength, details of the propagation process in the layer might be unnecessary in light of the expectation that variations in the displacements across the layer thickness will be small. Thus in Ref. 7 a basic analysis was presented in which the details of the propagation in the layer were ignored but the layer's influence was preserved. Specifically, it was found that the effect of the layer is manifested in the form of a modifier to the interface stress-continuity conditions between the liquid and the solid substrate. This leads to an approximate simplified expression for the reflection coefficient.

It is of interest to note that all physical effects of the reflected beam can be explained by examining the behavior of the appropriate reflection coefficient. Generally speaking, the inclusion of the layer was found to give rise to dispersive effects in both the surface wave speed and the lateral displacement of the beam. These two effects further influence the distortion of the reflected beam. The specific influence of the layer, however, depends highly upon its material characteristics as compared with those of the substrate. Besides the trivial case in which the layer's properties are identical with

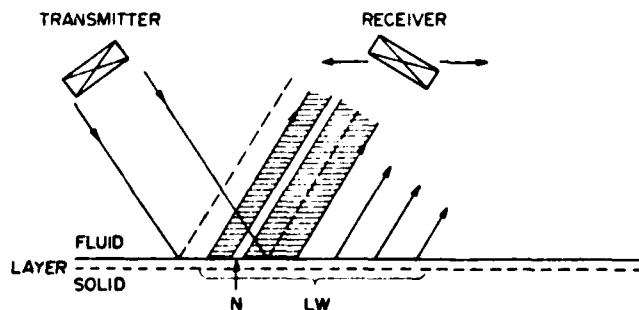


FIG. 1. Schematic of leaky wave experiment. The transmitter is fixed relative to sample, while receiver scans along interface. Dashed lines in reflected field indicate specular reflection. Shaded regions contain most of the acoustic power. Null zone is denoted by N , and leaky wave reflected field by LW .

those of the substrate, the layer can either load or stiffen the substrate. The loading situation occurs when the layer's elastic properties are softer than those of the substrate, and stiffening occurs for layers stiffer than the substrate.

In our previous investigations^{6,7} we concentrated on establishing the behavior of the zeroth-order surface mode of the loading case. It is found that the frequency dependence of the surface wave speed and of the beam displacement vary from those corresponding to the substrate at $Q=0$ ($Q=k_{10}d$ where k_{10} is the shear wavenumber of the substrate and d is the layer thickness) to those corresponding to the layer as $Q \rightarrow \infty$, as expected. Further examination of the reflection coefficient reveals the existence of an infinite number of higher order leaky surface modes. The phase velocities of these modes behave in a different manner from that of the zeroth-order mode, however. Specifically, each of these modes exists beyond a critical value of Q , at which its phase velocity is bounded by the substrate's transverse wave speed and asymptotically approaches the layer's transverse wave speed as $Q \rightarrow \infty$. Furthermore, the corresponding beam displacements of these modes grow indefinitely as Q approaches its critical values and infinity. The purpose of this paper is to present results pertaining to the leaky surface mode's cutoff behavior in the cases of loaded and stiffened half-spaces. This includes both calculations and measurements.

I. THEORY

In what follows we present a short summary of the theoretical analysis of the present problem. For the complete details of the analysis we refer the reader to our earlier paper.⁸ The plan is to introduce for each medium the potential functions Φ and Ψ corresponding to longitudinal and transverse wave motion, respectively. Formal solutions of the field equations when expressed in terms of these potentials

are then combined with the proper interface continuity conditions to yield amplitudes of the wave potentials. Among these amplitudes will be the reflected beam amplitude which yields the reflection coefficient. The formal solutions for the incident and reflected wave potentials in the half-space, layer, and fluid are given by

$$\Phi_s = \phi_{s1} \exp(i\zeta_{1s} z + i\eta), \quad (1)$$

$$\Psi_s = \psi_{s1} \exp(i\zeta_{1s} z + i\eta), \quad (2)$$

$$\Phi_0 = \phi_{01} \exp(i\zeta_{10} z + i\eta) + \phi_{02} \exp(-i\zeta_{10} z + i\eta), \quad (3)$$

$$\Psi_0 = \psi_{01} \exp(i\zeta_{10} z + i\eta) + \psi_{02} \exp(-i\zeta_{10} z + i\eta), \quad (4)$$

$$\Phi_f = \phi_{f1} \exp[i\zeta_f(z+d) + i\eta] + \phi_{f2} \exp[-i\zeta_f(z+d) + i\eta], \quad (5)$$

where all ϕ 's and ψ 's are unknown amplitudes, the subscripts f, o, s refer to fluid, layer, and solid half-space, respectively, and the subscripts 1 and 2 refer to incident and reflected waves. The wave-vector components are given by

$$\zeta_{\alpha\beta} = (k_{\alpha\beta}^2 - \xi^2)^{1/2}, \quad k_{\alpha\beta} = \omega/c_{\alpha\beta}, \quad (6)$$

where $\alpha = l, t$ and $\beta = f, o, s$; ω is the circular frequency, and $\eta = \zeta x - \omega t$. The invariant x component of the wave vector is just $\xi = k_f \sin \theta_i$, where θ_i is the angle of incidence. For the fluid there can be no ambiguity concerning the mode, so the wave properties are denoted by a single subscript.

By combining the potentials with the proper interface continuity conditions on stresses and displacements at the two interfaces and defining the reflection coefficient

$$R = \phi_{f2}/\phi_{f1}, \quad (7)$$

one can, using Cramer's rule, conveniently display R as

$$R = \frac{|\Gamma_s - (\rho_f c_f^2 \Gamma_f / \rho_0 c_{10}^2 \bar{\zeta}_f)|}{|\Gamma_s + (\rho_f c_f^2 \Gamma_f / \rho_0 c_{10}^2 \bar{\zeta}_f)|}, \quad (8)$$

where

$$\Gamma_s = \begin{bmatrix} 1 & 0 & -\bar{\zeta}_{10} & 0 & -1 & \bar{\zeta}_{1s} \\ 0 & \bar{\zeta}_{10} & 0 & 1 & -\bar{\zeta}_{1s} & -1 \\ \bar{\mu}_0(\bar{\zeta}_{10}^2 - 1) & 0 & 2\bar{\mu}_0\bar{\zeta}_{10} & 0 & 1 - \bar{\zeta}_{1s}^2 & -2\bar{\zeta}_{1s} \\ 0 & -2\bar{\mu}_0\bar{\zeta}_{10} & 0 & \bar{\mu}_0(\bar{\zeta}_{10}^2 - 1) & 2\bar{\zeta}_{1s} & 1 - \bar{\zeta}_{1s}^2 \\ \bar{\zeta}_{10} \sin \bar{\omega}\bar{\zeta}_{10} & -i\bar{\zeta}_{10} \cos \bar{\omega}\bar{\zeta}_{10} & (1 - \bar{\zeta}_{10}^2)/2 \times \sin \bar{\omega}\bar{\zeta}_{10} & i(\bar{\zeta}_{10}^2 - 1)/2 \times \cos \bar{\omega}\bar{\zeta}_{10} & 0 & 0 \\ -i(\bar{\zeta}_{10}^2 - 1) \times \cos \bar{\omega}\bar{\zeta}_{10} & (\bar{\zeta}_{10}^2 - 1) \times \sin \bar{\omega}\bar{\zeta}_{10} & -2i\bar{\zeta}_{10} \cos \bar{\omega}\bar{\zeta}_{10} & 2\bar{\zeta}_{10} \sin \bar{\omega}\bar{\zeta}_{10} & 0 & 0 \end{bmatrix} \quad (9a)$$

$$\Gamma_f = \begin{bmatrix} 1 & 0 & -\bar{\zeta}_{10} & 0 & -1 & \bar{\zeta}_{1s} \\ 0 & \bar{\zeta}_{10} & 0 & 1 & -\bar{\zeta}_{1s} & -1 \\ \bar{\mu}_0(\bar{\zeta}_{10}^2 - 1) & 0 & 2\bar{\mu}_0\bar{\zeta}_{10} & 0 & 1 - \bar{\zeta}_{1s}^2 & -2\bar{\zeta}_{1s} \\ 0 & -2\bar{\mu}_0\bar{\zeta}_{10} & 0 & \bar{\mu}_0(\bar{\zeta}_{10}^2 - 1) & 2\bar{\zeta}_{1s} & 1 - \bar{\zeta}_{1s}^2 \\ \bar{\zeta}_{10} \sin \bar{\omega}\bar{\zeta}_{10} & -i\bar{\zeta}_{10} \cos \bar{\omega}\bar{\zeta}_{10} & (1 - \bar{\zeta}_{10}^2)/2 \times \sin \bar{\omega}\bar{\zeta}_{10} & i(\bar{\zeta}_{10}^2 - 1)/2 \times \cos \bar{\omega}\bar{\zeta}_{10} & 0 & 0 \\ -\bar{\zeta}_{10} \sin \bar{\omega}\bar{\zeta}_{10} & i\bar{\zeta}_{10} \cos \bar{\omega}\bar{\zeta}_{10} & -\sin \bar{\omega}\bar{\zeta}_{10} & i \cos \bar{\omega}\bar{\zeta}_{10} & 0 & 0 \end{bmatrix} \quad (9b)$$

AD-A145 990

RESEARCH IN QUANTITATIVE NDE TECHNIQUES(U) SYSTEMS
RESEARCH LABS INC DAYTON OH RESEARCH APPLICATIONS DIV
D A STUBBS ET AL. MAR 84 SRL-6575 AFMAL-TR-84-4026

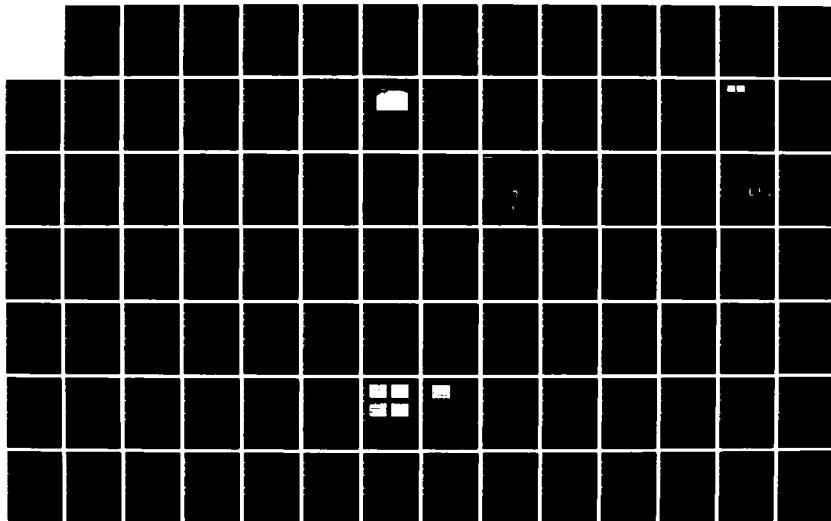
2/3

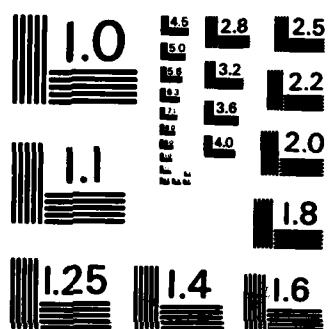
UNCLASSIFIED

F33615-80-C-5015

F/G 13/8

NL





MICROCOPY RESOLUTION TEST CHART
NATIONAL BUREAU OF STANDARDS-1963-A

and

$$\bar{\xi}_{\text{eff}} = \frac{\xi_{\text{eff}}}{\xi}, \quad \bar{\mu}_0 = \frac{\mu_0}{\mu_s}, \quad \bar{\omega} = \frac{\omega d}{c_s} = \frac{Q c_{\text{eff}}}{c_s}. \quad (10)$$

Here, c_s is the Rayleigh wave speed, and μ_s is the shear modulus of the substrate. For later reference in the analysis, we further assume that a Gaussian beam is incident from the fluid onto the fluid-solid layer interface. Its incident field is represented by

$$\phi_{f1}(x, z) = \frac{1}{2\pi} \int_{-\infty}^{\infty} \hat{\phi}_{f1}(\xi) \exp(i\xi x + i\xi_f z) d\xi, \quad (11a)$$

where

$$\hat{\phi}_{f1}(\xi) = \exp[-(\xi - k_i)^2 (a_0/2)^2] / \cos \theta_i. \quad (11b)$$

The caret indicates a Fourier transform, $k_i (= k_f \sin \theta_i)$ and θ_i are the wave vector and angle of incidence, and a_0 is the incident acoustic beam half-width projected onto the x axis. Upon its reflection, the incident beam of Eq. (11) is modulated by the reflection coefficient R , and the reflected field is thus given by

$$\phi_{f2} = \frac{1}{2\pi} \int_{-\infty}^{\infty} \hat{\phi}_{f1}(\xi) R(\xi) \exp(i\xi x - i\xi_f z) d\xi. \quad (12)$$

The representation of the reflected field in Eq. (12) completes the description of finite-beam reflection from fluid-solid interfaces. This integral can be evaluated analytically by making several assumptions about the reflection coefficient and the incident beam profile, as was done in the analysis of Bertoni and Tamir⁸ for a fluid over an isotropic half-space. Since Rayleigh wave propagation on a layered half-space in contact with a fluid is equivalent to propagation on an unlayered half-space of suitably modified elastic behavior, we find that the above approximate analysis can be extended to include a layer.^{6,7} Alternatively, the integral of Eq. (12) may be evaluated numerically, enabling consideration of other beam profiles.

II. QUALITATIVE DESCRIPTION OF LEAKY MODE EXTRACTION

Insight on the problem of nonspecular reflection of finite acoustic beams from fluid-solid interfaces can be gained from an examination of the reflection coefficient $R(\theta)$ as a function of angle of incidence and Q . The expression (8) for the reflection coefficient contains, as a by-product, the characteristic equation for the propagation of modified (leaky) Rayleigh surface waves which propagate along the fluid-layered solid interface. The vanishing of the denominator in Eq. (8), namely,

$$|\Gamma_s + (\rho_f c_f^2 \Gamma_f / \rho_0 c_{f0}^2 \bar{\xi}_f)| = 0 \quad (13)$$

defines the characteristic equation for such waves. Furthermore, in the absence of the fluid, i.e., for $\rho_f = 0$, Eq. (13) reduces to

$$|\Gamma_s| = 0 \quad (13a)$$

which defines the characteristic equation for Rayleigh surface waves on a solid layer bonded to a semi-infinite solid substrate.^{9,10}

For given real frequency ω (or Q), the real wavenumber solutions $\xi_p = k_r$ of (13a) define propagating Rayleigh sur-

face modes. It is found that in the case of a loading layer an infinite number of modes exist, whereas in the case of a stiffening layer only a single mode exists. It is important to indicate that in the absence of the layer only a single real solution will exist. This will be the classical surface wave mode which propagates on a half-space. In the presence of the liquid these real wavenumbers will be perturbed rather mildly and become complex. This, of course, is confirmed by Eq. (13) which admits the complex solutions

$$\xi_p = k_r + i\alpha. \quad (14)$$

From Eq. (14) the phase velocity is given as $c_r = \omega/k_r$, and α is the attenuation coefficient. Notice that α vanishes in the absence of the fluid and hence no attenuation (leaking of energy in the fluid) occurs. Hence, in the presence of the fluid these surface waves are called leaky waves. It is also known that c_r is hardly affected by the presence of the fluid.⁶ However, as has been shown earlier⁶⁻⁸ α is very important because it is related to the lateral displacement of the reflected beam. In fact, the beam displacement parameter Δ_r is defined to be equal to $2/\alpha$.

Since we have concluded that the vanishing of $|\Gamma_s|$ defines the propagating surface modes, then it is clear from (8) that as $|\Gamma_s| \rightarrow 0$, $R \rightarrow -1$ and hence $|R| = 1$. Also at this critical location, the phase of R passes through π .⁶ Thus, close to the zeros of $|\Gamma_s|$ where $|R| \rightarrow 1$, we find that we have an alternative method for deducing the leaky wave propagation constant. Accordingly, the reflection coefficient at any Rayleigh angle can be represented by expanding its phase factor about the incident wave vector in powers ξ and retaining the leading term⁶⁻⁸

$$R(\xi) \sim \exp[i(\xi - k_r)S'(k_r)], \quad (15)$$

where k_r is the Rayleigh wave vector, and $S'(k_r)$ is the derivative with respect to ξ of the phase of R evaluated at k_r . By substituting from (15) into (12) and combining similar terms in the exponential, it is shown that the beam displacement parameter Δ_r can be expressed as

$$\Delta_r = -S'(k_r). \quad (16)$$

Furthermore, Eqs. (15) and (16) are also valid at any incident angle above the transverse critical angle, permitting straightforward calculation of Δ_r away from the mode critical angles. (This point is illustrated later in Fig. 9.)

III. RESULTS AND DISCUSSIONS

A. Loading layers

Samples of the results obtained for a copper layer loading a stainless steel substrate are illustrated in Fig. 2. A series of four curves are collected which display the appearance of higher order modes and their Q dependence.

In accordance with the definitions of c_r and Δ_r , one can also determine the dispersive behavior of each mode as will be described below. In the first frame at $Q (= k_r d) = 0$ the magnitude of R represented as a broken curve attains a value of 1.0 near 29° , the transverse critical angle, and remains at 1.0 for all higher incident angles. Here, all of the information in $R(\theta)$ is contained in its phase. This quantity experiences a small variation at the transverse critical angle and a rapid reversal near 31° , the Rayleigh critical angle. The phase re-

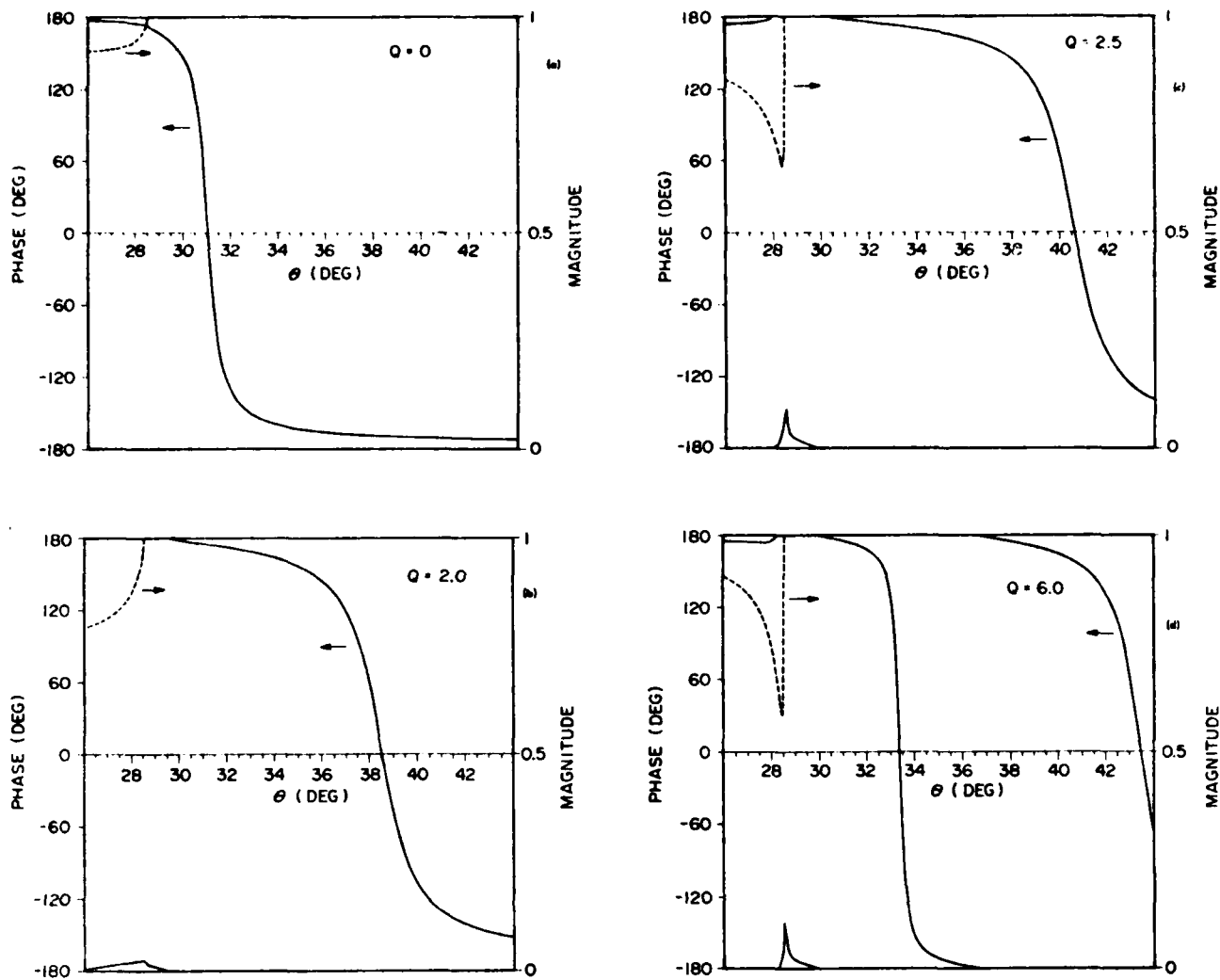


FIG. 2. Phase and magnitude of the reflection coefficient versus incident angle for several values of Q . Materials are a copper layer on a stainless steel half-space. The phase variable has been arbitrarily shifted by 180° .

versal in $R(\theta)$ leads to the generation of the zero-order leaky Rayleigh waves for finite beams incident at or near its occurrence, as can be inferred from the integral in Eq. (12). In Fig. 2(b) at $Q = 2.0$ this angle has moved to near 38.5° , and the beam displacement parameter Δ , has decreased as indicated by the curve's smaller slope. This clearly displays the dispersive behavior of this mode. At $Q = 2.5$ in Fig. 2(c) the variation in R near 28.5° suggests the appearance of an additional propagating leaky surface mode. In Fig. 2(d) this new mode has moved to 33.3° and yet another higher order mode is about to begin propagation from the transverse critical angle. In fact, an infinite number of such modes exist for the loading layer, as also noted in the review article by Farnell and Adler⁹ for the case with no fluid present. The quantitative wave-speed dispersion of these modes for the layered half-space is presented in Fig. 3. At the left the zeroth-order mode is displayed, for which we have presented data in previous work.⁶ Higher order modes are labeled M2, M3, etc. These modes have a cutoff at the half-space transverse wave speed, and at large values of Q their phase velocity approaches the layer transverse wave speed asymptotically.

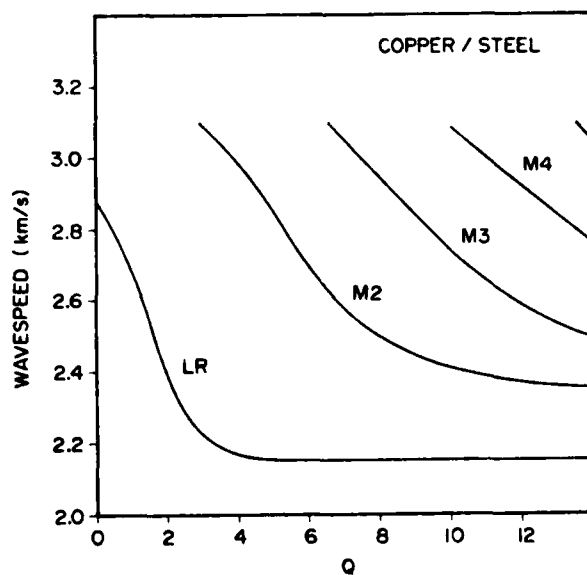


FIG. 3. Phase velocity versus Q of the zeroth and higher order modes for a loaded half-space.

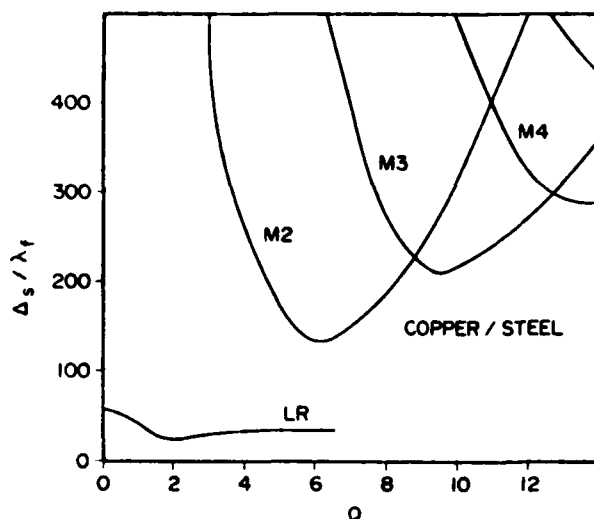


FIG. 4. Beam displacement parameter versus Q of the zeroth and higher order modes for a loaded half-space.

We have compared these calculations to existing data on a water-cadmium-iron system¹¹ and find acceptable agreement.

The new element which appears when the fluid is included in the problem is the lossy part of the wave vector, represented as Δ_s/λ_1 vs Q in Fig. 4. Higher order leaky modes are indicated as before, and the zeroth leaky mode, denoted LR, is included from our previous work⁶ for comparison. The minimum observed in the normalized displacement parameter for the zeroth mode near $Q = 2.2$ also appears in the results for the higher order modes. Here, however, the absolute values are much larger, and the curves diverge at the wave cutoffs. For increasing Q past each minimum, the normalized displacement parameters of the higher order modes rise monotonically, in contrast to the zeroth

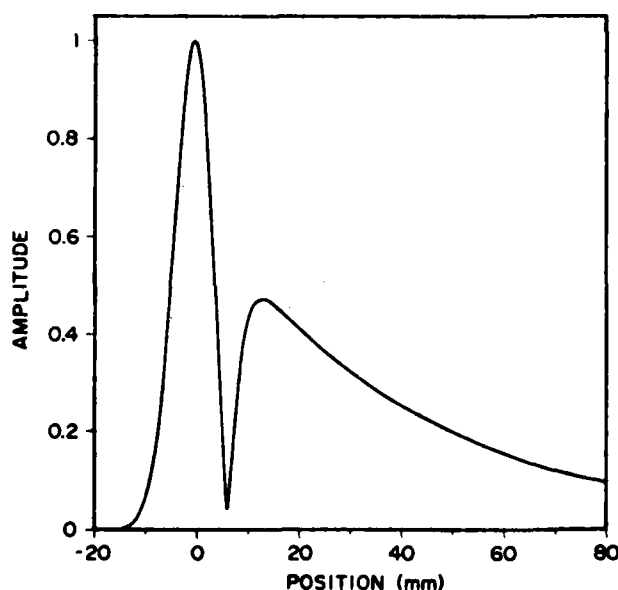


FIG. 5. Amplitude distribution of reflected Gaussian acoustic beam incident at critical angle of M2 mode.

mode where Δ_s/λ_1 approaches an asymptotic value.¹²

Finally, as an example of how a reflected beam is influenced by the M2 mode when a suitable combination of incident angle and Q is chosen, we represent the amplitude of the reflected field as a function of receiver position as shown in Fig. 5. The large peak on the left corresponds to the component illustrated within the region of the geometrical reflection of Fig. 1, while the leaky M2 wave with its trailing field is located on the right. Between these two signal elements is a zone of strong phase cancellation. The behavior of the reflected beam in the vicinity of this higher order leaky mode is qualitatively similar to that for the zero-order wave,^{6,7} a bimodal amplitude distribution with a decaying surface wave separated by a sharp null. One noteworthy difference is caused by the magnitude of the beam displacement parameter. When this quantity is large, as is the case here, energy leaks more slowly from the surface wave into the fluid, accounting for the long tail on the distribution and the relatively small leaky wave peak near $x = 12$ mm.

B. Stiffening layer

When the layer material has a higher transverse wave speed than that of the substrate, the propagation characteristics of leaky surface waves are substantially changed. In fact, only a single leaky surface mode is found to exist. This mode begins propagation at the half-space wave speed for $Q = 0$, and its phase velocity increases with increasing Q as the stiffening effect of the layer blends in. At the point where the compound wave speed nearly equals the transverse phase velocity of the half-space, the mode ceases to propagate. This cutoff is clearly a consequence of the fact that the half-space will not support a surface mode excitation which propagates faster than its bulk transverse wave.

To confirm the existence of only a single mode, we depict in Fig. 6 a history of the variation of the reflection coefficient with four values of Q for a chromium layer stiffening a steel half-space. As in Fig. 2 we plot magnitude and phase of $R(\theta)$, noting that the zero crossing of the phase curves denotes the Rayleigh angle. From Fig. 6(a) to Fig. 6(b) the slope of the phase curve at the abscissa has sharpened considerably indicating an increase in the beam displacement parameter Δ_s . This behavior continues in Fig. 6(c) at $Q = 1.8$. Then at $Q = 1.86$ in Fig. 6(d), above the cutoff value of 1.82, the phase curve no longer crosses zero, and the mode ceases to propagate as a surface wave. Since only a single phase crosses zero and that it ceases to cross zero beyond the critical value of Q , we conclude that only a single leaky mode exists. Similar numerical calculations of chromium over brass also confirm the above conclusion.

The wave-speed dispersion for two cases of a stiffened half-space is demonstrated in Figs. 7 and 8 for chromium on stainless steel and chromium on brass, respectively. The solid curves are taken from the theory developed in the last section, and the discrete points represent measurements on the reflected field to deduce the Rayleigh angle from the occurrence of beam distortion and displacement effects. Details of the experimental procedure and sample preparation have been given elsewhere.¹³ All wave speeds used in our computations are collected in Ref. 14. In both Figs. 7 and 8

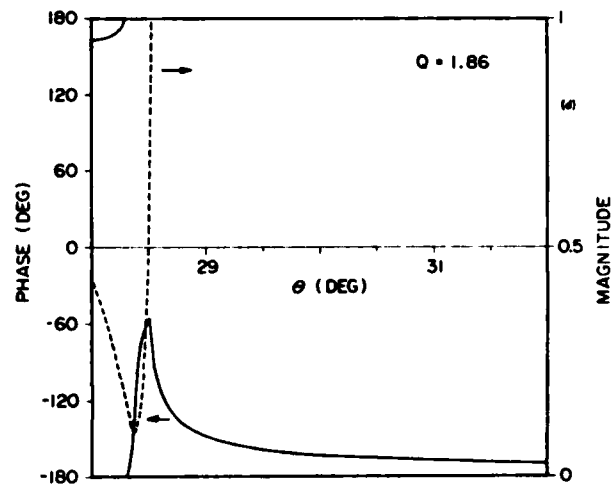
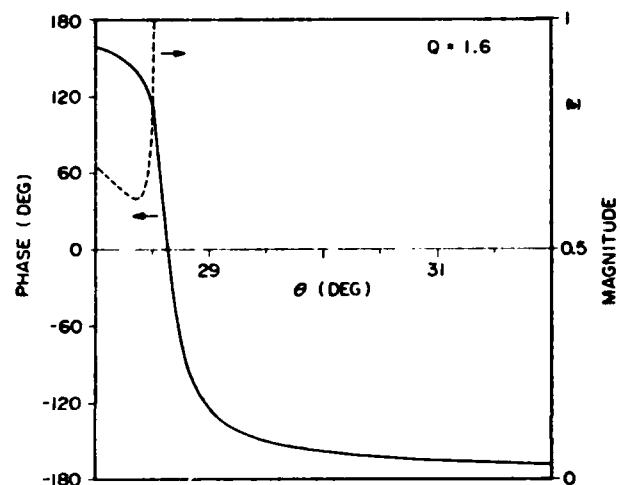
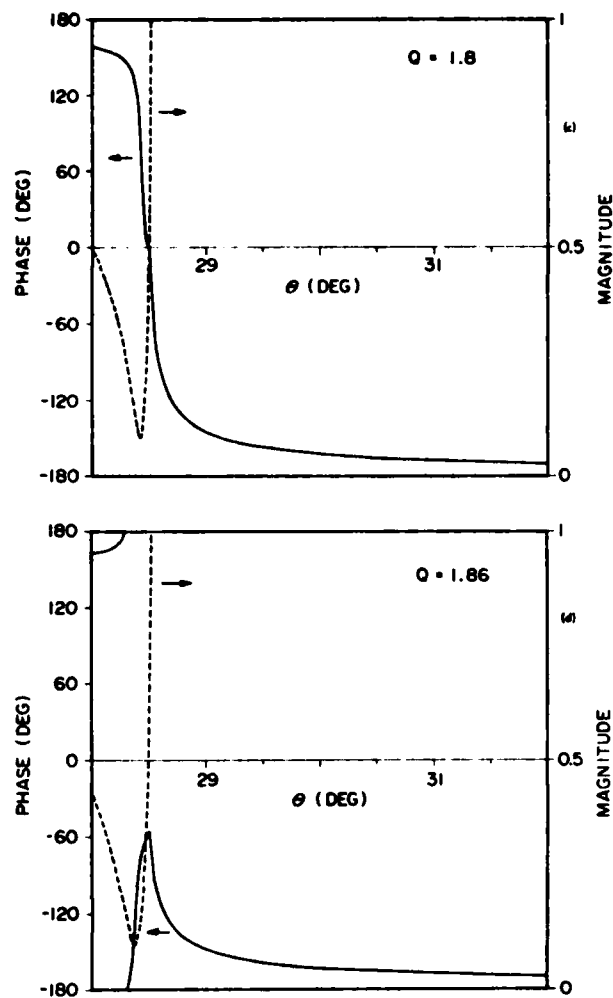
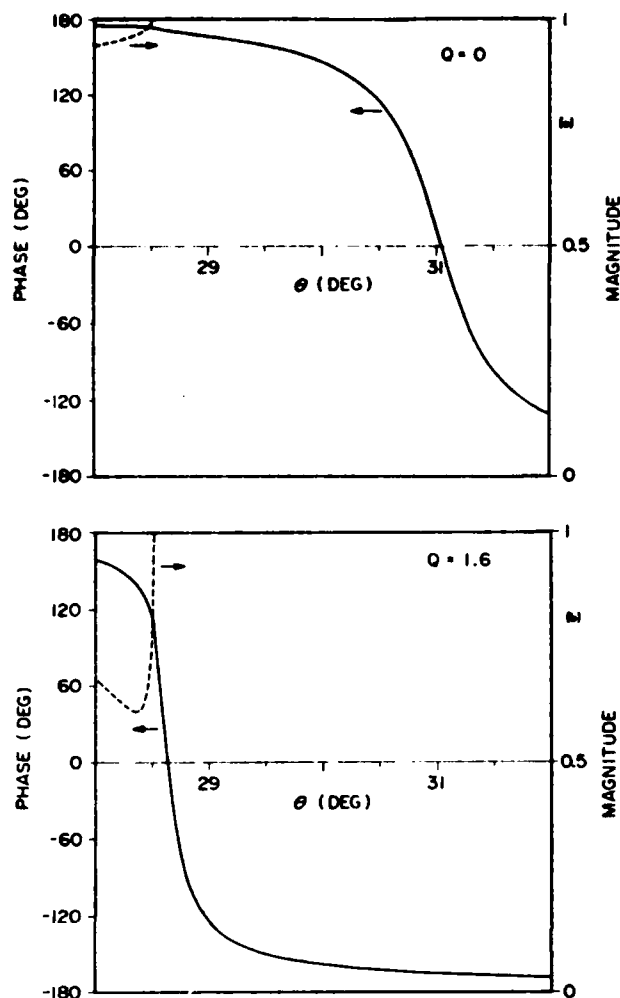


FIG. 6. Phase and magnitude of the reflection coefficient versus incident angle for a stiffened half-space of chromium on stainless steel. The phase variable has been arbitrarily shifted 180° .

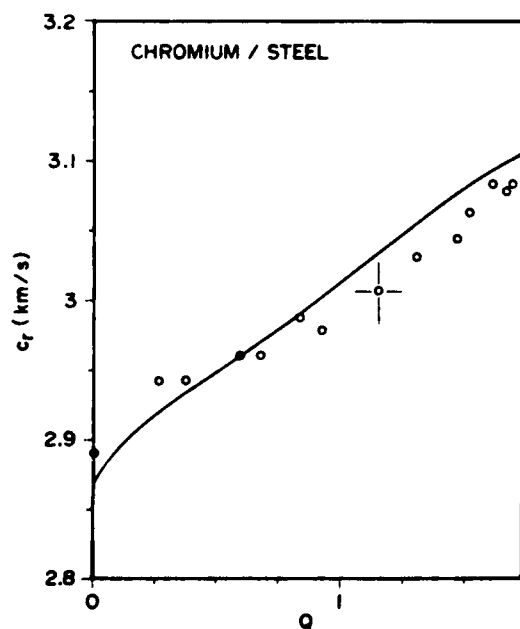


FIG. 7. Phase velocity of leaky Rayleigh mode versus Q for a stiffened half-space. Experimental data are plotted discretely; continuous curve is model calculation from Eq. (10). Experimental uncertainty is indicated by a typical error bar.

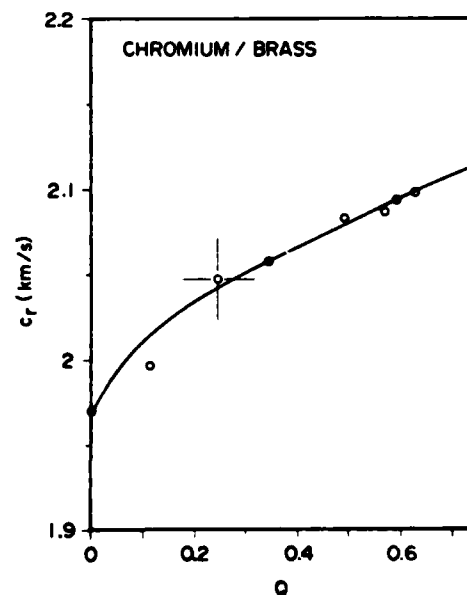


FIG. 8. Phase velocity of leaky Rayleigh mode versus Q for a stiffened half-space. Solid curve is model calculation. Experimental data are plotted discretely; uncertainty is indicated by a typical error bar.

experimental uncertainty is indicated by a typical error bar. Although measurements near the wave cutoff are complicated by the rapid variation in Δ_s/λ_f , agreement with the prediction of the model calculation presented earlier is reasonably good. At the cutoff, the Rayleigh wave speed is a few tenths of a percent higher than the substrate transverse velocity c_{tt} , resulting from the presence of the fluid.

The nonzero imaginary part of the Rayleigh propagation constant leads to the beam displacement or energy leakage effects discussed earlier. This quantity can be conveniently represented in dimensionless form as Δ_s/λ_f , where the beam displacement parameter Δ_s is given by either $2/\text{Im}(\xi_p)$ or by $-S'(k_r)$ of Eq. (16), and the ratio of Δ_s to the fluid wavelength has no explicit frequency dependence. Here, ξ_p is the complex leaky wave pole. As we indicated in the Introduction, the normalized beam displacement parameter increases without limit as Q_c , the value of Q at the mode cutoff, is approached. Beyond that point the mode ceases propagation for the case of the stiffened half-space. This behavior can be easily deduced from Fig. 9. In this figure, using the somewhat relaxed form $\Delta_s(\xi) = -S'(\xi)$ of Eq. (16), we calculate the normalized beam displacement parameter as a function of angles of incidence that are close to Rayleigh critical angles for four values of Q . As can be easily seen each curve displays a sharp maximum with a nearly symmetric decrease as one moves away from the Rayleigh angle. The widths of the curves tend to narrow, and their peaks increase in amplitude with increasing Q . This behavior is intuitively correct since we expect that far from the critical angles, specular geometrical reflection will be restored.

Since the wave-speed dispersion of the single Rayleigh mode for the stiffened half-space is determined by solving numerically a complicated transcendental equation, an exact general expression for the value of Q_c as a function of material parameters cannot easily be derived, as others have

noted.¹⁵ However, we can make an analytical estimate of Q_c from our previously reported⁷ approximate analysis of leaky waves in the presence of thin layers. Neglecting the influence of the fluid, we expand the characteristic equation in powers of ωd and substitute for the wave vector its approximate value at the cutoff, $\xi = k_{tt}$. Then retaining only the first-order terms and solving for Q_c , we obtain

$$Q_c^{-1} \approx \bar{\mu}_0 [1 - (c_{tt}/c_{tt})^2]^{1/2} [1 - (c_{tt}/c_{tt})^2] \quad (17)$$

If this result is specialized to the case of chromium on steel, we estimate $Q_c \approx 1.96$ compared to the value of 1.32 as predicted from the numerical investigation of the exact solution shown in Fig. 7. For chromium on brass the agreement is not quite as good.

Let us finally consider the distribution of the reflected acoustic amplitude along the direction of the propagating surface wave modes. With the fluid-solid interface in the x - y plane and an acoustic beam incident at θ_i in the x - z plane, we seek the reflected field parallel to the x axis at a fixed value of z , say $z = Z$. In previous work^{6,7} we have shown that the approximate analysis of the unlayered fluid-solid interface⁸ could be extended to include the layered half-space by solving a boundary-condition equation for the elastic behavior of the compound system. As long as the assumptions implicit in the derivation of the analytical expression for the reflected field are satisfied in the layer case, the extension is quite accurate, as we have shown experimentally for the zeroth-order mode of the loading layer.

In all cases where cutoffs occur, the energy distributions are qualitatively different from this well behaved mode, however. In their analysis of acoustic-beam reflection from a fluid-solid interface, Bertoni and Tamir⁶ evaluated an approximate form of the integral represented in Eq. (12) by contour integration. Since for their case a single nondispersive mode existed, they assumed that the only important contribution to this integral comes from a LR pole of order one at ξ_p . This assumption is certainly satisfied for the unlayered half-space as long as the integrand of Eq. (12) is small near other rapid variations in $R(\xi)$, like the one at k_{tt} . Practically, this will be the case if $k_r - k_{tt} > \pi/a_0$. For the loading layer this assumption is still accurate for the zeroth-order mode. For those modes which begin to appear or cease abruptly, however, this assumption is no longer valid as one approaches the mode cutoff. The rapid change in the reflection coefficient at the cutoff adds a contribution to the reflected field which is not accounted for in the approximate evaluation of Eq. (12). Examples of this progressive divergence of the approximate model from a numerical evaluation of Eq. (12) are given in Figs. 10 and 11 for acoustic beams incident at the respective Rayleigh angles. Here, we represent the extended analytical expression by a dashed curve and a 200-quadrant numerical integration using Simpson's rule by a solid curve for the case of chromium on steel. Below $Q = 1.0$ the two curves are nearly indistinguishable. At $Q = 1.0$ in Fig. 10, where $k_r - k_{tt} \sim \pi/a_0$, some small disparity is observed, particularly in the null zone. This difference increases as k_r approaches k_{tt} and becomes very pronounced in the vicinity of the cutoff, as shown in Fig. 11 at $Q = 1.76$. Increasing the number of integration quadrants

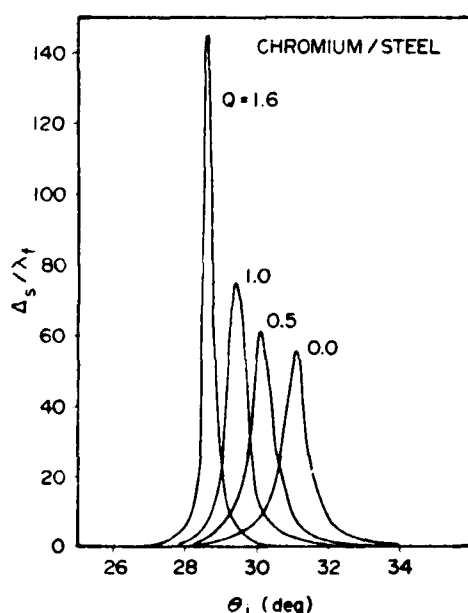


FIG. 9. Beam displacement parameter as a function of incident angle for a stiffened half-space.

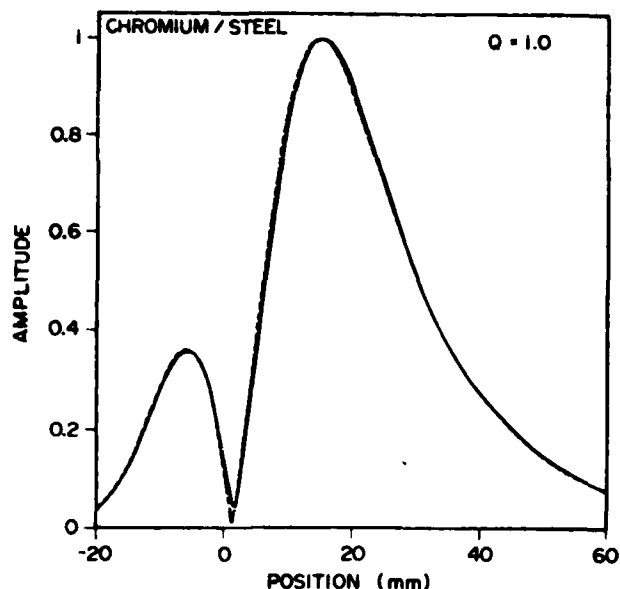


FIG. 10. Reflected beam amplitude distribution for a stiffened half-space. Solid curve is numerical evaluation of integral in Eq. (12); dashed curve is extended analytical model.

fourfold does not significantly affect the results. Above Q_c (≈ 1.82) no propagating solution for the layered half-space exists.

An example of the comparison between measurements of the reflected field from a stiffened substrate and the results of our model is shown in Fig. 12. The data are acquired by fixing the relative positions of transmitting transducer and sample, and stepping the receiver across the reflected beam with 1-mm resolution, as in Fig. 1. We employ specially designed Gaussian-profile transducers⁶ intended to approximate the beam profile assumed in the extended analytical

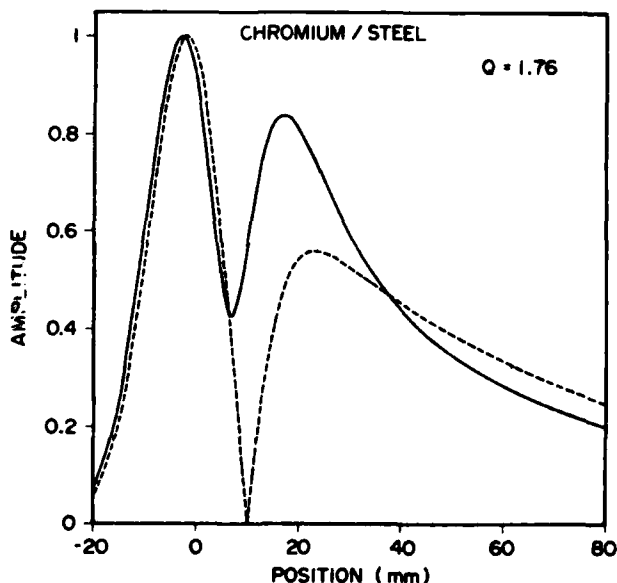


FIG. 11. Reflected beam amplitude distribution for a stiffened half-space. Solid curve is numerical evaluation of integral in Eq. (12); dashed curve is extended analytical model.

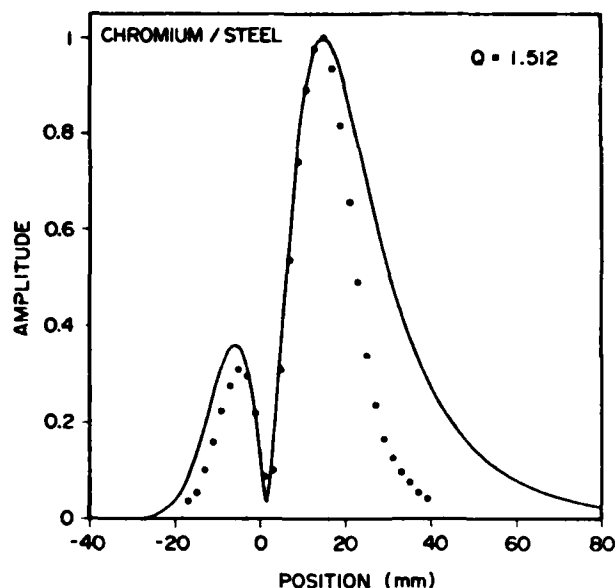


FIG. 12. Reflected beam amplitude distribution for a stiffened half-space. Solid curve is extended analytical model; discrete points are data.

model. Good agreement is evident in the relative amplitudes at the two peaks in the distribution as well as their positions. The shape of the theoretical curve follows the data reasonably well until the trailing-field portion above about 20 mm. The disparity here may be caused by diffraction or absorption losses unaccounted for in the model.

IV. CONCLUSIONS

In conclusion, we have presented calculations and measurements on the reflection of finite acoustic beams from fluid-solid interfaces either loaded or stiffened by layers in welded contact with the solid. In particular, we have concentrated on the discussions relating to the cutoff phenomena of propagating leaky surface modes. Numerical results and data have been reported on wave-speed dispersion for a stiffening layer of chromium on stainless steel and chromium on brass and the reflected-beam amplitude distribution for chromium on stainless steel. Generally, very good agreement is observed. Detailed calculations of the reflection coefficient $R(\theta)$ for stiffened and loaded half-spaces are given, and a straightforward method for deducing surface-wave propagation constants from R at arbitrary incident angles is discussed. The dispersion of the beam displacement parameter, related to the imaginary part of the surface-wave propagation constant, has been calculated as a function of reduced layer thickness using our model. All modes displaying cutoff behavior lead to unbounded beam displacement parameters at the respective wave cutoffs. We have compared results of an extended analytical model to numerical integration of the reflected beam distribution and have found increasing disparity as the wave cutoff is approached.

ACKNOWLEDGMENTS

It is a pleasure to acknowledge the competent technical assistance of K. D. Shimmin and R. H. Latiff. We wish to

thank T. J. Moran for a critical reading of the manuscript. Research of A.H.N. is supported by NSF Grant CME 8021054 and AF Contract F33615-80-C-5015.

- ¹M. A. Breazeale, L. Adler, and G. W. Scott, *J. Appl. Phys.* **48**, 530-537 (1977).
- ²T. D. K. Ngoc and W. G. Mayer, *J. Acoust. Soc. Am.* **67**, 1149-1152 (1980); *J. Appl. Phys.* **50**, 7948-7951 (1979).
- ³J. M. Claeys and O. Leroy, *J. Acoust. Soc. Am.* **75**, 585-590 (1982).
- ⁴M. deBilly, L. Adler, and G. Quentin, *J. Acoust. Soc. Am.* **72**, 1918-1020 (1980).
- ⁵M. Hattunen and M. Luukkala, *Appl. Phys.* **2**, 257-263 (1973).
- ⁶D. E. Chimenti, A. H. Nayfeh, and D. L. Butler, *J. Appl. Phys.* **53**, 170-176 (1982).
- ⁷A. H. Nayfeh, D. E. Chimenti, L. Adler, and R. L. Crane, *J. Appl. Phys.* **52**, 4985-4994 (1981).
- ⁸M. L. Bortoni and T. Tamir, *Appl. Phys.* **2**, 157-172 (1973).
- ⁹G. W. Farnell and E. L. Adler, in *Physical Acoustics*, edited by W. P. Mason and R. N. Thurston (Academic, New York, 1972), Vol. IX, pp. 35-128.
- ¹⁰J. D. Achenbach and S. P. Keshava, *J. Appl. Mech.* **34**, 397-405 (1967).
- ¹¹M. Luukkala and M. Hattunen, *Appl. Phys. Lett.* **19**, 56-57 (1971).
- ¹²Similar asymptotic values are discussed and reported in the literature, see for example discussions on p. 107 of *Waves in Layered Media* by Brekhouskikh regarding the displacement of total reflected beams.
- ¹³D. E. Chimenti and A. H. Nayfeh, in *Ultrasonics Symposium Proceedings*, edited by B. R. McAvooy (IEEE, New Jersey, 1981), pp. 291-294.
- ¹⁴Wave speeds and densities used in the computations are (stainless steel) $c_a = 5.69$, $c_u = 3.1$ km/s, $\rho_s = 7.9$ g/cm³; (brass) $c_a = 4.37$, $c_u = 2.1$, $\rho_s = 8.5$; (copper) $c_{10} = 4.76$, $c_{10} = 2.3$, $\rho_0 = 8.9$; (chromium) $c_{10} = 6.6$, $c_{10} = 4.0$, $\rho_0 = 7.2$; $c_f = 1.48$, $\rho_f = 1.0$.
- ¹⁵Reference 9, pp. 86-88.

APPENDIX B

PUBLICATION ON TRANSVERSE STRESS IN RAYLEIGH SURFACE WAVES

Transverse stresses in plane and cylindrical Rayleigh waves

D. A. Lee,^{a)} R. L. Crane,^{b)} and D. A. Stubbs^{c)}
Wright-Patterson Air Force Base, Ohio 45433

(Received 26 July 1983; accepted for publication 3 October 1983)

Plane and cylindrical Rayleigh waves are shown to involve tractions perpendicular to the propagation direction, on planes perpendicular to both the free surface and direction of propagation. Experiments show that backscatter from interruptions of these transverse tractions is sufficiently efficient to allow the observation of planar cracks the planes of which are perpendicular to the free surface and contain the propagation direction.

PACS numbers: 43.20.Bi, 43.35.Pt

INTRODUCTION

The most frequently occurring flaws in highly loaded structures are surface-connected fatigue cracks. Surface wave ultrasonic techniques are often used to locate and size these flaws. In such cases, the interrogating transducer is positioned such that surface waves are propagated normal, or at least obliquely, to the plane of the crack. Indeed, most discussions to date concentrated on this particular inspection geometry.¹ Sometimes, as in the case of a fatigue crack originating on the surface of a highly loaded bolt hole, the flaw lies in a plane containing the direction of propagation (see Fig. 1). Conventional wisdom would dictate that such a flaw would be undetectable with conventional Rayleigh wave inspection methods. However, as this paper will show, both classical Rayleigh waves and cylindrical Rayleigh waves, that is, axisymmetric waves guided along the surface of a circular cylindrical hole,² involve nonzero tractions on the free surface perpendicular to the propagation direction, which in principle will be scattered not only by flaws lying in planes oblique to the propagation direction, but also by flaws lying in planes containing the propagation direction.

We present straightforward theoretical developments to show that the transverse tractions result from nonzero Poisson stresses in the plane case, and from a combination of geometric effects and the Poisson stresses in the cylindrical case. We present experimental results which show that backscattering of plane Rayleigh waves by interruption of transverse tractions is a sufficiently efficient process to be observed.

1. PLANE RAYLEIGH WAVES

We briefly recapitulate the well-known basic theory of this case for the sake of completeness and to establish notation. Such textbook discussions as Achenbach's,³ and Lord Rayleigh's original paper,² are excellent sources of more details.

Rayleigh waves² may be viewed as being composed of an appropriate combination of special irrotational and solenoidal elastodynamic waves. Specifically,

$$\mathbf{u} = \nabla\phi(y,z,t) + \nabla \times [\psi(y,z,t)\mathbf{e}_x], \quad (1)$$

where

^{a)} US Air Force Institute of Technology.

^{b)} Air Force Wright Aeronautical Laboratories (AFWAL/MLLP).

^{c)} Systems Research Laboratories

$$\phi = \alpha \exp(ikz - kAy - i\omega t), \quad (2)$$

$$\psi = \beta \exp(ikz - kBy - i\omega t). \quad (3)$$

The irrotational displacement field $\nabla\phi$ will satisfy the Navier-Cauchy equation

$$a^2 \nabla(\nabla \cdot \mathbf{u}) - b^2 \nabla \times \nabla \times \mathbf{u} = \frac{\partial^2 \mathbf{u}}{\partial t^2}, \quad (4)$$

where a and b denote, respectively, the material's dilation wave speed and shear wave speed, provided

$$A = (1 - c^2/a^2)^{1/2}. \quad (5)$$

The solenoidal displacement field $\nabla \times \psi \mathbf{e}_x$ will satisfy (4) if

$$B = (1 - c^2/b^2)^{1/2}, \quad (6)$$

where the wave's propagation speed c is related to frequency ω and wavenumber k by

$$c \equiv \omega/k. \quad (7)$$

The condition of vanishing tractions on the free surface $y = 0$ leads to two homogeneous algebraic equations in α and β . The vanishing of the determinant of this system leads to

$$(2 - c^2/b^2)^2 - 4AB = 0, \quad (8)$$

which determines the Rayleigh wave speed c as a function of material properties a and b . Since the wave speed determined by (8) is independent of frequency, Rayleigh waves are not dispersive.

The only nonvanishing transverse tractions for these plane Rayleigh waves will be

$$\sigma_{xx} = \lambda u_{,11} + 2\mu(u_{,xx}) \quad (9)$$

$$= -\lambda k_a^2 \phi, \quad (10)$$

since $u_x = 0$, and $u_{,11} = \nabla^2 \phi = -k_a^2 \phi$. Thus

$$\begin{aligned} \sigma_{xx} &= [-\lambda \omega^2 \rho / (\lambda + 2\mu)] \alpha \exp(ikz - kAy - i\omega t) \\ &= [\nu / (1 - \nu)] \rho \omega^2 \alpha \exp(ikz - kAy - i\omega t), \end{aligned} \quad (11)$$

where ρ is the density of the medium. Equation (11) shows that the transverse tractions do not vanish, unless Poisson's ratio ν , or the parameter α is zero.

The parameter α does not vanish for propagating Rayleigh waves. The ratio of the Rayleigh wave parameters α and β is a function of Poisson's ratio; for $\nu = 0.25$, a value close to that found in many materials, $|\alpha/\beta| = 0.68$. Thus classical Rayleigh waves in typical materials involve transverse tractions.

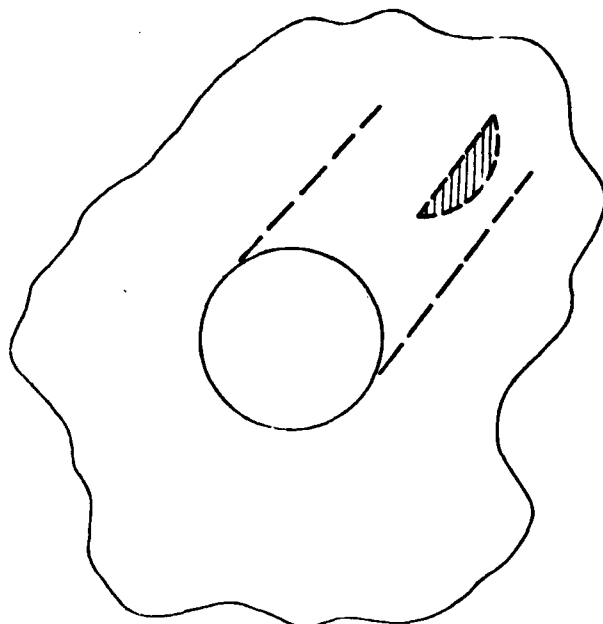


FIG. 1. A schematic representation of a crack extending radially from the internal surface of a hole in a solid half-space.

II. CYLINDRICAL RAYLEIGH WAVES

M. A. Biot described axisymmetric waves guided along the surface of a circular cylindrical hole.⁴ Since these cylindrical Rayleigh waves are not as widely discussed as the plane ones, we present the following detailed treatment.

In general coordinates, an irrotational wave's displacement field can be written

$$u^i = g^{ik} \phi_{,k} \quad (12)$$

while a solenoidal wave's displacement field can be expressed in the form

$$u^i = (1/\sqrt{g}) \epsilon^{ijk} A_{k,j} \quad (13)$$

where the once-covariant tensor A_k is a function of position and time, as is the scalar ϕ .

In (12) and (13), g^{ij} denotes the contravariant metric tensor elements of the coordinate system. A comma preceding an index denotes covariant differentiation, e.g.,

$$A_{k,j} \equiv \frac{\partial A_k}{\partial x^j} - \left\{ \begin{matrix} m \\ kj \end{matrix} \right\} A_m.$$

The permutation tensor elements ϵ^{ijk} may be defined as

$$\epsilon^{ijk} \equiv \begin{cases} \text{sgn}(\pi) & \text{if } (i,j,k) \text{ is permutation } \pi \text{ of } (1,2,3) \\ 0, & \text{otherwise} \end{cases} = \epsilon_{ijk}.$$

These elements are special in that they transform both as three-times contravariant relative tensor elements of weight +1 and as three-times covariant relative tensor elements of weight -1.

The Navier-Cauchy equation⁵ may be written in general coordinates as

$$a^2 u^i_{,km} g^{mi} - b^2 \epsilon^{ijk} \epsilon_{k,lm} u^m_{,p} g^{pr} = \frac{\partial^2 u^i}{\partial t^2} \quad (14)$$

Seeking an irrotational solution of (14), one finds that

$$u^m_{,p} g^{pk} = g^{mr} \phi_{,r} g^{rk}$$

is symmetric in m and k , so that the second term of the left side of (14) is identically zero. The remaining terms of (14) require

$$\left(a^2 g^{ij} \phi_{,n} - \frac{\partial^2 \phi}{\partial t^2} \right)_{,i} g^{jk} = 0,$$

which will be met if

$$a^2 g^{mj} \phi_{,mj} = \frac{\partial^2 \phi}{\partial t^2} \quad (15)$$

One may take (15) as the defining equation for irrotational waves.

Turning to solenoidal waves with displacement fields of the form (13), one sees that

$$u^m_{,m} = (1/\sqrt{g}) \epsilon^{mjk} A_{k,jm} \equiv 0,$$

by the symmetry of $A_{k,jm}$ with respect to j and m , so that now the first term on the left side of (14) is identically zero. The remaining terms lead, after some manipulation, to

$$\epsilon^{ijk} \left[-b^2 \epsilon_{knm} \epsilon^{mrn} g^{pn} A_{s,rp} - \frac{\partial^2 A_k}{\partial t^2} \right]_{,j} = 0, \quad (16)$$

for which it is sufficient that the quantity in square brackets is identically zero. But that condition leads, after use of the identity

$$\epsilon_{knm} \epsilon^{mrn} \equiv \delta_k^n \delta_m^r - \delta_k^r \delta_m^n,$$

to

$$b^2 (g^{pr} A_{k,rp} - g^{rp} A_{s,pk}) = \frac{\partial^2 A_k}{\partial t^2}.$$

But the defining tensor A_k of the solenoidal waves is itself solenoidal, so that

$$g^{rp} A_{s,p} \equiv 0. \quad (17)$$

Then the defining equations for a solenoidal wave may be written as (17) together with

$$b^2 g^{rp} A_{k,rp} = \frac{\partial^2 A_k}{\partial t^2}. \quad (18)$$

While the forms of tensor equations (15) and (18) are succinct and easy to remember, these forms are not usually the most convenient ones to use when writing out the detailed statements which those equations imply in a given coordinate system. Direct evaluation of (18), for example, usually requires evaluation of Christoffel symbols and their derivatives.

Explicit "unfolding" of (15) for a specific coordinate system is made easier by the well-known identity³

$$g^{rm} \phi_{,rm} \equiv \frac{1}{\sqrt{g}} \frac{\partial}{\partial x^n} \left(\sqrt{g} \frac{\partial \phi}{\partial x^n} \right), \quad (19)$$

by virtue of which (15) is equivalent to

$$\frac{a^2}{\sqrt{g}} \frac{\partial}{\partial x^n} \left(\sqrt{g} \frac{\partial \phi}{\partial x^n} \right) = \frac{\partial^2 \phi}{\partial t^2}. \quad (20)$$

Explicit delineation of (18) is simplified in most cases by the following considerations: the elements T^i , defined by

$$T^i \equiv (1/\sqrt{g})\epsilon^{ijk}A_{k,j}$$

are once-contravariant (oriented) tensor coordinates. Also, they may be evaluated explicitly without evaluating Christoffel symbols, since

$$\epsilon^{ijk}A_{k,j} = \epsilon^{ijk}\frac{\partial A_k}{\partial x^j} = \epsilon^{ijk}\left\{\begin{matrix} n \\ jk \end{matrix}\right\}A_n, \quad (21)$$

and the last term in (21) is identically zero by virtue of the symmetry of the Christoffel symbol in its lower indices j and k , and the antisymmetry of ϵ^{ijk} in those indices. Thus the S_i ,

$$S_i \equiv g_{ir}T^r = \frac{g_{ir}}{\sqrt{g}}\epsilon^{rjk}\frac{\partial A_k}{\partial x^j}$$

are once-covariant, oriented tensor coordinates. Repeating the previous arguments of this paragraph then shows that the R_i ,

$$R_i \equiv (g_{im}/\sqrt{g})\epsilon^{mnp}S_{p,n} = \frac{g_{im}}{\sqrt{g}}\epsilon^{mnp}\frac{\partial S_p}{\partial x^n} = \frac{g_{im}}{\sqrt{g}}\epsilon^{mnp}\frac{\partial}{\partial x^n}\left(\frac{g_{pr}}{\sqrt{g}}\epsilon^{rjk}\frac{\partial A_k}{\partial x^j}\right),$$

are once-covariant tensor coordinates, which can be written out without evaluating Christoffel symbols. In rectangular Cartesian coordinates,

$$R_k = \epsilon_{knp}\epsilon_{pjr}\frac{\partial^2 A_r}{\partial x^j \partial x^n}.$$

Now, the quantity

$$V_k \equiv \epsilon_{knm}\epsilon^{mrs}A_{s,rs}$$

appearing in (16) is also a set of once-covariant tensor coordinates. In rectangular Cartesian coordinates,

$$V_k = \epsilon_{knm}\epsilon_{mrs}\frac{\partial^2 A_s}{\partial x^r \partial x^n} \equiv R_k.$$

But then $R_k \equiv V_k$, since coordinates of a given tensor character which are equal in one coordinate system are equal in all coordinate systems. Thus a set of equations equivalent to (17) and (18) is (17) and

$$-b\frac{g_{im}}{\sqrt{g}}\epsilon^{mnp}\frac{\partial}{\partial x^n}\left(\frac{g_{pr}}{\sqrt{g}}\epsilon^{rjk}\frac{\partial A_k}{\partial x^j}\right) = \frac{\partial^2 A_i}{\partial t^2}. \quad (22)$$

Equation (22) is more convenient for expansion than Eq. (15), since no Christoffel symbols appear in (22). Moreover, the operations on the left side of (22) can all be accomplished by fairly straightforward matrix multiplications and differentiations.

We apply the preceding material of this section to describe axisymmetric waves guided along a circular cylindrical hole, setting

$$\phi(r, \theta, z, t) \equiv \alpha f(r) \exp(ikz - i\omega t), \quad (23)$$

$$A_\theta \equiv \beta rg(r) \exp(ikz - i\omega t), \quad (24)$$

$$A_r \equiv 0 \equiv A_z,$$

in cylindrical coordinates (r, θ, z) . The vector field A_k defined by (24) is solenoidal. On writing out (15) and simplifying, one finds

$$f'' + (1/r)f' - k^2 A^2 f = 0. \quad (25)$$

Similarly, (22) leads to

$$g'' + (1/r)g' - (k^2 B^2 + 1/r^2)g = 0. \quad (26)$$

Imposing the condition that the fields vanish as $r \rightarrow \infty$ leads to homologs of (2) and (3) as

$$\phi = \alpha K_0(kAr) \exp(ikz - i\omega t), \quad (27)$$

$$A_\theta = \beta r K_1(kBr) \exp(ikz - i\omega t), \quad (28)$$

$$A_r \equiv 0 \equiv A_z.$$

The requirement that tractions vanish on the free surface of the cylindrical hole, $r = R$, leads to two homogeneous linear algebraic equations in α and β , and eventually, to the dispersion relation

$$\left| \begin{array}{cc} \frac{2b^2 - c^2}{b^2} K_0(kAR) + \frac{2A}{KR} K_1(kAR) & 2B \left(K_0(kBR) + \frac{K_1(kBR)}{kBR} \right) \\ 2AK_1(kAR) & (2 - c^2/b^2) K_1(kBR) \end{array} \right| = 0, \quad (29)$$

which is equivalent to Eq. (7.16) of Ref. 1.

The only nonvanishing transverse traction for these waves is σ_2^z ;

$$\begin{aligned} \sigma_2^z &= \lambda u_{,1}^z + 2\mu u_{,2}^z \\ &= [-\alpha \lambda k^2 K_0(kAR) - (2\alpha\mu/r)kAK_1(kAR) \\ &\quad - (2ik\beta\mu/r)K_1(kBR)] \exp(ikz - i\omega t). \end{aligned} \quad (30)$$

Inspection of (30) shows, first, that in the cylindrical case as in the plane case, transverse tractions are present, and, second, that here geometric effects—the terms with the factor

μ/r —contribute to the transverse tractions, in addition to the Poisson-ratio effects of the term with the factor $\alpha\lambda$. In the limit of large ratios of R to wavelength ($kR \rightarrow \infty$), the geometric terms vanish, but the Poisson-ratio term tends in effect to the term obtained in Sec. I for the plane case. It is in this sense that the remark of Ref. 3, "...an axial symmetric deformation gives rise to circumferential stresses which do not exist in the two-dimensional case" should be interpreted.

III. EXPERIMENT

The predictions of the above analysis were verified by observing the reflection of a Rayleigh wave from a surface-connected crack. For these experiments glass was chosen

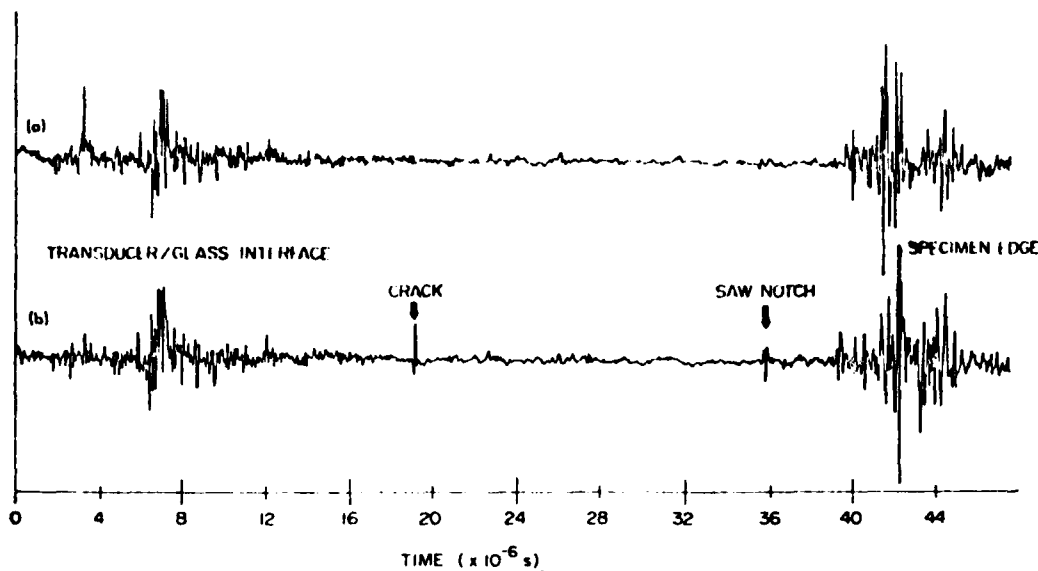


FIG. 2. Oscilloscope time records showing, in the trace (a), the surface wave reflections from a pristine glass plate. The echoes between 0 and 12 μ s are from the transducer/glass interface. The echoes between 36 and 48 μ s are from the end of the plate. Trace (b) shows the echoes from the plate with a crack that was started from the saw notch.

as the solid media since it eliminated any concern about grain scattering which is common to metal specimens. Also, in the absence of grain boundaries long, straight cracks could be produced in the glass by localized rapid heating of the specimen. In fact, the flaws produced by this method were so smooth and straight that water, which acted as a stress corrosion agent, had to be added to the tip of each crack to prevent its subsequent closure and healing. All cracks produced in this manner were perpendicular to the surface of the glass plates. A standard 10-MHz ultrasonic surface-wave transducer was used both to send and receive the interrogating pulses. For Rayleigh waves launched perpendicular to the plane of the crack the familiar large return echo was observed at the appropriate time. For the case of a Rayleigh wave propagating parallel to the plane of the flaw a smaller yet clearly distinguishable echo was observed as shown in Fig. 2. For comparison, a trace is shown from a plate that did not contain a crack. What is particularly impressive about these data is that they were obtained without the use of significant signal enhancement.

In order to ensure that the reflection of the Rayleigh wave was caused by the presence of the crack and not the stress field ahead of it, the following experiment was performed. A piece of electrical tape was placed just over the tip of the crack and a knife edge forced into the edge of the

tape to ensure intimate contact. The surface wave transducer was then placed to launch waves both parallel and perpendicular to the plane of crack. A wedge was driven into the mouth of the crack to increase the stress field at the crack tip. The intensity of this stress field was confirmed photoelastically. At no stress level prior to fracture was a reflection from the crack tip observed for either surface wave propagation direction. Even after 64 averages no reflection from the vicinity of the crack tip could be discerned. When the tape and knife edge was removed, the crack reflection was immediately apparent. We therefore concluded that the observed reflection was indeed due to the presence of the free surface of the crack.

¹*Metals Handbook, Vol. 11—Nondestructive Inspection and Quality Control* (American Society for Metals, Metals Park, OH, 1976).

²Lord Rayleigh, *The Theory of Sound* (Dover, New York, 1945).

³J. O. Achenbach, *Wave Propagation in Elastic Solids* (Elsevier, New York, 1973), Sec. 3.4, p. 85 ff.

⁴M. A. Biot, *J. Appl. Phys.* **23**, 998–1000 (1952).

⁵I. S. Sokolnikoff, *Tensor Analysis* (Wiley, New York, 1964), p. 89.

APPENDIX C

PUBLICATIONS ON ACOUSTIC REFLECTION FROM COMPOSITE MATERIAL

LEAKY LAMB WAVES IN FIBER-REINFORCED COMPOSITE PLATES

Y. Bar-Cohen*

Systems Research Laboratories
Dayton, OH 45440

D. E. Chimenti

Air Force Wright Aeronautical Laboratories
Wright Patterson Air Force Base, OH 45433

INTRODUCTION

Leaky ultrasonic waves are characterized by the continuous conversion of ultrasonic energy at an interface from one mode (usually a surface wave) into a bulk wave. For a fluid-solid interface the surface wave mode can be any surface-connected elastic wave having a significant particle displacement normal to the interface. Then, if the bulk fluid wavespeed is less than the surface wavespeed, ultrasonic energy will leak into the fluid at an angle determined by $\arcsin(v_f/v_s)$. Likewise, surface waves can be generated by the inverse phenomenon. A brief review of recent work on leaky Rayleigh waves has been given by Nayfeh, et al.¹ Leaky Lamb waves in isotropic materials have been investigated both theoretically²⁻⁴ and experimentally.⁵

In the present work we report observations of leaky Lamb wave behavior in fiber-reinforced, plastic laminates. As might be expected by analogy to isotropic materials, the phase velocity of the Lamb modes which we studied is found to depend on frequency and plate thickness. Moreover, a dependence on relative orientation between the fibers and the plane of incidence of the sound wave has been established empirically.

*Present address: Douglas Aircraft Company, Dept. C1-E29
3855 Lakewood Blvd., Long Beach, CA 90846

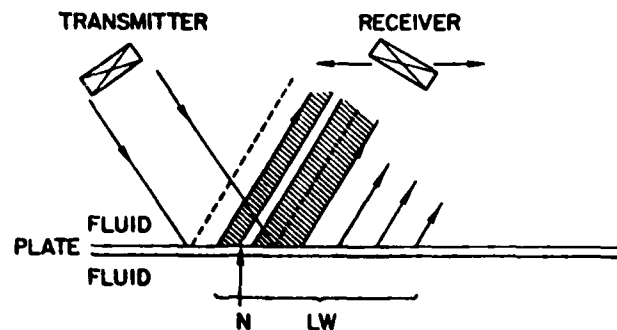


Fig. 1. Schematic of leaky Lamb wave experiment. LW indicates leaky wave, while N refers to null zone between components of reflected field. A similar radiation pattern, not shown, exists below the plate.

EXPERIMENTAL PROCEDURE

The ultrasonic system employed in these measurements is of conventional design, except for the mechanical positioning system which permits very accurate angulation (± 0.05 degree) of the transmitting and receiving transducers. The transmitter is excited with long tone bursts, and the received signal is monitored with the fixed gate of a boxcar integrator as the receiver scans across the reflected beam. Further experimental details can be found elsewhere.⁶

RESULTS AND DISCUSSION

In this section we present the results of measurements performed in the following way. Both transmitting and receiving transducers are adjusted to the same angle with respect to the sample normal. The specimen and transmitter are held in a fixed position, while the receiver scans stepwise across the reflected field, parallel to the sample surface, as seen in Figure 1. We then display the receiver amplitude as a function of receiver position. Since we employ piston radiators, we have obtained a reference field

indicating the beam distribution and relative amplitude of sidelobes by reflecting the sound beam from a tungsten foil (0.2mm) placed directly over the sample. Subsequently, data are collected at several frequencies demonstrating the generation of leaky Lamb waves. An example of these data is shown in Figure 2.

The reflected beam profile of the reference beam is indicated with a solid line which peaks near $x = 24\text{mm}$. Then, the solid curve at 2.0 MHz demonstrates the displacement and distortion in the reflected field characteristic of leaky waves, which were also observed by others both for Lamb and Rayleigh waves^{5,6} in isotropic materials. At frequencies well removed from the condition for Lamb wave generation, the reflected beam from the composite sample shows much the same profile as the reference reflection. Another example of this behavior is shown in Figure 3 where a similar series of curves have been obtained for a cross-ply, glass-epoxy composite $([0,90]_{25})$ plate with a thickness of 2mm. In this case the plane of incidence contains the 0° fiber direction. Leaky waves are generated at 2.92 MHz, while the profiles recorded at 200 kHz above and below the resonant frequency do not show the same strong distortion and displacement of the reflected beam.

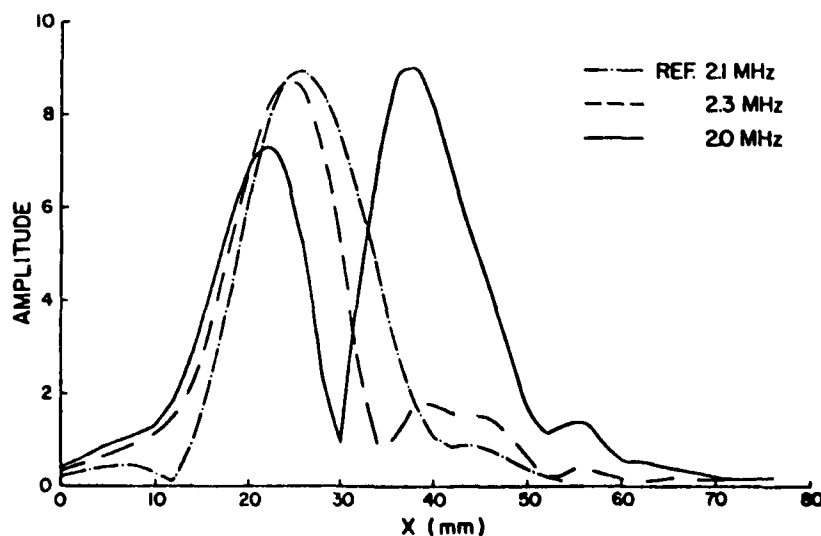


Fig. 2. Reflected beam profiles for a unidirectional glass-epoxy composite plate 1mm thick showing a leaky Lamb wave at 2.0 MHz. Reference reflection from tungsten foil indicates approximate incident beam profile.

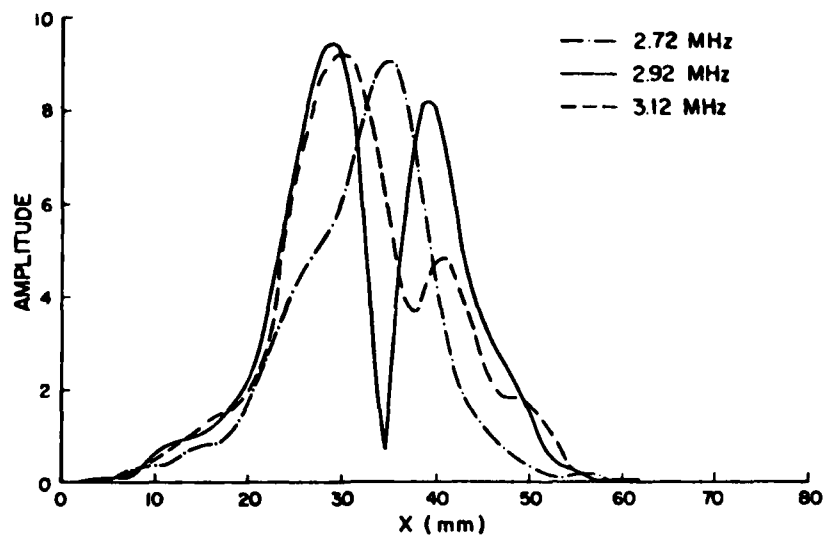


Fig. 3. Reflected beam profiles for cross-ply composite plate 2mm thick. Leaky Lamb wave generated at 2.92 MHz.

Continuing with this method of examining Lamb modes in the composite, we have constructed an experimental dispersion curve for the two lowest order symmetric modes. These data are collected in Figure 4. We tentatively identify the left-hand curve as the S_0 mode and the right-hand curve as the S_1 mode by analogy to these modes in isotropic plates. For incident angles less than 15 degrees no leaky Lamb wave could be observed, while for incidence greater than 24 degrees, no characteristic bimodal reflected beam profile could be generated at any frequency. As an additional empirical investigation we studied the effect of fiber misalignment with respect to the plane of incidence. As the unidirectional sample was rotated so that its fibers were a few degrees out of the plane of incidence, the incident angle corresponding to Lamb wave generation rose slightly, indicating a lower effective plate wavespeed.

To provide partial confirmation of these results, leaky Lamb waves in composites have been observed using pulsed Schlieren visualization. For an angle of incidence of 16.5 degrees and a frequency of 2 MHz in the cross-ply specimen, the incident and reflected fields are shown in Figure 5. Since the stroboscopic light source has a very short duration, the 180-degree phase difference between specular and leaky wave components of the reflected field can easily be seen. The trailing field of the leaky wave component can be observed decaying to the right. The

dark region dividing the two components of the reflected field is a null zone produced by phase cancellation.

CONCLUSIONS

Leaky Lamb wave behavior has been observed in unidirectional and cross-ply composite laminate plates and confirmed in pulsed Schlieren visualization. Two distinct modes are observed, and their dispersion has been determined experimentally over a limited range of frequency times plate thickness, as well as incident angle.

ACKNOWLEDGEMENTS

This work partially supported by AF Contract F33615-80-C-5015. The authors wish to acknowledge the programming support of K.D. Shimmin, W.C. Hoppe, and D.A. Stubbs.

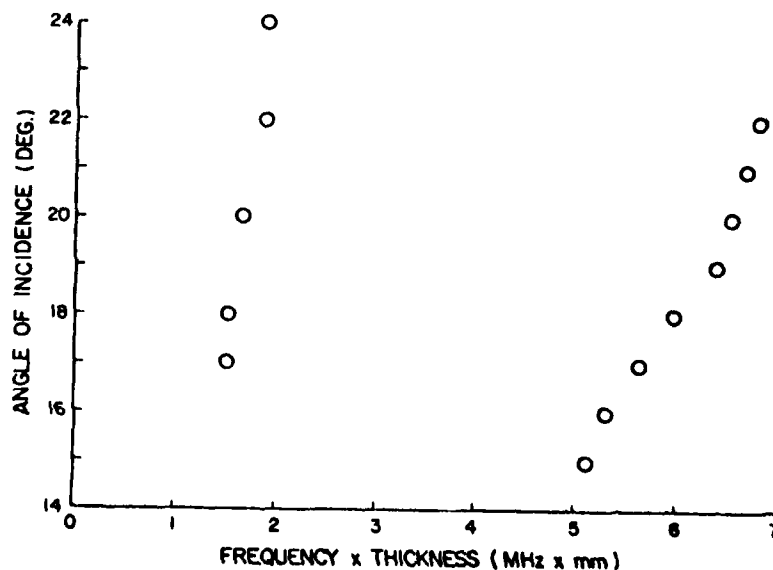


Fig. 4. Dispersion curve for cross-ply composite plate demonstrating zeroeth and first order symmetric Lamb modes.

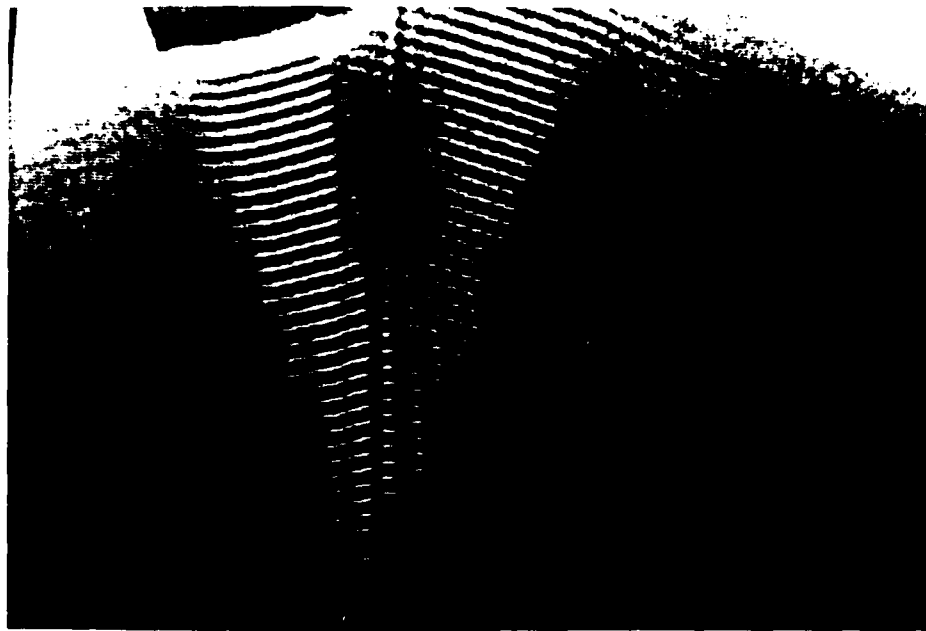


Fig. 5. Schlieren photograph of acoustic field distribution showing leaky Lamb waves on unidirectional composite plate. Angle of incidence is 16.5 degrees, and frequency of tone burst is 2. MHz.

REFERENCES

1. A. H. Nayfeh, D. E. Chimenti, L. Adler, and R. L. Crane, Ultrasonic leaky waves in the presence of a thin layer, J. Appl. Phys. 52:4985 (1981).
2. A. D. Stuart, Acoustic radiation from submerged plates. I. Influence of leaky wave poles, J. Acoust. Soc. Am. 59:1160 (1976).
3. T. D. K. Ngoc and W. G. Mayer, Influence of plate mode structure and Gaussian beam profile characteristics on ultrasonic reflection and transmission, IEEE Trans. Sonics Ultrason. SU-29:112 (1982).
4. D. K. Ngoc and W. G. Mayer, A general description of ultrasonic nonspecular reflection and transmission effects for layered media, IEEE Trans. Sonics Ultrason. SU-27:229 (1980).

5. T. J. Plona, L. E. Pitts and W. G. Mayer, Ultrasonic bounded beam reflection and transmission effects at a liquid/solid-plate/liquid interface, J. Acoust. Soc. Amer. 59:1324 (1976).
6. D. E. Chimenti, A. H. Nayfeh, and D. L. Butler, Leaky Rayleigh waves on a layered halfspace, J. Appl. Phys. 53:170 (1982).

Reflection of acoustic waves from water/composite interfaces

Adnan H. Nayfeh

Department of Aerospace Engineering and Applied Mechanics, University of Cincinnati, Cincinnati, Ohio 45221

Robert L. Crane

Air Force Wright Aeronautical Laboratories, Wright-Patterson AFB, Ohio 45433

Wally C. Hoppe

Systems Research Laboratories, Inc., Dayton, Ohio, 45440

(Received 13 April 1983; accepted for publication 31 August 1983)

Theoretical and experimental results are presented for the reflection of acoustic waves from liquid-fibrous composite interfaces. For this purpose the composite is oriented such that the fibers are parallel to the propagation directions. Because of the complex microstructure of composites, continuity conditions exist on both the macro (water/composite interface) and micro (fiber/matrix interface) scales. Due to the number and nature of these conditions exact solutions are exceedingly difficult, if not impossible to obtain. As an alternative we formulate an approximate analysis in which the composite medium is replaced by a homogeneous, yet dispersive medium. In the process of replacing the composite with such a material model, the micro continuity conditions are utilized. The validity of the analytical model is verified by comparisons with experimental results obtained from graphite/epoxy and boron/epoxy composites specimens. Results are found to correlate very well with the analytical model, especially at low frequency ranges.

PACS numbers: 43.20.Fn, 68.25. + j, 81.70. + r

I. INTRODUCTION

The high specific strength and stiffness of composite materials has lead to their wide spread use in efficient structures. Since most of these structures are subjected to cyclic loads which can lead to rapid degradation in load carrying capability, initial inspection and continued monitoring of these materials for detection and sizing of strength degrading flaws is necessary in order to ensure adequate structural reliability. Unfortunately, many of the current inspection techniques can not be directly utilized for this purpose because of the inhomogeneous, anisotropic nature of composites. In addition, the kinds, types, and numbers of internal flaws that must be detected and quantified for structural integrity models differ substantially from those traditionally encountered. Currently the most useful technique for inspecting composite structures is ultrasonic *c*-scanning which was developed to inspect homogeneous, isotropic materials, i.e., metals. Before this technique can be fully exploited for inspecting composites, a firm understanding of the interaction between ultrasonic waves and the material is necessary. This paper examines one aspect of this problem, namely, the reflection of ultrasonic waves from composite materials.

II. THEORETICAL DEVELOPMENT

Consider the case of an acoustic wave normally incident onto a water/composite interface as shown in Fig. 1. For our purposes we have oriented the composite such that the fibers are parallel to the propagation direction and assumed that the composite consists of a hexagonal array of fibers embedded in a compliant matrix. We wish to calculate the amount of acoustic energy reflected at the fluid/composite interface. We know that in the case of homogeneous materials the reflection coefficient is independent of frequency, while in the

case of composites, the reflection coefficient is a function of frequency due to their dispersive nature. In order to investigate this phenomenon, we must first solve the field equations in both the fluid and the composite and then satisfy the appropriate interfacial continuity relations at the interface between the media. Because of the complex microstructure of composites, continuity conditions exist on both the macro and micro scales. On the macro scale the continuity conditions across the fluid-composite interface must be satisfied, while on the micro scale appropriate conditions along the fiber and matrix interface must be fulfilled. Due to the number and nature of these conditions exact solutions would be exceedingly difficult, if not impossible to obtain. As an alternative we shall formulate an approximate analysis in which the composite medium is replaced by a homogeneous, yet dispersive medium. In the process of replacing the composite with such a material model, the micro continuity conditions

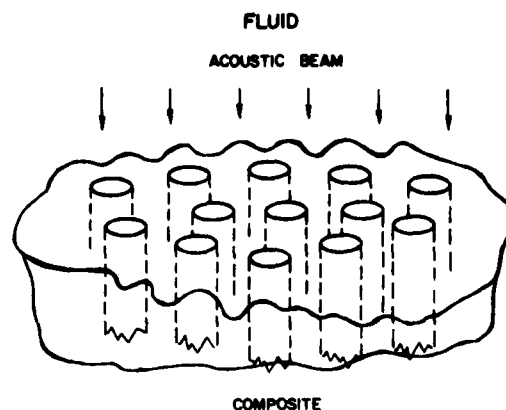


FIG. 1. Model.

(i.e., along fiber-matrix interfaces) will be utilized. Recently, a variety of approaches have been used to describe both the static and dynamic behavior of composites in the absence of the fluid.¹⁻⁶ In particular, we shall follow the lines of our recent static analysis concerning thermomechanically induced interfacial stresses in fibrous composites⁴ in order to derive an equivalent dynamic model for the homogenized composite.

A. Continuum modeling of the composite

Due to the symmetry inherent in the composite microstructure and the alignment of the direction of propagation with the fibers we begin by approximating the composite as a hexagonal array of concentric cylinders with perfect interface bonds which are subject to vanishing shear stresses and radial displacements on their outer boundaries as illustrated in Fig. 2. For this approximation, the relevant field equations are

$$\frac{\partial \sigma_x}{\partial x} + \frac{1}{r} \frac{\partial}{\partial r} (r \sigma_{xr}) = \rho \ddot{u}, \quad (1)$$

$$\frac{\partial \sigma_r}{\partial r} + \frac{\partial \sigma_{xr}}{\partial x} + \frac{1}{r} (\sigma_r - \sigma_\theta) = 0, \quad (2)$$

$$\sigma_x = (\lambda + 2\mu) \frac{\partial u}{\partial x} + \frac{\lambda}{r} \frac{\partial}{\partial r} (rv), \quad (3)$$

$$\sigma_r = (\lambda + 2\mu) \frac{\partial v}{\partial r} + \frac{\lambda v}{r} + \lambda \frac{\partial u}{\partial x}, \quad (4)$$

$$\sigma_{xr} = \mu \left(\frac{\partial v}{\partial x} + \frac{\partial u}{\partial r} \right). \quad (5)$$

which hold for both the fiber and matrix components. In our subsequent analysis we shall refer to the fibers as material 1 and to the matrix as material 2.

In addition to Eqs. (1)–(5) the following symmetry and continuity relations hold

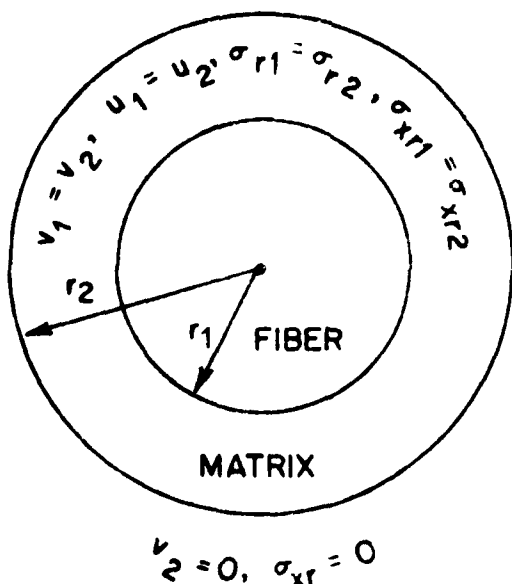


FIG. 2. Representative repeating cell of the composite.

$$v_1(x, 0) = 0, \quad \sigma_{xr1}(x, 0) = 0, \quad (6)$$

$$v_2(x, r_2) = 0, \quad \sigma_{xr2}(x, r_2) = 0, \quad (7)$$

$$v_1 = v_2, \quad u_1 = u_2, \quad \sigma_{xr1} = \sigma_{xr2}, \quad \sigma_{r1} = \sigma_{r2} \quad \text{at } r = r_1. \quad (8)$$

If Eqs. (1) and (3) are averaged according to

$$\bar{(\quad)}_1 = \frac{1}{\pi r_1^2} \int_0^{r_1} 2\pi(\quad)_1 r dr, \quad (9a)$$

$$\bar{(\quad)}_2 = \frac{1}{\pi(r_2^2 - r_1^2)} \int_{r_1}^{r_2} 2\pi(\quad)_2 r dr, \quad (9b)$$

and the symmetry and continuity relations (6)–(8) are used, then we obtain the following equations

$$n_1 \frac{\partial \bar{\sigma}_{x1}}{\partial x} - \rho_1 n_1 \frac{\partial^2 \bar{u}_1}{\partial t^2} = -\tau, \quad (10a)$$

$$n_2 \frac{\partial \bar{\sigma}_{x2}}{\partial x} - \rho_2 n_2 \frac{\partial^2 \bar{u}_2}{\partial t^2} = \tau, \quad (10b)$$

$$n_1 \bar{\sigma}_{r1} - (\lambda_1 + 2\mu_1) n_1 \frac{\partial \bar{u}_1}{\partial x} = \lambda_1 S, \quad (11a)$$

$$n_2 \bar{\sigma}_{r2} - (\lambda_2 + 2\mu_2) n_2 \frac{\partial \bar{u}_2}{\partial x} = -\lambda_2 S. \quad (11b)$$

where n_1 and n_2 are the volume fractions of fiber and matrix, respectively, and

$$n_1 = r_1^2 / r_2^2, \quad n_2 = 1 - n_1. \quad (12)$$

In Eqs. (10) and (11) τ and S are defined as

$$\tau = 2n_1 \sigma^* / r_1, \quad S = 2n_1 v^* / r_1 \quad (13)$$

with σ^* and v^* being the values of shear stress σ_{xr} and normal displacement v at $r = r_1$. Relations (4) and (5) may be utilized to calculate τ and S . To this end and guided by the symmetry relations (6) and (7), we assume that $v_1(r, x)$, $\sigma_{xr1}(r, x)$, $v_2(r, x)$, and $\sigma_{xr2}(r, x)$ vary according to

$$v_1(r, x) = A_1(x)r, \quad (14a)$$

$$\sigma_{xr1}(r, x) = B_1(x)r, \quad (14b)$$

$$v_2(r, x) = A_2(x) \left(\frac{r^2}{r^2} - 1 \right) r, \quad (14c)$$

$$\sigma_{xr2}(r, x) = B_2(x) \left(\frac{r^2}{r^2} - 1 \right) r, \quad (14d)$$

where A_1, B_1, A_2, B_2 are independent of r . Notice that for $r = r_1$ (14) yields the same values for v^* and σ^* as in Eq. (13).

In the case of material 1 we multiply Eq. (5) by r^2/r_1^2 , neglect $\partial u/\partial x$ compared with $\partial u/\partial r$ (see Refs. 1–3 for justification), integrate according to definition (9a), and we get

$$u^* - \bar{u}_1 = \frac{r_1}{4} \frac{\sigma^*}{\mu_1}, \quad (15)$$

where

$$u^* = u(r_1, x). \quad (16)$$

Furthermore, in the case of material 2 we multiply Eq. (5) by $(r^2 - r_2^2)/(r_2^2 - r_1^2)$, integrate according to Eq. (9b), and we obtain

$$u^* - \bar{u} = \frac{Qr_1}{4} \frac{\sigma^*}{\mu_2}, \quad (17)$$

where

$$Q = \frac{4}{n_1^2} \left[\frac{3}{4} + \frac{1}{2} \ln(n_1) + n_1 \left(\frac{n_1}{4} - 1 \right) \right]. \quad (18)$$

By eliminating u^* from (15) and utilizing the continuity condition (7) we solve for σ^* and hence for τ , yielding

$$\tau = \frac{1}{r_2^2 K} (\bar{u}_2 - \bar{u}_1), \quad (19)$$

where

$$K = (\mu_2 + \mu_1 Q) / 8\mu_1 \mu_2. \quad (20)$$

A similar analysis can be carried out to solve for S . By imposing the continuity condition on σ_r we get

$$S = F \left(\mu_2 \frac{\partial \bar{u}_2}{\partial x} + \mu_1 Q \frac{\partial \bar{u}_1}{\partial x} \right), \quad (21)$$

where

$$F = (\lambda_2 - \lambda_1) / [T(\mu_1 Q + \mu_2)], \quad (22)$$

$$T = \frac{1}{n_1 m} [(\lambda_1 + \mu_1)n_2 + (\lambda_2 + \mu_2)n_1 + \mu_2].$$

Finally, substituting Eqs. (19) and (21) into Eqs. (10) and (11) yields

$$\bar{\rho}_1 \frac{\partial^2 \bar{u}_1}{\partial t^2} - a_{11} \frac{\partial^2 \bar{u}_1}{\partial x^2} - a_{12} \frac{\partial^2 \bar{u}_2}{\partial x^2} = \frac{\bar{u}_2 - \bar{u}_1}{r_2^2 K}, \quad (23a)$$

$$\bar{\rho}_2 \frac{\partial^2 \bar{u}_2}{\partial t^2} - a_{22} \frac{\partial^2 \bar{u}_1}{\partial x^2} - a_{21} \frac{\partial^2 \bar{u}_2}{\partial x^2} = \frac{\bar{u}_1 - \bar{u}_2}{r_2^2 K}, \quad (23b)$$

$$n_1 \bar{\sigma}_{x1} = a_{11} \frac{\partial \bar{u}_1}{\partial x} + a_{12} \frac{\partial \bar{u}_2}{\partial x}, \quad (24a)$$

$$n_2 \bar{\sigma}_{x2} = a_{21} \frac{\partial \bar{u}_1}{\partial x} + a_{22} \frac{\partial \bar{u}_2}{\partial x}, \quad (24b)$$

where

$$\begin{aligned} a_{11} &= (\lambda_1 + 2\mu_1)n_1 + \lambda_1 \mu_1 FQ, \\ a_{22} &= (\lambda_2 + 2\mu_2)n_2 - \lambda_2 \mu_2 F, \\ a_{12} &= \lambda_1 \mu_2 F, \quad a_{21} = -\lambda_2 \mu_1 FQ, \\ \bar{\rho}_1 &= \rho_1 n_1, \quad \bar{\rho}_2 = \rho_2 n_2. \end{aligned} \quad (25)$$

B. Derivation of the reflection coefficient

Equations (23) and (25) constitute a system of coupled field equations which describe the dynamic behavior of a composite. The composite has been replaced by a higher order dispersive continuum. The influence of the microinterface continuity conditions can be seen in the coupling coefficients. In what follows we shall combine this analysis with the equations for the fluid in order to derive an expression for the reflection coefficient for their common boundary or interface.

Representative displacement and stress boundary conditions for the homogenized composite will be matched with the corresponding values for the liquid at the interface, $x = 0$, according to the rule of mixtures

$$u_s = \bar{u}_1 n_1 + \bar{u}_2 n_2, \quad (26a)$$

$$\sigma_{xs} = \bar{\sigma}_{x1} n_1 + \bar{\sigma}_{x2} n_2. \quad (26b)$$

Thus, the liquid-solid interface continuity conditions are

$$u_f = u_s, \quad \sigma_{xf} = \sigma_{xs}, \quad \text{at } x = 0. \quad (27)$$

The composite field Eqs. (23) and (24) are complemented with the following fluid field equations

$$\frac{\partial^2 u_f}{\partial x^2} - \frac{1}{c_f^2} \frac{\partial^2 u_f}{\partial t^2} = 0, \quad (28a)$$

$$\sigma_{xf} = \lambda_f \frac{\partial u_f}{\partial x}. \quad (28b)$$

In the special case of normal incident waves from the liquid onto the liquid/composite interface we assume solutions of the form

$$u_f = U_{f1} e^{i(\omega t + k_f x)} + U_{f2} e^{i(\omega t - k_f x)}, \quad (29)$$

$$(\bar{u}_1, \bar{u}_2) = (U_1, U_2) e^{i(\omega t + qx)}, \quad (30)$$

where $k_f = \omega/c_f$ is the liquid wave number, ω is the angular frequency and q is the composite wave number. As a by product of this analysis we note that by using (30) to satisfy Eqs. (23a) and (23b) the values of q and $D = U_2/U_1$ are found to be restricted by the dispersion relations

$$q^4 - 2\gamma q^2 + \delta = 0, \quad (31)$$

$$D = \frac{U_2}{U_1} = \frac{r_2^2 K (a_{11} a^2 - \bar{\rho}_1 \omega^2) + 1}{1 - a_{12} r_2^2 k q^2}, \quad (32)$$

with

$$\gamma = \frac{(\bar{\rho}_1 a_2 + \bar{\rho}_2 a_1) \omega^2 r_2^2 K - (a_{11} + a_{22} + a_{12} + a_{21})}{2r_2^2 K (a_{11} a_{22} - a_{12} a_{21})}, \quad (33a)$$

$$\delta = \bar{\rho}_1 \bar{\rho}_2 \omega^4 r_2^2 K - (\bar{\rho}_1 + \bar{\rho}_2) \omega^2. \quad (33b)$$

Substituting from Eqs. (29) and (30) into Eqs. (28a), (28b) and (23a), (23b), followed by formulating u_s and σ_{xs} using the rule of mixtures (26a), (26b) and finally satisfying the interface continuity relations (27), we find the reflection coefficient $R = U_{f2}/U_{f1}$ to be

$$R = \frac{\lambda_f k_f (n_1 + n_2 D) - q(\alpha_1 + \alpha_2 D)}{\lambda_f k_f (n_1 + n_2 D) + q(\alpha_1 + \alpha_2 D)}, \quad (34)$$

where

$$\alpha_1 = a_{11} + a_{21}, \quad (35a)$$

$$\alpha_2 = a_{22} + a_{12}. \quad (35b)$$

Since

$$k_f = \frac{\omega}{c_f}, \quad q = \frac{\omega}{c}, \quad \text{and } \lambda_f = \rho_f c_f^2,$$

Eq. (34) can be rewritten in the equivalent form

$$R = \frac{\rho_f c_f c (n_1 + n_2 D) - (\alpha_1 + \alpha_2 D)}{\rho_f c_f c (n_1 + n_2 D) + (\alpha_1 + \alpha_2 D)}, \quad (36)$$

where, for a given ω , the value of the phase velocity c and the displacement ratio D can be calculated from relations (31) and (32). Notice that in the special case where both composite components are the same material Eq. (36) reduces to

$$R = \frac{\rho_f c_f - \rho_s c_s}{\rho_f c_f + \rho_s c_s}, \quad (37)$$

as expected. This can be seen since D reduces to unity, c reduces to c_s , and $\alpha_1 + \alpha_2$ reduces to $\rho_s c_s^2$.

III. COMPARISON WITH EXPERIMENTAL DATA

In order to verify the validity of the analytical model, attempts were made to measure the reflection coefficient of two common composite materials directly using the method proposed by Papadakas.⁷ Unfortunately, the very larger attenuation coefficient of these materials did not permit a reliable measurement of the second back surface reflection required by this method. We, therefore, were forced to measure the longitudinal phase velocity of each specimen and calculate the reflection coefficient with the homogeneous media relationship

$$R = \frac{\rho_f c_f - \rho_i c}{\rho_f c_f + \rho_i c} \quad (38)$$

Our measurement of acoustic velocity used standard interferometric measurement techniques.⁸ In order to ensure that the observed dispersion in velocity was not an artifact of either the measurement technique or the instrumentation, the compressional velocity of a piece of quartz glass was measured over the frequency range of 1–15 MHz. The phase velocity of this specimen was found to be 5.45×10^3 cm/s with an estimated accuracy of $\pm 2\%$ over this range of frequency. An error analysis of the experimental procedure showed that the experimental results presented in this paper are accurate to within $\pm 2\%$.

The two types of composite specimens utilized for reflection measurements were graphite/epoxy and boron/epoxy. In both cases specimens were fabricated with high volume concentrations of fibers, 60 vol. % in the former and 45 vol. % in the latter case. The specific properties utilized in our calculations are listed in Ref. 9. Specimens were machined from large pieces of this material such that all fibers were aligned parallel to the direction of wave propagation. A schematic representation of these specimens is shown in Fig. 1.

The results of the phase velocity experiment for graphite/epoxy is shown in Fig. 3. The corresponding reflection coefficient were calculated using the relationship for homogeneous media, i.e., Eq. (38) with the mixture density of 1.583 g/cc. It is obvious that these results show negligible

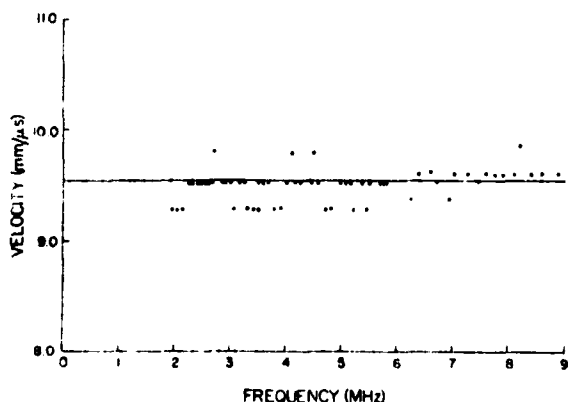


FIG. 3. Longitudinal phase velocity vs frequency for an acoustic beam propagating parallel to the fiber direction in a 60 vol. % graphite/epoxy composite (solid line is theory, dots are experiment).

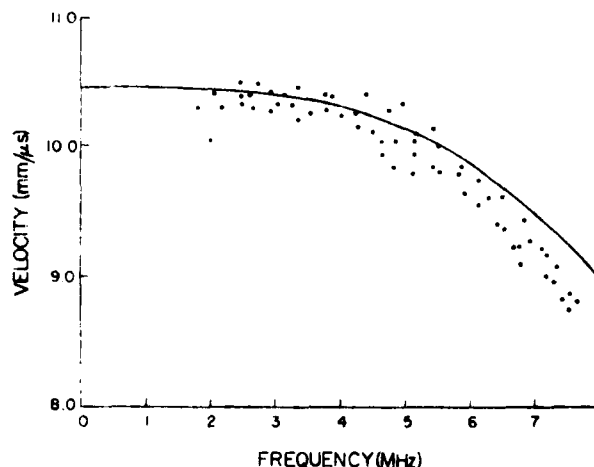


FIG. 4. Longitudinal phase velocity vs frequency for an acoustic beam propagating parallel the fibers in a 45 vol. % boron/epoxy composite (solid line is theory, dots are experiment).

dispersion, i.e., phase velocity and reflection coefficient variation with frequency are undetectable. This conclusion is not unexpected given the very small size of the graphite fiber. A photomicrograph of the actual surface of this specimen is shown in Fig. 6(a). The reader will note that not only are the fibers tightly packed in an approximate hexagonal network, but the fiber diameter is approximately $8 \mu\text{m} \pm 1 \mu\text{m}$. For this size range the acoustic wave, with a wavelength in water of $150 \mu\text{m}$ sees the composite as if it were an average of both fiber and matrix properties weighted by their respective volume fractions.

The same measurements were made with the boron/epoxy sample and the results are displayed in Figs. 4 and 5, respectively. As in the case of the graphite epoxy, the homogeneous media relation, Eq. (38) was used to calculate the reflection coefficient. For these calculations a density of 1.968 g/cc was used. The theoretical predictions of our approximate model are shown by the solid lines.

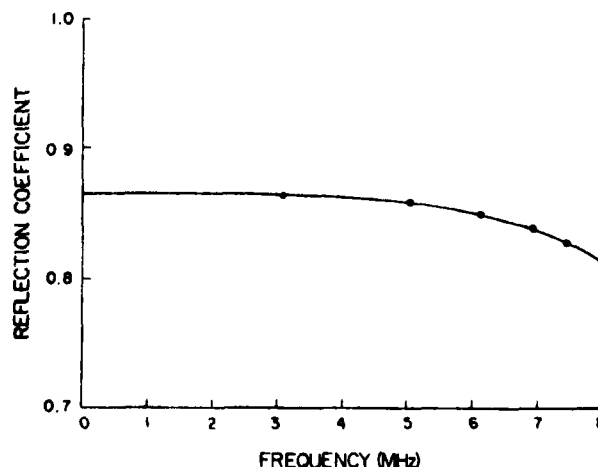


FIG. 5. Calculated and measured reflection coefficient for a boron/epoxy composite in water [solid line theory, dots representative data points calculated via Eq. (38)].

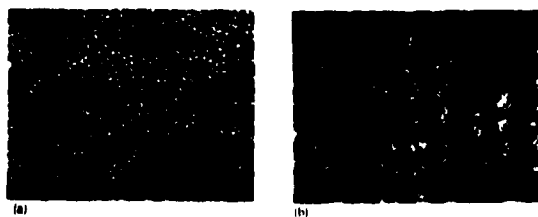


FIG. 6. (a) A micrograph of the graphite/epoxy composite. Fiber diameter is approximately $8 \pm 1 \mu\text{m}$. (b) A micrograph of a boron/epoxy composite. Fiber diameter is approximately $100 \pm 3 \mu\text{m}$.

For the present case the experimental data confirm the dispersion predicted by our model, i.e., Eq. (36). A photo micrograph of the surface of the specimen shown in Fig. 6(b) explains why. The reader will note that the microdimension of the effective repeating cell of boron/epoxy composites are substantially larger than those of graphite/epoxy. Since the repeating unit of this composite is approximately the same size as the acoustic wavelength. The extent of the dispersion observed in this material was expected. In fact, the agreement between theory and experiment is quite satisfactory given the assumptions used in the derivation of our model. The difference between the analytical prediction and data above 7 MHz is due to the increasing inaccuracy of the approximate analysis as is manifested in the linear approximations of Eq. (14). Furthermore, the fact that the model does not take into account the higher frequency attenuating property of epoxy adds to this discrepancy.

IV. CONCLUSIONS

We have presented an approximate analysis for the reflection of an acoustic wave from a water/composite inter-

face. In this analysis the heterogeneous microstructure of the composite is replaced with a homogeneous, dispersive medium. In this process we replaced the microscopic continuity relations with macroscopic relations in order to satisfy the conditions of the analysis. The validity of this analysis was verified from experimental data which showed that the model works well in the lower frequency ranges. In the frequency range where the wavelength of the incident wave approaches the characteristic size of the composite microstructure the validity of the model begins to break down as shown by the deviation of data from the analytical prediction.

ACKNOWLEDGMENT

Research of A. Nayfeh is supported by NSF Grant CME 8021054 and AF Contract F33615-80-C-5015.

¹G. A. Hegemier, G. A. Gurtman, and A. H. Nayfeh, *Int. J. Solids Struct.* **9**, 395 (1973).

²A. H. Nayfeh and G. A. Gurtman, *J. Appl. Mech.* **41**, 106 (1974).

³A. H. Nayfeh and E. A. Nassar, *J. Appl. Mech.* **45**, 822 (1977).

⁴A. H. Nayfeh, *Fibre Sci. Technol.* **10**, 195 (1977).

⁵C. T. Sun, J. D. Achenbach, and G. Herrmann, *J. Appl. Mech.* **35**, 467 (1968).

⁶A. Bedford and M. Stern, *J. Appl. Mech.* **38**, 8 (1971).

⁷E. P. Papadakis, *J. Appl. Phys.* **42**, 2990 (1971).

⁸R. Truell, C. Elbaum, and B. B. Chick, *Ultrasonic Methods in Solid State Physics* (Academic, New York, 1969), Chap. 2.

⁹The Lamé Constants λ and μ are given by 4.73×10^9 and 1.95×10^9 N/m² for epoxy; 88.9×10^9 and 177.2×10^9 N/m² for boron and 114.5×10^9 , 24×10^9 N/m² for graphite. The corresponding densities are 1.22, 2.34, and 1.8 g/cm³ for epoxy, boron, and graphite, respectively.

APPENDIX D

PUBLICATIONS ON ULTRASONIC BACKSCATTERING FROM NDE OF COMPOSITES

CHARACTERIZATION OF MULTIPLE DEFECTS IN COMPOSITES
USING A NEW ULTRASONIC TECHNIQUE

Y. Bar-Cohen
Research Applications Division
Systems Research Laboratories, Inc.
Dayton, OH 45440-3696

and

R. L. Crane
AFWAL Materials Laboratory
(AFWAL/MLLP)
Wright-Patterson AFB, OH 45433

The utilization of the peculiar ultrasonic wave propagation inherent in composite materials is usually thought of as being too complicated for application to nondestructive inspection situations. However, recent experimental studies have shown that a significant increase in backscattering for acoustic waves at normal incidence to the fiber axis or to the surface of discontinuities can be used to detect and characterize such multiple defects as matrix cracking, fiber orientation and misalignment, and ply gaps.

INTRODUCTION

During the last decade, the use of composites in aeronautical structures has increased tremendously due to the recognition of their high specific strength and modulus. As is the case with other structural materials, composites contain production and service-induced defects which grow during usage. In order to anticipate and prevent premature failure of composite materials, new NDE methods are required. Conventional ultrasonic methods, which are widely used for the detection of delaminations, are not capable of detecting subtler forms of damage because they were developed for detection of single flaws in homogeneous, isotropic materials. Composites, however, are inhomogeneous and usually contain many initial flaws whose density increases as a function of fatigue life. Recent studies of acoustic backscattering from composites indicate that a technique based on this phenomenon has the potential to overcome the limitations of the conventional ultrasonic techniques. This methodology utilizes the inhomogeneous, anisotropic, and layered nature of composites to detect specifically oriented microstructural features such as fibers and cracks.

The significance of acoustic scattering phenomena to the characterization of scatterers by analysis of the acoustic-field distribution was recognized in the last century. Most studies have been concentrated on single scatterers in homogeneous media to determine the information that can be extracted about the scatterer from measurements of the acoustic field.¹ However, the case of multiple scattering from an array of cylinders, i.e., fibers in composites, is more complicated. The work in this area (see, for example, Refs. 2 and 3) has been limited to randomly spaced low-volume-fraction fibers and non-layered media. Due to the dearth of applicable theoretical work, the authors examined backscattering of composites from an experimental point of view. The results were found to be quite useful, as this paper will show.

475

Presented at Dualtest - I, Pittsburgh, PA, October 4-7,
1982; published in Conference Proceedings.

EXPERIMENTAL PROCEDURE

The ultrasonic set-up used for the backscattering experiments consisted of one of several 6.1-mm-diam. transducers and a Panametrics PR5052 pulser/receiver. The interrogating pulses had a central frequency in the range between 5 and 25 MHz. This frequency range yielded ka values between 0.05 and 1.0, where k is the wave number and a is the nominal diameter of the commercially available graphite or glass fibers. Experimental data on backscattering were averaged using a Princeton Applied Research Model 162 Boxcar Averager to reduce noise. These data were also used to produce acoustic images with the aid of conventional X-Y and polar C-scan recording instrumentation.

In the experiments, a turntable was used to enable one angle of a spherical coordinate system to be held constant while the other was varied continuously. The transducer and turntable with test specimen were immersed in water which served as a delay line and coupling medium. The measurements were taken at angles of incidence in the range 0 to 90 deg. and angles of rotation in the range 0 to 180 deg. The composite specimens included graphite/epoxy (T300 fiber/5200 resin) and glass/epoxy (Scotch 1002) with thicknesses which ranged from 2 to 13 plies.

RESULTS AND DISCUSSION

The backscattered acoustic field of a unidirectional composite is shown in Figure 1. The data reach a maximum only at a small angular range of the normal to the fiber axis. Elsewhere, scattering is uniform and low unless other sources of scattering such as surface roughness, internal voids, or porosity are located along the acoustic beam path. The effects of surface roughness were reduced by sanding the test specimen or coating it with a strippable varnish. These results suggest the utility of using backscatter signals to determine ply orientation as well as fiber alignment within a specific ply. Figure 2 shows the effect of precessing the transducer around the normal to the plane of the fibers. By varying the angle of incidence in a plane normal to the fiber direction in a unidirectional composite, the data shown in Figure 3 were obtained. This figure indicates the existence of two backscattering maxima which seem to be related to the longitudinal and one of two possible shear velocities.

The magnitude of acoustic backscattering varies according to the type and size of the defect; for example, transverse-crack scattering is about 25 dB above that due to the fibers in graphite/epoxy laminates. It is, therefore, quite easy to discriminate crack scattering from that due to fibers and to generate an image of cracks in the various layers of composites. A quasi-isotropic graphite/epoxy specimen was fatigue loaded to 80% of the ultimate strength and 5000 cycles and C-scanned using this technique. The result, as shown in Figure 4, clearly indicates the presence of transverse cracks due to cyclic loading at the various ply orientations. The effect of the incidence angle on the backscattering image of these defects is shown in Figure 5. As can clearly be seen, the closer this angle is to the "critical" angle, the higher the signal-to-noise ratio. Unfortunately, raising the angle of incidence lowers the resolution due to shadowing of cracks by those in the foreground. These facts required optimization of the incidence angle, which was found empirically for graphite/epoxy to be approximately 21 deg. The results of using this optimized technique to scan a group of fatigued specimens are shown in Figure 6. Transverse cracks are generated also as a result of static stresses, as shown in Figure 7 where a sample was loaded to 90% of the ultimate tensile strength. These results demonstrate the usefulness of backscattering in studying the process of crack growth in composite materials.

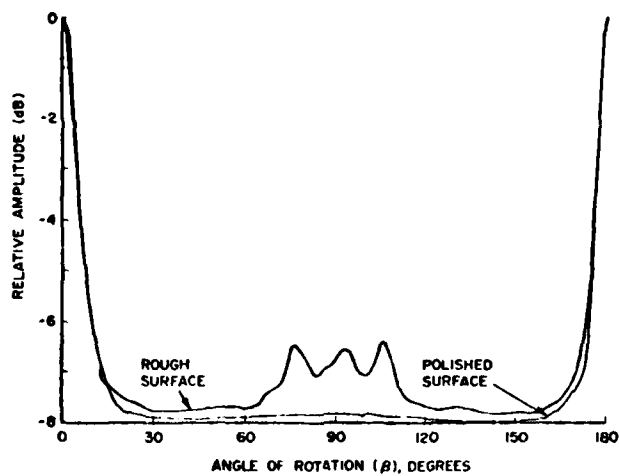


Figure 1. Backscattering from a Uni-directional $[0^\circ]_8$ Glass/Epoxy Composite. The effect of surface roughness is shown. The angle of incidence $\alpha = 30^\circ$.

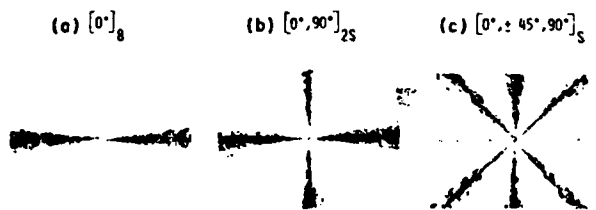


Figure 2. Polar Plots of Backscattering from Three Glass/Epoxy Eight-Ply Specimens. Fiber orientation is clearly indicated.



Figure 3. Backscattering as a Function of Angle of Incidence for Glass/Epoxy Composite, at the Plane of the Normal to the Fiber Axes ($\beta = 0^\circ$). The two critical angles are clearly indicated.

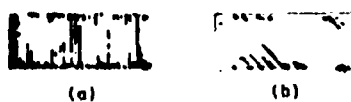


Figure 4. Backscattering Scan of Quasi-Isotropic Graphite/Epoxy Specimen Fatigue Loaded to 75% of Ultimate Strength and 5000 Cycles.



Figure 5. Acoustic Backscattering Images of Fatigue Damage at the 90° Orientation of $[0^\circ, 90^\circ + 45^\circ]_S$ Graphite/Epoxy Specimen Loaded to 75% of Ultimate Strength and 5000 Cycles and Tested at Various Angles of Incidence.

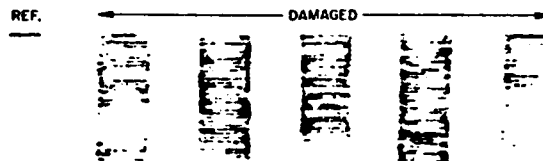


Figure 6. C-Scan Imaging of Transverse Cracks (90°) in $[0^\circ, 90^\circ, \pm 45^\circ]_s$ Graphite/Epoxy Specimens Fatigue Loaded to 75% of Ultimate Strength and 5000 Cycles.

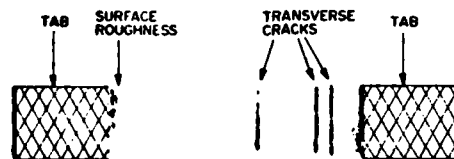


Figure 7. C-Scan Backscattering Image of Static Loaded (90% of Ultimate Strength) Graphite/Epoxy $[0^\circ, 90^\circ, \pm 45^\circ]_s$ Specimen. Angle of incidence $\alpha = 21^\circ$.

It can be concluded that backscattering measurements can be used to determine fiber orientation and misalignment. Moreover, minute internal transverse cracks such as those which occur during cyclic or static loading can be imaged and tracked.

ACKNOWLEDGEMENT

The authors wish to express their appreciation to Noel Tracy and Dan Laufersweiler of Universal Technology Corporation, Dayton, OH, for their assistance.

REFERENCES

1. Lord Rayleigh, The Theory of Sound, New York: Dover Publications, 1945, First American Edition.
2. Cheng, S. L., "Multiple Scattering of Elastic Waves by Parallel Cylinders," Journal of Applied Mechanics, 36, no. 9 (1969): 523.
3. Vezzetti, D. J. and Aks, S. O., "Review - Ultrasonic Scattering Theory II: Scattering from Composites," Ultrasonic Imaging 2, no. 3 (1980): 195.

NONDESTRUCTIVE EVALUATION OF COMPOSITE
MATERIALS WITH BACKSCATTERING MEASUREMENTS

by

Y. Bar-Cohen
Systems Research Laboratories, Inc., Dayton, Ohio
and

R. L. Crane
AFWAL/MLLP, WPAFB, Ohio

ABSTRACT

Initial experiments have been performed to characterize the scattering of acoustic waves from glass/epoxy and graphite/epoxy composite panels. Experiments were conducted in the region $0.1 \leq ka \leq 1.0$ on both types of fiber reinforced composites. The data clearly show that a maximum in the backscattering ultrasonic energy occurs for orientations which place the fiber axis perpendicular to the propagation vector.

INTRODUCTION

The propagation of elastic wave through fiber reinforced composite is a very complex process. As it travels through the material, the acoustic wave is dramatically affected by the anisotropic nature of the layered composite. Significant changes also result from the multiple scattering events that occur because of the myriad of stiff fibers in a soft plastic matrix. Only recently have theoretical and experimental studies begun to unravel the subtleties of the acoustic wave/composite interaction.

The objective of this research work has to study the multiple scattering phenomena in fiber reinforced composites, as revealed by backscattering measurements.

RESULTS AND DISCUSSION

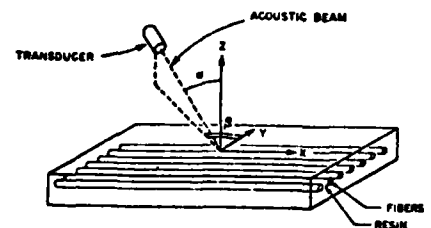
An experimental apparatus was built to permit rotating test specimen while maintaining a constant angle of incidence. By varying the fiber diameter and the frequency of the incident wave, tests were conducted in the pseudo-Rayleigh scattering range $0.1 \leq ka \leq 1.0$, where k is the wave number and a is the fiber diameter. The composite materials examined were graphite/epoxy and glass/epoxy. A schematic of the experimental set-up and nomenclature are shown in Fig. 1. Measurements of backscattering were averaged over 32 points on the specimen for a constant incident angle. As expected, the backscattering (scattering detected by the sending transducer) is maximum for orientations that place the fibers in a specific ply perpendicular to the ultrasonic beam, (see Fig. 2). Also shown in Fig. 2 is the effect of surface roughness which contributed about 1 dB to the backscattered energy. This can be nearly eliminated by polishing the specimen surface. In Fig. 3 a schematic diagram is shown as a guide in determining fiber angle in a quasi-isotropic laminate. Using this simple convention then Figs. 4 and 5 demonstrate the ease of using backscattering information to determine ply orientation.

The width of the backscattering peak is affected by both the beam divergence and the uniformity of fiber alignment. If beam divergence is constant, then the peak width may be used to estimate the amount of waviness in an otherwise parallel row of fibers. To demonstrate this, a sample with a 30° misalignment was fabricated. The effect of

this misalignment is shown along with perfectly aligned sample in Fig. 6. The increased bandwidth was capable of determining misalignment to an accuracy of $\pm 1^\circ$ of arc. This is shown in Fig. 7, where the actual angle versus the calculated misalignment angles are plotted.

Backscattering is observed whenever a discontinuity is encountered by the acoustic. Defects such as a porosity with spherical symmetry, result in a uniform increase of scattering over wide angles as shown in Fig. 8.

It is concluded that backscattering measurements may be used to determine fibers orientation, misalignment and in some cases the presence of porosity. Further work is underway to quantify the angular dependence and intensity of backscattering in composite materials.



WHERE:

α - ANGLE OF INCIDENCE

β - ANGLE BETWEEN Y-AXIS AND THE TRANSMITTER
BEAM TRAJECTORY ON THE LAYER PLANE

Fig. 1. Schematic representation of experimental set-up used to measure backscattering from composite samples.

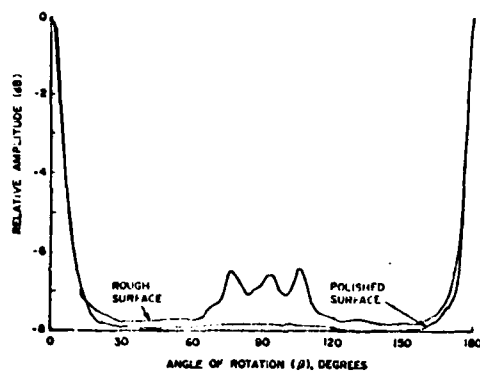


Fig 2 Backscattering from unidirectional $([0]_8)$ Gl/Ep composite for a 30° angle of incidence. The effect of surface roughness is also shown.

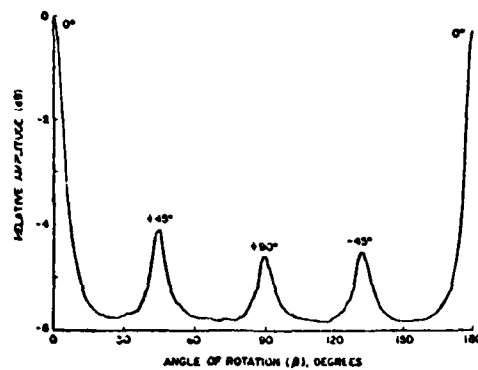


Fig 4 Backscattering from a quazi-isotropic $([0, \pm 45, 90]_s)$ composite for a 30° angle of incidence. Scattering from each ply is apparent (see Figure 3).

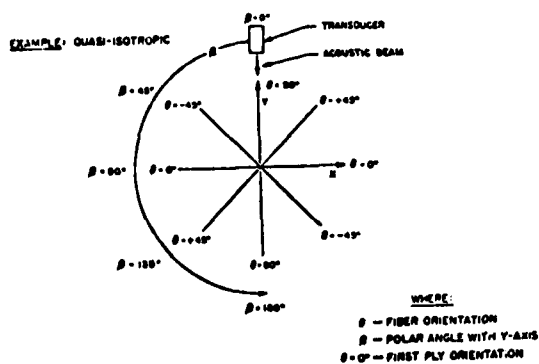


Fig. 3 Angular convention used to determine fiber orientation in backscattering experiments.

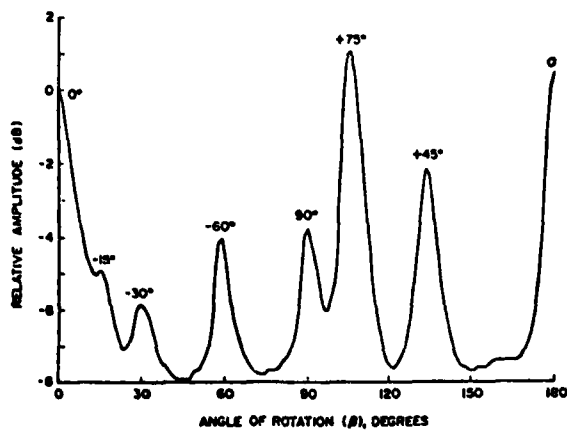


Fig. 5 Backscattering from graphite/epoxy composite $[0^\circ, -15^\circ, -30^\circ, +45^\circ, -60^\circ, +75^\circ, 90^\circ]_s$. Angle of incidence was 40° .

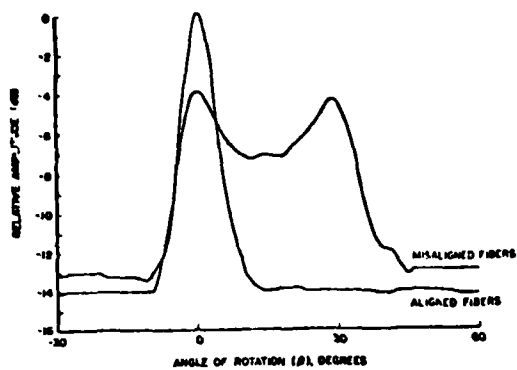


Fig. 6 The effect of misalignment on backscattering from single-ply glass/epoxy material.

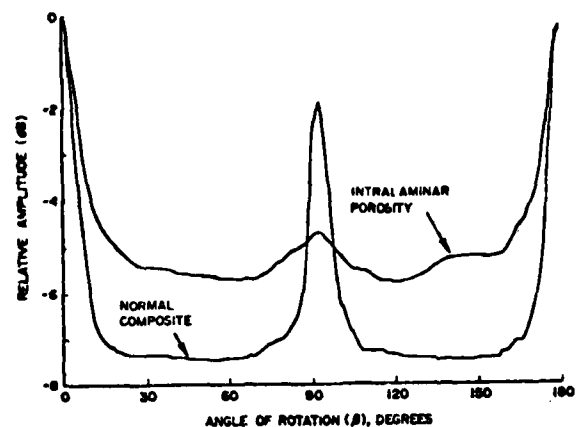


Fig. 8 Backscattering from $[0,90]_{2s}$ glass/epoxy composite both with and without porosity. Glass micro-balloons were used to simulate porosity.

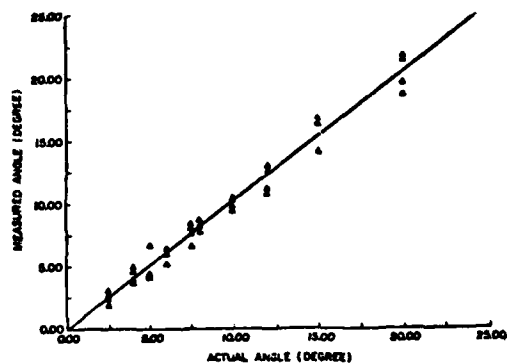


Fig. 7 Comparison of measured and actual fiber misalignment in glass/epoxy composite material.

Acoustic-Backscattering Imaging of Subcritical Flaws in Composites

by Y. Bar-Cohen and R. L. Crane

Abstract

Experimental studies of acoustic backscattering in the Rayleigh region, i.e., $0.05 \leq ka \leq 1.0$, from fiber-reinforced composites were conducted. A significant increase in backscattering was observed for those orientations which place the axis of the fibers or other discontinuities at normal incidence to the acoustic beam. Using this technique, fiber orientations and the distribution of cracks within specific plies were easily mapped.

INTRODUCTION

During the past decade, fiber-reinforced composites have found increasing utilization in primary (safety-of-flight) aircraft components. Current USAF damage-tolerant design philosophy requires the detection and tracking of service-induced damage using nondestructive evaluation (NDE) methods. Presently, ultrasonic techniques are widely used for this purpose. However, these NDE methods were developed principally for the inspection of metal structures and, therefore, are optimized for the detection of single flaws in homogeneous, isotropic monolithic materials. Unfortunately, the detection of flaws in composites is particularly difficult because of the inhomogeneous, anisotropic, and layered nature of these materials. Another complication arises from the fact that composites do not accumulate damage via the growth of a single self-similar flaw, but rather by initiation of a myriad of small matrix cracks. For many composites currently in use in aircraft structures, this matrix cracking ultimately leads to the development of a delamination late in the fatigue life. For stiffness-critical structures, this can be defined as the end point of the structure's useful life. Given these considerations and the fact that previous investigations (see, for example, Ref. 1) of the classic ultrasonic techniques have yielded results of limited applicability to composites, the authors decided to investigate ultrasonic backscattering which utilizes the inhomogeneous, layered



Dr. Yoseph Bar-Cohen is the NDE principal investigator in the Research Applications Division of Systems Research Laboratories, Inc., Dayton, OH. His research interests are primarily in the area of ultrasonic characterization of defects in metallic and composite materials. He received his B.Sc. (1970), M.Sc. (1972), and Ph.D. (1979) in physics from the Hebrew University of Jerusalem. From 1972 to 1979, Bar-Cohen was the senior NDE specialist for the aircraft industry in Israel. He was responsible for developing nondestructive methods, procedures, and specifications for testing and evaluation of aircraft materials and components. Bar-Cohen has a Level III qualification, by examination, in UT, RT, MT, PT, and ET. From 1979 to 1980, he was a Post-Doctoral Research Fellow at the Air Force Wright Aeronautical Laboratories, under an award from the National Research Council. For inquiries concerning this work, the author may be contacted at (513) 254-5980.



Robert Crane received his Bachelor of Engineering degree from The Ohio State University in 1965. He received his M.S. and Ph.D. degrees from the same institution in 1966 and 1969, respectively. In addition, he has done graduate work at the University of Chicago. His present position is with Nondestructive Evaluation Branch of the AFWAL Materials Laboratory. He has performed research in the areas of ultrasonic techniques, computer tomography and the integration of physical measurements with fracture mechanics. His current research has as its goal the development of NDE tools for composite materials. Crane is Chairman of the Sonics Committee and the immediate Past Chairman of Miami Valley Section.

nature of the composite to detect and image dominant microstructural features.

The scattering of waves has been the subject of numerous publications because much can be deduced about the scatterer from measurements of the angular distribution and magnitude

of the scattered energy. Recent developments in the field of acoustic scattering of sound waves by single objects in homogeneous solid or fluid media have served extensively to determine what information concerning the size, shape, and orientation of the scatterer can be gleaned from ultrasonic measurements (see, for example, Refs. 2 and 3). The situation is much more difficult to analyze in the case of composite materials because sound energy is both reflected at the interface between layers and scattered by the fibers and numerous inherent flaws within each ply. A detailed analysis of experimental data must, therefore, depend upon a consideration of multiple scattering. Diffuse scattering by dispersoids has received much attention in recent years, particularly with regard to biological materials.⁴ While theoretical analyses of multiple scattering in solids have been performed,^{5,6} researchers have only recently attempted to rationalize analytical predictions with quantitative measurements. For example, O'Donnell and Miller⁷ were able to obtain reasonable agreement between analysis and experiment for a plastic containing approximately 4.0 volume percent voids. While this and most previous work has been done with media containing spherical voids, very little work—either analytical or empirical—has been devoted to the examination of the scattering of coaxially aligned cylinders. The analysis of Varadan, *et al.*,⁸ examined the forward scattering of randomly dispersed coaxial fibers; but the results are not generally applicable to composites because of the limitation of the analysis to low-volume-fraction non-layered media. The work of Bose and Mal,⁹ Data,¹⁰ Chang¹¹ and Golovchan and Guz¹² are similarly limited in applicability. Therefore, the present work examines—from an experimental standpoint—backscattering from composites. The results are quite useful in attempts to track or monitor mechanical damage in composites.

EXPERIMENTAL PROCEDURE

The four types of composites examined in this investigation were glass/epoxy (fabricated from Scotch 1002), graphite/epoxy (T300 fiber/5200 resin), 5.6-mil boron/epoxy, and silicon carbide (5.6 mil)/titanium (Ti-6Al-4V). Various cross-ply lay-ups were used for both the glass/epoxy and graphite/epoxy materials; but for the other two materials, only unidirectional specimens were fabricated. All specimens consisted of 2 to 14 plies, depending upon the complexity of the lay-up; e.g., unidirectional panels usually contained two plies, while quasi-isotropic panels contained eight. All systems were fabricated using standard autoclave cycles which had been optimized for minimum porosity in the finished laminates. To investigate the effect of porosity upon backscattering, one specimen was fabricated with hollow glass microspheres,* 80 μ m in diam., dusted between glass/epoxy tapes during lay-up. Because of the highly localized nature of the porosity, no attempt was made to measure accurately its volume fraction. However, estimates from gravimetric measurements indicate it to be ≈ 2.0 percent.

Because of the potential of the backscattering technique to image both fiber orientation and processing errors, both angle-ply and single-ply sheets were examined. For ply-orientation determination a special $[0^\circ, -15^\circ, -30^\circ, +45^\circ, -60^\circ, +75^\circ, 90^\circ]$, specimen was fabricated using standard curing procedures. The utility of the technique in examining fiber flaws was investigated with a single layer of uncured graphite/epoxy. For these experiments, fiber waviness was simulated by distorting the fiber tows into a single-cycle sine-wave pattern with a wavelength of about 6.5 cm and an amplitude of 0.25 cm.

The imaging of small cracks within the composite was carried out on specimens having first-ply failure cracks. These were obtained by fatiguing eight-ply quasi-isotropic graphite/epoxy specimens until several lineal densities of transverse cracks were obtained. The fatigue loading was carried out with a standard ramp loading spectrum, with a maximum load of 75 per-

cent of the ultimate tensile failure load and $R = 0.1$. This spectrum easily produced specimens with 90° and $+45^\circ$ ply cracks in a relatively short time (5000 cycles). The number and location of these cracks were easily established with edge replication and the standard radiographic technique using an x-radiation opaque penetrant.

The instrumentation used in these experiments is shown schematically in Fig. 1. A wide-band, flat, 6.35 mm diam. transducer located at the far field was driven by a Panametrics PR5052 pulser/receiver. In experiments requiring high resolution, a 6.35 mm diam., 25-MHz, 12.7 mm focus wide-band transducer was used. The center frequency of the interrogating pulse of ultrasound was varied from 5.0 to 25.0 MHz which yielded values of ka in the range 0.05 to 1.0, where k is the wave number that is equal to $2\pi/\text{wavelength}$ and a is the nominal diameter of the scattering object. In several experiments, data were time averaged using a Princeton Applied Research boxcar averager to reduce system noise. All experiments were conducted in a water bath which served as an ultrasonic couplant and a delay line.

A schematic representation of the transducer and specimen reference axis is given in Fig. 2. The angles of incidence of measurement were taken in the range $0^\circ \leq \alpha \leq 90^\circ$ and the angles of rotation in the range $0^\circ \leq \beta \leq 180^\circ$. The angle of incidence α was measured from the normal to the tested lam-

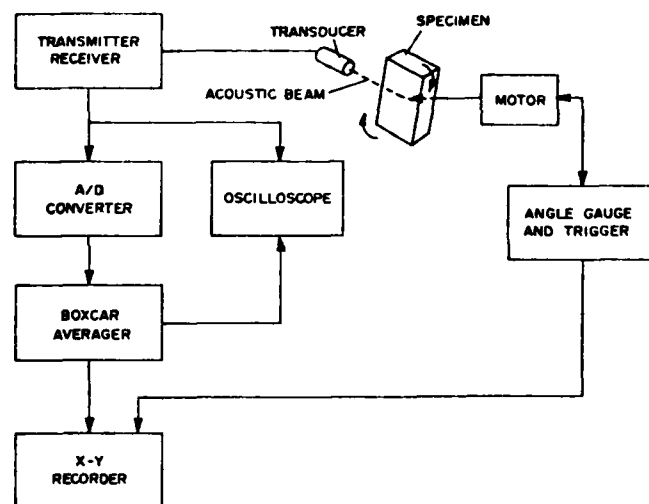
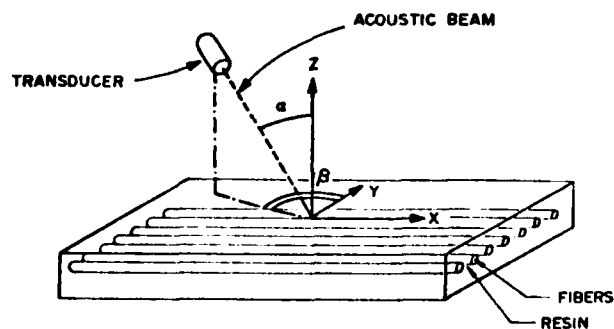


Figure 1—Schematic representation of electronic instrumentation used in backscattering experiments.



WHERE:

α - ANGLE OF INCIDENCE

β - ANGLE BETWEEN Y-AXIS AND THE TRANSMITTER BEAM TRAJECTORY ON THE LAYER PLANE

Figure 2—Schematic diagram of experimental system used to measure backscattering from composite samples.

*Emmerson and Commings, Inc., Canton, MA.

mate, whereas β was measured counterclockwise with respect to the plate Y axis. The reference system thus obtained is equivalent to the standard notation of ply orientation,¹³ with the first layer of the laminate determining the coordinate system in which X is the fiber direction. In the various experiments, one angle was maintained constant and the other has been changed. For studies of backscattering phenomena, the amplitude of backscattering was recorded as a function of angular position. The results obtained served to determine the optimum position in which the transducer should be located for subcritical-flaw imaging.

RESULTS AND DISCUSSION

Investigation of the backscattering field of unidirectional composite materials indicates, as shown in Fig. 3, that the data reach a maximum only at a small angular range of the normal to the fiber axis. Elsewhere, scattering is uniform and low unless other sources of scattering are located along the acoustic-beam path. Surface roughness is also a source of such scattering, but its characteristics can be substantially eliminated by sanding the test specimen using a No. 180-grid metallographic paper. Surface-roughness scattering can also be reduced (2 dB) by coating the surface with a lacquer which can be stripped.⁶ Although the scattering amplitude from the surface roughness is relatively low (see Fig. 3), for the sake of simplicity, all test specimens during the present investigation were hand sanded smooth to permit accurate imaging of small defects.

The effect of changing the angle of incidence α upon backscattering amplitude is shown in Fig. 4. Two maxima are observed in each of the characteristic curves which represent graphite/epoxy and silicon/carbide composites. These maxima occur at the quasi-critical angles and are dependent upon the quasi-longitudinal and quasi-shear wave velocities which are functions of the angle β .¹⁴ The fact that maximum scattering is observed at these angles has been used to advantage, and most experiments were conducted at the angle of incidence which provided the most intense signals, namely, higher signal-to-noise ratio. However, no attempt was made to optimize the transducer orientation for maximum scattering by a simultaneously changing α as a function of β or vice versa, and all experiments were conducted with at least one constant angle.

Backscattering as a function of angle of rotation, β , for a quasi-isotropic graphite/epoxy specimen is shown in Fig. 5. It is quite obvious that each layer of the composite reflects over a small range of the angle β , which is normal to the fiber axis of the specific layer of interest.

It was noted that the intensity of the scattering from glass/epoxy is 3 to 5 dB higher than that from the graphite/epoxy composite. This is presumably due to the much larger difference in acoustic impedance between glass and epoxy as compared to that between graphite and epoxy—the acoustic impedances of graphite, glass, and epoxy are 6.89, 14.48, and 3.48×10^5 gm/cm² sec., respectively. The difference in impedance for glass/epoxy is almost three times that for graphite/epoxy. This does not completely explain the difference in scattered intensity since the difference in fiber (i.e., scatterer) diameter and the number of scatterers per unit volume must also be considered. Unfortunately, the only models of scattering from a layer of cylinders which have been developed thus far present quite difficult computational problems.^{11,12} Therefore, a rationalization of analysis and experiment is not possible at this time.

A schematic diagram demonstrating the angular relationship between the scattering angle, β , and ply orientation is shown in Fig. 6. It should be noted that the X and Y axes of the composite plate are uniquely related to the axis of the scanning system. The scan of a specially fabricated graphite/epoxy composite is shown in Fig. 7. In this case, it is obvious that in order to specify ply orientation uniquely, the relationship between

*The Sherwin Williams Corp., Cleveland, OH, Stripple Lacquer M69W1.

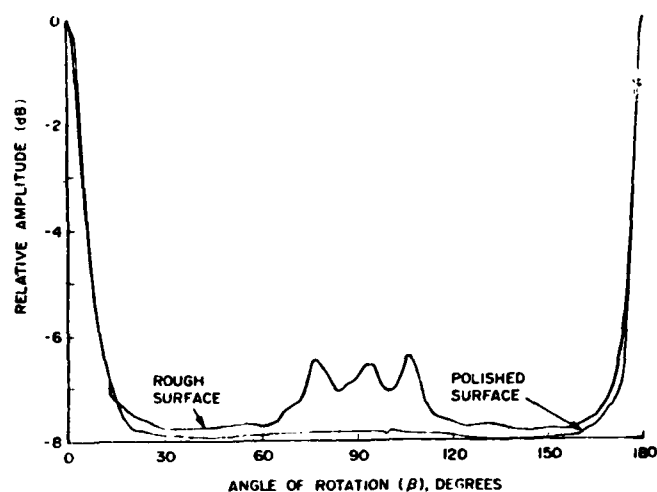


Figure 3—Backscattering from a unidirectional $[0^\circ]_s$ glass/epoxy composite. The effect of surface roughness is also shown. The angle of incidence $\alpha = 30^\circ$.

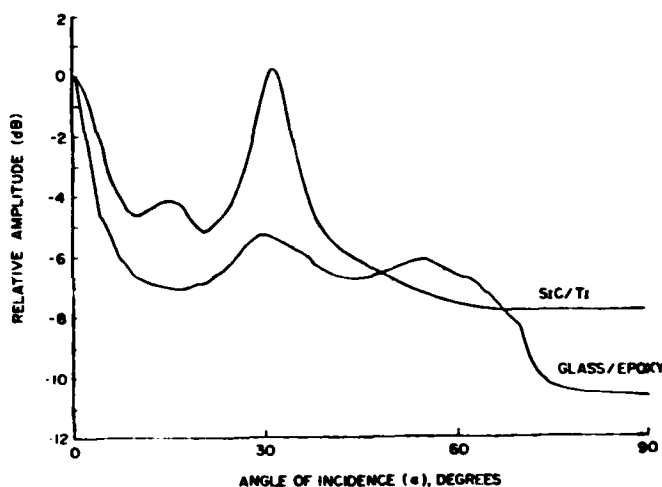


Figure 4—Comparison of backscattering from both a SiC/Ti and a glass/epoxy composite as a function of angle of incidence. Rotational angle $\beta = 0$.

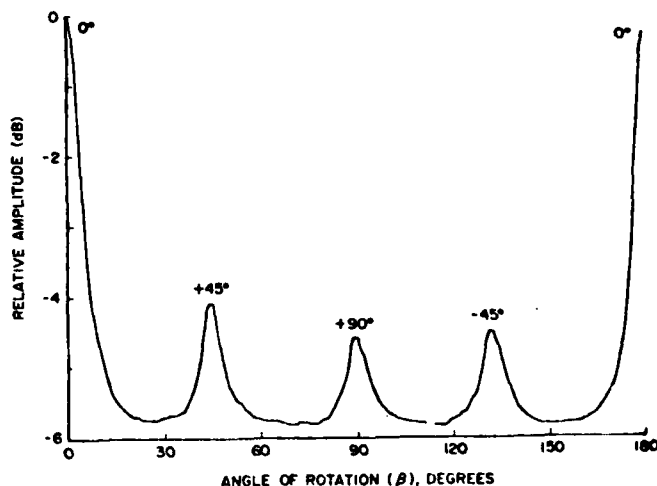
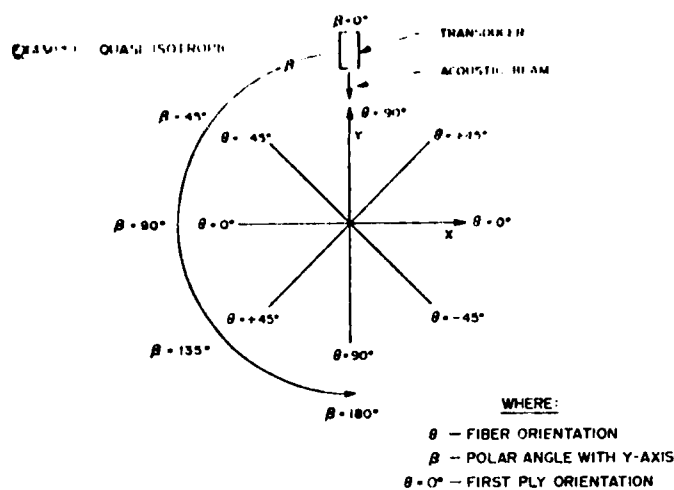
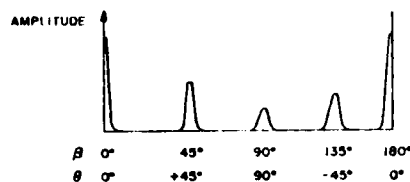


Figure 5—Backscattering from a quasi-isotropic $[0^\circ, \pm 45^\circ, 90^\circ]_s$ graphite/epoxy composite. Scattering from each ply is apparent. Angle of incidence $\alpha = 30^\circ$.



RESULTING BACKSCATTERING



GENERAL RULE:

θ CAN BE DETERMINED FROM THE ABOVE CURVE AS FOLLOWS:

$$\theta = \beta - \delta \cdot 180^\circ, \text{ WHERE: } \delta = \begin{cases} 0 & \beta \leq 90^\circ \\ 1 & \beta > 90^\circ \end{cases}$$

Figure 6—Schematic diagram of composite plate and measurement coordinate system.

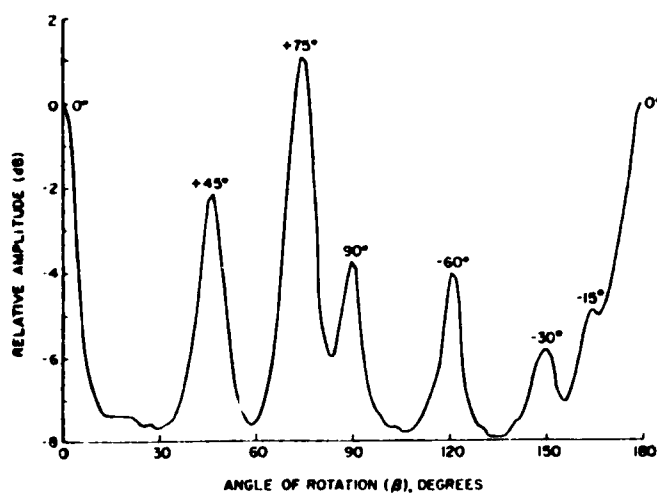


Figure 7—Backscattering from a $[0^\circ, -15^\circ, -30^\circ, +45^\circ, -60^\circ, +75^\circ, 90^\circ]_s$ graphite/epoxy composite $\alpha = 40^\circ$.

the measurement coordinate system and that associated with the composite must be carefully specified; for example, the $[0^\circ, -15^\circ, -30^\circ, +45^\circ, -60^\circ, +75^\circ, 90^\circ]_s$ composite could easily become a $[0^\circ, +15^\circ, +30^\circ, -45^\circ, +60^\circ, -75^\circ, 90^\circ]_s$, if the specimen were inverted, making the +X axis the -X axis. In Fig. 7, it appears that the effect of the changing critical angle

as a function of β can explain the increased backscattering from the 75-deg. layer as compared to the 0 deg. layer at $\alpha = 10^\circ$.

An alternate method of displaying backscattering data is the polar plot using the C-scan system in the rotation mode, where scattering intensity is plotted as a function of angle of rotation, as shown in Fig. 8. Data for this plot were obtained for unidirectional $[0^\circ]_s$, cross-ply $[0^\circ, 90^\circ]_{2s}$ and quasi-isotropic $[0^\circ, 90^\circ, \pm 45^\circ]_s$ graphite/epoxy material. The effects of surface roughness are shown in Fig. 8(c) as the background speckle in the $90^\circ \pm 12.5^\circ$ directions. This roughness is the result of the bleeder-cloth impression on the surface of the plate.

Since the backscattering discussed thus far arises from the fibers and, therefore, is highly dependent upon their orientation, it was natural to extend these experiments to the investigation of the effects of slight misalignments within a specific ply. If the focal spot of the transducer covers an area containing minor misalignments, i.e., fiber waviness, and the axis of rotation is located at the center of the misaligned fiber bundle, then this should cause a broadening of the scattering angular-spectrum peak. For a sharply bent composite tape of dimensions which are smaller than the acoustically scanned area, the backscatter peak is broadened and splits into two peaks as shown in Fig. 9(a). If the peak width is calibrated against known angles of deviation, then it is a simple matter to estimate the

a. $[0^\circ]_s$

$\theta = 0^\circ$

b. $[0^\circ, 90^\circ]_{2s}$

$\theta = 90^\circ$

c. $[0^\circ, 90^\circ, \pm 45^\circ]_s$

$\theta = +45^\circ$ $\theta = 0^\circ$ $\theta = -45^\circ$

$\theta = 90^\circ$ SURFACE ROUGHNESS SIGNATURE

Figure 8—Polar plots of backscattering from three glass/epoxy eight-ply specimens (Specimens a and b were polished). Fiber orientation is clearly indicated.

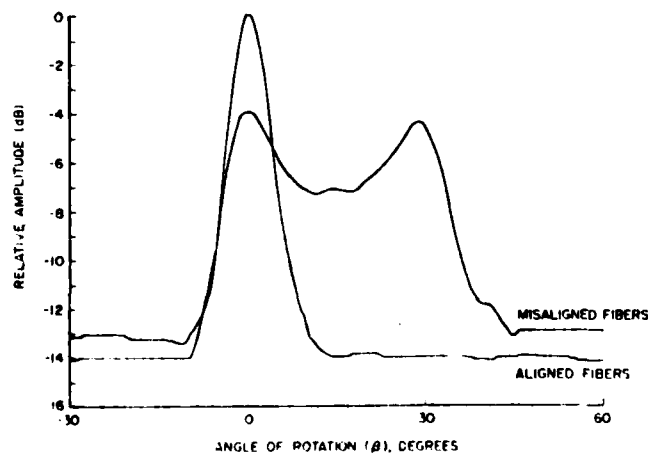


Figure 9(a)—Effect of fiber misalignment upon width of backscattering peak.

local waviness of the fiber tows. This is shown in Fig. 9(b), where good agreement between estimated and actual misalignments is observed.

While it was a relatively simple matter to measure fiber errors from peak broadening, it was far more instructive - although more difficult - to image the fiber array. This was accomplished by plotting the intensity of the backscattering as a function of position using polar C-scan instrumentation. Care was taken to use a focused transducer with focal spot size which was very small (0.3 mm) compared to the wavelength of the fiber-tow sine-wave displacement. The resulting image is shown in Fig. 10(a). As can be seen, a rather informative acoustic image of the fiber misalignment was obtained.

As noted earlier, discontinuities scatter whenever the normal to their surface is parallel to the acoustic main lobe of the transducer. Transverse cracks have preferred-direction scattering; and in graphite/epoxy laminates, a very strong scattering (~ 30 dB) was observed. This was determined by recording the scattering from the 90° ply of a quasi-isotropic graphite/epoxy laminate that had been fatigued to a point where this ply had numerous transverse cracks, as depicted in Fig. 11(a). The experiment was conducted in such a way that only back-scattered intensity levels above those associated with fiber scattering were recorded. It is apparent that the 0.13 mm high interply cracks are efficient reflectors of acoustic energy. It should also be noted that the $+45^\circ$ and -45° plies both above and below the ply of interest contained the same type of cracks; however, they are resolved separately as shown in Fig. 11(b). The cracks are imaged on a ply-by-ply basis. A radiograph of these specimens after treatment with opaque penetrant clearly showed these cracks and confirmed the accuracy of the acoustic image. The radiograph is not included here because the printed picture had much less resolution than that of the radiographic film and many crack indications were lost in the transfer process.

While the scattering due to the surface roughness caused by the bleeder-cloth impression is limited to specific directions, porosity gives rise to omni-directional scattering due to the spherical symmetry of each pore, dispersed through the composite. To document the effects of porosity, a $[0^\circ, 90^\circ]_{25}$ glass/epoxy laminate was fabricated with numerous hollow glass microspheres dusted between the 0° and 90° plies. The results of the scattering measurements are shown in Fig. 12. Since the outermost ply was unaffected by the porosity addition, scattering from it is undiminished. However, the enhanced background is caused by omni-directional scattering of the inter-laminar porosity. It is also apparent that much less ultrasonic energy reaches the 90° ply because its backscattering is significantly reduced. Interlaminar porosity scatters and, therefore, attenuates both the incoming and backscattered waves.

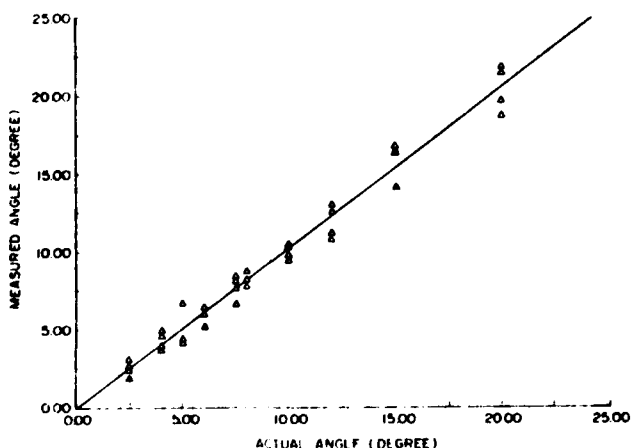


Figure 9(b) - Comparison of measured versus actual fiber misalignment in a single ply of glass/epoxy.

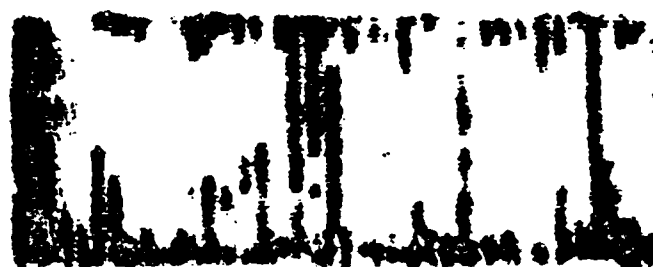


(a)

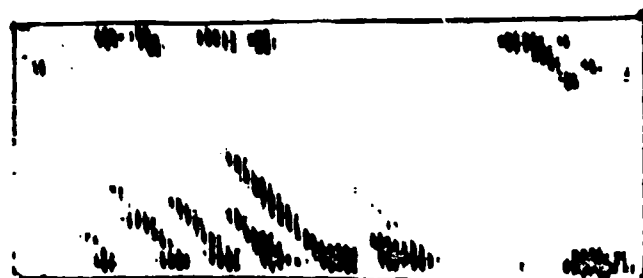


(b)

Figure 10 - Polar-scan imaging of misalignment a) sine texture, b) discrete misalignment of $0^\circ, \pm 30^\circ$. Scale factor is 1:1.



(a)



(b)

Figure 11 - Backscattering scan of quasi-isotropic composite a) $\beta = 90^\circ$, b) $\beta = 45^\circ$. Transverse cracks at 90° and 45° are separately resolved. Specimen was fatigue loaded to 75% of ultimate strength and 5000 cycles. Scale factor is 2:1.

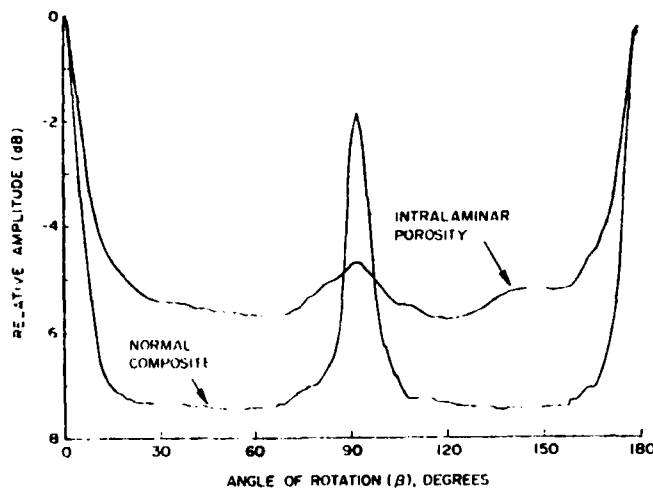


Figure 12—Backscattering from a $[0^\circ, 90^\circ]_{25}$ glass/epoxy composite, both with and without added interlaminar porosity.

CONCLUSIONS

The conclusions of the study are summarized below:

1. The backscattered acoustic field of a composite can be utilized to determine both gross fiber orientation and small misalignments of fiber bundles.
2. If the backscattered acoustic field is sampled in a rastered pattern across a composite plate, then it is possible to image or map the intralaminar cracks associated with ply failure. The process is analogous to C-scanning, the only difference being that the interrogating transducer must be carefully oriented with respect to both the composite plate and the flaws within a ply.
3. Backscattering requires development of analytical techniques if it is to serve as a quantitative tool for characterizing composite materials.

Acknowledgment

The authors wish to express their appreciation to Noel Tracy and Dan Laufersweiler of Universal Technology Corporation, Dayton, OH, for their assistance.

References

1. I. M. Daniel, S. W. Shramm, and T. Liber, "Fatigue Monitoring in Composites by Ultrasonic Mapping," *Materials Evaluation*, Vol. 29, No. 9, 1981, pp. 834-839.
2. P. M. Morse and K. V. Ingard, *Theoretical Acoustics*, 1968. McGraw-Hill, NY.
3. S. O. Aks and D. J. Vezzetti, "Ultrasonic Scattering Theory I: Scattering by Single Objects," *Ultrasonic Imaging*, Vol. 2, No. 2, 1980, pp. 85-101.
4. D. J. Vezzetti and S. O. Aks, "Review—Ultrasonic Scattering Theory II: Scattering from Composites," *Ultrasonic Imaging*, Vol. 2, No. 3, 1980, pp. 195-212.
5. M. Lax, "Multiple Scattering of Waves," *Review of Modern Physics*, Vol. 23, No. 4, 1951, pp. 287-310.
6. P. C. Waterman and R. Truell, "Multiple Scattering of Waves," *Journal of Mathematical Physics*, Vol. 2, No. 4, 1961, pp. 512-537.
7. M. O'Donnell and J. G. Miller, "Quantitative Broadband Ultrasonic Backscatter: An Approach to Nondestructive Evaluation in Acoustically Inhomogeneous Materials," *Journal of Applied Physics*, Vol. 52, No. 2, 1981, pp. 1056-1065.
8. V. K. Varadan, V. V. Varadan, and Y. Pao, "Multiple Scattering of Elastic Waves by Cylinders of Arbitrary Cross Section, I. SH Waves," *Journal of the Acoustical Society of America*, Vol. 63, No. 5, 1978, pp. 1310-1319.
9. S. K. Bose and A. K. Mal, "Longitudinal and Shear Waves in a Fiber-Reinforced Composite," *International Journal of Solid Structures*, Vol. 9, 1973, pp. 1075-1085.
10. S. K. Data, "Propagation of SH-Waves through a Fiber-Reinforced Composite—Elliptical Cylinders," *Journal of Applied Mechanics*, Vol. 42, No. 3, 1975, pp. 165-170.
11. S. L. Chang, "Multiple Scattering of Elastic Waves by Parallel Cylinders," *Journal of Applied Mechanics*, Vol. 36, No. 9, 1969, pp. 523-527.
12. V. T. Golovchan and A. N. Guz, "Diffraction of Elastic Waves by an Infinite Array of Circular Cylinders," *Soviet Physics-Doklady*, Vol. 14, No. 5, 1969, pp. 503-505.
13. S. Tsai and H. Hahn, *Introduction to Composite Materials*, 1980. Technomic Publishing Co., West Port, CT.
14. M. J. P. Musgrave, *Crystal Acoustics*, 1970. Holden-Day, San Francisco, CA.

NONDESTRUCTIVE EVALUATION OF FIBER-REINFORCED
COMPOSITES WITH BACKSCATTERING MEASUREMENTS

R. L. Crane

Air Force Wright Aeronautical Laboratories
AFWAL/MLLP
Wright-Patterson Air Force Base, OH 45433

Y. Bar-Cohen

Systems Research Laboratories, Inc
2800 Indian Ripple Road
Dayton, OH 45444

ABSTRACT: Experimental studies of acoustic backscattering in the Rayleigh region, i.e., $0.1 \leq ka \leq 1.0$, from fiber-reinforced composites were conducted. A significant increase in backscattering was observed for those orientations which place the axis of the fibers or other discontinuities at normal incidence to the acoustic beam. Using this technique, fiber orientations and the distribution of cracks within specific plies were easily mapped.

Introduction

During the past decade fiber-reinforced composites have found increasing utilization in primary (safety-of-flight) aircraft components. As with metal structures composites require detecting and tracking of service-induced damage and general material degradation using nondestructive evaluation (NDE) methods. One of the most widely used techniques for this purpose is ultrasonic measurements. However, this NDE method was developed principally for the inspection of metal structures, i.e., it is optimized for the detection of single flaws in homogeneous, isotropic, monolithic materials. Unfortunately, the detection of flaws in composite materials is particularly difficult because of the inhomogeneous, anisotropic, layered nature of the materials. Another complication arises from the fact that composites do not appear to degrade via the growth of a single dominant flaw, but rather by the growth of a damage zone consisting of a myriad of very small cracks. These difficulties led us to investigate ultrasonic backscattering (see Fig 1) which utilizes the inhomogeneous, layered nature of the composite to detect and image dominant microstructural features, such as cracks, fibers, etc.

Presented at the 29th Defense Conference on Nondestructive Testing, November 17-20, 1980, McClellan Air Force Base, CA; published in Conference Proceedings.

The scattering of waves has been the subject of numerous publications, because one can deduce much about the scatterer from measurements of the angular distribution and magnitude of the scattered energy. Recent attention to the scattering of sound waves by single objects in homogeneous solid or fluid media has defined what information concerning the size and identity of the scatterer can be gleaned from acoustic measurements (see for example, Refs (1) and (2)). The situation is much more difficult to analyze in the case of composite materials, because sound energy is reflected at the interface between layers and scattered by the fibers and numerous inherent flaws within each ply. Analysis of experimental data must, therefore, depend upon a consideration of multiple scattering. The diffuse scattering by dispersoids has received much attention in recent years, particularly with regard to biological materials (3). While theoretical analyses of multiple scattering in solids have been performed (4,5), researchers have only recently attempted to rationalize analytical predictions with quantitative measurements of the phenomenon. O'Donnell and Miller (6) were able to obtain reasonable agreement between analysis and experiment for a plastic containing approximately 4.0 volume percent voids. While this and most previous work has been done with media containing spherical voids, very little work--either analytical or empirical--has examined the scattering of coaxial aligned cylinders. The analysis of Varadan, et al (7), examined the forward scattering of randomly dispersed, coaxial fibers; but the results are not generally applicable to composites because of the limitation of the analysis to low-volume-fraction, non-layered media. The work of Base and Mal (8) and Data (9) are similarly limited in applicability. Therefore, the present work examines--from an experimental standpoint--backscattering from composites. The results of the experiments are quite useful to those attempting to track or monitor mechanical damage to composites.

Experimental Procedures

Four types of composites were examined in this investigation. These were glass/epoxy (fabricated from Scotch 1002), graphite/epoxy (T300 fiber/5200 resin), 5.6 mil boron/epoxy and silicon carbide (5.6 mil)/titanium (Ti-6Al-4V). Various cross-ply lay-ups were used for both the glass/epoxy and graphite/epoxy materials; but for the other two materials, only unidirectional specimens were fabricated. All specimens consisted of 2 - 14 plies, depending upon the complexity of the lay-up; e.g., unidirectional panels usually contained two plies, while quasi-isotropic panels contained eight. All systems were fabricated using standard autoclave cycles which had been optimized for minimum porosity in the finished laminates. One specimen was specifically designed to contain a high level of interlaminar porosity. For this purpose, hollow glass micro-spheres¹ - 80 um in diameter were dusted between glass/epoxy tapes during lay-up. Because of the highly localized nature of the porosity,

no attempt was made to accurately measure the volume fraction of porosity. However, estimates of the amount from gravimetric measurements indicate it to be - 2.0 percent.

The instrumentation used in these experiments is shown schematically in Fig 2. The 6.35 mm (0.25 in.) diameter piezoelectric transducer was driven by a Panametrics PR5052 pulser/receiver. The center frequency of the interrogating pulse of ultrasound was varied from 5.0 to 20.0 MHz. This gave values of ka in the range 0.1 to 1.0--where k is the wave number and equal to $2\pi/\text{wavelength}$, and a is the nominal diameter of the scattering object. In several experiments data were time-averaged using a Princeton Applied Research box-car averager to reduce system noise.

Referring to Fig 3, backscattered data were taken for angles of incidence in the range $0^\circ \leq \alpha < 90^\circ$ and angles of rotation in the range $0^\circ \leq \beta < 180^\circ$. It should be noted that the angle α is always measured from the vertical, and β is measured clockwise with respect to the plate x-axis. This is similar to standard notation of ply orientation. In the experiments in which β was varied, the specimen was mounted on a rotating table in a water bath which served as an ultrasonic couplant and delay line. The amplitude of backscattered sound was recorded as a function of angular position.

Results and Discussion

The backscattered ultrasonic signal for a typical unidirectional composite material is shown in Fig 4. It is obvious from these data that a maximum in backscattered energy occurs over a small angular range on either side of normal incidence to the fiber axis. That is, reflection of the ultrasonic beam occurs only when the incident beam is approximately at right angles to the axis of the fibers within a particular layer. The effect of surface roughness is also shown. While surface roughness was not a problem in most experiments, the surfaces of several specimens were sanded smooth to permit accurate imaging of small defects.

The backscattering as a function of angle of incidence, α , for both unidirectional glass/epoxy and silicon-carbide composites is shown in Fig 5. Even though the specimens were quite thin, i.e., two plies, the effects of angle of incidence are adequately demonstrated. The peaks in both curves occur at two quasi-critical angles. Because both the longitudinal and shear-wave velocities change as a function of α and β , the curves in Fig 5 change with each new orientation, β , of the transducer and specimen. Since backscattering is more intense at the critical angles, most experiments were conducted at the angle of incidence which provided the most intense signals.

Backscattering as a function of angle of rotation, β , for quasi-isotropic graphite/epoxy is shown in Fig 6. It is quite obvious that each layer of the composite reflects over a small range of angle β . Since the frequency of the insonifying pulse was ~ 5 MHz, the ka is ~ 0.16 , assuming the wavelength of the fast shear wave to be 0.37 mm. Rayleigh scattering predominates in this region of ka . It was also noted that the intensity of the scattering from glass/epoxy is ~ 3 to 5 dB higher than that from the graphite/epoxy composite. This is presumably due to the much larger difference in acoustic impedance between glass and epoxy as compared to that between graphite and epoxy--the acoustic impedances of graphite, glass, and epoxy are 6.89, 14.48, and 3.48×10^5 gm/cm² sec., respectively. The difference in impedance for glass/epoxy is almost three times that of graphite/epoxy. This cannot completely account for the difference in scattered intensity since the difference in fiber/scatterer diameter and the number of scatterers per unit volume must also be considered. Unfortunately, the only models of scattering from a layer of cylinders developed thus far present quite difficult computational problems (10). Therefore, a rationalization of analysis and experiment is not possible at this time.

A schematic diagram demonstrating the angular relationship between the scattering angle, β , and ply orientation is shown in Fig 7. The only point that should be noted from this diagram is that the x and y axes of the composite plate are uniquely related to the axis of the scanning system. The scan of a specially fabricated graphite/epoxy composite is shown in Fig 8. In this case it is obvious that in order to uniquely specify ply orientation, the relationship between the measurement coordinate system and that associated with the composite must be carefully specified; for example, the $\{0^\circ, -15^\circ, -30^\circ, +45^\circ, -60^\circ, +75^\circ, 90^\circ\}_S$ composite could easily become a $\{0^\circ, +15^\circ, +30^\circ, -45^\circ, +60^\circ, -75^\circ, 90^\circ\}_S$ if the plate were inverted so that the +x axis becomes the -x axis.

A polar plot of scattering intensity as a function of angle of rotation is shown in Fig 9. Data were obtained for a unidirectional, $\{0^\circ\}_8$, $\{0^\circ, 90^\circ\}_{2S}$ and quasi-isotropic $\{0^\circ, 90^\circ, +45^\circ\}_S$ graphite/epoxy material. The effects of surface roughness are shown in Fig 9(c) as the background speckle with a preferred orientation in the 0° and 90° directions. This is the result of the bleeder-cloth impression on the surface of the plate. If a strippable lacquer² is used to coat the surface, then a reduction (~ 2 dB) in scattering from surface roughness is observed.

Since the scattering discussed so far arises from the fibers and is dependent upon their orientation, it was a natural extension of these experiments to investigate the effects of slight misalignments within a specific ply. If the focal spot of the transducer covers an area that has minor misalignments, i.e., fiber waviness, then this should cause

a broadening of the scattering peak. For sharp bends in the composite tape, peak broadening eventually leads to two peaks as shown in Fig 10. If the peak width is calibrated against known angles of misalignment, then it is a simple matter to estimate the local waviness of the fiber tows. This is shown in Fig 11 with good agreement between estimated and actual misalignment.

While the scattering due to the surface roughness caused by the bleeder-cloth impression is limited to specific directions, porosity gives rise to omnidirectional scattering due to spherical voids dispersed throughout the composite. To document the effects of porosity, a $\{0^\circ, 90^\circ\}_{25}$ glass/epoxy laminate was fabricated with numerous hollow epoxy microspheres dusted between the 0° and 90° plies. The results of the scattering measurements are shown in Fig 12. Since the outermost ply was unaffected by the porosity addition, scattering from it is undiminished. However, the enhanced background caused by omnidirectional scattering of the interlaminar porosity is most evident. It is also apparent that much less ultrasonic energy reaches the 90° ply since its backscattering is significantly reduced. Interlaminar porosity scatters and, therefore attenuates both the incoming and backscattered waves.

While both porosity and the fibers of a composite are strong scatterers of ultrasonic energy, cracks should be even stronger scatterers. This supposition was tested by recording the scattering from the 90° ply of a quasi-isotropic graphite epoxy laminate that had been fatigued to a point where the 90° ply had numerous transverse cracks. The experiment was conducted in such a manner that only backscattered intensity levels above those associated with fiber scattering were recorded. The results are shown in Fig 13. It is quite obvious that interply cracks are being recorded and not the fibers when the fatigued specimens are compared with unloaded or pristine specimens. It should also be noted that the $+45^\circ$ and -45° plies both above and below the ply of interest contained the same type of cracks, but these are not shown. A radiograph of these specimens after treatment with opaque penetrant clearly shows the extent of this damage. The radiograph is not included for two reasons. First, the printed picture has much less resolution than that of the radiographic film, and many crack indications are lost in the transfer process. Second, since the acoustic image is obtained off the axis of the crack, several cracks may appear as one, limiting a one-to-one correlation.

Conclusions

The conclusions of the study are summarized below:

1. The backscattered acoustic field of a composite can be utilized to determine both gross fiber orientation and small misalignments of fiber bundles in a specific ply.

2. If the backscattered acoustic field is sampled in a rastered pattern across a composite plate, then it is possible to image or map the intralaminar cracks associated with ply failure. The process is analogous to c-scanning. The only difference in the technique is that the interrogating transducer must be carefully oriented with respect to both the composite plate and the probable orientation of flaws within a ply.

3. Work is continuing on a method of separating the omnidirectional scattering of porosity from that of oriented flaws. If this process can be made quantitative, then a tool will be available that will permit mapping of most of the currently known pernicious flaws in a composite.

Acknowledgement

The author wish to express their appreciation to Noel Tracy of Universal Technology Corporation, Dayton, OH, for his assistance.

References

1. Morse, P. M. and Ingard, K. V., Theoretical Acoustics, McGraw-Hill, NY, 1968.
2. Aks, S. O. and Vezzetti, D. J., "Ultrasonic Scattering Theory I: Scattering by Single Objects," Ultrasonic Imaging, Vol 2, No. 2, 1980, pp. 85-101.
3. Vezzetti, D. J. and Aks, S. O., Ultrasonic Imaging, Vol 2, No. 3, 1980, pp. 195-212.
4. Lax, M., "Multiple Scattering of Waves," Review of Modern Physics, Vol 23, No. 4, 1951, pp. 287-310.
5. Waterman, P. C. and Truett, R., "Multiple Scattering of Waves," Journal of Mathematical Physics, Vol 2, No. 4, 1961, pp. 512-537.
6. O'Donnell, M. and Miller, J. G., "Quantitative Broadband Ultrasonic Backscatter: An Approach to Nondestructive Evaluation in Acoustically Inhomogeneous Materials," To appear in Journal of Applied Physics.
7. Varadan, V. K., Varadan, V. V. and Pao, Y., "Multiple Scattering of Elastic Waves by Cylinders of Arbitrary Cross Section, I. S. H. Waves," Journal of the Acoustical Society of America, Vol 63, No. 5, 1978, pp. 1310-1319.
8. Base, S. K. and Mal, A. K., "Longitudinal and Shear Waves in a Fiber-Reinforced Composite," International Journal of Solid Structures, Vol 9, 1973, pp. 1075-1085.
9. Data, S. K., "Propagation of SH-Waves through a Fiber-Reinforced Composite-Elliptical Cylinders," Journal of Applied Mechanics, Vol 42, No. 3, 1975, pp. 165-170.
10. Chang, S. L., "Multiple Scattering of Elastic Waves by Parallel Cylinders," Journal of Applied Mechanics, Vol 36, No. 9, 1969, pp. 523-527.

Footnotes

¹Emmerson and Commings, Inc., Canton, MA.

²The Sherwin Williams Corp., Cleveland, OH, Stripple Alcquer M69W1

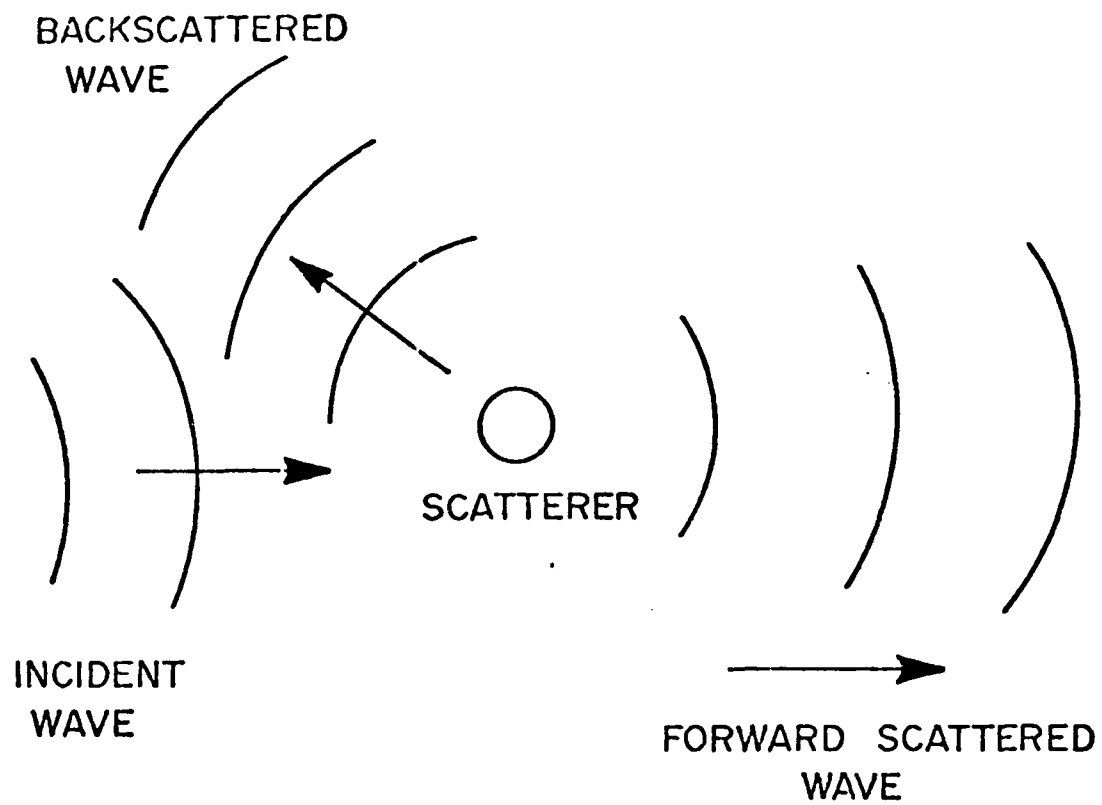


Fig 1. Schematic of Acoustic Scattering

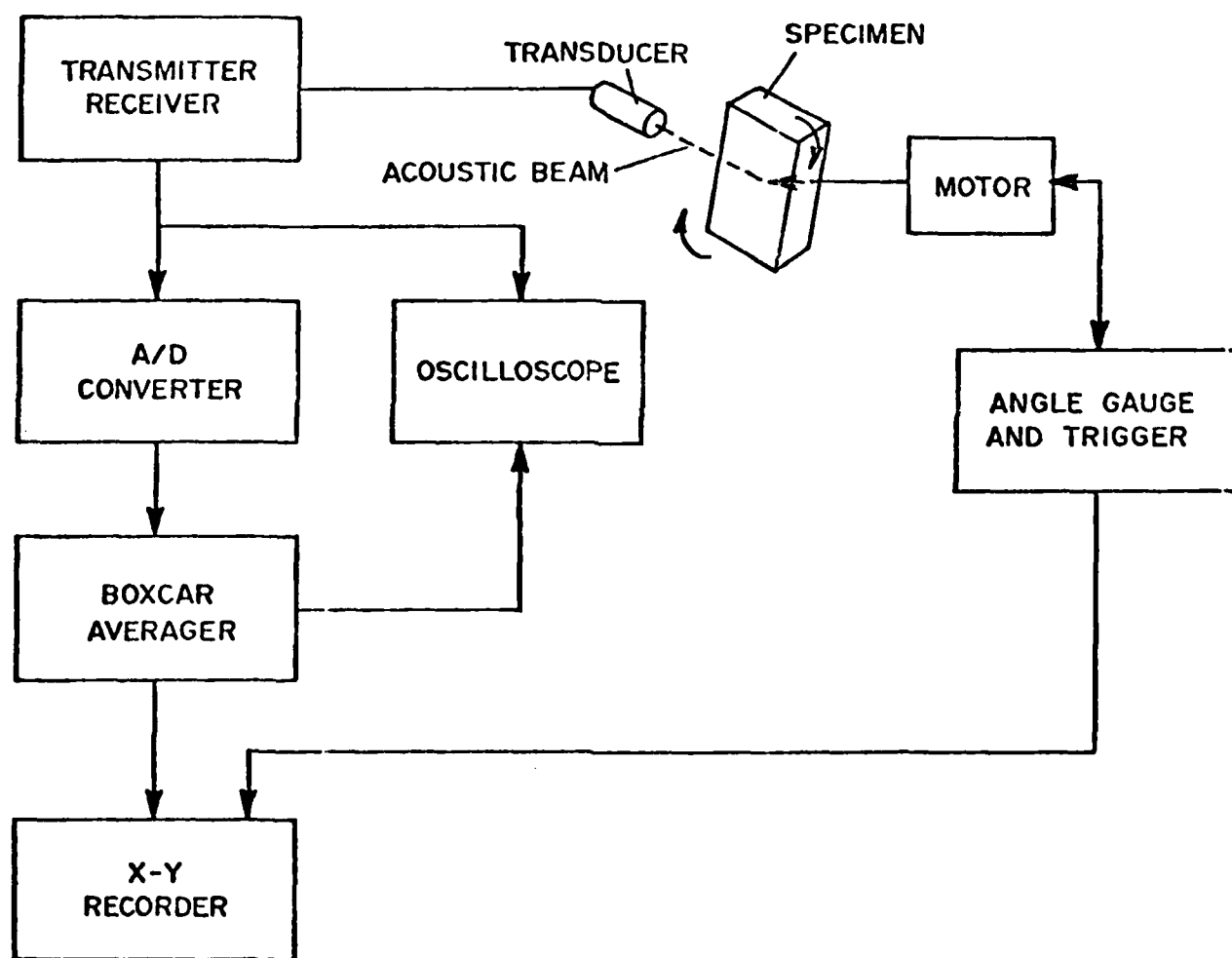
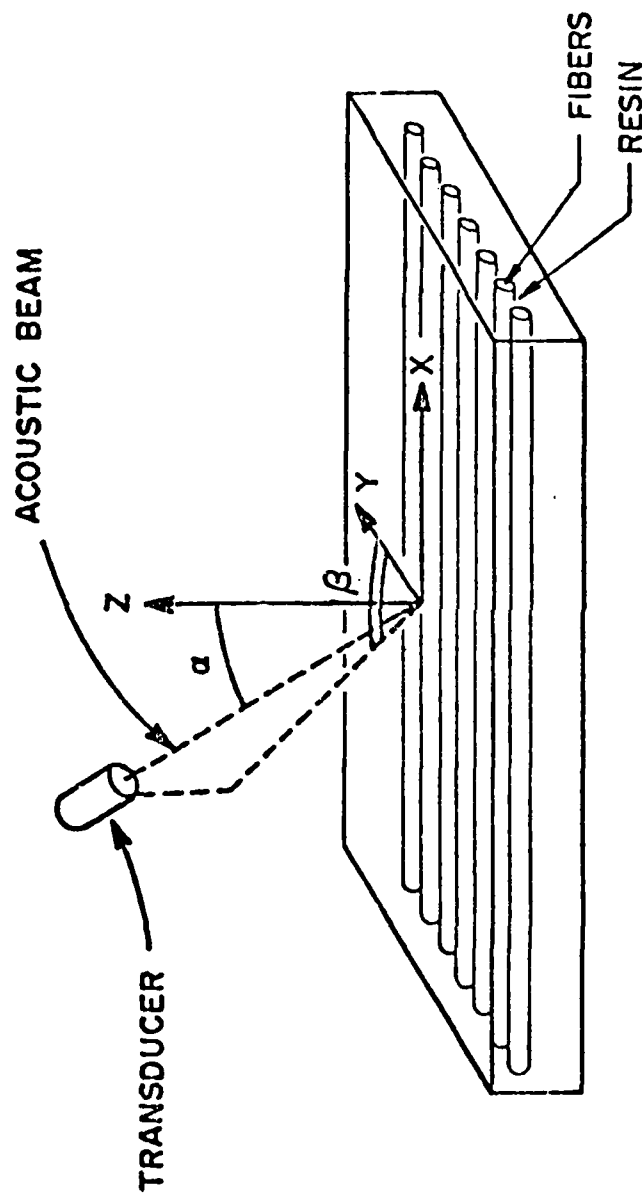


Fig 2. Schematic Representation of Electronic Instrumentation Used in Backscattering Experiments.



WHERE:

α - ANGLE OF INCIDENCE

β - ANGLE BETWEEN Y-AXIS AND THE TRANSMITTER
BEAM TRAJECTORY ON THE LAYER PLANE

Fig 3. Schematic of Experimental Set-up Used to Measure Backscattering from Composite Samples.

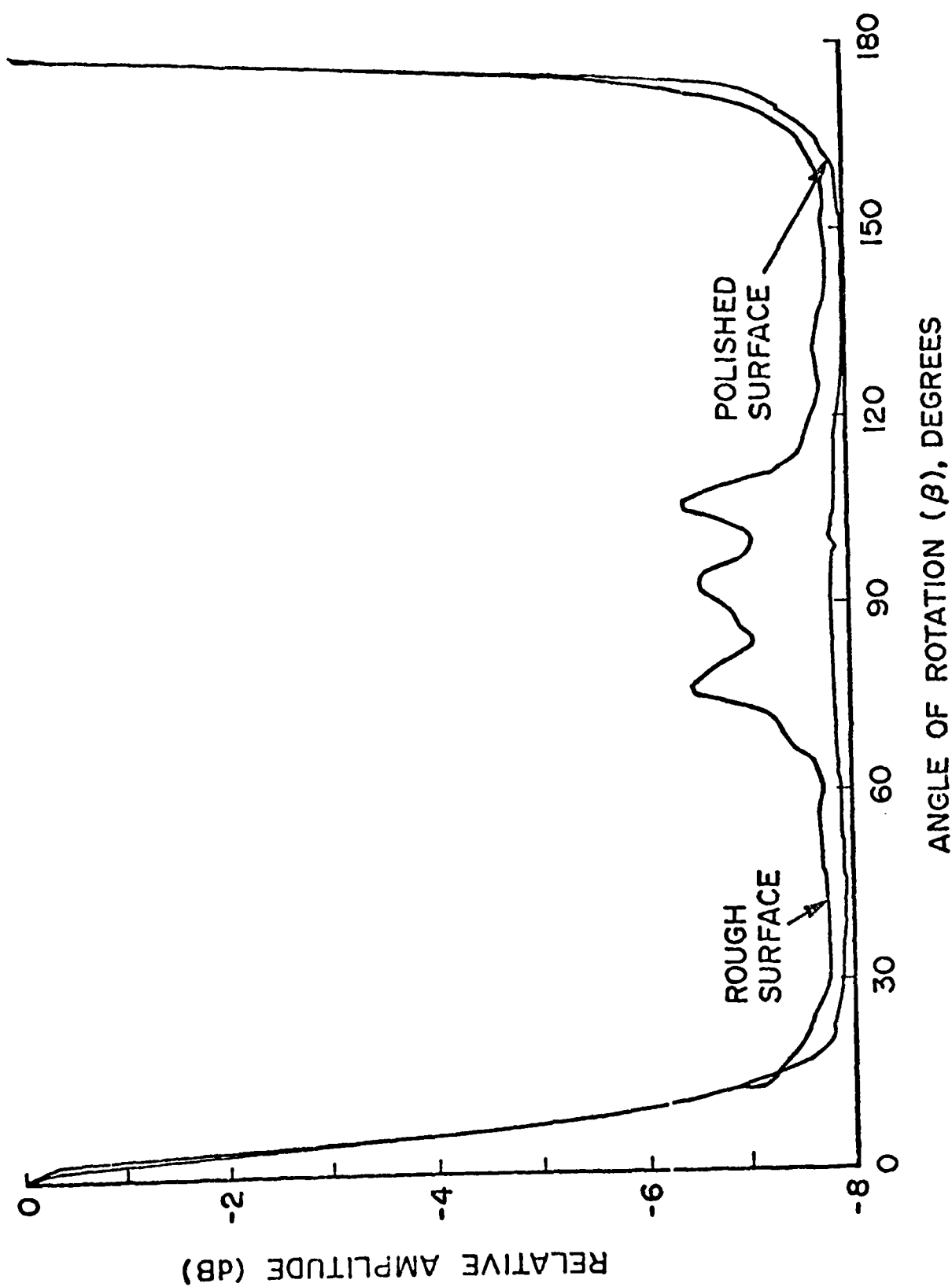
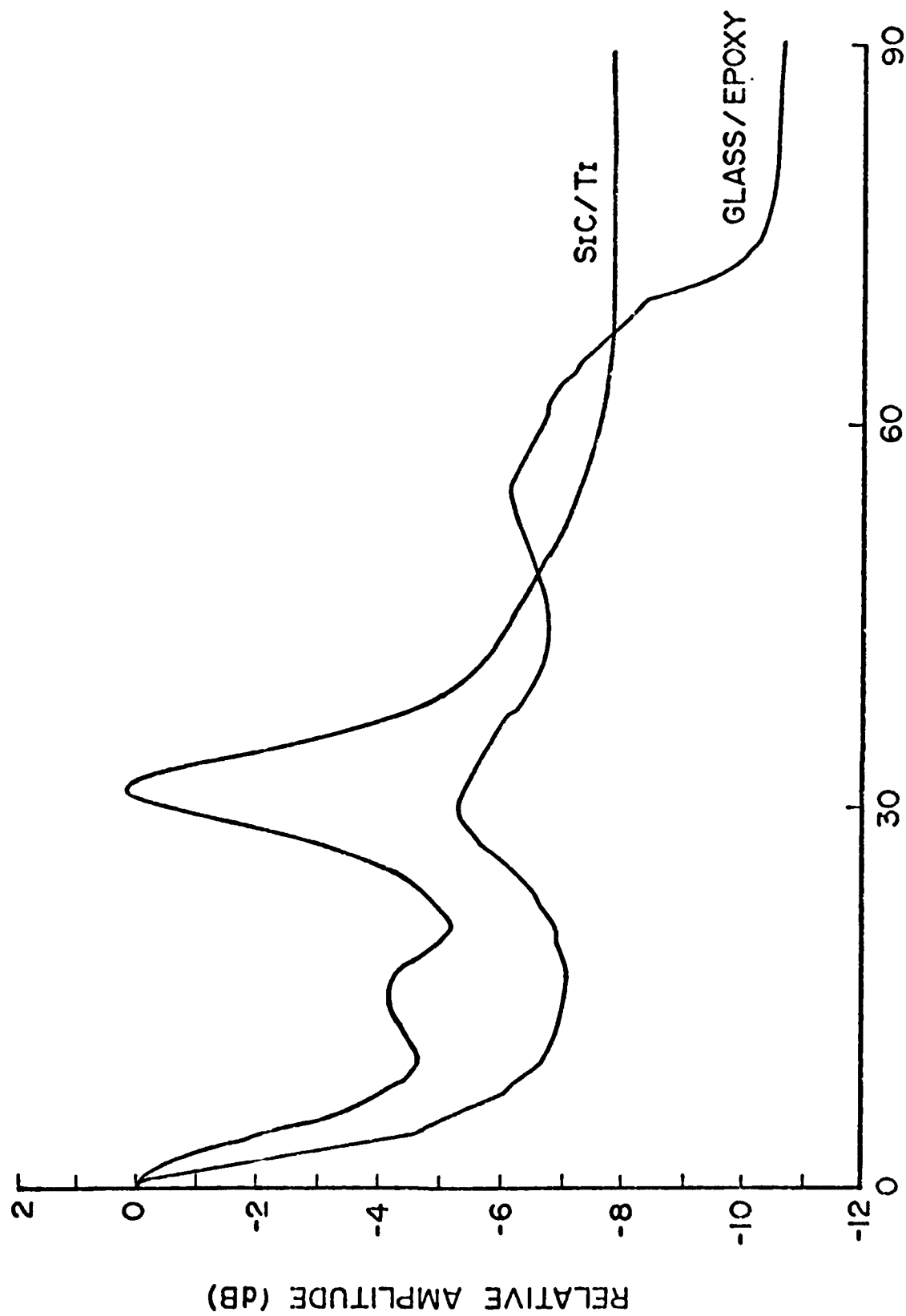
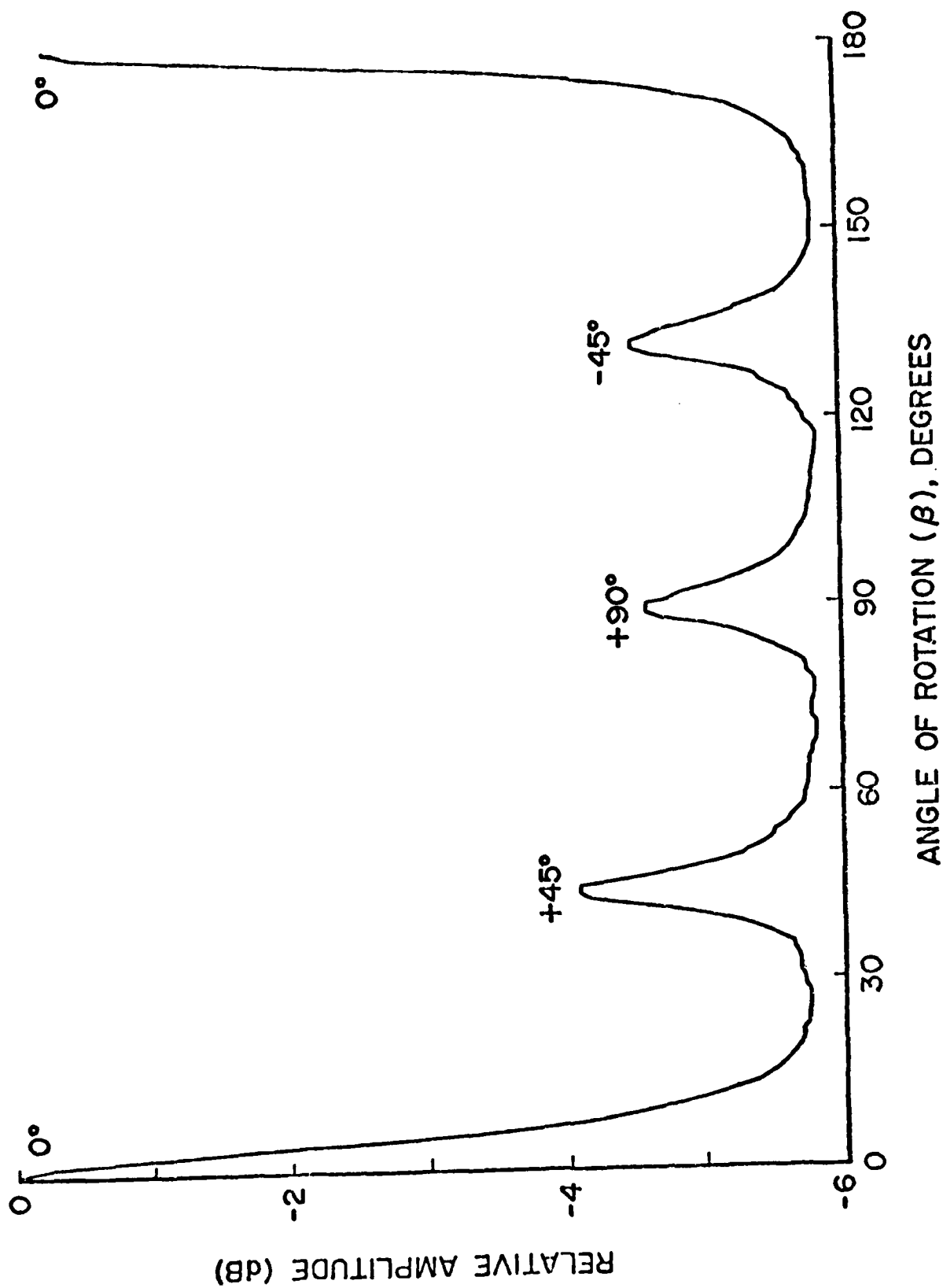


Fig 4. Backscattering from a Unidirectional $\{0^0\}_8$ glass/epoxy composite. The effect of surface roughness is also shown. The angle of incidence $\alpha = 30^0$.



ANGLE OF INCIDENCE (α), DEGREES

Fig 5. Comparison of Backscattering from Both a SiC/Ti and a Glass/Epoxy Composite as a Function of Angle of Incidence. Rotational Angle $\beta = 0$.



ANGLE OF ROTATION (β), DEGREES

Fig 6. Backscattering from a Quasi-Isotropic $\{0^\circ, +45^\circ, 90^\circ\}_s$ Graphite/Epoxy Composite. Each Ply is Evident. Angles of Incidence $\alpha = 30^\circ$.

Diagram illustrating the geometry of a quasi-isotropic piezoelectric transducer. The transducer is represented by a rectangular block on the left, labeled "QUASI-ISOTROPIC" and "TRANSDUCER". An "ACOUSTIC BEAM" is shown entering the transducer from the left. The beam's direction is defined by the angle β relative to the horizontal axis. The beam's path is shown as a curved line with arrows indicating the direction of propagation. The beam's path is labeled with angles $\beta = 0^\circ$, $\beta = 45^\circ$, $\beta = 90^\circ$, $\beta = 135^\circ$, and $\beta = 180^\circ$. The beam's path is also labeled with angles $\theta = 0^\circ$, $\theta = +45^\circ$, $\theta = 90^\circ$, $\theta = -45^\circ$, and $\theta = 0^\circ$. The beam's path is also labeled with angles $\theta = 0^\circ$, $\theta = +45^\circ$, $\theta = 90^\circ$, $\theta = -45^\circ$, and $\theta = 0^\circ$.

θ — FIBER ORIENTATION
 β — POLAR ANGLE WITH Y-AXIS
 $\theta = 0^\circ$ — FIRST PLY ORIENTATION

Fig 7. Schematic Diagram of Composite Plate and Measurement Coordinate Systems.

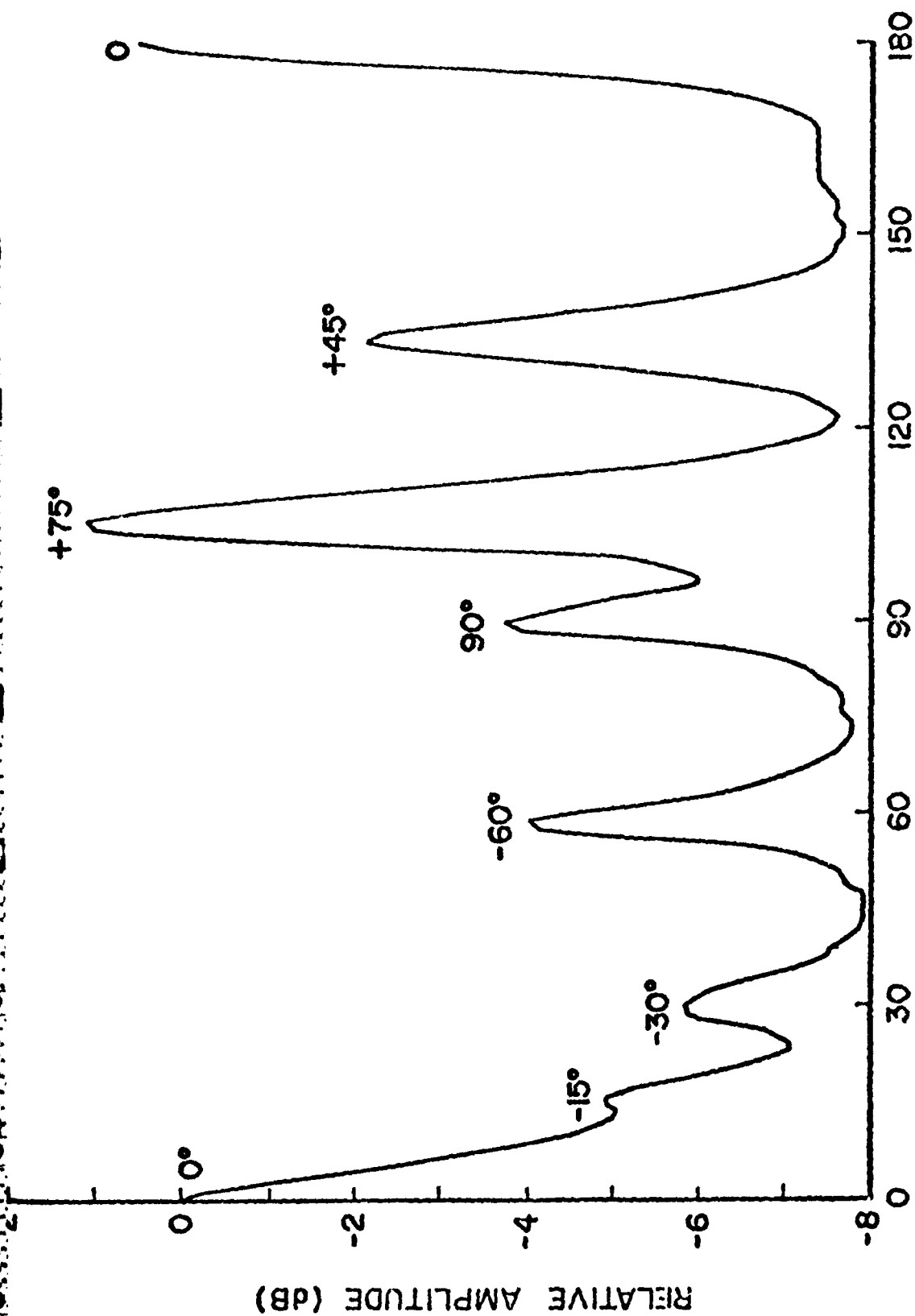
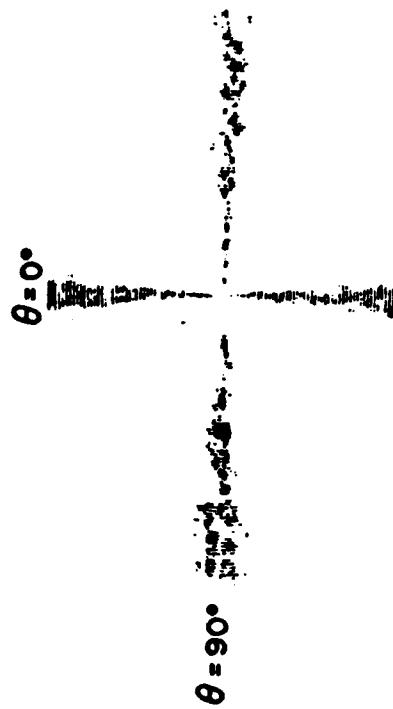


Fig 8. Backscattering from a $\{0^\circ, -15^\circ, -20^\circ, +45^\circ, -60^\circ, +75^\circ, 90^\circ\}_S$ Graphite/Epoxy Composite $\alpha = 40^\circ$.

a. $[0^\circ]_8$



b. $[0^\circ, 90^\circ]_{2S}$



c. $[0^\circ, 90^\circ, \pm 45^\circ]_S$



Fig 9. Polar Plots of Backscattering from Three Graphite/Epoxy Composites as a Function of Angle of Rotation β .

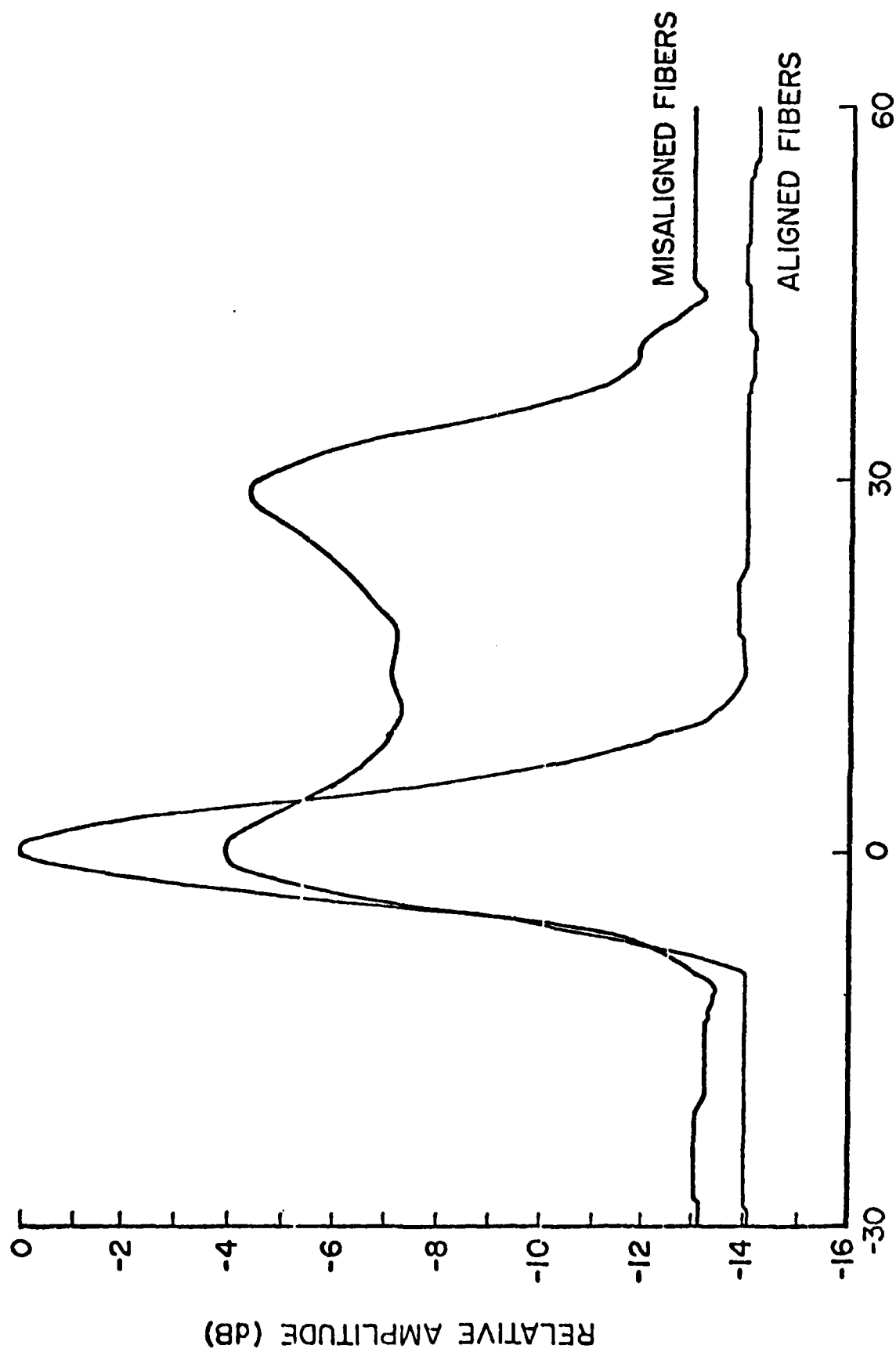


Fig 10. Effect of Fiber Misalignment on Width of Backscattering Peak.

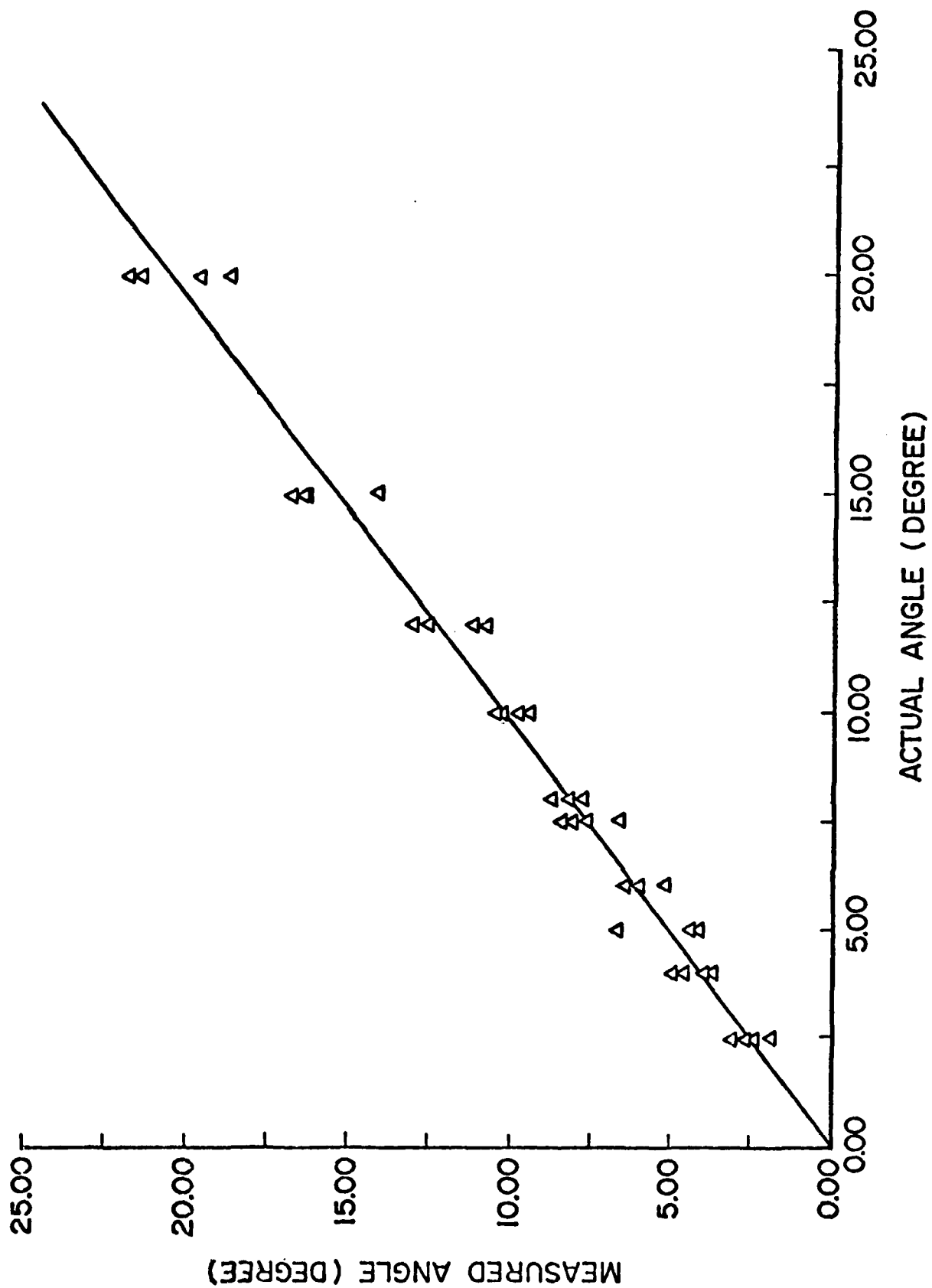


Fig 11. Comparison of Measured Versus Actual Fiber Misalignment in a Single Ply of Glass/Epoxy.

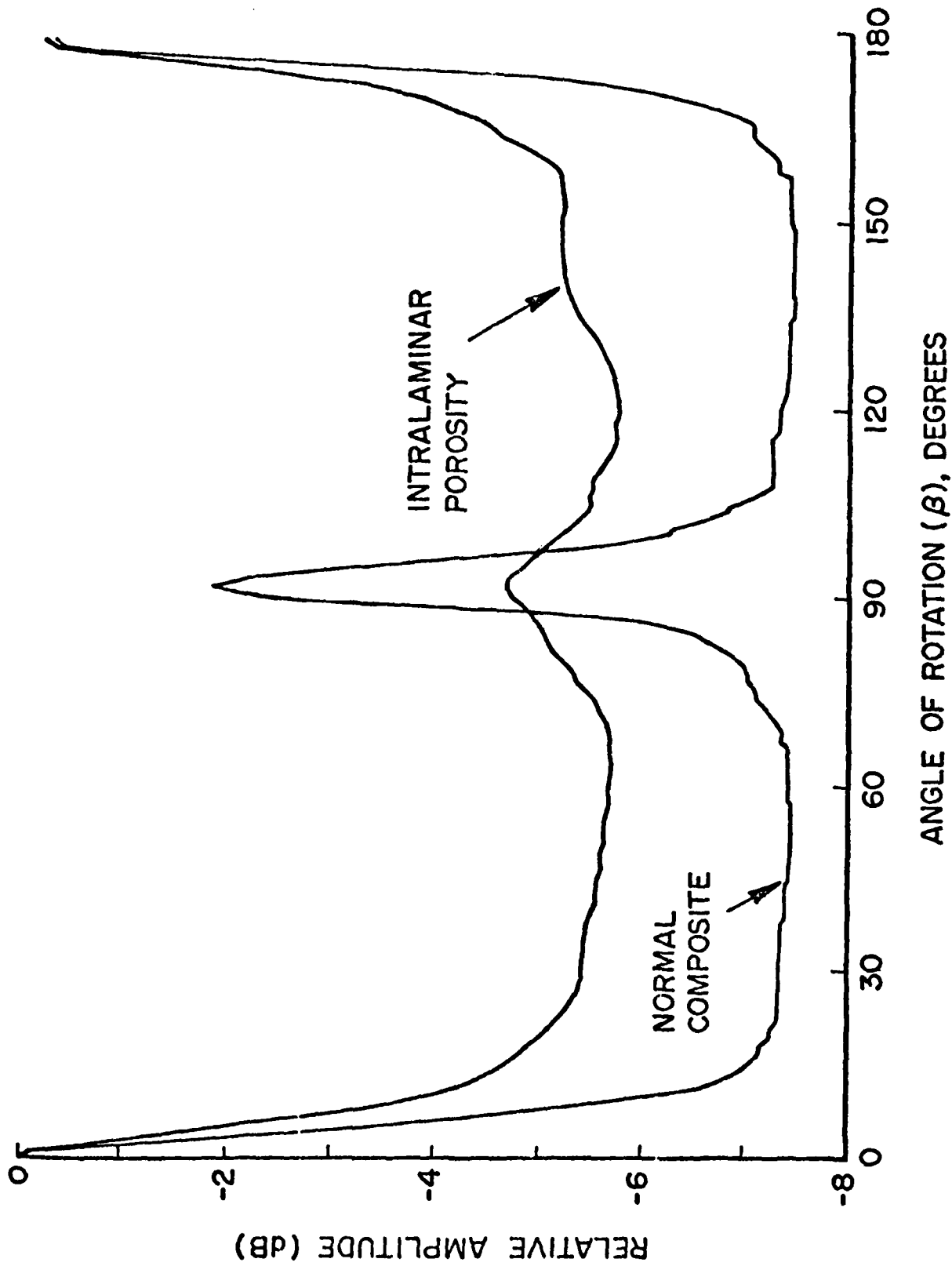


Fig 12. Backscattering from a $\{0^\circ, 90^\circ\}_{2S}$ Glass/Epoxy Composite, Both With and Without Added Interlaminar Porosity.

a. REFERENCE
SPECIMENS



b. FATIGUED
SPECIMENS
(50 KSI, 20 kc)



Fig 13. Backscatter Scan of Quasi-Isotropic Composites for $\alpha = 40^\circ$ and $\beta = 90^\circ$. Both Pristine Specimens and Those with 90° Ply Cracks are Shown.

APPENDIX E

C-SCAN SYSTEM

ANALOG-TO-DIGITAL UNIT

A 12-bit analog-to-digital (A/D) converter unit is used to digitize and store one scan line of a C-scan (see Fig. E-1). Digitization is accomplished with a Datal/Intersil Miniature Modular Data Acquisition System, Model MDAS-16. Up to 16 separate, single-ended, analog inputs are available. Control of the A/D is maintained with a microcomputer (μ C). A Motorola MC6809E was chosen as the microprocessor (μ P). The A/D may be triggered from two sources--the μ C and an external device. An external trigger would originate from an instrument such as the position encoder unit. A detailed description of the MDAS-16 can be found in the specification sheet on that item.

Operation of the A/D unit is controlled by the μ C. The μ C consists of a microprocessor unit (MPU or μ P), 3 Kbyte of random access memory (RAM) including 1 Kbyte for scratchpad use and 2 Kbyte for buffer storage, provision for up to 8 Kbyte of erasable/programmable read-only memory (EPROM), an IEEE-488 Interface, and two peripheral interface adapters (PIA's).

EPROM is used to store the program which the μ C employs to control its operation. This program divides the duties of the μ C into two main parts--one which reads the output of the MDAS-16 when it has acquired data and then stores that data in the buffer memory and the second which controls the communication of data and commands over the IEEE-488 interface bus [also referred to as the general purpose interface bus (GPIB)]. Since the A/D has 12-bit words, up to 1024 data points can be stored in the buffer memory. With an appropriate change in software, fewer bits of the A/D could be used, thus increasing the storage capacity of the buffer.

The MDAS-16 is presently wired for ± 10 -V signals. The digital output is in 2's complement form. The PIA's are used to interface the A/D with the μ C. Channel selection is controlled by the μ C through the GPIB. An L.E.D. display is used to indicate to the user which channel is active.

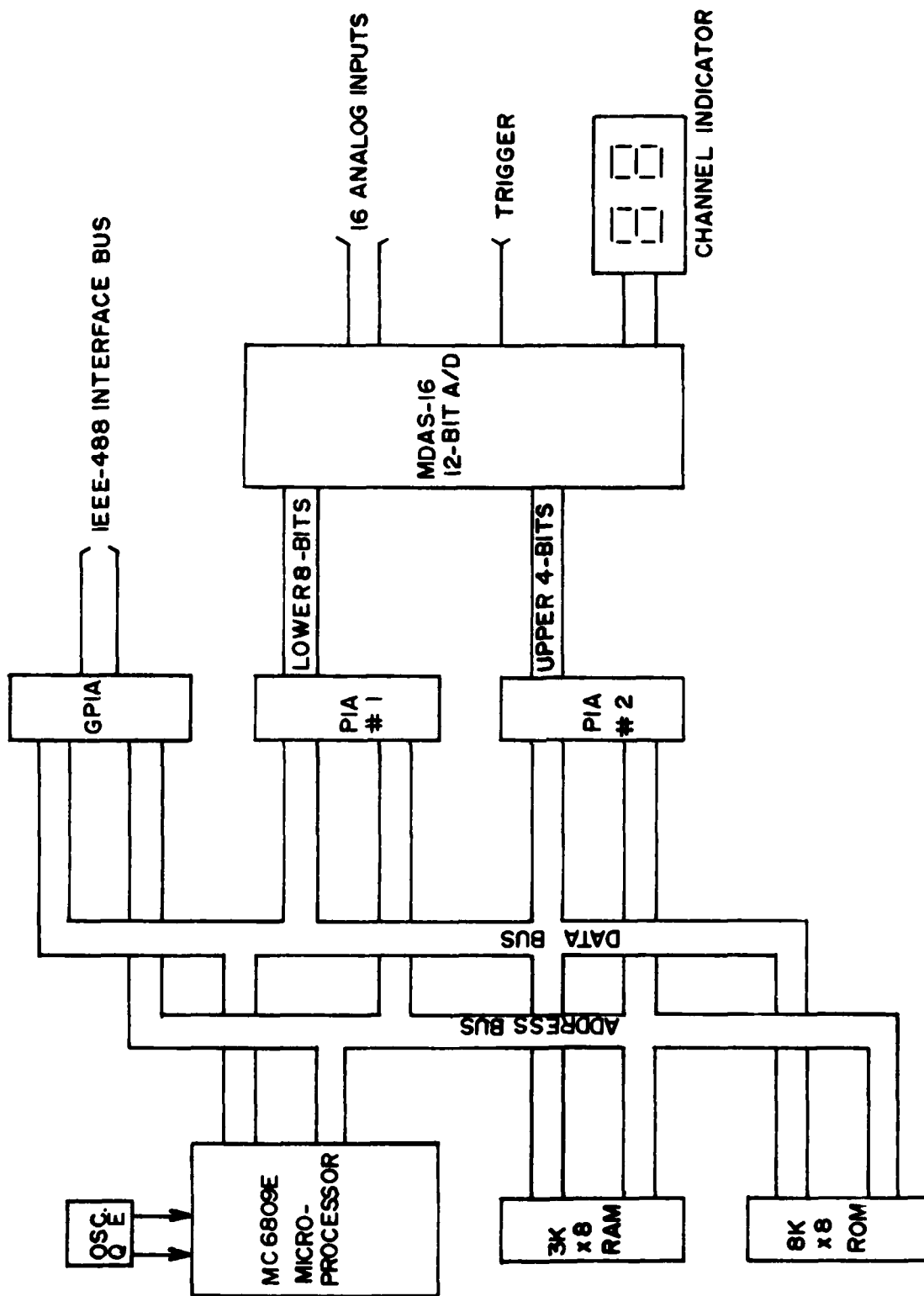


Figure E-1. Block Diagram of Analog-to-Digital Unit.

As stated, the A/D unit is capable of receiving commands/data and transmitting data over the GPIB. Electrically this is accomplished by means of a Motorola MC68488 GPIA integrated circuit along with two MC3447 bus transceivers. The GPIA handles the GPIB protocol to relieve the μ C of that task. Through the GPIB an external controller such as the LSI-11 or HP-9825 computer could change channels, initiate an acquisition sequence, change the number of data points taken, etc.

The front panel of the instrument has only two switches--a power switch and a reset switch. The function of the power switch is obvious. Actuation of the reset switch causes the reset input of the μ P to be asserted, the result being the same as if the unit were turned off and then on again. It is faster to reset the unit in this way due to the fact that the power supplies remain active for a short period of time after the power to the unit is turned off. Internally a set of switches defines the A/D's address on the GPIB. The address chosen should be different from that of any other device being used on the same GPIB system at the same time.

POSITION ENCODER UNIT

The purpose of the position encoder is to supply trigger pulses to the A/D unit at programmed intervals-of-distance of a mechanical translator. As with the A/D unit, the position encoder (PE) uses a μ C to control its operation (see Fig. E-2). Interfacing to the C-scan computer (LSI-11) is accomplished with the GPIB. Provision is made for the future addition of electronics to handle the output of a rotary shaft encoder during the performance of polar scans.

Position information is obtained from linear-scale optical spars located on the C-scan water tank. Two axes are supplied--X and Y. Pulses from the spars are processed by a digital readout system manufactured by Mitutoyo. For operation in the English system of measurement, the resolution is 0.0005 in. The position displayed is a distance relative to a user-defined zero reference point. Multiplexed binary-coded-decimal (BCD) information is available on connectors at the back of the readout system. Modifications to some of the signal lines going to these connectors allow other internal signals to be used by the PE.

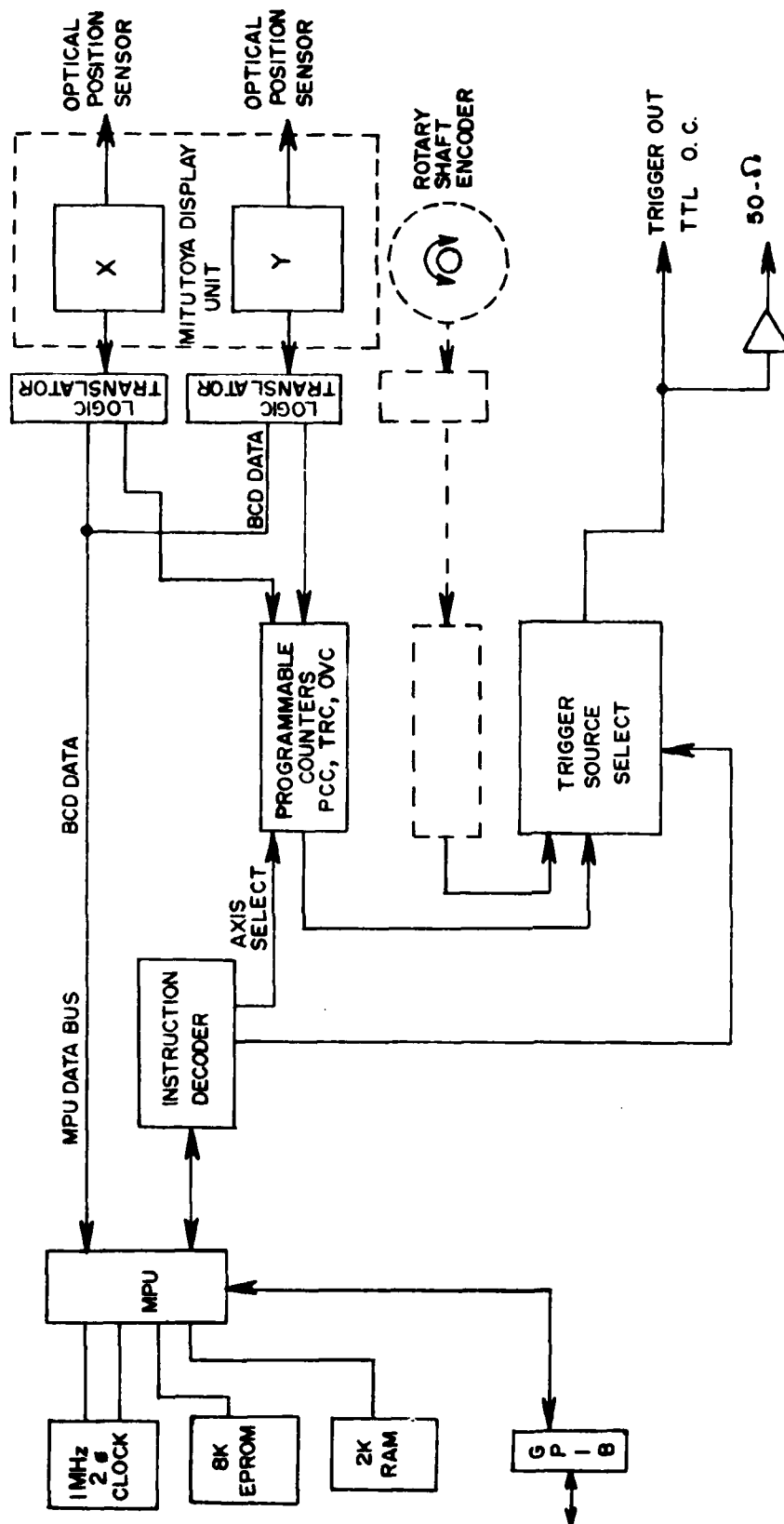


Figure E-2. Block Diagram of Position Encoder Unit.

Level translators are used to interface the Mitutoyo readout system to the PE since the logic circuits in the readout system use a + 12-V power supply, while those in the PE use + 5V.

Programmable up/down counters are used to count conditioned pulses from the spars. The three counters are: position-change (PCC), trigger (TRC), and overscan (OVC). One set of counters is used for both axes. Only one axis at a time is used to generate trigger pulses, the one used being determined by external programming. The frequency of trigger pulse generation, in terms of distance traveled, is determined by the PCC. If the decision is made to generate a trigger pulse every 10 mils, the PCC is programmed to count 10 pulses (it counts 1.0-mil displacement pulses). For every trigger pulse generated by the PCC, the TRC is decremented by one. The TRC is programmed with the number of data points to be taken on one scan line. When the TRC reaches zero, trigger pulses are inhibited and the OVC tracks the mechanical translator.

Both the PCC and TRC are wired as down counters, while the OVC is wired as a true up/down counter. The PCC generates the trigger pulses.

The μ C for the position encoder is essentially the same one used for the A/D unit. There are slight differences in some of the integrated circuits used. The main difference is that less RAM is used (no buffer storage is required) and no PIA's are incorporated. The programmable counters are memory mapped.

There are two types of outputs for the trigger pulses; the primary one drives a TTL open-collector transistor, and the second drives a 50- Ω load, such as a terminated coaxial transmission line.

The BCD data from the digital readout system are also provided. It may be desirable to have this information, although it is not used as position feedback for the stepper-motor control system. Therefore, these data are made available to the μ C and thus to the LSI-11 (through the GPIB).

APPENDIX F

PUBLICATION ON DETECTION OF DEFECTS IN COMPLEX SHAPES

DETECTION OF DEFECTS IN COMPLEX-SHAPE STRUCTURES

N. K. Batra
Systems Research Laboratories, Inc.
2800 Indian Ripple Road
Dayton, OH 45440

and

R. L. Crane
NDE Branch
AFWAL Materials Laboratory
Wright-Patterson Air Force Base, OH 45433

Abstract

A major limitation to the manufacture of net- and near-net-shape components is the inability to perform an adequate ultrasonic inspection of the part. The lensing of the sound beam in areas with small radii of curvature creates blind or uninspected zones. The fabrication of a mating part which would encapsulate the component could substantially alleviate this difficulty. To investigate this concept, a half-cylinder with a near-surface defect along with its mating part was fabricated and used in a parametric study of the important acoustic parameters. The two blocks were acoustically coupled with water and the transmission and reflection coefficients determined as functions of the angle of incidence. It was demonstrated that with adequate precautions, ultrasound can be transmitted into a complex-shape part, and the backscattered signal from defects may be detected for angles of incidence up to 80° . Results are compared with theoretical predictions. Application of the above technique to practical complex-shape structures is discussed.

1. INTRODUCTION

A major limitation to the fabrication of net-net-shape components is the current inability to perform adequate non-destructive inspection of the entire volume of the part ultrasonically. This is principally due to two phenomena which are inherent to such inspection process:

- 1) a "dead zone" caused by the large front-surface reflection which masks many reflections from small flaws just beneath the couplant/part interface, and
- 2) the lensing of the sound beam in areas of enhanced stress concentration. The use of a mating part which would encapsulate the component could substantially alleviate this latter difficulty. While some inspectors have used simple matching

shapes for nondestructive inspection of complex-shape parts, a quantitative description of the process and its advantages and disadvantages is lacking. This paper presents a description of an investigation into this concept.

2. THEORETICAL CONSIDERATIONS

The propagation of sound through layered media has been of longstanding interest to the seismological community.^(1,2) More recently the problem of acoustic-wave interaction with a fluid layer sandwiched between two solid half-spaces was examined by Chang, *et al.*,⁽³⁾ in their consideration of the ultrasonic reflectivity of fatigue

Presented at the 13th Symposium on NDE, April 22, 1981, San Antonio, TX; published in Conference Proceedings.

and duration are incident upon the fluid layer. This assumption is not violated in practice so long as tone bursts of acoustic energy are long in duration as compared to the travel time across the layer. Second, the angle of incidence must be small or the layer sufficiently thin to permit much of the incident beam to reverberate many times within the layer. If these conditions are met, a steady-state solution for each layer may be written in terms of longitudinal (ϕ) and transverse (ψ) wave potentials

$$\psi_3 = D_3 e^{i(\omega t - ax - e_3 y)}$$

(2)

$$\omega = 2\pi f$$

$$\begin{aligned} a &= k_1 \sin \theta_1 = k_2 \sin \theta_2 = k_3 \sin \theta_3 \\ &= \kappa_1 \sin \gamma_1 = \kappa_3 \sin \gamma_3 \end{aligned} \quad (3)$$


161

It should be noted that this law has two consequences. First, the incident and exiting longitudinal waves are parallel. Second, since the fluid media will nearly always have the lowest wave speed, the angle of incidence at either interface will always be less than the first critical angle.

The boundary conditions that must be satisfied in this problem are the continuity of the normal components of displacement (v_y) and stress (σ_{yy}). In addition, since the layer is a fluid, the tangential component of stress (τ_{xy}) must vanish at both interfaces ($y = 0$ and $y = h$). These conditions may be expressed as follows. At $y = 0$

$$\begin{aligned} v_y(1) &= \frac{\partial \phi_1}{\partial y} - \frac{\partial \psi_1}{\partial x} = \frac{\partial \phi_2}{\partial y} = v_y(2) \\ \sigma_{yy}(1) &= -\rho_1 \left[\omega^2 \phi_1 + 2b_1^2 \left(\frac{\partial^2 \psi_1}{\partial x \partial y} + \frac{\partial^2 \phi_1}{\partial x^2} \right) \right] \\ &= -\rho_2 \omega^2 \phi_2 = \sigma_{yy}(2) \\ \sigma_{xy}(1) &= \mu_1 \left(2 \frac{\partial^2 \phi_1}{\partial x \partial y} + \frac{\partial^2 \psi_1}{\partial y^2} - \frac{\partial^2 \psi_1}{\partial x^2} \right) = 0 \end{aligned} \quad (4)$$

A similar set of boundary conditions holds for $y = h$. Substituting Eq. (1) into the boundary conditions (4) yields six simultaneous linear equations. The unknowns B_1 , D_1 , A_2 , B_2 , A_3 , and D_3 are usually separated from the known quantity A_1 . However, in the present case, only the ratios of the amplitude functions are solved for, i.e., the longitudinal and shear reflection coefficients B_1/A_1 and D_1/A_1 and similarly the transmission coefficients A_3/A_1 and D_3/A_1 . It is a simple matter to write a computer program to solve the equations utilizing standard matrix methods. If the reflected and transmitted power densities are normalized to the area of the incident beam, then energy-flux coefficients for each wave are obtained. (7) Plots of typical computer-

generated data for conditions in this study are shown in Figs. 2-5. These will be dealt with more extensively later.

It is instructive to consider the special case of a fluid layer sandwiched between solid half-spaces. For this case, there are only four wave-potential equations and two boundary conditions at each interface. This leads to a matrix of four equations which can be solved with a moderate amount of effort. The equation for the transmission coefficient is

$$\frac{A_3}{A_1} = \frac{2c_3 \cos \theta_1 e^{i\eta}}{c_1 \cos \theta_3 [E^2 \cos^2(d_2 h) + F^2 \sin^2(d_2 h)]^{1/2}} \quad (5)$$

where $E = (\rho_3 d_1 / \rho_1 d_3) + 1$ and

$$F = (\rho_2 d_1 / \rho_1 d_2) + (\rho_3 d_2 / \rho_2 d_3).$$

If the phase factor $e^{i\eta}$ is ignored, then it is apparent that maxima in the transmitted energy occur for values of $d_2 h = (\omega h \cos \theta_2 / c_2)$ equal to an integer multiple of π . For the case of normal incidence, the resonant coupling of energy across the liquid layer is perfect, i.e., $A_3/A_1 = 1$. Since the transcendental terms that occur in the analysis of the solid/liquid/solid have the same argument as those in Eq. (5), it is not surprising that the resonant coupling occurs here too for values of $d_2 h = n\pi$, $n = 1, 2$, etc. This resonant condition can be satisfied by a suitable choice of the independent variables ω , h , and θ_1 , as demonstrated in Figs. 3-5. This phenomenon is well known in optics and is used in the coating of lenses to diminish glare. Our attempt here is to apply it to the transmission of sound in complex-shape objects.

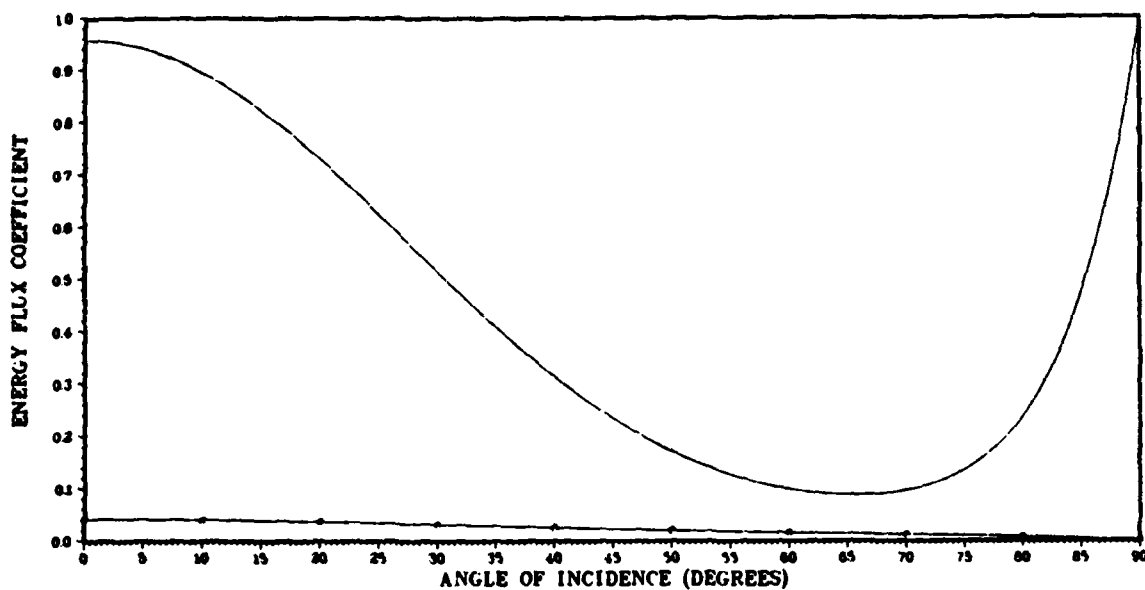


Figure 2. Transmitted (Curve with Circles) and Reflected Energy-Flux Coefficients Versus Angle of Incidence. A 10-MHz longitudinal wave is incident onto a 0.005-cm-thick water layer sandwiched between two aluminum half-spaces.

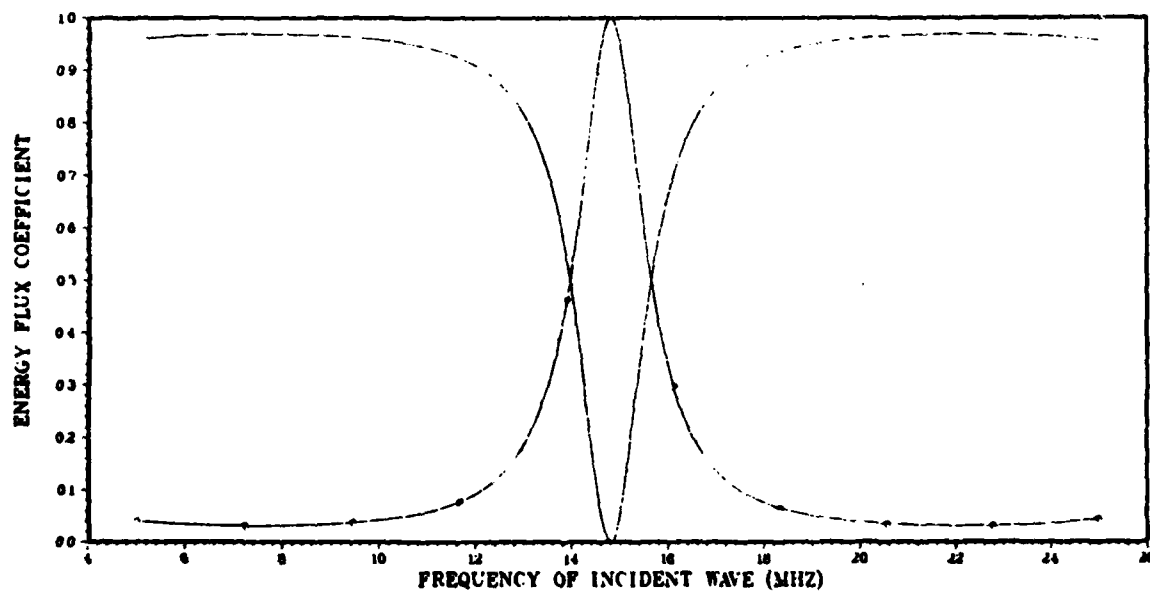


Figure 3. Transmitted (Curve with Circles) and Reflected Energy-Flux Coefficients Versus Frequency of the Incident Longitudinal Beam. The beam is incident normal to a 0.005-cm water layer sandwiched between two aluminum half-spaces.

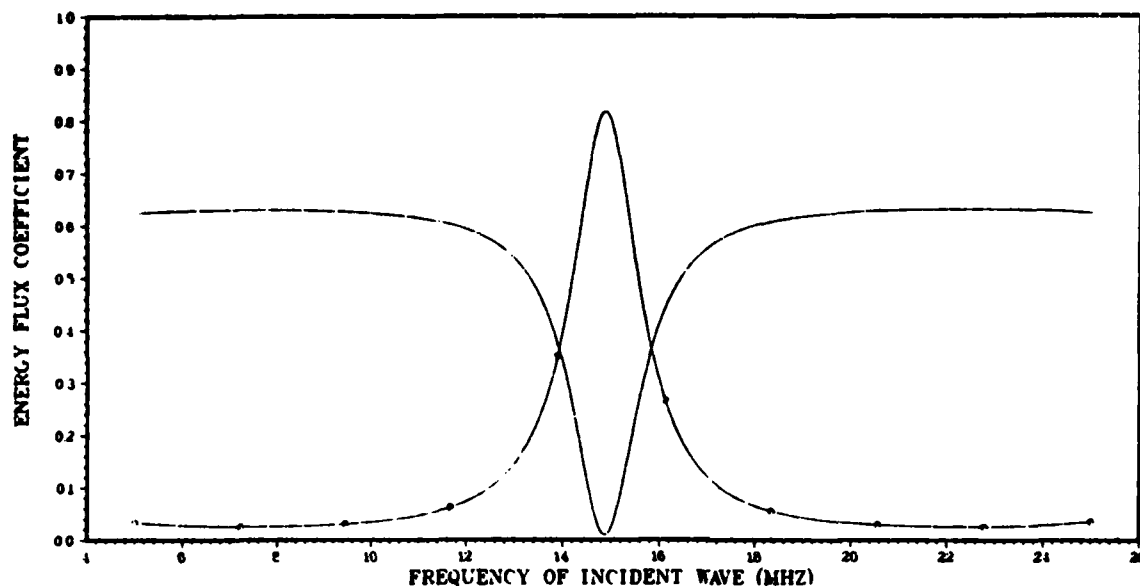


Figure 4. Transmitted (Curve with Circles) and Reflected Energy-Flux Coefficients Versus Frequency of the Incident Longitudinal Acoustic Beam. The angle of incidence is 25° , and the structure is aluminum/water (0.005-cm thick)/aluminum.

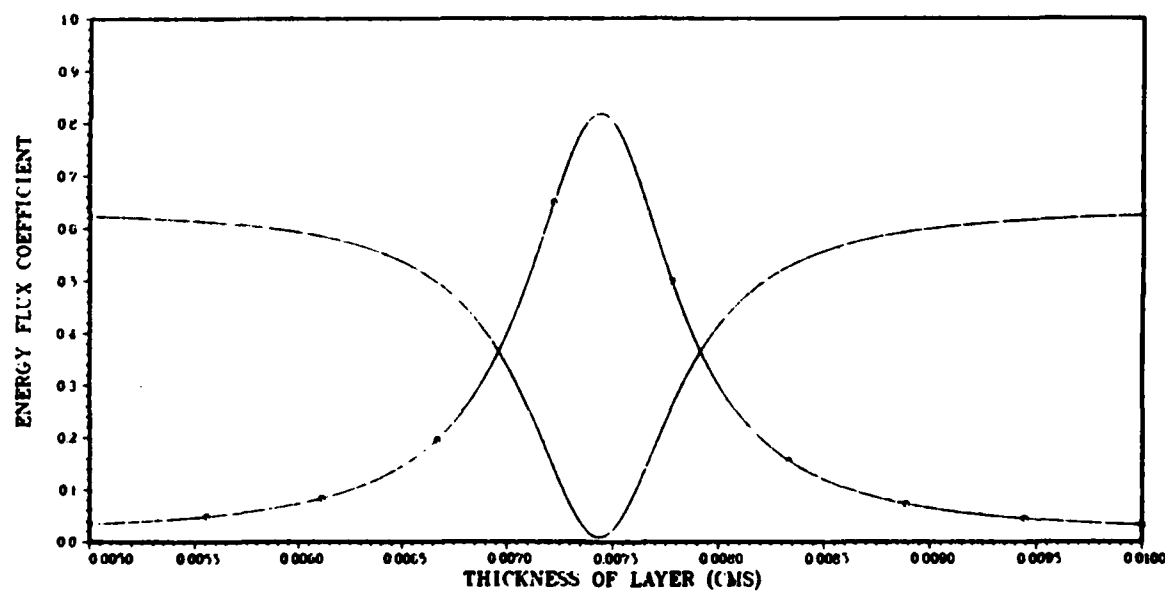


Figure 5. Transmitted (Curve with Circles) and Reflected Energy-Flux Coefficients Versus Thickness of Water Layer in an Aluminum/Water/Aluminum Structure. The angle of incidence is 25° for the longitudinal beam, and the frequency is 10 MHz.

3. EXPERIMENTAL PROCEDURE

For a systematic study of the transmission across a fluid layer sandwiched between two solid media, a semi-cylindrical specimen as shown in Fig. 6

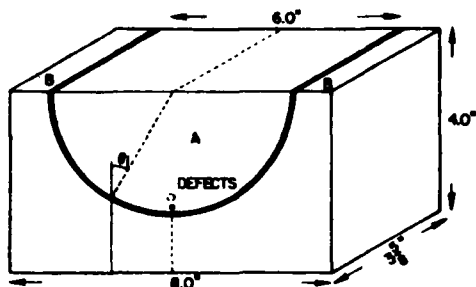


Figure 6. Simulated Defect in Complex-Structure; Structure is Shown with Mating Part.

was fabricated. The half-cylinder and its mate were carefully machined to be within ± 0.0127 mm (0.0005-in.) of perfect matching, including the 0.05-mm fluid layer. This specimen was designed to permit ease of variation of the angle of incidence. The layer thickness was held constant at 0.051 mm (0.0020 in.) via the surface tension of water. No measurable variations of layer thickness were noted for either changes in temperature or the pressure of the contact. These measurements were made with a cathetometer and are accurate to within 0.001 mm (0.0005 in.). The half-cylinder contained two 1.37-mm (0.054-in.) diam. side-drilled holes; one was placed 1.5 mm (0.006 in.) and the other 1.2 cm (0.5 in.) from the convex surface, and both were drilled to a depth of 3.8 cm (1.5 in.). The block was placed within a water bath that served both as a couplant and a delay line. In the experiments which utilized contact transducers, a couplant consisting of glycerin was used to ring the transducer onto the specimen. Because of the size of the aluminum-block specimen, the results were independent of the coupling method.

Since the interface fluid layer is very thin, the lateral deviation of the transmitted wave across the interface into the mated part is very small.

A schematic diagram of the instrumentation used in this series of experiments is shown in Fig. 7. The received

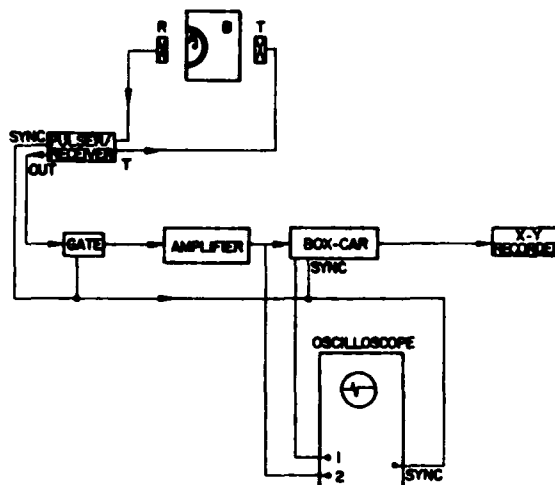


Figure 7. Experimental Setup for Detecting Defects in Complex-Shape Structures.

signal is gated and amplified by a Matec receiver (Model 625). A Princeton Applied Research box-car signal averager (Model 162) was used to improve the signal-to-noise ratio. The signal was recorded digitally with a Northern Scientific signal analyzer (Model 575) to permit convenient plotting with the x-y plotter.

4. RESULTS AND DISCUSSION

The results of the analytical development are plotted in Figs. 2 and 5. In Fig. 2, the longitudinal energy-flux coefficients are plotted as a function of angle of incidence to the layer for a 10-MHz acoustic beam. Only the longitudinal energy ratios are plotted; the shear components were calculated, but they are not plotted in the interest of clarity.

The rather smooth curves are a result of the fact that there are no critical angles for this structure. This would be true for most metal/water/metal systems. Figure 3 is a computer-generated plot of the energy-flux coefficients as a function of the frequency of the incident longitudinal acoustic wave. The angle of incidence is 0° , and the thickness of the water layer is 0.005 cm (0.002 in.). Note that the peak in the transmitted energy occurs at 14.8 MHz, as predicted by the equation $d_2 h = n\lambda$. Comparing the results in Figs. 3 and 4, it is apparent that the maximum is shifted to 14.9 MHz and decreased in amplitude as the angle of incidence is increased to 25° . Similarly if the frequency of the incident wave is held constant at 10 MHz and the thickness of the water layer is varied, then the curves in Fig. 5 are obtained. As in the previous case, the lower energy transfer is due to the 25° angle of incidence. The maximum in transmitted energy occurs for a thickness of 0.00745 mm (0.003 in.). In this investigation if either a layer thickness of 0.00745 cm with a 10-MHz longitudinal wave, or conversely, a 15-MHz beam with the 0.0051-cm water layer had been examined, then much larger transmitted signals would have been observed. Unfortunately, experimental difficulties did not permit the examination of either of these optimum situations. The available transducers limited the frequency of consideration to 10 MHz, and the surface tension of water and the geometry of the cylinder limited the layer thickness to 0.005 cm (0.002 in.).

To test the validity of the theoretical development, the levels of transmitted longitudinal energy were recorded as a function of angle of incidence using

the half-cylinder alone and then the half-cylinder with its mate. The

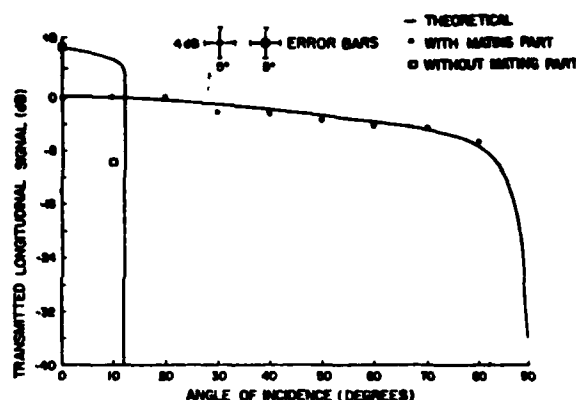


Figure 8. Transmitted 10-MHz Longitudinal Signal Through Near-Net-Shape Structure Versus Angle of Incidence. Solid line is theoretical curve. (●) are experimental points with mating part, and (□) are points without mating part. Note that practically no signal is transmitted for angles of incidence greater than first critical angle through complex-shape part without mating part.

transmitted acoustic signal was displayed on an oscilloscope and calibrated in dB. The normalized data for the half-transmitted longitudinal energy for the cylinder with its mate are plotted in Fig. 8. As expected for the half-cylinder in water, the transmitted longitudinal energy quickly falls to zero at the first critical angle at 13.8° . In all cases the theoretical curve was normalized to the normal-incidence energy level. The addition of the mating part to the half-cylinder dramatically changes the amount of energy transmitted to the receiving transducer for angles greater than 8° . However, at normal incidence the two additional interfaces and additional 2.54 cm of aluminum decreases the transmitted longitudinal signal by 7 dB. The amount of acoustic energy transversing the specimen remains

effectively independent of angle of incidence to -80° . While this could be predicted from the analytical data of Fig. 2, such good agreement is surprising, given the assumptions of the analysis. The frequency of the incident pulse is not constant; furthermore, the small beam diameter should have resulted in substantial deviations between theory and experiment at angles greater than 30° .

Because of the excellent agreement between theory and experiment for the transmission experiments, backscattering experiments were undertaken. For this purpose holes were drilled into each face of the half-cylinder and sealed to exclude water so that the cylindrical defects present nearly an infinite impedance mismatch. The half-cylinder and matching shape were placed in a water bath and the backscattered amplitude recorded as a function of angle of incidence. Data were normalized to normal-incidence data and plotted in Fig. 9. The agreement

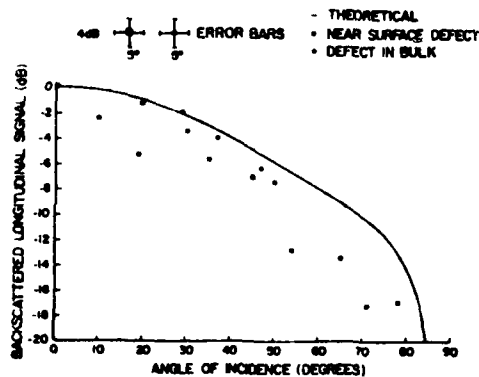
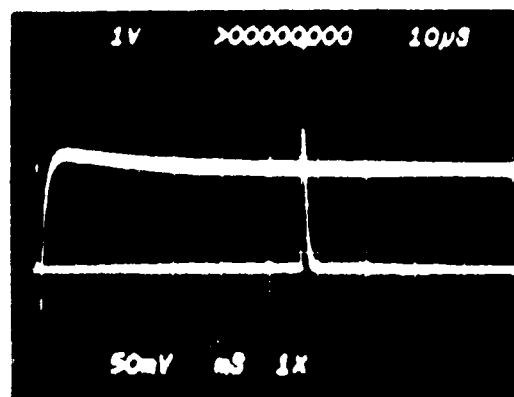


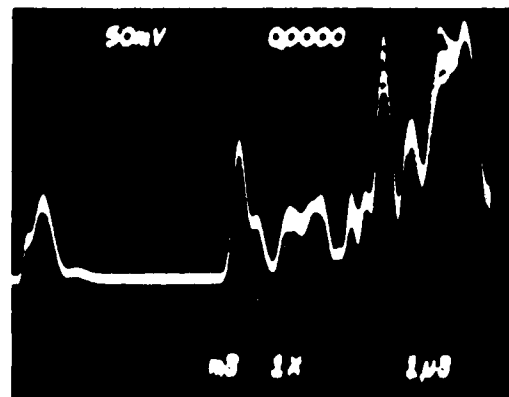
Figure 9. Backscattered, 10-MHz Longitudinal Signal from Defect in Complex-Shape Structure Versus Angle of Incidence. Solid line is theoretical curve, (●) indicate backscattered signal from near-surface defect, and (□) indicate backscattered signal from defect in bulk of complex-shape component.

between theory and experiment is quite good up to an angle of incidence of -50° . The agreement is due, in part, to the fact that the same-size cross-section reflector was seen by the acoustic beam, independent of the angle of incidence. It should be noted that the more rapid fall-off of the reflection signal is due to the fact that the acoustic beam must traverse the water layer twice, suffering losses due to reflection on each pass. It should also be noted that both side-drilled holes were temporally resolvable on the oscilloscope. While the reflection from the fluid layer is large, it is diminished by the present geometry to permit resolution of the backscattered signal from near-surface voids.

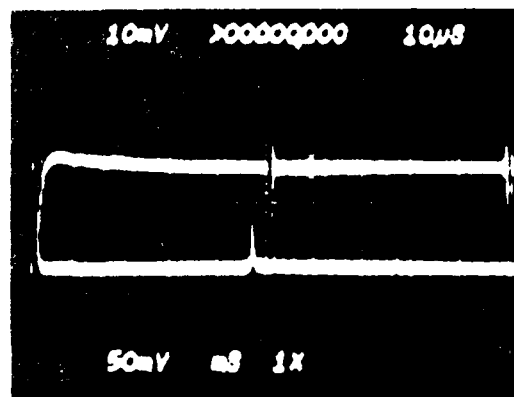
To demonstrate the practical convenience of using mating parts, a common 16-mm (5/8-in.) diam. bolt with a hexagonal nut, with opposite faces 24 mm (0.93 in.) apart, as its mate was examined in a water bath. For this purpose two matching transducers were aligned perpendicular to a face of the nut. When this assembly was placed in the water bath, the transmitted signal was clearly apparent at the proper time for transmission across a steel nut/bolt assembly (Fig. 10). In order to ensure that this is indeed a signal transmitted through the threaded bolt and not surface waves transmitted through the sides of the nut, the following experiment was performed. A nut, without bolt but with the hole covered to exclude water, was placed under water using contact transducers. No transmitted signal was observed (Fig. 11b). For the same experimental setup with nut and bolt, a large transmitted signal was noted in the appropriate time window (Fig. 11a).



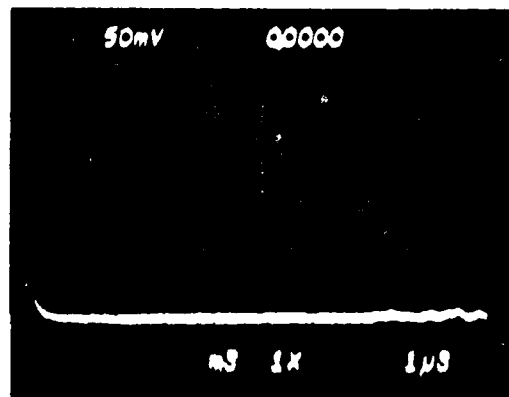
(a)



(a)



(b)



(b)

Figure 10. (a) Received Signal Through Water When Two Transducers are Aligned.

- (b) Transmitted Signal Through Assembly of Bolt and Nut Intercepting Transducers. Notice that signal is attenuated and arrives 11μsec earlier due to higher speed of sound in steel. Upper trace is pulse-echo signal from front surface of nut.

Figure 11. (a) Transmitted Signal Through Bolt and Nut Using Contact Transducers.

- (b) Transmission Through Airtight Nut. Absence of signal indicates absence of surface waves through sides of nut.

To examine further the potential of the above results for detecting the defects in the bolt, the backscattered signal from various interfaces was studied using the contact transducer on the nut and bolt in a water bath. Backscattered signals from both the front and the rear interfaces of the inside surface of the mating nut with the bolt were observed

at ~ 1.8 and $5.8 \mu\text{sec}$, respectively (Fig. 12). The temporal position of

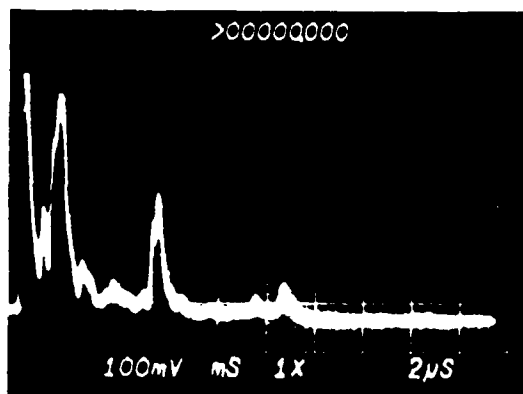


Figure 12. Backscattered Signal from the Front and Rear Interfaces of the Inside Surface of Mating Nut and Bolt. Calculated position of signals X_1 ($1.8 \mu\text{sec}$) and X_2 ($6.2 \mu\text{sec}$) agrees well with observed values of 1.8 and $5.8 \mu\text{sec}$, respectively. If there were defects in the bolt, the backscattered signal would be above the noise level and would lie between X_1 and X_2 .

these echoes agreed well with the calculated values of 1.8 and $6.2 \mu\text{sec}$, which demonstrates that an appreciable amount of acoustic energy can be transmitted into a structure having an irregular shape surface such as a threaded bolt.

At the conclusion of this study, the possibility of designing a matching part and couplant system that would transfer energy more efficiently at all angles of incidence was considered. The analysis of the interaction of acoustic waves and solid layers by Schmerr⁽⁸⁾ was used.

In this analysis the part and its mate were assumed to be aluminum, and the intermediate layer was specified as the inorganic salt ammonium di-hydrogen phosphate (ADP). Since both the longitudinal and shear-wave speeds for ADP are quite high,⁽⁹⁾ there should be efficient

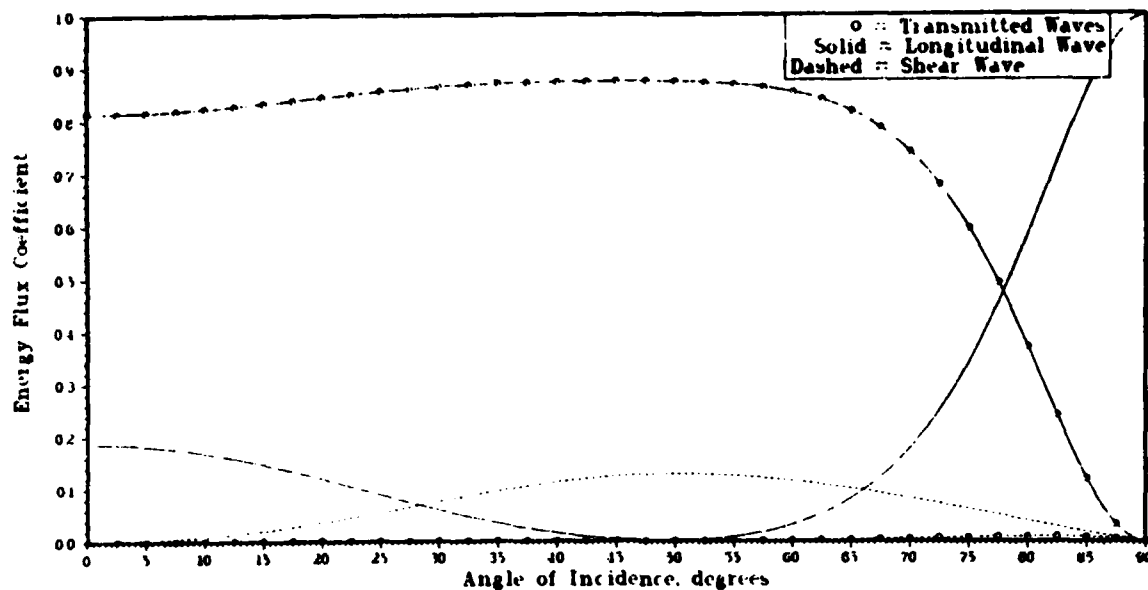
transfer of energy across a solid couplant layer. Highly efficient transmission of both longitudinal and shear energy is possible with such a system. This supposition is borne out by the results of the analysis shown in Fig. 13. The choice of an inorganic salt as a couplant is not so unreasonable as it might appear. Since many of these compounds melt at quite low temperatures (190°C for ADP), it is conceivable that they could be cast between a part and its mate and then separated after inspection, either by remelting or dissolving in water.

5. CONCLUSION

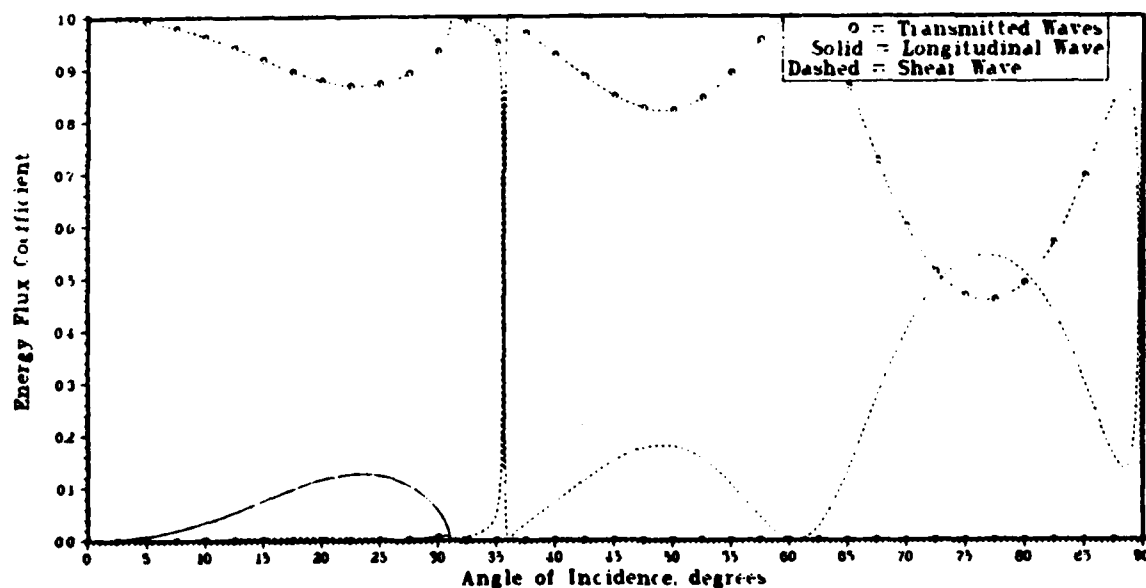
This study has demonstrated that it is theoretically, experimentally, and practically possible to utilize effectively the concept of a mating part to inspect ultrasonically complex-shape components. It is possible to inspect not only defects in areas that result in very high angles of incidence but also defects nearer the surface which are more easily detected because of the reduced interface reflections. In addition, the inspection can be conducted in a straightforward manner without any spatial reorientation of the transducers. Also considered, but not experimentally investigated, was the possibility of using a solid couplant layer between the component and its mate. This would permit the use of shear-wave inspection techniques with their inherently simpler interpretation.

ACKNOWLEDGEMENT

This work supported in part under USAF Contract F33615-80-C-5015.



(a)



(b)

Figure 13. (a) Transmission of 10-MHz Longitudinal Wave Incident upon Al/ADP (0.031 cm)/Al. Transmitted longitudinal wave is almost constant up to an angle of incidence of $\sim 60^\circ$.

(b) Transmission of 10-MHz Shear Wave Incident upon Al/ADP (0.031 cm)/Al.

REFERENCES

1. C. B. Officer, Introduction to the Theory of Sound Transmission (McGraw Hill, New York, 1958).
2. W. M. Ewing, W. S. Jardetzky, and F. Press, Elastic Waves in Layered Media (McGraw Hill, New York, 1957).
3. F. H. Chang, J. C. Couchman, and B. G. W. Yee, "The Effects of Stress on the Detection of Fatigue Cracks by Ultrasonic Techniques," in Proceedings of the Ninth Symposium on NDE (Southwest Research Institute, San Antonio, TX, 1973), pp. 423-433.
4. W. T. Thompson, "Transmission of Elastic Waves Through a Stratified Solid Medium," J. Appl. Phys. 21(21), 89 (1950).
5. W. T. Thompson, "The Equivalent Circuit for the Transmission of Plane Elastic Waves through a Plate at Oblique Incidence," J. Appl. Phys. 21(12), 1215 (1950).
6. L. M. Brekhovskikh, Waves in Layered Media (Academic Press, New York, 1960).
7. J. D. Achenbach, Wave Propagation in Elastic Solids (American Elsevier, New York, 1973), pp. 166-168.
8. L. W. Schmerr, Private Communication, Dept. of Engineering Science, Iowa State University, Ames, IA.
9. G. W. C. Kaye and T. H. Laby, Tables of Physical and Chemical Constants (Longman, London, 1959).

APPENDIX G

PUBLICATION ON ACOUSTIC DIFFRACTION FROM A CORRUGATED SURFACE

EFFECTIVE INTERFACIAL CONDITIONS FOR ELASTIC WAVE PROPAGATION
IN MEDIA SEPARATED BY THIN ROUGH LAYERS†

by

Adnan H. Nayfeh
Consultant, Systems Research
Laboratories, Dayton Ohio

ABSTRACT

Effective approximate interfacial continuity conditions are derived for the propagation of elastic waves in two solid media that are separated by a periodically rough-surfaced layer. For small layer thickness and roughness, superimposed effects in the forms of jumps in stresses and displacements across the layer's surfaces are obtained. When examined in conjunction with existing solutions for smooth interfaces these new conditions are found to predict and explain the various effects produced by roughness. These include the predictions of scattering directions, ranges (in frequency and angles of incidence) of surface wave excitations and mode conversions. Results are found to compare favorably with existing experimental data.

† Research is supported by NSF Grant CME 8021054 and AF Contract F33615-80-C-5015.

In Preparation for Publication.

1. Introduction

Studies of the propagation of elastic waves in layered media have long been of interest to researchers in the fields of geophysics and acoustics. Applications of these studies include such technologically important areas as the predictions of earthquakes, underground fault mapping, oil and gas exploration, architectural noise reduction, and the design of ultrasonic transducers. Common to all of these studies is the degree of the interactions between the layers, which manifest themselves in the form of reflection and transmission coefficients. These interactions depend, among many factors, upon the properties, direction of propagation, frequency of the incident waves, and number and nature of the interfacial conditions. Extensive works on this subject until the mid 60's have been reported in the literature as is evidenced from the books by Ewing, Jardetzky and Press¹ and Brekhovskikh².

In recent years further advances in the study of elastic waves in layered media have resulted from the analysis of the dynamic behavior of composite materials.³⁻⁵ Most of layered media, and in particular those which are man-made, are composed of thin layers bonded together with various agents. In assessing the influence of thin interfacial layers on the overall behavior of the medium we have developed an approximate analysis which ignores the details of the propagation process in the layer but includes its influence in a modifier to the stress interface continuity conditions.^{6,7} The basic premise which led to this approximation is that for very thin layers the detailed analysis may be unnecessary in light of the fact that the variations in displacements across their thicknesses will be small.

In most applications, the material surface interface exhibits some degree of roughness. Degrees of relative tolerance of roughness depend upon the specific applications. For sensitive applications, such as ultrasonics, rough

surfaces give rise to wave scattering and hence to mode conversion and attenuation. Rough surfaces also vary in severity; the distribution of roughness may be orderly or completely random. For an orderly (i.e. periodic) roughness the amplitude and period of the undulations completely specify the geometry. It is obvious that orderly rough surfaces have effective thicknesses whose values are the distances between the lowest and highest peaks.

The scattering of elastic waves by periodically rough surfaces have been the subject of numerous investigations both analytically and experimentally. La Casce and Tamarkin⁸ seem to be the first to present experimental data on the scattered elastic waves from a periodically rough surface. They compared their data with the then existing theories of Rayleigh,⁹ Eckart¹⁰ and Brekhovskikh.¹¹ All of these theories were approximate and dealt with nonpenetrating solids (i.e. in all of these the reflection coefficients were assumed unity). However, several recent investigations have been reported in the literature which deals with scattering from elastic rough surfaced media; these include the experimental investigations of Jungman *et al.*,¹² the theoretical and experimental investigations of Chuang and Johnson,¹³ the experimental investigating of Breazeale and Torbett¹⁴ and the theoretical investigations of Fokkema *et al.*¹⁵⁻¹⁸ Jungman *et al* presented several experimental results which clearly demonstrated the existence of sharp minima in the spectra of the scattered waves. These minima are similar to anomalies observed in 1902 by Wood and Optics¹⁹ and which had prompted the early theoretical investigations of Rayleigh and more recently of Hessel and Oliner.²⁰ Chuang and Johnson¹³ investigated theoretically and experimentally the scattering of elastic waves from liquid-solid interfaces using an extended boundary conditions approach. The elastodynamic diffractions from a variety of two media interfaces have also been studied by Fokkema and Van den Berg¹⁵ and by Fokkema¹⁶⁻¹⁸ using an integral equation representation.

Generally speaking periodic surfaces scatter waves along preferred directions. As will be seen later, these directions are uniquely defined by specifying the

frequency, direction of propagation and periodicity of the surface in accordance with a grating formula that is analogous to that used for the optical phenomenon.^{19,20} The amplitude of the scattered energy along these directions, will also depend upon the depth of the roughness, however.

In this paper we take a rather simple approach to characterize the influence of interfacial roughness. For surfaces whose roughness is assumed "small" (this will be quantified later, once the function characterizing the roughness is specified) we could construct an approximate model in which the effect of roughness manifests itself as a modifier to interfacial continuity conditions. Specifically it will result in jumps in the interfacial stresses which otherwise will not exist at flat interfaces. The nature of these jumps will be different from those due to the inclusion of a thin smooth layer. This occurs because the jumps due to roughness are geometric rather than material induced.

In order to maintain generality we shall derive effective interfacial conditions for two media which are separated by a thin, rough-surfaced layer of different material. We shall, however, restrict our model to the case in which both surfaces of the layer have the same roughness characteristics. Specifically, we assume that the surfaces of the layer are separated by a distance $2h$ (i.e., the effective layer thickness) and have identical one-dimensional periodicity which are in-phase, as shown in figure 1. This latter requirement is motivated by the desire to obtain as a special case results for two rough half-spaces in full contact.

The utility of our analysis will be tested by direct comparisons with existing theoretical and experimental results. As will be seen, our model readily predicts the scattering directions, and the conditions that favor the creation of anomalies and mode conversions. The prediction of the actual partitioning of scattered energy will require the development of solutions to the field equations in both major media subject to the derived effective continuity conditions. These solutions will be treated in subsequent investigations, however.

2. Formulation of the Problem

Consider a thin elastic, periodically rough surfaced layer of effective thickness $2h$ tightly bonded to two elastic half-spaces of different materials as shown in figure 1. A coordinate system is chosen with the origin located at the center line of the layer. Thus, the layer effectively extends from $-h \leq z \leq h$ with media 1 and 2 extend from $z = -h$ to $z = -\infty$ and $z = h$ to $z = \infty$, respectively. We shall assume that the roughness is one-dimensional and is described by the periodic function $g(x) = g(x+\Lambda)$ such that the mean value of $g(x)$, namely $\langle g(x) \rangle$, is zero. We restrict our analysis to the two-dimensional case where the incident and reflected waves are independent of y . Alternatively, all particle motions are confined to the x - z plane.

In order to study the wave motion in such system, we must solve the appropriate field equations in each of the three media incorporating the appropriate continuity conditions. These include the momentum and constitutive relation equations

$$\frac{\partial \sigma_{xx}}{\partial x} + \frac{\partial \sigma_{xz}}{\partial z} = \rho_\alpha \ddot{u}_\alpha \quad (1)$$

$$\frac{\partial \sigma_{zx}}{\partial z} + \frac{\partial \sigma_{xz}}{\partial x} = \rho_\alpha \ddot{w}_\alpha \quad (2)$$

$$\sigma_{xx} = (\lambda_\alpha + 2\mu_\alpha) \frac{\partial u_\alpha}{\partial x} + \lambda_\alpha \frac{\partial w_\alpha}{\partial z} \quad (3)$$

$$\sigma_{zx} = (\lambda_\alpha + 2\mu_\alpha) \frac{\partial w_\alpha}{\partial z} + \lambda_\alpha \frac{\partial u_\alpha}{\partial x} \quad (4)$$

$$\sigma_{xz} = \mu_\alpha \left(\frac{\partial u_\alpha}{\partial z} + \frac{\partial w_\alpha}{\partial x} \right). \quad (5)$$

Here $\alpha = 1, 0, 2$ designate medium 1, the layer and medium 2, respectively, σ_{xx} , σ_{zx} , and σ_{xz} are the stress components, u_α and w_α are the displacement components, ρ_α is the mass density, and λ_α and μ_α are the Lamé elastic constants of material α . The associated interfacial boundary conditions are then given by

$$\begin{aligned} u_1 &= u_0, \quad w_1 = w_0, \quad \sigma_{x1} v_x + \sigma_{xz1} v_z = \sigma_{x0} v_x + \sigma_{xzo} v_z, \\ \sigma_{xz1} v_x + \sigma_{z1} v_z &= \sigma_{xzo} v_x + \sigma_{zo} v_z, \quad \text{on } z = -h + g(x) \end{aligned} \quad (6a)$$

$$\begin{aligned}
u_0 &= u_2, w_0 = w_2, \sigma_{x0} v_x + \sigma_{xz0} v_z = \sigma_{x2} v_x + \sigma_{xz2} v_z \\
\sigma_{xz0} v_x + \sigma_{z0} v_z &= \sigma_{xz2} v_x + \sigma_{z2} v_z, \text{ on } z = h + g(x)
\end{aligned} \tag{6b}$$

where v_x and v_z are the components of the normal to the surface $g(x)$ along x and z directions, respectively.

In principle, solutions to Eqs. (1) - (5), subject to the continuity conditions (6a) and (6b), could be formally obtained. The results would be quite complicated algebraically, however. Furthermore, the detailed analysis of the wave motion in the layer would greatly complicate the problem. An attempt to obtain the exact solution to this problem could, therefore, obscure important features of the solution for a thin layer. However, since we are mainly interested in the case of a thin layer with small roughness (thickness and roughness amplitude small compared to the incident wavelength), we can proceed in a much less cumbersome way by including the effects of both the roughness and layer as nonzero homogeneous terms in the boundary conditions. To this end, we shall develop modified boundary conditions, referring to the reformulated problem as the "reduced model." This can be done as follows: first we develop modified conditions for the smooth thin layer and second we develop modified conditions for rough interfaces without layers and finally we combine both results to obtain the overall effective interface conditions.

3. The Reduced Model

3.1 The Smooth Thin Layer

In Ref. 7 we derived effective stress continuity relations in the forms of jumps in the values of normal and shear stresses at fluid-solid-layer-solid interface. In what follows we shall derive similar relations for all three solid media. To this end we particularize Eqs. (1) - (5) for a smooth layer by setting $\alpha = 0$. The stress continuity conditions in (6a) and (6b), therefore, become

$$\sigma_{z1} = \sigma_{z0}, \sigma_{xz1} = \sigma_{xzo} \text{ at } z = -h \quad (8a)$$

$$\sigma_{z0} = \sigma_{z2}, \sigma_{xzo} = \sigma_{xz2} \text{ at } z = h \quad (8b)$$

Since we assume that $2h$ is finite but small, variations in the displacements u_0 and w_0 across the thickness of the layer can be neglected.⁷ If accordingly

$\frac{\partial w_0}{\partial z}$ and $\frac{\partial u_0}{\partial z}$ are neglected and Eqs. (1) - (5) with $\alpha = 0$, are integrated for $\alpha = 0$ across the thickness of the layer according to

$$\bar{(\quad)} = \frac{1}{2h} \int_{-h}^h (\quad) dz, \quad (9)$$

one obtains

$$2h[(\lambda_0 + 2\mu_0) \frac{\partial^2 u_0}{\partial x^2} - \rho_0 \ddot{u}_0] = \sigma_{xzo}(-h) - \sigma_{xzo}(h) \quad (10)$$

$$2h[\mu_0 \frac{\partial^2 w_0}{\partial x^2} - \rho_0 \ddot{w}_0] = \sigma_{zo}(-h) - \sigma_{zo}(h) \quad (11)$$

Using the continuity relations (8a,b) Eqs. (10) and (11) may be recast into forms

$$2h[(\lambda_0 + 2\mu_0) \frac{\partial^2 u_0}{\partial x^2} - \rho_0 \ddot{u}_0] = \sigma_{xz1}(-h) - \sigma_{xz2}(h) \quad (12)$$

$$2h[\mu_0 \frac{\partial^2 w_0}{\partial x^2} - \rho_0 \ddot{w}_0] = \sigma_{z1}(-h) - \sigma_{z2}(h) \quad (13)$$

Equations (12) and (13) are significant since they are the only relations that reflect the effect of the layer via the modified longitudinal and shear

stress boundary conditions. In the absence of the layer ($h = 0$) they reduce to $\tau_{z1}(0) = \tau_{z2}(0)$, $\sigma_{xz1}(0) = \sigma_{xz2}(0)$, which are the classical stress continuity relations. With these approximations the displacement continuity conditions in Eqs. (6a,b) reduce to

$$u_0 = u_1 = u_2, w_0 = w_1 = w_2, \text{ on } z = 0 \quad (14)$$

In light of (14), to first order approximation in h , Eqs. (12) and (13) can be recast into the approximate forms

$$2h[(\lambda_0 + 2\mu_0) \frac{\partial^2 u_0}{\partial x^2} - \rho_0 \ddot{u}_0] = \sigma_{xz1}(0) - \sigma_{xz2}(0) \quad (15)$$

$$2h[\mu_0 \frac{\partial^2 w_0}{\partial x^2} - \rho_0 \ddot{w}_0] = \sigma_{z1}(0) - \sigma_{z2}(0) \quad (16)$$

For the case of a fluid-solid interface $\sigma_{xz1}(0) = 0$ and equations (15) and (16) reduce to those reported in Ref. 7.

3.b Rough Surface Modified Continuity Relations

In the absence of the layer (i.e., for $h = 0$) a single rough interface $g(x)$ will exist between media 1 and 2. Furthermore, the stress continuity conditions (6a,b) reduce to the single relation

$$\sigma_{x1} v_x + \sigma_{xz1} v_z = \sigma_{x2} v_x + \sigma_{xz2} v_z,$$

$$\sigma_{xz1} v_x + \sigma_{z1} v_z = \sigma_{xz2} v_x + \sigma_{z2} v_z, \text{ on } z = 0 \quad (17)$$

as opposed to the corresponding flat surface stress continuity relations

$$\sigma_{z1}^0 = \sigma_{z2}^0, \sigma_{xz1}^0 = \sigma_{xz2}^0, \quad (18)$$

where the superscript 0 is added to designate the flat surface stresses as illustrated in figure 2. From this figure we identify the normal $v(x)$ to the surface at the location x as

$$v = \sin \beta \underline{i} + \cos \beta \underline{k} \quad (19a)$$

with

$$\frac{dg}{dx} = g' = \tan \beta. \quad (19b)$$

Thus due to the one-dimensional nature of roughness, $v_y = 0$.

At this stage we insure the smallness of the roughness by requiring that $|g(x)|$ be small compared with incident wave length, and also that g' be small for a periodic surface this implies that the period of roughness is large compared with its depth). Accordingly we conclude that β is very small and hence (19) implies that

$$v_z \sim 1, v_x \ll 1. \quad (20)$$

Thus, using (19b), equations (17a,b) reduce, when retaining the first order of approximation v_{x1} to

$$\sigma_{xz1} - \sigma_{xz2} = (\sigma_{x2} - \sigma_{x1})g' \quad (21a)$$

$$(\sigma_{z1} - \sigma_{z2}) = (\sigma_{xz2} - \sigma_{xz1})g' \quad (21b)$$

which can also be combined to yield the extra relation

$$(\sigma_{z1} - \sigma_{z2}) = (\sigma_{x2} - \sigma_{x1})g'^2 \quad (22)$$

With reference to figure 2 we can expand σ_{ij} ($i, j = x, z$) in power series about σ_{ij}^0 which, for the lowest order of approximation in g , yields

$$\sigma_{ij} = \sigma_{ij}^0 + \frac{\partial \sigma_{ij}^0}{\partial z} g \quad (23)$$

If (23) is substituted into (21a) and (22) and the relation (18) is used we get, up to the first order of approximation in powers of g and g' ,

$$\sigma_{xz1} - \sigma_{xz2} = (\sigma_{x1}^0 - \sigma_{x2}^0) g' + \frac{\partial}{\partial z} (\sigma_{xz1}^0 - \sigma_{xz2}^0) g \quad (24)$$

$$\sigma_{z1} - \sigma_{z2} = \frac{\partial}{\partial z} (\sigma_{z1}^0 - \sigma_{z2}^0) g \quad (25)$$

Equations (24) and (25) constitute the modified interfacial stress conditions which hold across the rough surface between two media 1 and 2; they clearly display jumps in the values of the interfacial stresses. One can easily see that when $g = g' = 0$ they correctly reduce to the stress continuity condition required for flat interfaces.

3.c Combined Effective Conditions

Finally, for the case of combined thin layer with small rough surfaces, we may combine equations (24) and (25) with equations (15) and (16) and finally obtain the effective stress continuity relations

$$2h \left[\left(\frac{1}{\rho_0} + 2u_0 \right) \frac{\partial^2 u_0}{\partial x^2} - \rho_0 \frac{\partial^2 u_0}{\partial t^2} \right] = (\sigma_{xz1} - \sigma_{xz2}) - ((\sigma_{x1}^0 - \sigma_{x2}^0)g' + \frac{\partial}{\partial z} (\sigma_{xz1}^0 - \sigma_{xz2}^0)g) \quad (26)$$

$$2h \left[u_0 \frac{\partial^2 w_0}{\partial x^2} - \rho_0 \frac{\partial^2 w_0}{\partial t^2} \right] = (\sigma_{z1} - \sigma_{z2}) - \frac{\partial}{\partial z} (\sigma_{z1}^0 - \sigma_{z2}^0)g \quad (27)$$

Notice that the appropriate stress boundary conditions for the cases of flat interface without a layer; a flat surface with a layer; and a rough surface without a layer can be obtained by setting $h = 0$, $g = 0$; $g = 0$; and $h = 0$, respectively.

4. Discussions and Comparisons with Available Experimental Data

Equations (26) and (27) are significant since they constitute the only relations that reflect the influence of the thin layer and surface roughness. Examination of these equations indicate that both the layer and roughness give rise to dispersive effects in the propagating waves which would not exist in their absence. Furthermore, we see that terms which are multiplied by g and g' constitute induced (due to roughness) interface sources which propagate as body and surface waves on the media. These waves produce anomalies which, as will be seen later, propagate at discrete angles (the scattering directions). Thus, complete characterization of the approximate influence of interfacial layer and roughness, for a particular situation, can be obtained by solving the appropriate field equations subject to the continuity relations (26) and (27). It should be noted, however, that many of the anomalies attributed to roughness such as the scattering directions and the energy minima in the frequency spectrum of the scattered waves can be deduced by examining equations (26) and (27) in conjunctions with existing classical solutions for smooth surfaces. In what follows we shall concentrate on these effects while leaving the development of complete solutions to specific problems for subsequent investigations.

The dispersive effects due to the presence of a smooth layer on the propagation of surface waves along a liquid-solid interface was compared with experimental data in Ref. 7. Unfortunately, because of the paucity of experimental data on the combined influence of a thin, rough-surfaced layer, our following discussion will be limited to the influence of roughness where limited experimental data exist. For our comparisons we choose some representative data from the works of Jungman *et al.*¹² and Chuang and Johnson.¹³ Chuang and Johnson presented both experimental and theoretical diffraction efficiencies for a periodic rough water/acrylic interface. Longitudinal waves were incident from

the water at various angles. For future reference their zeroth order mode efficiencies versus angle of incidence is depicted in figure 3. In their investigations they choose an acrylic sample with symmetric sawtooth profile having a period, $\Lambda = 5$ mm, with a height of .52 mm. They performed experiments at the frequency 500 kHz , and their calculations assumed a longitudinal wave speed in water of 1493 m/s and longitudinal and shear speeds in the acrylic of 2660 and 1390 m/s, respectively. Jungman *et al* reported experiments on the reflection of normally incident waves from a variety of interfaces. For our purposes we depict their data for the reflection from a stainless steel-vacuum interface which is shown in figure 4. The stainless steel sample had a period of $\Lambda = 1500 \mu$, the height of 500μ and longitudinal and shear speeds of 5790 and 3100 m/s, respectively.

In order to compare our analysis with these data, we must also utilize the corresponding reflection coefficients from smooth liquid-solid and solid-vacuum interfaces. These are readily available in the literature as²

$$R_{ls} = \frac{(2\xi^2 - k_2^2)^2 - 4\xi^2(\xi^2 - k_1^2)^{1/2}(\xi^2 - k_2^2)^{1/2} - i k_2^4/\rho [(\xi^2 - k_1^2)/(\xi^2 - k_2^2)^{1/2}]}{(2\xi^2 - k_2^2)^2 - 4\xi^2(\xi^2 - k_1^2)^{1/2}(\xi^2 - k_2^2)^{1/2} + i k_2^4/\rho [(\xi^2 - k_1^2)/(\xi^2 - k_2^2)^{1/2}]} \quad (28a)$$

where $\rho = \rho_f/\rho_s$

and

$$R_{sv} = \frac{(2\xi^2 - k_2^2)^2 - 4\xi^2(\xi^2 - k_1^2)^{1/2}(\xi^2 - k_2^2)^{1/2}}{(2\xi^2 - k_2^2)^2 + 4\xi^2(\xi^2 - k_1^2)^{1/2}(\xi^2 - k_2^2)^{1/2}} \quad (29)$$

where ξ is the propagation wave number, k_1 and k_2 are the longitudinal and shear wave numbers for the solid and k_f is the wave number for the fluid. The wave number ξ is related to the appropriate wave number k of the medium from which the wave is incident by

$$\xi = k \sin \theta_i \quad (30)$$

where θ_i is the angle of incidence and $k = k_f$ for the incident wave from the fluid is required by (25) and $k = k_s$ for the incident wave from the solid as required by (29). As a reminder, ξ enters the solutions (23) and (29) from the assumed form of solutions to the field equations

$$\phi_i(x, z) = \phi_i(z) e^{i\xi x} \quad (31)$$

where ϕ_i stands for any of the stresses or displacements.

To this end setting $h = 0$, equations (26) and (27) reduce to

$$\sigma_{xz1} - \sigma_{xz2} = (\sigma_{x1}^0 - \sigma_{x2}^0)g' - \frac{\partial}{\partial z}(\sigma_{xz1}^0 - \sigma_{xz2}^0)g \quad (32)$$

$$(\sigma_{z1} - \sigma_{z2}) = \frac{\partial}{\partial z}(\sigma_{z1}^0 - \sigma_{z2}^0)g \quad (33)$$

Since any periodic function with period Λ can be expanded in a Fourier series, $g(x)$ may be represented by

$$g(x) = \sum_{n=-\infty}^{\infty} g_n e^{i\gamma n x} \quad (34)$$

where

$$\gamma = \frac{2\pi}{\Lambda} \quad (35)$$

and

$$g_n = \frac{1}{\Lambda} \int_{-\frac{\Lambda}{2}}^{\frac{\Lambda}{2}} g(x) e^{-i\gamma n x} dx \quad (36)$$

If we substitute (34) into (32) and (33) we get

$$\sigma_{xz1} - \sigma_{xz2} = (\sigma_{x1}^0 - \sigma_{x2}^0) \sum_{n=-\infty}^{\infty} i\gamma n g_n e^{i\gamma n x} - \frac{\partial}{\partial z} (\sigma_{xz1}^0 - \sigma_{xz2}^0) \sum_{n=-\infty}^{\infty} g_n e^{i\gamma n x} \quad (37)$$

$$\sigma_{z1} - \sigma_{z2} = \frac{\partial}{\partial z} (\sigma_{z1}^0 - \sigma_{z2}^0) \sum_{n=-\infty}^{\infty} g_n e^{i\gamma n x} \quad (38)$$

In light of (31), the relations (37) and (38) suggest, that, once the admissible wave number ξ of the smooth surface is known, the inclusion of the

periodic roughness would require effective wave number in the form

$$\xi_n = \xi + \gamma n \equiv k \sin \theta_i + \gamma n \quad (39a)$$

By utilizing the various relations $\xi_n = k \sin \theta_n$, $k = 2\pi/\lambda$, $\lambda = c/f$, we can rewrite (39a) in the alternate forms

$$\sin \theta_n = \sin \theta_i + \frac{2\pi n}{\lambda k} \quad (39b)$$

$$\sin \theta_n = \sin \theta_i + \frac{n\lambda}{\lambda} \quad (39c)$$

$$\sin \theta_n = \sin \theta_i + \frac{nc}{\lambda f} \quad (39d)$$

where k , λ , c and f are the incident, wave-number, wave-length, speed and frequency respectively. The alternate forms (39a-d) are known as the grating formula for the propagation of incident body waves on the rough interface. Thus, there exist as many discrete wave numbers as the number of harmonic components of the surface. Each of these wave numbers give rise to a scattered body wave (mode). These modes will propagate at the discrete angles θ_n . It is obvious, however, that the number of the possible propagating body modes is restricted by the condition $|\sin \theta_n| \leq 1$. The results (39) are in full agreement with the theoretical and experimental predictions reported on figure 6 of Ref. 13.

The condition $|\sin \theta_n| = 1$, ($\theta_n = 90^\circ$) defines the cutoff modes which are scattered in the fluid along the interface. The cutoff modes seem to create surface anomalies which propagate with the fluids wave speed regardless of the specific properties of the solids substrate. With reference to equation (39d) trajectory of the optimum conditions for this mode to occur is depicted in the form of variations of θ_i with $\lambda f/n$ in figure 5. Predictions of this figure agree well with the experimental results reported in Refs. 12 and 14. Specifically, for the combinations $c = 1.49 \times 10^5$ cm/sec, $\lambda = .0178$ cm, $n = 1$ and $f = 6$ MHz used in Ref. 14, figure 4 shows that the cutoff mode anomaly occurs at the angle of incidence 23.3° which is comparable to the experimental result of 22.5° reported in ref. 14. Moreover, for $\theta_i = 0$ under which Jungman et al conducted their experiments, the

cutoff anomalies can occur according to figure 4 only at $\Lambda f/n = 1.49 \times 10^5$ cm/sec. Thus, for $n = 1$ and $\Lambda = .02$ cm, this yields the frequency $f = 7.45$ MHz which should be compared with the value 7.7 MHz at which the first anomaly occurs for the water-brass interface as depicted in figure 7 of Ref. 12. Similarly, for $n = 1$ and $\Lambda = .15$ cm one obtains $f = 1$ MHz which should be compared with the experimental value of 1.1 MHz where the first anomaly occurs for water-steel interfaces as depicted in figure 8 of ref. 12. Notice that these frequencies are independent of the substrates properties. The remaining anomalies displayed on figures 7, 8 and 10 of ref. 12 are excited by the creation of interfacial sources which propagate as body waves in the media as will be discussed below.

As was pointed out earlier the roughness induced interfacial sources can also excite waves that propagate along the interface. The conditions for these excitations can be deduced from the vanishing of the denominator of the appropriate reflection coefficient. This amounts to obtaining the zeros of the surface wave characteristic equation. Since according to (39a) each harmonic components of the periodic surface has its own wave number ξ_n , the n^{th} component will excite a surface wave when ξ_n (or c_n) coincides with the wave numbers ξ_s (or c_s) required to excite the surface wave on the smooth surface. Here c_n and c_s are the wave speeds of the n^{th} component and the surface wave on the smooth surface.

Specializing ξ_n to ξ_s , substituting $\xi_s = 2\pi f/c_s$ and $k = 2\pi f/\Lambda$ in (39a) we get the surface wave grating formula

$$\frac{c}{c_s} = \sin \theta_i + \frac{n\Lambda}{\Lambda f} \quad (40)$$

The value of c_s can be easily calculated for any smooth surface. In particular, for the two specific cases of water-acrylic ($c = 1.493 \times 10^5$ cm/sec) and stainless steel-air ($c = 5.79 \times 10^5$ cm/sec) interfaces they are calculated as 1.045×10^5 and 2.99×10^5 cm/sec, respectively. Accordingly, specializing (40) to these two specific cases we get

$$1.43 = \sin \theta_i + \frac{1.493 \times 10^5 n}{\Lambda f} \quad (41a)$$

$$1.94 = \sin \theta_1 + \frac{3.79 \times 10^5}{\lambda f} n \quad (41b)$$

for the water-acrylic and steel-air cases, respectively. Notice that, as long as the left hand side of the relation (40) is larger than unity, no zero order ($n = 0$) propagating body wave will be able to excite surface modes; this is because the condition $|\sin \theta_1| \leq 1$ will be violated. Under these circumstances this means that body waves will not excite waves along smooth interfaces as it happened to be the case of the two specific examples under consideration. In fact, for liquid-solid interfaces incident body waves from the liquid will not generate surface waves in the solid as long as the incident wave speed is higher than the shear wave speed in the solid. Furthermore, for solid-air interfaces body waves incident from the solid will not generate surface waves along its free smooth surface. For periodically rough interfaces, on the other hand, incident body waves can excite surface waves since the conditions (41a,b) can be easily satisfied for various modes. To this end in figure 6 we depict surface wave excitation trajectories (for various modes) in the plane consisting of angle of incidence vs frequency for the water-acrylic. In figure 7 we similarly depict the trajectories for the stainless steel-air interface.

The appropriate values of Λ used in the calculations were given earlier in this section. Any point on these trajectories correspond to an excited surface wave anomaly. In particular the point located at 56° and $.5 \text{ MHz}$ on the first evanescent mode ($n = 1$) of figure 6 agrees with the only existing experimental and theoretical predictions of fig. 7 of Ref. 13. Similarly for $\theta_1 = 0$, figure 7 predicts the frequency locations of the two excited surface wave anomalies by the first two evanescent modes ($n = 1, 2$) as was reported experimentally by Jungman *et al.*¹²

Finally, the mode conversions observed by Jungman *et al.* for normal incident waves on the periodic interface can be explained using the present model as follows: For normal incident waves from a solid onto its free smooth boundary the reflection coefficient will be unity. This can also be seen by setting

$\xi = 0$ (or equivalently $\theta_i = 0$) in equation (30). For periodic surfaces, however, setting $\theta_i = 0$ in the relation (39a) yields

$$\xi_n = \frac{2\pi n}{\Lambda} \quad (42)$$

which if replaces ξ in (30) yields the reflection coefficient for the n^{th} mode as

$$R_n = \frac{(2\xi_n^2 - k_2^2)^2 - 4\xi_n^2(\xi_n^2 - k_1^2)^{1/2}(\xi_n^2 - k_2^2)^{1/2}}{(2\xi_n^2 - k_2^2)^2 + 4\xi_n^2(\xi_n^2 - k_1^2)^{1/2}(\xi_n^2 - k_2^2)^{1/2}} \quad (43)$$

Since for the smooth surface the normal incident reflection coefficient is unity, inspection of (43) suggests that R_n will change its sign from 1 to -1 when

$$\xi_n = \frac{k_2}{\sqrt{2}} \quad (44)$$

Substituting from (44) into (42) and using the relation $k_2 = 2\pi f/c_2$, where c_2 is the shear wave speed in the solid, one gets

$$f = \frac{\sqrt{2} \pi c_2}{\Lambda} \quad (45)$$

For the first evanescent mode ($n = 1$), using the steel shear wave speed

$c_2 = 3.10 \times 10^5$ cm and $\Lambda = .15$ (see Ref. 12), Eq. (45) yields the frequency

$f = 2.93$ MHz which should be compared with the experimentally predicted value of 2.8 MHz in Ref. 12.

AD-A145 990

RESEARCH IN QUANTITATIVE NDE TECHNIQUES(U) SYSTEMS
RESEARCH LABS INC DAYTON OH RESEARCH APPLICATIONS DIV
D A STUBBS ET AL. MAR 84 SRL-6575 AFMAL-TR-84-4026
F33615-80-C-5015

3/3

UNCLASSIFIED

F/G 13/8

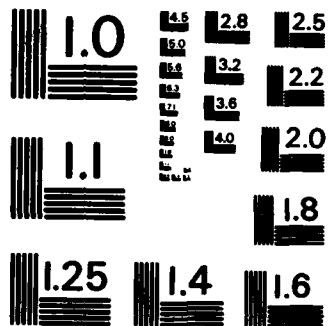
NL



END

FILMED

DTIC



MICROCOPY RESOLUTION TEST CHART
NATIONAL BUREAU OF STANDARDS-1963-A

REFERENCES

1. M. Ewing, W. Jardetsky and F. Press, Elastic Waves in Layered Media. McGraw Hill, New York (1957).
2. L.M. Brekhovskikh, Waves in Layered Media, Academic Press, New York (1960).
3. G.A. Hegemier, G.A. Gurtman and A.H. Nayfeh, Int. J. Solids Structures, 9, 345-414 (1973).
4. A.H. Nayfeh and G.A. Gurtman, J. Appl. Mech. 41, 106-110 (1974).
5. A.H. Nayfeh and J.I.J. Loh, Journal of Sound and Vibration 55(1), 19-26 (1977).
6. A.H. Nayfeh and E.A. Nassar, J. Appl. Mech. 45, 822-828 (1978).
7. A.H. Nayfeh, D.E. Chimenti, L. Adler, and R.L. Crane, J. Appl. Phys. 52, 4985-4994 (1981).
8. E.O. LaCasce, Jr. and P. Tamarkin, J. Appl. Phys. 27, 138-148 (1956).
9. Lord Rayleigh, Theory of Sound, Dover Publications, New York (937).
10. C. Eckart, J. Acoust. Soc. Am. 25, 566-570 (1953).
11. L.M. Brekhovskikh, J. Exptl. Theoret. Phys. USSR, 23, 275-304 (1952).
12. A. Jungman, L. Adler and G. Quentin, J. Appl. Phys. 53(7), 4673-4679 (1982).
13. S.L. Chuang and R. Johnson, J. Acoust. Soc. Am. 71(6) 1368-1376 (1982).
14. M.A. Breazeale and M.A. Torbett, Appl. Phys. letters, 29(8) 456-458 (1976).
15. J.T. Fokkema and P.M. van den Berg, J. Acoust. Soc. Am 62, 1095-1101 (1977).
16. J.T. Fokkema, Wave Motion 2, 375-393 (1980).
17. J.T. Fokkema, Wave Motion 3, 33-48 (1981).
18. F.T. Fokkema, Wave Motion 3, 145-157 (1981).
19. R.W. Wood, Phil. Mag. 4, 396-410 (1902).
20. A. Hessel and A.A. Oliner, Appl. Opts. 4(10) 1275-1297 (1965).

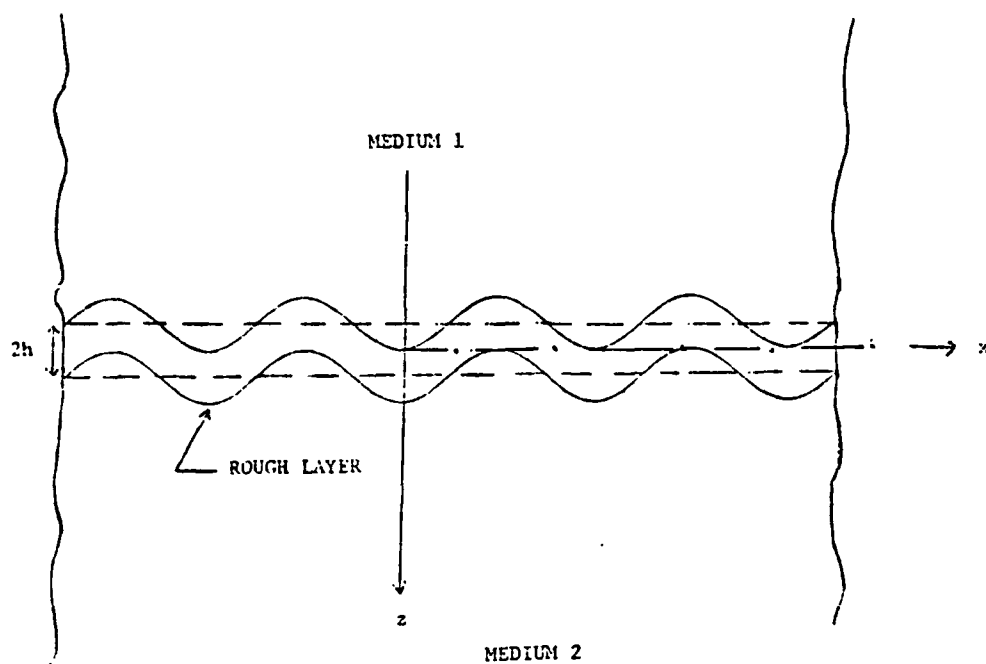


FIG. 1. LAYERED MEDIA GEOMETRY

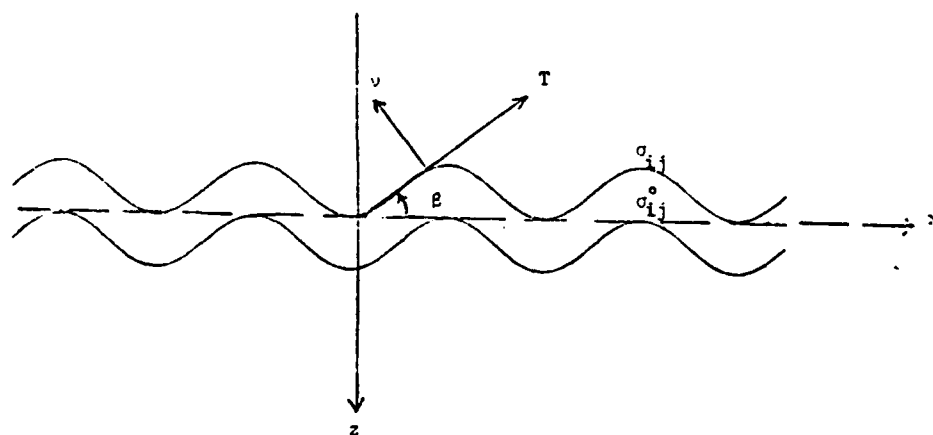


FIG. 2. ROUGH SURFACE GEOMETRY

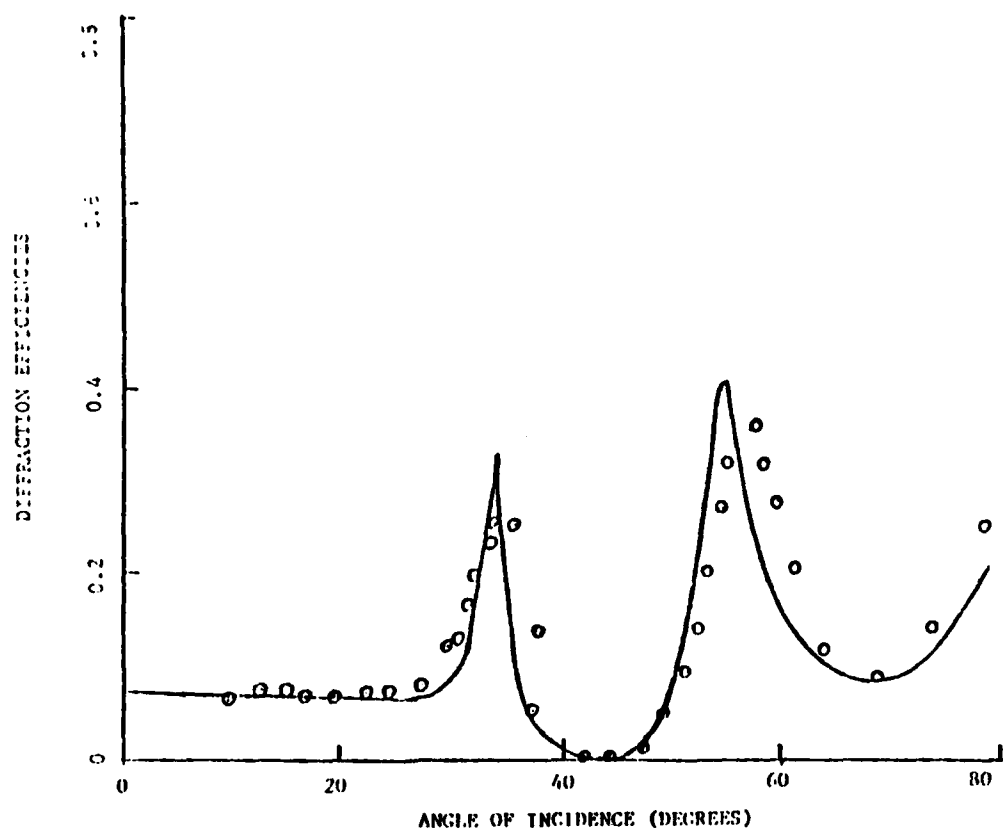


FIG. 3. DIFFRACTION EFFICIENCIES OF THE ROUGH SURFACE OF THE ZEROth ORDER. THE SOLID LINE IS THE THEORY AND THE DOTS ARE EXPERIMENT. (AFTER CHAUNG AND JOHNSON, REF. 17).

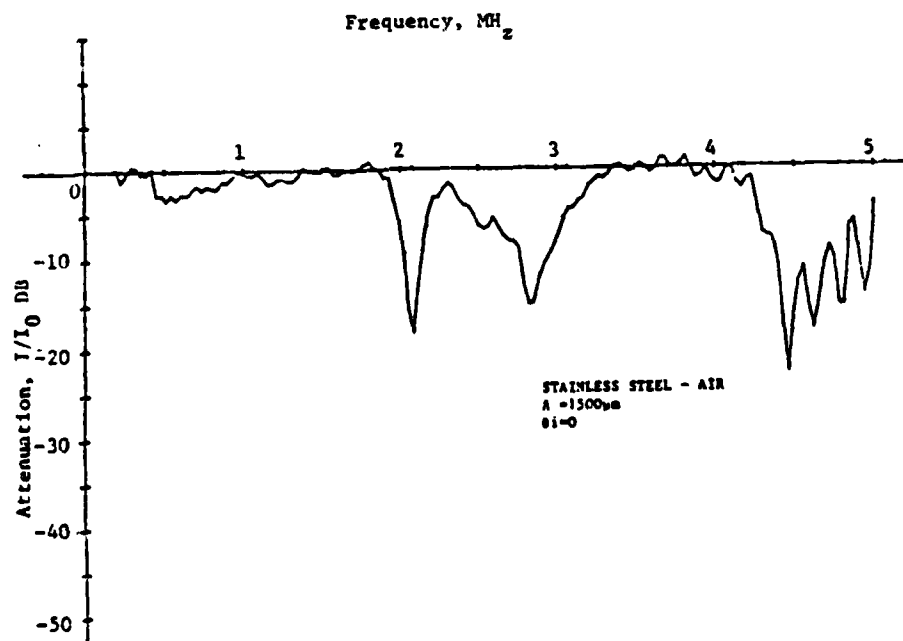


FIG. 4 BACKSCATTERED SPECTRUM, FROM A STEEL-AIR INTERFACE, $\theta_i = 0$ (AFTER JUNGHAN ET AL REF. 12)

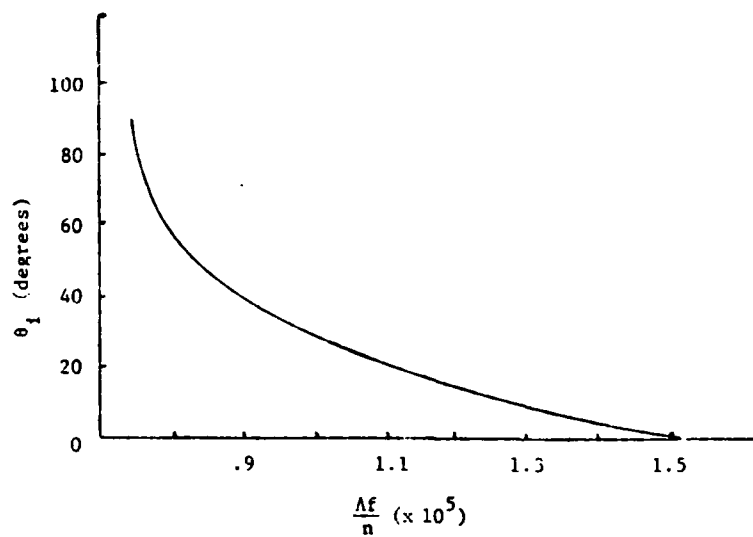


FIG. 5. TRAJECTORY OF THE CUTOFF MODES

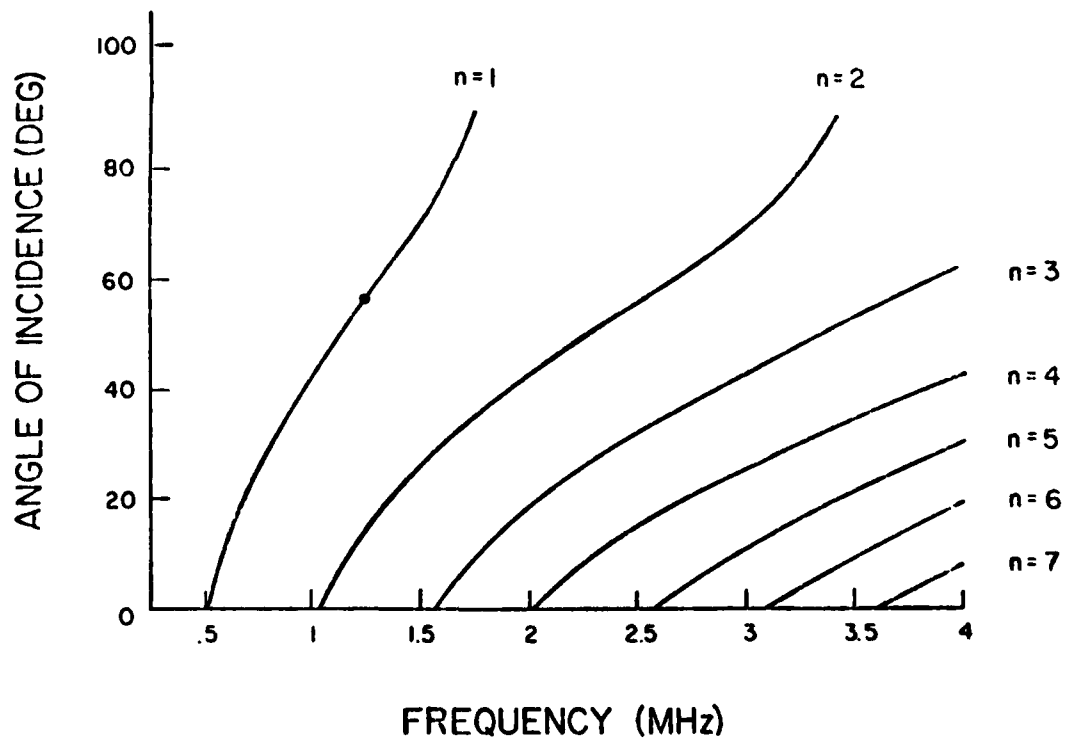


FIG. 6

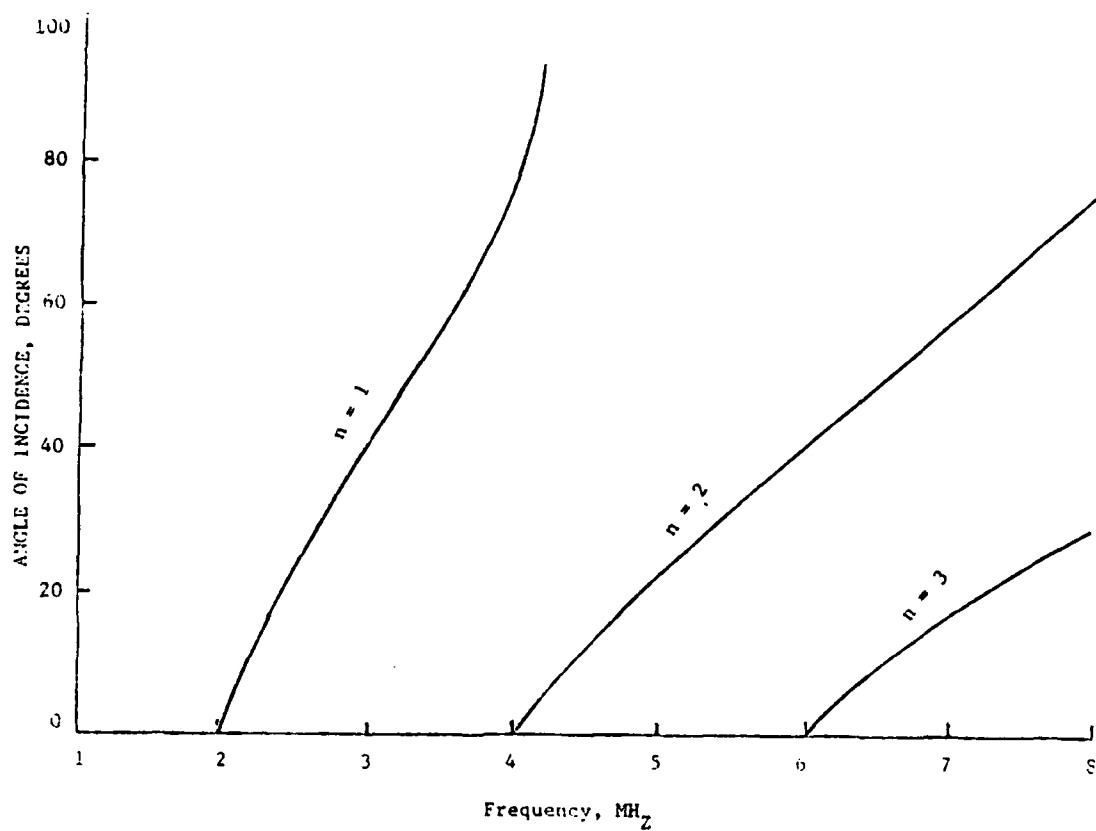


FIG. 7. SURFACE WAVE EXCITATION TRAJECTORIES FOR STAINLESS STEEL/AIR INTERFACE.

APPENDIX H

PUBLICATION ON HIGH-IMPEDANCE BACKINGS FOR BROADBAND ULTRASONIC TRANSDUCERS

Multiphase backing materials for piezoelectric broadband transducers

Y. Bar-Cohen,^{a)} D. A. Stubbs, and W. C. Hoppe

Systems Research Laboratories, Inc., 2800 Indian Ripple Road, Dayton, Ohio 45440-3696

(Received 8 June 1983; accepted for publication 29 January 1984)

A multiphase, high-impedance damper to be used as a backing material for broadband piezoelectric transducers is described. The use of three or more phases, including a high-impedance alloy matrix, allows dampers to be made reproducibly which have acoustical impedances in the range of $20\text{--}45 \times 10^5 \text{ g/(cm}^2\text{·s)}$. A simple model based upon the elastic properties of the constituents is described which was developed to predict the impedance of multiphase mixtures. This model was experimentally verified for two- and three-phase mixtures. Using this model a combination of tungsten, copper, and an indium-lead alloy was chosen as an optimum transducer backing. A backing made from these constituents was pressed onto a 10-MHz, PZT-5A blank, and the results of the pulse-echo response are presented.

PACS numbers: 43.88.Ar, 43.85.Bh, 43.88.Fx

INTRODUCTION

The most effective method of generating and receiving ultrasonic waves is through the use of piezoelectric crystals. An electrical impulse applied to such crystals excites a relatively long duration acoustic pulse due to the relatively high Q of the crystals. For NDE applications such as depth resolution and defect characterization, a need exists for acoustic pulses of very short duration. To reduce the pulse duration, a backing material having an impedance closely matched to that of the crystal should be used.¹ For practical purposes, i.e., for obtaining a transducer of small size, the backing material must have a very high attenuation to eliminate back reflections. As a common practice, two-phase mixtures consisting of a matrix and a powder filler are used.²⁻⁸ The matrix generally has a high absorption coefficient, and the filler induces strong scattering; this combination provides the required high attenuation. The proper selection of materials and volume fractions allows matching of the backing material and crystal impedances.

Tungsten/epoxy is the most widely used backing⁶⁻⁸ for commercial transducers due to its potential in providing a wide range of impedance values z between 3×10^5 and $100 \times 10^5 \text{ g/(cm}^2\text{·s)}$ and its sufficiently high attenuation. The characteristic curve of impedance versus volume fraction (Fig. 1) shows a very slow increase in impedance for increasing volume fraction of tungsten up to about 0.8, above which a sharp increase occurs. Matching the impedances of crystals such as PZT and LiNbO₃, having a specific acoustic impedance z , of about $30\text{--}35 \times 10^5 \text{ g/(cm}^2\text{·s)}$, requires a high-volume fraction of tungsten which is subject to physical packing limits. Moreover, the steep slope in this range makes reproducibility of backing impedance difficult to obtain. These problems are largely due to the low impedance of the epoxy matrix. These obstacles are common to most two-

phase combinations which serve as potential backing materials.³ In this recent work, the effect of using three phases or more upon the reduction of the curve steepness is examined. The use of a high-impedance matrix which eliminates the need for a high-volume fraction of fillers has also been investigated and will be discussed.

I. ANALYTICAL ASPECTS

The acoustic impedance of a composite backing material consisting of a matrix and a micro-size particulate can be described using analytical expressions which were developed for mechanical elastic theories.⁹ This approach is feasible when the particle size is much smaller than the acoustic wavelength, namely, $ka \ll 1$, where k = wavenumber and a = average particle radius. The analytical expressions for the impedance of a multiphase mixture are being treated in

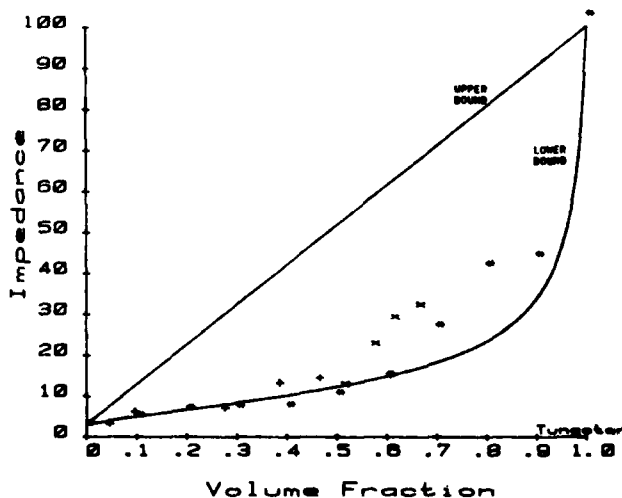


FIG. 1. Characteristic curves of impedance [$\times 10^5 \text{ g/(cm}^2\text{·s)}$] versus volume fraction of tungsten/epoxy. Upper and lower impedance bounds are drawn as solid lines. Experimental data from this research and the reported literature are plotted [where + : present research, o: (Ref. 7), and x: (Ref. 6)].

^{a)} Presently with McDonnell Douglas Corp. at Douglas Aircraft Company, Dept. C1-E29, 3855 Lakewood Blvd., Long Beach, CA 90846.

this paper as an extension of the expression for a mixture having two phases.

The specific acoustic impedance z of an isotropic homogeneous material is defined as

$$z = \rho c, \quad (1)$$

where ρ = density and c = acoustic bulk velocity which is expressed as

$$c = \left(\frac{E}{\rho} \frac{(1 - \nu)}{(1 + \nu)(1 - 2\nu)} \right)^{1/2}, \quad (1a)$$

where E = Young's modulus and ν = Poisson's ratio.

The effective acoustic impedance of a composite consisting of two different phases is determined by multiplying the effective density by the effective acoustic velocity. The effective density obeys the rule of mixtures,

$$\rho = f_1 \rho_1 + f_2 \rho_2, \quad (2)$$

where f is the volume fraction, ρ is the density, and the indices 1 and 2 indicate the respective constituents.

The effective velocity is determined by the effective values for the elastic modulus E and Poisson's ratio, ν . No rigorous solution which is dependent upon particle size, shape, distribution, and individual elastic parameters is feasible for a general particulate composite. Due to this limitation, it is common practice to determine the upper and lower bounds for the required elastic properties. The upper bound given in Eq. (3) has been determined by Paul⁹ who applied the principle of minimum potential energy to a two-phase composite mixture.

$$E < \frac{1 - \nu_1 + 2m(m - 2\nu_1)}{1 - \nu_1 - 2\nu_1^2} E_1 f_1 + \frac{1 - \nu_2 + 2m(m - 2\nu_2)}{1 - \nu_2 - 2\nu_2^2} E_2 f_2, \quad (3)$$

where

$$m = \frac{\nu_1(1 + \nu_2)(1 - 2\nu_2)f_1 E_1 + \nu_2(1 + \nu_1)(1 - 2\nu_1)f_2 E_2}{(1 + \nu_2)(1 - 2\nu_2)f_1 E_1 + (1 + \nu_1)(1 - 2\nu_1)f_2 E_2}. \quad (3a)$$

In the special case where $\nu_1 = \nu_2 = m$, the upper bound on the elastic modulus [see Eq. (3)] follows the rule of mixtures. The lower bound, which was determined by Paul using the principle of least work, is given by

$$E > (f_1/E_1 + f_2/E_2)^{-1}. \quad (4)$$

The bounds for Poisson's ratio are determined by the bounds on the elastic and shear moduli. The bounds for the shear modulus μ of the composite were derived by Paul using the methods stated above. These methods yield expressions for the effective μ which have the same form as those for the effective E . The expression for Poisson's ratio is determined using the bounding values of E and μ , as follows:

$$\nu = E/2\mu - 1. \quad (5)$$

The upper and lower bounds for the acoustic impedance of a tungsten/epoxy composite are shown as the solid lines in Fig. 1. A collection of data from the literature and this research is also plotted. The data follow closely the lower bound of the impedance curve up to 0.6 volume fraction of

tungsten. Above this volume fraction, the data seem to be somewhat above the lower bound; however, the lower bound gives a more accurate prediction than the upper bound.

The simplicity of using the lower bound for z combined with the fact that it approximately fits the existing data suggest its use as a simple model to predict the impedance of other particulate composites. A further test of this model was made using stainless steel 303L powder with a particle size less than 150 μm and a matrix of methylmethacrylate. The data and model predictions are shown in Fig. 2. The deviation of the model and data above 0.7 volume fraction of stainless steel is due to packing limitations causing porosity. This porosity is not accounted for in the predetermined volume fractions.

In order to obtain composite backings with impedances matching PZT or LiNbO₃ using the lower-bound model, it is necessary to have a tungsten/epoxy mixture with a volume fraction of tungsten > 0.75 . Since the maximum theoretical packing density of single-size spherical particles is 0.74, it is necessary to use different size particles to obtain the desired volume fraction. Further, because of the high slope of the impedance curve in this range, reproducibility of impedance becomes a problem. This also makes fine adjustments of the impedance difficult.

In an attempt to eliminate the problems due to the steep slope and high-volume-fraction filler, the authors used the model to evaluate the impedance of various mixtures. These problems were partially overcome using a high-impedance matrix. However, evaluation of two-phase theoretical results using practical types of fillers showed that the use of a high-impedance matrix was not sufficient. A study of the use of more than one type of filler showed a significant reduction in the slope of the characteristic impedance curves. Moreover, it provided a greater degree of freedom in the design of proper matching and attenuation for backing material.

A generalization of Eqs. (1), (2), (4), and (5), which are expressions for two-phase mixtures, has been made for mul-

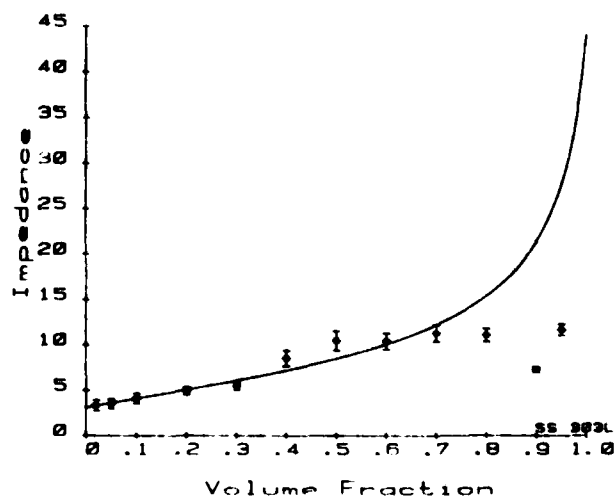


FIG. 2. Theoretical lower-bound impedance curve and experimental data plotted for a two-phase mixture of stainless steel 303L and MMA [impedance units are $\times 10^6 \text{ g/(cm}^2\text{.s)}$].

tiphase mixtures as shown in Eq. (6). The resulting expression for the impedance is given in Eq. (7).

$$E = \left(\sum_{i=1}^N \frac{f_i}{E_i} \right)^{-1}, \quad \mu = \left(\sum_{i=1}^N \frac{f_i}{\mu_i} \right)^{-1}, \quad \rho = \sum_{i=1}^N f_i \rho_i, \quad (6)$$

where

$$z > E \rho \left(\frac{2 - (E/2\mu)}{(E/2\mu)(3 - E/\mu)} \right)^{1/2}, \quad (7)$$

and N = the number of constituents. The applicability of this modified expression for multiphase mixtures has been tested experimentally.

II. EXPERIMENTAL

Test samples consisting of various types of fillers were made to evaluate the model for three-phase composites. For each sample powders with particle sizes of less than $150 \mu\text{m}$ were mixed in a V-shaped rotary mixer and then poured into a 1.905-cm-i.d. mold. The powder mixture was heated to 120°C under a pressure of $2.76 \times 10^7 \text{ Pa}$ (4 kpsi) and under vacuum to allow outgassing of the air from the mixture. At 120°C the pressure was increased to $2.76 \times 10^8 \text{ Pa}$ (40 kpsi), and the mixture was then heated to 165°C . The mold was air cooled under pressure, and the composite could be easily ejected. All samples obtained using this technique were tested visually and found to be a cohesive solid with evenly distributed constituents.

The impedance of each sample was determined by measuring its density and longitudinal sound velocity. The experimental setup consisted of a Panametrics 5052 PR pulse/receiver, a water tank, and a 2.25-MHz broadband transducer. The measurements of the sound velocity were conducted in a pulse-echo mode and the measurement of attenuation in a through-transmission mode. The time difference between the echoes from the front and back surfaces was measured using a Tektronix oscilloscope and a model 7D11 digital delay. The resultant velocity measurements had a typical relative error of 5%.

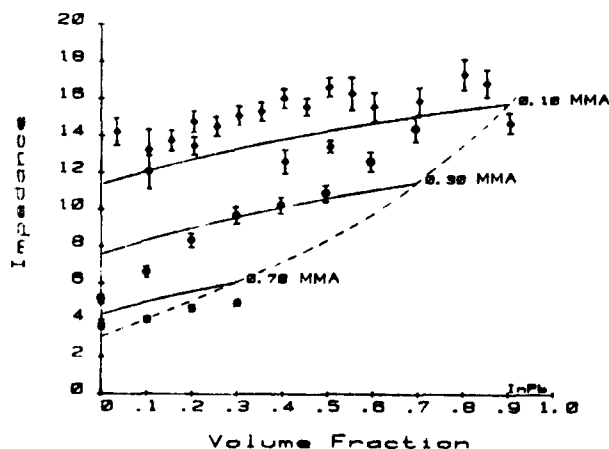


FIG. 3. Theoretical curves [see Eq. (6)] and corresponding experimental data for three-phase mixtures of Al/InPb 50-50 solder/MMA. The three solid lines represent 0.1, 0.3, and 0.7 volume fractions of the matrix MMA, and the x axis represents the volume fraction of InPb. For slope comparison, the two-phase impedance curve is plotted in dashed lines.

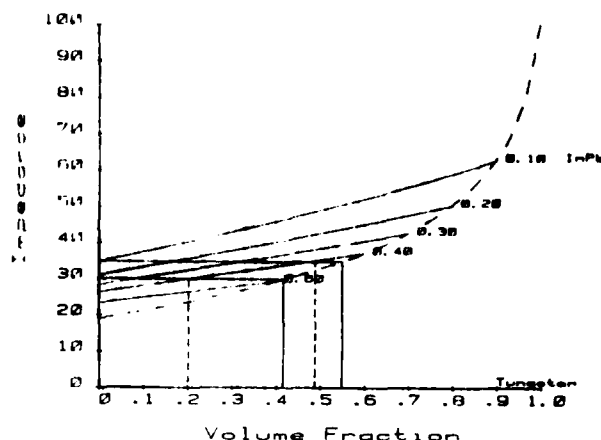


FIG. 4. Theoretical curves for a three-phase mixture of tungsten, copper, and InPb 50-50 solder. Solid horizontal lines represent selected volume fractions of the matrix InPb. Dashed curve shows impedance of two-phase mixture of W/InPb. Set of vertical solid lines shows range of tungsten that can be used to obtain impedances between 30 and $35 \times 10^3 \text{ g/(cm}^2\cdot\text{s)}$ for two-phase mixture of W/InPb. Set of vertical dashed lines shows applicable range of tungsten using three-phase mixture with 0.4 volume fraction of InPb matrix.

III. RESULTS AND DISCUSSION

Given the theoretical analysis, various combinations of matrix and fillers have been evaluated using a computer program based on Eq. (6). To select candidate materials for multiphase mixtures, the authors used Sec. IV—acoustic velocity data of Ref. 10 as a guide. To obtain characteristic curves enabling the prediction of the impedance of mixtures, families of curves were drawn with continuous changes of the volume fraction of the two phases, while the third (or higher number) constituents were varied in a discrete fashion. Each curve should be interpreted individually, where the volume fraction (f_3) of one phase is constant and its value is marked to the right of the curve, as can be seen in Figs. 3 and 4, for example. The effect of varying f_1 , i.e., $(1 - f_3 - f_2)$ on the characteristic impedance can be read along the abscissa up to the maximum volume fraction of $(1 - f_3)$.

TABLE I. Reproducibility of impedance of a three-phase mixture (0.70 MMA, and varying volume fractions of Al and InPb).

Volume fraction of InPb	$Z_{exp} \pm \sigma$ [$\times 10^3 \text{ g/(cm}^2\cdot\text{s)}$]	$Z_{av} \pm \sigma$ [$\times 10^3 \text{ g/(cm}^2\cdot\text{s)}$]	Coefficient of variation (σ/Z_{av})
0.00	3.45 ± 0.15	3.57 ± 0.13	0.04
	3.60 ± 0.16		
	3.65 ± 0.16		
0.10	3.82 ± 0.14	4.04 ± 0.27	0.07
	4.02 ± 0.15		
	4.27 ± 0.17		
0.20	3.59 ± 0.10	4.26 ± 0.76	0.18
	4.54 ± 0.15		
	4.64 ± 0.16		
0.30	4.83 ± 0.15	5.01 ± 0.31	0.06
	4.93 ± 0.15		
	5.28 ± 0.18		

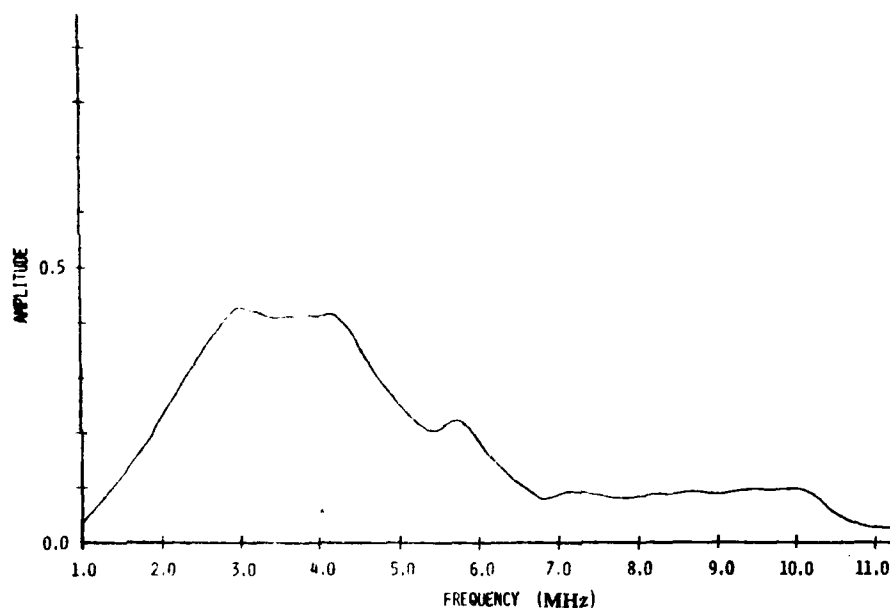
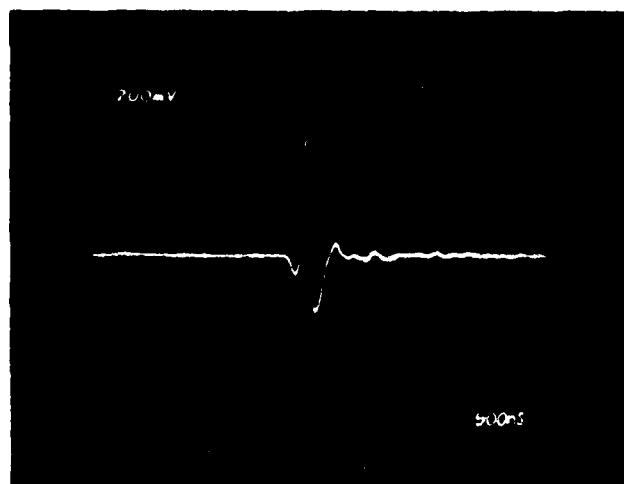


FIG. 5. (a) Pulse-echo response of a PZT-5A 10-MHz piezoelectric crystal backed with three-phase mixture of W/Cu/InPb. Time base scale is 500 ns/div; vertical scale is 200 mV/div. (b) Frequency response of transducer in (a). Vertical scale in amplitude in arbitrary units; x axis represents frequency in megahertz.

To verify the theory, a three-phase combination has been made consisting of methylmethacrylate (MMA) as a matrix (melting point of about 149 °C) and two fillers—solder alloy InPb 50–50 particles (less than 44 μm in diam) and aluminum particles (less than 44 μm in diam). Experimental results for 0.1, 0.3, and 0.7 volume fractions of MMA show a reasonable agreement with theoretical predictions, as can be seen in Fig. 3. The set of three curves in Fig. 3 demonstrates the much lower slope of the data, as compared to the two-phase case of MMA/InPb 50–50 (dashed line). To determine the reproducibility, three samples of each volume fraction of solder, consisting of 0.7 MMA, were prepared. The test results are compared in Table I and show a 8.8% average coefficient of variation.

Once the feasibility of reducing the steepness of the curve was demonstrated, efforts were dedicated to obtaining a high-impedance mixture in the range $30 \times 10^5 < z < 35 \times 10^5 \text{ g}/(\text{cm}^2\cdot\text{s})$. A study of the acoustic properties of various polymers¹⁰ revealed that none had an impedance greater than $3.75 \times 10^5 \text{ g}/(\text{cm}^2\cdot\text{s})$. Although metals such as Sn, Pb, or Cu might be used as a matrix, packing and cohesion problems

occur.⁴ A low melting point solder alloy InPb 50–50 was found to meet the requirements for a suitable matrix. This alloy has a z equal to $20 \times 10^5 \text{ g}/(\text{cm}^2\cdot\text{s})$, a melting point of about 190 °C, and is available in particulate form of less than 44 μm in diam. The dashed line in Fig. 4 is a graph of impedance versus volume fraction for a mixture of tungsten and this solder. As expected, there is a considerable increase in the overall impedance compared to tungsten/epoxy (see Fig. 1).

Copper, which has an intermediate impedance of $42 \times 10^5 \text{ g}/(\text{cm}^2\cdot\text{s})$, was chosen as the third constituent and produced the set of solid lines shown in Fig. 4. Each curve has a lower slope than the corresponding two-phase curve in the given impedance range. For any volume fraction of matrix, the addition of the third phase lowers the impedance slightly, but the ability to “fine tune” the impedance is greatly enhanced. When using a tungsten/solder mixture, the desired impedance range of $30 \times 10^5 < z < 35 \times 10^5 \text{ g}/(\text{cm}^2\cdot\text{s})$ is covered by varying the volume fraction of tungsten in the range 0.42–0.55. However, for the three-phase mixture using, for example, a solder matrix volume fraction of 0.4, this

impedance range is covered by varying the volume fraction of tungsten from 0.19–0.49 which is more than twice the range of that of the two-phase mixture.

The attenuation values of the mixtures consisting of W/Cu/InPb 50–50, having an impedance in the range $30 \times 10^5 < z < 35 \times 10^5 \text{ g/(cm}^2\text{-s)}$, were in the range of 10–20 dB/cm, compared to the value of 25 dB/cm which can be obtained with epoxy/tungsten. However, it is probable that the attenuation could be increased by adding an attenuative filler such as rubber particles. A backing consisting of tungsten/copper/solder, having a predicted impedance of $32 \times 10^5 \text{ g/(cm}^2\text{-s)}$ and experimental value of $32.4 \times 10^5 \text{ g/(cm}^2\text{-s)}$ has been fabricated. This backing has been formed directly on a PZT-5A 10-MHz crystal, recommended for fundamental operation, by pressing it in the die in a single-stage process to produce a transducer. In cases of defects in the damper, such as porosity or cracking, repair can be made simply by reheating and recompressing the crystal-backing combination. As an added benefit, the electrical conductivity of the backing has eliminated the common difficulty of accessing the back electrode. Testing this transducer in a pulse-echo mode demonstrated the potential of the multi-phase backing technique, as shown in Fig. 5(a), where the very short duration signal obtained is displayed. The frequency response of the transducer is given in Fig. 5(b), where its broad bandwidth is demonstrated ($Q = f/\Delta f = 1.09$).

IV. CONCLUSIONS

The use of a three-phase mixture as a backing material for ultrasonic transducers effectively broadens the transducer bandwidth with high reproducibility. Analytical results were obtained using an effective lower-bound elastic modulus and were verified experimentally for a mixture of Al/InPb 50–50/MMA. It was shown that mixtures consisting of two fillers and a high-impedance matrix allow the

elimination of the major problems encountered with two-phase mixtures, specifically low reproducibility and low impedance. A backing material consisting of a mixture of W/InPb 50–50/Cu formed directly onto a PZT-5A, 10-MHz crystal produced a broadband signal with a significantly low Q .

ACKNOWLEDGMENTS

The authors wish to express their gratitude to Dr. R. L. Crane, AFWAL/MLLP, Wright-Patterson Air Force Base, Ohio, for his supportive comments and to Steve Pitman of SRL for his support in the preparation of the samples. This work was supported under USAF Contract No. F33615-80-C-5015.

¹M. Redwood, "The Study of Waveforms in the Operation and Detection of Short Ultrasonic Pulses," *Appl. Mater. Res.* 76–84 (Nov. 1963).

²V. M. Merkulova, "Acoustical Properties of Some Solid Heterogeneous Media at Ultrasonic Frequencies," *Sov. Phys.-Acoust.* 11(1), 55–59 (1965).

³P. J. Torvik, "Note on the Speed of Sound in Two Phase Mixtures," *J. Acoust. Soc. Am.* 48, 432–433 (1970).

⁴S. Rokhlin, S. Golan, and Y. Gefen, "Acoustic Properties of Tungsten-Tin Composites," *J. Acoust. Soc. Am.* 69, 1505–1506 (1981).

⁵V. V. Sazhin, F. I. Isaenko, and V. A. Konstantinov, "Mechanical Damper for Ultrasonic Probes," *Sov. J. NDT* 9(5), 505–507 (1973).

⁶J. D. Larson and J. G. Leach, "Tungsten-Polyvinyl Chloride composite Materials—Fabrication and Performance," 1979 Ultrasonic Symposium Proceedings, IEEE Cat. 79 CH14822SU, pp. 342–345.

⁷S. Lees, R. S. Gilmore, and P. R. Kranz, "Acoustic Properties of Tungsten-Vinyl Composites," *IEEE Trans. Sonics Ultrason.* SU-20(1), 1–2 (1973).

⁸K. F. Bainton and M. G. Silk, "Some Factors which Affect the Performance of Ultrasonic Transducers," *Br. J. NDT* 22, 15–20 (1980).

⁹B. Paul, "Prediction of Elastic Constant of Multiphase Materials," *Trans. Met. Soc. AIME* 218, 36–41 (1960).

¹⁰D. E. Chimenti and R. L. Crane, "Elastic Wave Propagation through Multilayered Media," AFML-TR-79-4214 (Air Force Materials Laboratory, Wright-Patterson Air Force Base, OH, April 1980).

END

FILMED

10-84

DTIC